Quantifying the AGN-driven ionised outflows in local Ultra-luminous Infrared Galaxies

Robert A. W. Spence

Department of Physics & Astronomy

The University of Sheffield

A thesis submitted in candidature for the degree of

Doctor of Philosophy at the University of Sheffield

September 2018

Declaration

I declare that no part of this thesis has been previously accepted, or is currently being submitted, for any other degree, diploma, certificate or qualification in this University or elsewhere.

This thesis is my own work unless otherwise stated.

The following chapters are based on these publications:

Chapter 3:

Spence et al. (2016), "*No evidence for large-scale outflows in the extended ionized halo of ULIRG Mrk 273*", published in MNRAS in March 2016.

Chapter 4:

Spence et al. (2018), "*Quantifying the AGN-driven outflows in ULIRGs (QUADROS) III: measurements of the radii and kinetic powers of 8 near-nuclear outflows*", published in MNRAS in May 2018.

Acknowledgements

The first person I need to thank is my beautiful wife, Rachel, for putting up with me over the last four years, and supporting my decision to pursue a PhD. It has not always been easy, but I hope I can go on to prove it was worth it. I love you, always. Next, I thank my parents, Karen and Allan Spence, for supporting my education and allowing me to achieve everything I have done so far in my life. It goes without saying that I could not have done any of it without them. I also need to thank my wonderful in-laws, Jane and Terry Blake, for agreeing to let me use their home as an office while I wrote this thesis. I can't thank you both enough. It also goes without saying that I thank Clive Tadhunter, who has been the most knowledgeable, supportive and patient academic supervisor any student could possibly ask for. Thank you for all of the time and effort you have invested in guiding me through our research, I can only hope I have proven to be a worthy student. A special thanks also goes to Marvin Rose, who after arriving in the department during my second year became an invaluable source of advice, and a great friend. Thank you for everything. Also, thanks to Patricia Bessiere for teaching me how to reduce my data when I had just started and had no idea what I was doing. Next up is Paul Kerry, for helping to get my laptop and software up and running, and keeping everything updated throughout. The department would be at a loss without him. I would also like to acknowledge the role of all of my fellow PhD students, who have made these past 4 years far more bearable than they would have been otherwise. Special thanks go to Martin McAllister and Manu Bernhard, who were the first people I met when I first came for my interview all the way back in 2014, and surprisingly managed not to put me off accepting the offer. You have provided me with much entertainment over the years and I am truly grateful to have met you both. I will certainly miss all of the afternoons spent throwing foam darts

into mugs, playing office sports and contemplating the mysteries of the Universe while playing ping pong in Interval beer garden. Thanks also to Amber Wilson, for letting me be an honorary house-mate during my visits to Sheffield while I was writing up. I'd also like to acknowledge Dan Griffiths and Dave Sahman, my fellow "class of 2018" colleagues, with whom I have greatly enjoyed sharing an office over the years. Finally, thanks to Katie Tehrani, Jonny Pierce, Liam Hardy, Chris Rosslowe, Heloise Stevance, Claire Esau, Steven Parsons, Liam Grimmett, Martin Dyer, Becky Arnold and all of the other PhD students and members of staff who have made the Department of Physics and Astronomy an enjoyable place to work during the last four years of my life. Best of luck to you all.

Rob.

Thesis Summary

Active-Galactic-Nuclei(AGN)-driven outflows are now routinely incorporated into models of major gas-rich mergers, as a mechanism for regulating galaxy growth. This is required to reproduce the correct observables (e.g. M-σ relation) in such simulations. Despite this, the true importance of the AGN-driven outflows remains controversial from an observational perspective. In particular, the properties of these outflows – such as the radii, densities, mass outflow rates and coupling efficiencies – have proven challenging to quantify, and previous estimates vary over many orders of magnitude.

Here, high-resolution imaging and wide-spectral-coverage spectroscopy has been used to accurately quantify the warm outflows in a sample of 9 local ($z < 0.175$) Ultra Luminous Infrared Galaxies (ULIRGs). These objects, which represent the most rapidly-evolving galaxies in the local Universe, are expected to contain particularly powerful outflows, and provide key targets for studying AGN-driven outflows in detail. Using [OIII] emission lines, the near-nuclear outflows are shown to be compact ($0.05 \lesssim R_{out} \lesssim 6$ kpc, median ~ 0.8 kpc), and, using trans-auroral [OII] and [SII] emission lines, they are shown to have relatively high densities ($300 \lesssim n_e \lesssim 18000$ cm^{-3}, median $\sim$ 2000 cm^{-3}). In addition, the mass outflow rates ($0.1 \lesssim \dot{M} \lesssim 20$ M$_\odot$yr^{-1}, median $\sim$ 2 M$_\odot$yr^{-1}), and coupling efficiencies ($0.03 \lesssim \dot{E}/L_{AGN} \lesssim 2.5$ %, median $\sim$ 0.4 %), are relatively modest compared with those required by most simulations. Even under optimistic assumptions, these are only consistent with theoretical expectations if a relatively modest fraction ($\sim$10 %) of the energy initially transferred by the AGN is transmitted to the warm outflows. Furthermore, the more extended ($R \gtrsim 5$ kpc) low-surface-brightness emission-line regions seen in 60 % of a more extended sample of local ULIRGs have been shown to contribute little to the total outflow powers.

Overall, this thesis contributes some of the most accurately derived properties for the warm outflows in local AGN, and provides observational results which can be used for testing the merger models.

Contents

List of Figures

List of Tables

List of acronyms

ULIRG - **U**ltra **L**uminous **I**nfra**R**ed **G**alaxy
AGN - **A**ctive **G**alactic **N**uclei
LINER - **L**ow **I**onisation **N**uclear **E**mission-line **R**egion
BLR - **B**road **L**ine **R**egion
NLR - **N**arrow **L**ine **R**egion
IR - **I**nfra**R**ed
SMBH - **S**uper-**M**assive **B**lack **H**ole
WHT - **W**illiam **H**erschel **T**elescope
VLT - **V**ery **L**arge **T**elescope
HST - **H**ubble **S**pace **T**elescope
GTC - **G**ran **T**elescopio **C**anarias
ING - **I**saac **N**ewton **G**roup
ESO - **E**uropean **S**outhern **O**bservatory
QUADROS - **Q**uantifying **U**LIRG **A**GN-**DR**iven **O**utflow**S**
RA - **R**ight **A**scension
ISIS - **I**ntermediate dispersion **S**pectrograph and **I**maging **S**ystem
STIS - **S**pace **T**elescope **I**maging **S**pectrograph
IRAF - **I**mage **R**eduction and **A**nalysis **F**acility
CCD - **C**harge-**C**oupled **D**evice
FWHM - **F**ull **W**idth at **H**alf **M**aximum
OSIRIS - **O**ptical **S**ystem for **I**maging and low-intermediate-**R**esolution **I**ntegrated **S**pectroscopy
TF - **T**unable **F**ilter
OS - **O**rder **S**orter
RoboDIMM - **ROBO**tic **D**ifferential **I**mage **M**otion **M**onitor
TDE - **T**idal **D**isruption **E**vent

Chapter 1

Introduction

1.1 Active galactic nuclei

It is now widely accepted that at the centre of most, if not all, large galaxies is a super-massive black hole (see Rees, 1974; Balick & Brown, 1974; Kormendy & Ho, 2013, and references therein). Surrounding this super-massive black hole (SMBH) is a reservoir of gas, dust and stars which together forms the central bulge of the host galaxy. When the gas, dust or stars in the central regions, or from external sources, stray too close to the event horizon, they can be disrupted and accreted (e.g. Pringle et al., 1973; Narayan & Quataert, 2005). This process of accretion can be extremely efficient and produce a large amount of radiation across the entire electro-magnetic spectrum (X-rays to radio waves). When this occurs, the SMBH in the nucleus of the galaxy is considered to be "active", and the luminous cores referred to as Active Galactic Nuclei (AGN). Consequently most, if not all, galaxies are likely to host AGN at some point in their evolution, including our own Milky Way (see Su et al., 2010; Zubovas et al., 2011, and references therein).

The environments of AGN provide us with a unique astronomical laboratory to examine the physics of one of the most extreme, naturally occurring processes in the known Universe. As well as appearing luminous in imaging (and therefore relatively easy to detect), the intense radiation from AGN ionises the surrounding inter-stellar medium and produces emission-lines in the resultant spectra. Analysis of such emission lines provides us with a wealth of information.

1.1.1 Types of AGN

Over the past decades, AGN have been classified into different categories and are referred to by many different names. Because these names appear frequently throughout this thesis, an overview is given here.

Strong emission lines in galaxy spectra – now known to be caused by AGN – were observed at the start of the 20th century, in photographic spectra of bright nearby nebulae (Fath, 1909; Slipher, 1915). However, it was not until 1943 that a systematic study of these optical emission line nebulae was undertaken by Carl Seyfert (Seyfert, 1943). For this reason, the first type of AGN are called "Seyfert" galaxies. Seyfert galaxies are typically spiral or irregular galaxies, and are divided into two classes: type I and type II. Type I Seyferts generally show broad, permitted emission lines alongside narrow emission lines – which may be both permitted and forbidden – in their spectra. On the other hand, type II Seyferts show only narrow permitted and forbidden emission lines. An example of an AGN spectrum, for the type I Seyfert galaxy NGC 1275, is shown in Figure 1.1. The commonly observed forbidden and permitted emission lines are labelled. In comparison, the spectrum of a typical star-forming galaxy shows combined absorption features from the atmospheres of individual stars, along with emission lines which are narrower than those in AGN and show a smaller range of ionisation. High ionisation lines (such as [NeV]λ3425 and [FeVII]λ6087) are not found in stellar spectra.

The study of AGN was furthered when certain bright, discrete radio

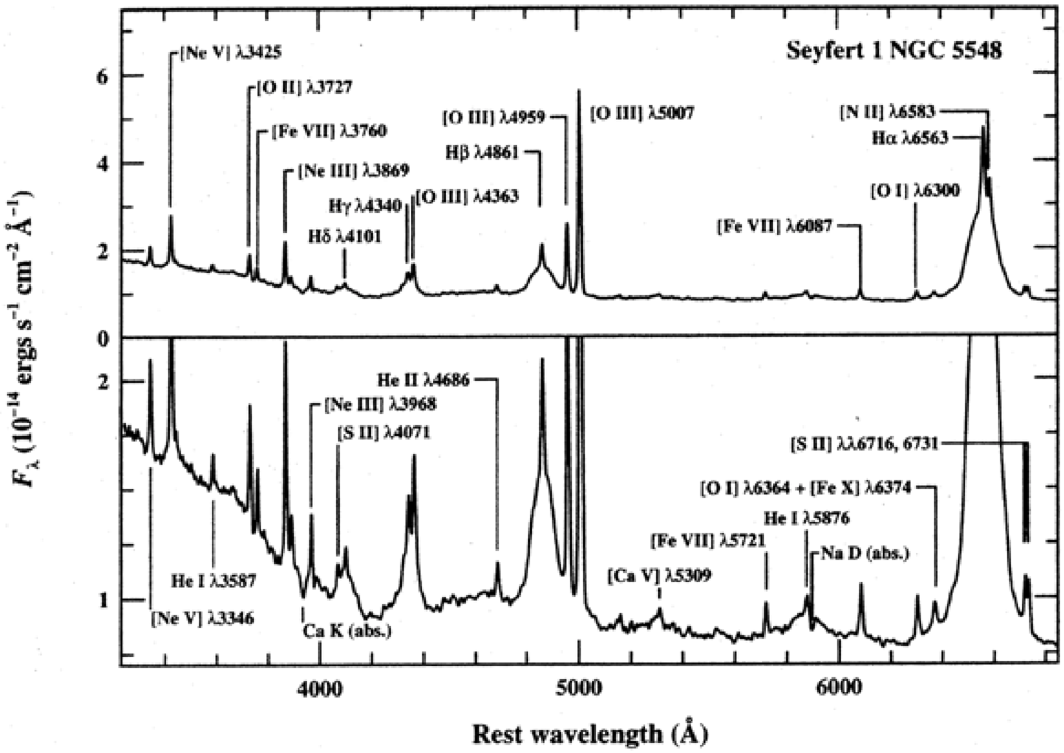

Figure 1.1: The optical spectrum of the Seyfert I galaxy NGC 5548. The prominent broad and narrow emission lines are labelled, as are strong absorption features of the host galaxy spectrum. The vertical scale is expanded in the lower panel to show the weaker features. The full width at half maximum (FWHM) of the broad components is $\sim$ 6000 km s^{-1} and the width of the narrow components is $\sim$ 400 km s^{-1}. This spectrum is the mean of several observations made during 1993 with the 3 m Shane Telescope and Kast spectrograph at the Lick Observatory. Figure and caption adapted from Peterson (1997), accessed via the Astronomical Glossary of the NASA/IPAC Extragalactic Database (NED).

sources, such as Cygnus A and Centaurus A, were first identified with galaxies outside the Milky Way (Hey et al., 1946; Bolton, 1948; Baade & Minkowski, 1954). This marked the discovery of the first radio-loud AGN. A (somewhat arbitrary) radio power dividing line between "radio-quiet" and "radio-loud" is often placed at $L_{1.4GHz} = 10^{24}$ W Hz^{-1}. Based on this cut, around 10% of AGN are "radio-loud". Radio galaxies are considered a second type of AGN, and occur in two classes: low-excitation radio galaxies (LERG) and high-excitation radio galaxies (HERG). As the names suggest, LERGs show weak, low ionisation emission lines in their spectra, whereas HERGs show spectra similar to those of Seyfert galaxies, and can be either type I or type II depending on whether broad, permitted emission lines are present. In addition, radio galaxies are seen to emit powerful jets of radio emission, which can extend to many tens of kiloparsecs and, unlike Seyferts, radio-loud AGN are typically found in elliptical galaxies. Note that, while Seyfert galaxies are considered "radio-quiet" compared to powerful radio galaxies such as Cygnus A, their radio emission can still be significant compared with that of typical spiral galaxies.

In the late 1950s and early 1960s it was found that the optical counterparts of some AGN resembled luminous point-like sources, appearing like nearby stars. However, redshifts obtained from the emission line spectra of the AGN confirmed that they were in fact very distant with respect to the Milky Way, and hence must be extremely luminous (e.g. Schmidt, 1963). In fact, in such cases the AGN are so luminous they outshine the light of all stars in their host galaxies. This led to the terms quasi-stellar radio source (commonly shortened to quasar) or quasi-stellar object (QSO). Quasars represent some of the most distant observable objects in the Universe, with the furthest confirmed (at the time of writing) at a redshift of 7.54 (Bañados et al., 2018), corresponding to the Universe being 800 Million years old (i.e. only 6 % of the current estimated age of the Universe). Quasars are essentially more luminous versions of Seyfert galaxies and, like all AGN, can be both radio-quiet and radio-loud. A commonly applied limit used to distinguish quasars from Seyferts, based on the luminosity of the [OIII] emission line, is $L_{[OIII]} > 3 \times 10^{8}$ $\mathrm{L}_{\odot}$ (Zakamska et al., 2003). Similarly to Seyferts, quasars can be one of two types based on their spectra. Type I quasars show strong optical and X-ray continuum emission, as well as strong, narrow permitted and forbidden lines and broad, permitted lines. In contrast, type II quasars, while showing strong narrow permitted and forbidden lines, lack broad permitted lines and strong non-stellar continuum.

The final type of AGN that are relevant for this thesis are Low Ionisation Nuclear Emission-line Regions (LINERs). As the name suggests, these are objects whose nuclear spectra show only low ionisation emission lines, which are often weak. While LINER spectra are typically assumed to be associated with low-power AGN (e.g. Ferland & Netzer, 1983) – and are treated as such in this thesis – it is still debatable whether these objects are in fact AGN. Instead, they may represent gaseous regions which have been ionised to a low level by other processes, such as shock ionisation (Heckman, 1980) or hot stars (e.g. Terlevich & Melnick, 1985). Indeed, a study by Singh et al. (2013) suggests that the most probable explanation for LINER-like emission is photo-ionisation by hot, evolved (post Asymptotic Giant Branch) stars.

1.1.2 AGN unification

A major topic within the field of AGN is the theory of AGN unification. This theory attempts to explain the different types of AGN spectra, not by intrinsic differences between the emitting sources, but by purely orientation effects.

The generally accepted model consists of a super-massive black hole immediately surrounded by an accretion disk (see Antonucci, 1993; Urry & Padovani, 1995, and references therein). Surrounding this is a dusty obscuring structure, usually modelled as a torus (doughnut-shape). In the regions perpendicular to the torus are the broad- and narrow-line regions. The broad-line region (BLR) consists of high-velocity, high density gas clouds (typically moving at 3000 – 10000 km s^{-1}), which orbit close to the black hole (10 light days – few light months). When these clouds are

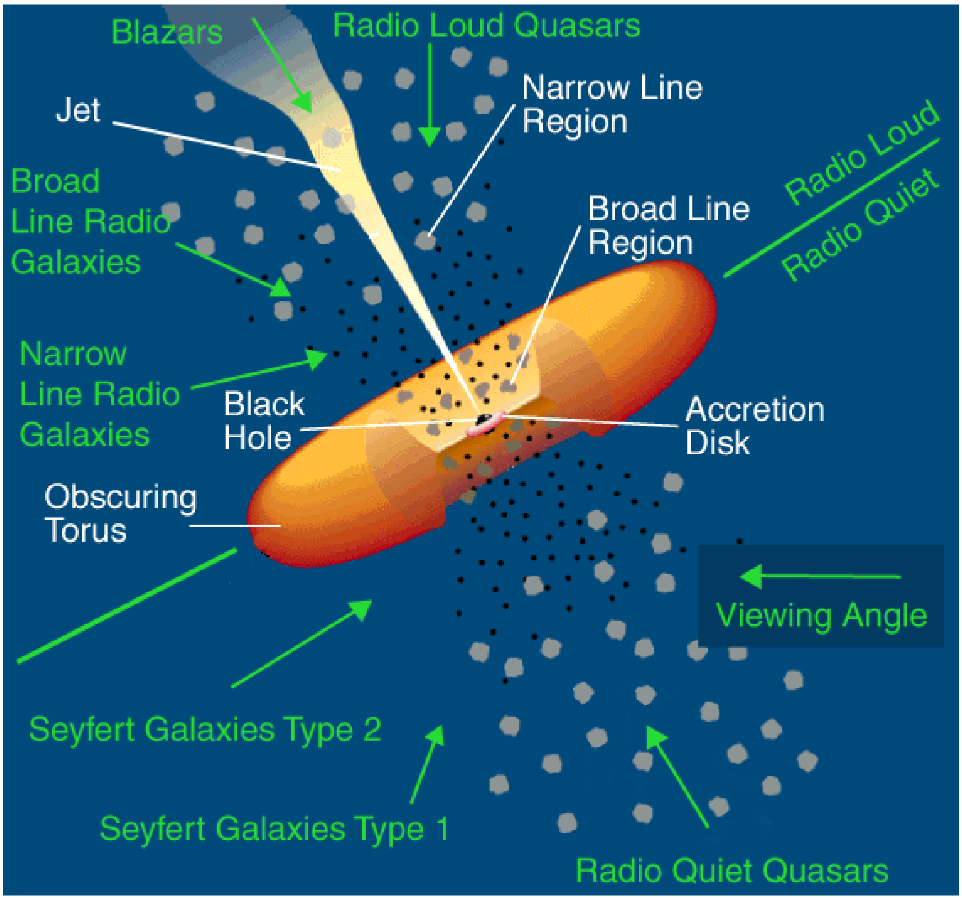

Figure 1.2: Diagram of an AGN, indicating the viewing angles associated with each observed type of AGN. Credit: Urry & Padovani (1995) and Reynolds et al. (2014)

photo-ionised by the intense radiation emitted by the accretion disk, they emit the broad, permitted emission lines seen in type I spectra. Further from the central black hole is the narrow-line region, consisting of clouds at larger radii (typically 10 pc – 1 kpc) and hence lower velocities of 300 – 1000 km s^{-1} (Osterbrock & Ferland, 2006). When illuminated by the central AGN, these clouds emit the narrow permitted and forbidden lines observed in both type I and type II spectra. In this way, the unification theory posits that the observed differences between type I and II AGN spectra can be explained in terms of the observer's line of sight relative to the obscuring torus. This is illustrated by Figure 1.2.

The galaxies analysed in this thesis, with a couple of exceptions, are radio-quiet. For radio-quiet AGN, a quasar would be observed when the nuclear structure is viewed perpendicular to the obscuring torus, provided that the black hole was accreting at a high enough rate to provide "quasar" luminosity. In this case, the observer would have a direct line of sight through the narrow- and broad-line regions to the luminous accretion disk at the centre, producing a spectrum which contains strong continuum emission from the accretion disk, along with both broad permitted, and narrow permitted and forbidden emission lines. Type I Seyferts would be observed in cases where the accretion disk is less luminous, or the line of sight is directed at a more intermediate angle to the plane of the torus. A less direct line of sight to the luminous core would produce a spectrum with a weaker continuum, but still both the broad and narrow emission lines. In contrast, type II Seyferts would be observed if the line of sight was close to the plane of the torus. In this scenario, the luminous central source and broad-line region would be obscured by the torus, thus leading to a type II spectrum where only narrow-line forbidden and permitted emission is observed. These differences also apply to radio-loud AGN, however in these cases a radio jet is also present, allowing for an additional type of AGN – a blazar – if the line of sight is aligned directly into the radio jet.

This unification scenario is successful at explaining the major differences observed between many different types of AGN spectra and is sufficient for the purposes of this work; however, it is not without its issues, and, over the past decades, various modifications have been suggested (see Ramos Almeida & Ricci, 2017). Nonetheless, a detailed discussion on AGN unification is beyond the scope of this thesis. For further information, see the review of Netzer (2015).

1.2 Links between super-massive black holes and their host galaxies

Observational results over the past two decades have provided compelling evidence to suggest that the evolution of super-massive black holes, and that of their host galaxies, are linked. In addition, it has been shown that the energy released by accretion during the lifetime of a SMBH is much larger than the gravitational binding energy of the gas in a typical galaxy (see Harrison et al., 2018). This means that SMBHs have the potential to greatly influence their host galaxies, and understanding this interaction could be key to obtaining a complete understanding of galaxy evolution.

The fundamental results in the literature are the various scaling relationships that have been observed between the SMBHs and large-scale host galaxy properties. Of particular importance to this thesis are the apparent correlations between central SMBH masses and bulge masses and velocity dispersions of their host galaxies (e.g. see Magorrian et al., 1998; Tremaine et al., 2002; McConnell & Ma, 2013). Figure 1.3, for example, shows the relationship between SMBH mass, bulge mass and velocity dispersion for nearby galaxies presented by Kormendy & Ho (2013). Correlations such as these indicate that some form of co-evolution between the SMBH and their host galaxies must exist. For this to be the case, information from the black hole must pass to the host galaxy bulge and beyond. The gravitational sphere of influence of a black hole, however, is extremely small compared to the radius of a typical galactic bulge. A common expression for the gravitational sphere of influence, with radius $\mathrm{r_{SMBH}}$, is given by the following equation:

$$\mathrm{r_{SMBH}} = \frac{\mathrm{GM_{SMBH}}}{\sigma^2}, \tag{1.1}$$

where G is the gravitational constant, M_{SMBH} is the mass of the SMBH and σ is the stellar velocity dispersion of the host galaxy bulge (Peebles, 1972). For the Milky Way, for example, r_{SMBH} ~3 parsecs, which corresponds to only ~0.2% of the radius of the Galactic bulge. Therefore, the gravitational force of the central black hole alone is clearly not enough to maintain the observed relationships between the properties of the SMBH and its host galaxy. Instead, it has been suggested that some other form of "feedback" between the SMBH and host galaxy must be required in order to accomplish this.

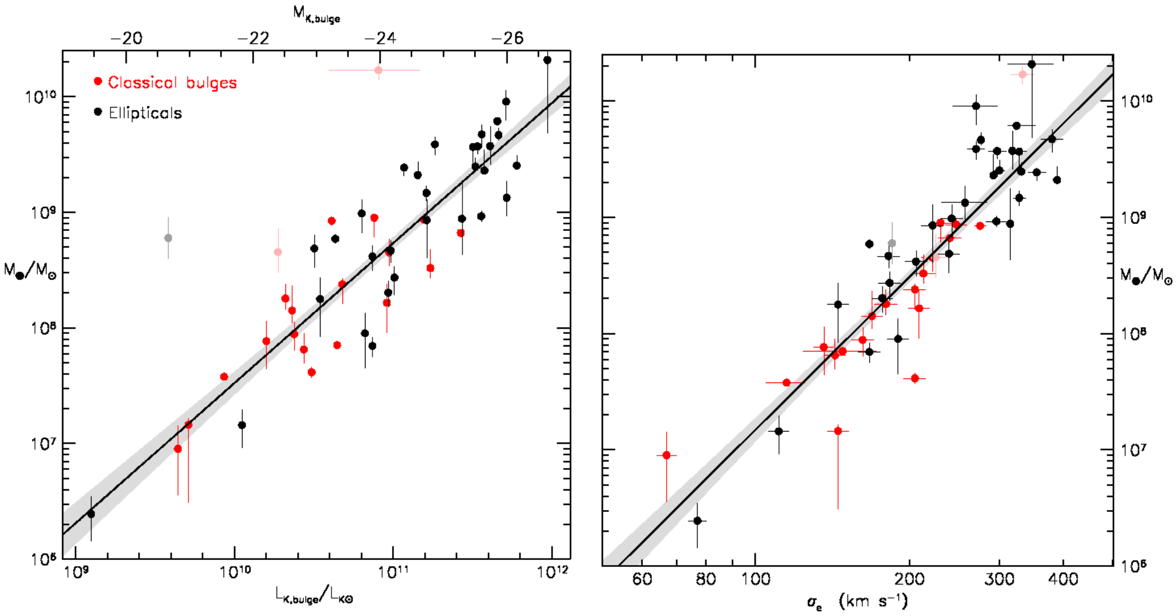

Figure 1.3: Correlations of dynamically measured SMBH masses with (left) K-band absolute magnitudes and luminosities and (right) velocity dispersions for (red) classical bulges and (black) elliptical galaxies. The lines are symmetric least-squares fits to all the points except the outliers (points in light colours), NGC 3842, and NGC 4889. The shaded region indicates the 1σ error bars. Credit: Kormendy & Ho (2013).

1.3 AGN feedback and outflows

AGN feedback is the term commonly given to a process in which the AGN at the centres of galaxies can affect the evolution of the galaxies in which they reside. In addition to the correlations discussed above, the need for AGN feedback is further motivated by comparing the observed galactic stellar mass function with the maximum stellar mass function predicted by the Millenium simulation (Bower et al., 2006; Croton et al., 2006). Figure 1.4, taken from Mutch et al. (2013), shows this comparison. The red dotted line represents the maximum possible stellar mass content as a function of halo mass. This is what would be observed if all the gas falling into the dark matter halos, as predicted by the simulations, were to cool efficiently. The blue solid line represents the observed galactic stellar mass function in the local Universe (Bell et al., 2003). Clearly, at the low and high mass ends of the plot, the observed star formation is significantly less efficient than that of the simulation. At the low mass end, this can be achieved by supernova feedback, which is able to overcome the gravitational potential of the halo and efficiently eject gas and dust from the galaxy. This reduces the availability of this material to fuel further star formation episodes. At the high mass end, however, the larger gravitational potential of the halos means the energy injected by supernovae is no longer sufficient to remove gas from the galaxy. Instead, feedback from the central SMBHs is believed to be largely responsible for reducing the star formation efficiency in this regime (e.g. Croton et al., 2006; Mutch et al., 2013).

1.3.1 Types of AGN feedback

There are two mechanisms by which AGN can, theoretically, influence their host galaxies outside of the gravitational sphere of influence. These are (i) through direct radiation, and (ii) by driving gas away from the nucleus through outflows, and, in the radio-loud case, relativistic radio jets (see Antonuccio-Delogu & Silk, 2008; Fabian, 2012; King & Pounds,

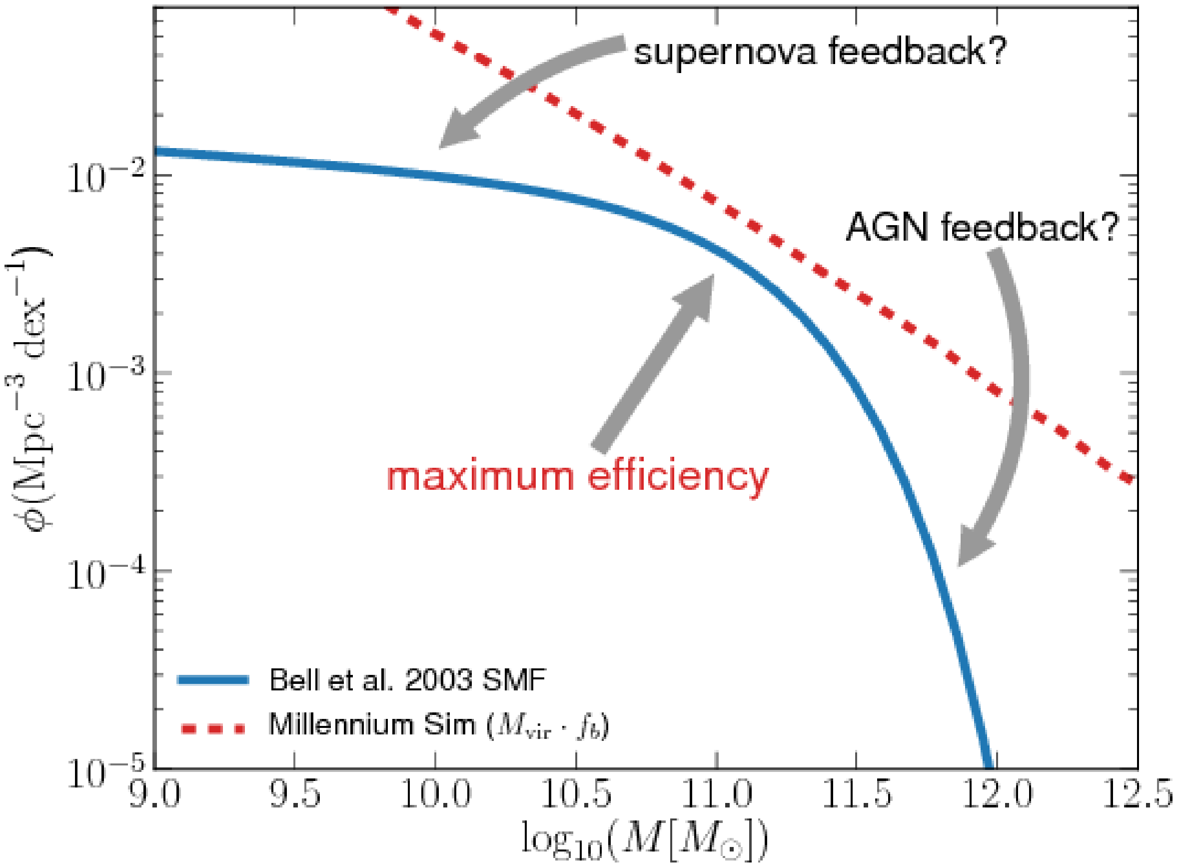

Figure 1.4: A comparison of the observed galactic stellar mass function (blue solid line) and the halo mass function of the Millennium Simulation (red dashed line). The closer the stellar mass function is to this line, the more efficient star formation is in halos of the corresponding mass. The differing slopes at both high and low masses indicates that star formation (as a function of halo mass) is less efficient in these regimes. Credit: Mutch et al. 2013.

2015). The energy these mechanisms inject into the host galaxies, galaxy clusters and groups are expected to regulate galaxy growth by:

- preventing the hot gas in dark matter halos from cooling to form stars, or
- heating and/or ejecting gas that has already cooled through outflows/winds and thereby quenching star formation.

Highly ionised hot gas, however, interacts very weakly with radiation due to its low Thomson scattering cross-section. This suggests that direct radiation is unlikely to be the primary way in which AGN prevent the hot gas halos in large clusters and groups of galaxies from cooling. In contrast, jets and winds can transmit their mechanical energy to the large-scale gas far more effectively. Arguably the best evidence, to date, for AGN feedback is provided by high resolution X-ray imaging and spectroscopy of the hot gas in galaxy clusters and giant elliptical galaxies. These observations reveal giant cavities and shock fronts inflated by the radio jets, and provide direct evidence that energy injection from the AGN is preventing the hot gas from cooling (see Best et al., 2006; McNamara & Nulsen, 2007). In addition, evidence for jets/cloud interactions with cooler phases of interstellar gas is provided by Clark et al. (1997), Villar-Martín et al. (1999), Morganti et al. (2013), and Villar-Martín et al. (2017). However, given that only ∼10% of AGN show evidence for powerful radio jets, theoretical expectations are that AGN-driven outflows should play an equally, if not more, significant role in quenching star formation and controlling galaxy growth. However, observational evidence for this feedback mechanism is far more controversial.

1.3.2 Simulations of outflows

Silk & Rees (1998) and Fabian (1999) stimulated interest in AGN-driven outflows by using simple analytical models to show that only a few percent of a quasar's luminosity is needed to couple to the surrounding medium in order to create a galaxy-wide outflow. In the following two decades, AGN feedback has become routinely included in semi-analytic and hydrodynamical models of galaxy evolution in order to reproduce observational results, such as the galaxy mass function, or BH-bulge scaling relations, as discussed in Section 4.7. Without AGN feedback in the form of galaxy-wide outflows, the models predict galaxies with luminosities, masses and colours which are inconsistent with current observations. Recently, comparison between the physical parameters of the outflows required by computational models and those inferred through observations has become a topic of strong debate. In order to reproduce the correct observables in the simulations, the models are tuned to certain parameters. If these parameters are not consistent with those measured observationally, then the theory and/or implementation of feedback within the simulations may need to be revised.

The hydrodynamical simulations of major mergers performed by Di Matteo et al. (2005) provided the first self-consistent model to show that AGN feedback was able to account for the M$_{BH}$-σ relation. This study traced both black hole growth, star formation and gas dynamics during major mergers of gas-rich spiral galaxies. The models showed that, once the black holes reached a critical mass, the AGN generated outflows that drove away gas and prevented further star formation (i.e. regulated galaxy growth). This helped explain the observed connection between the SMBH masses and stellar masses of galaxies (Figure 1.3, see also Johansson et al., 2009), and potentially the down turn at the high mass end of the galactic stellar mass function (Figure 1.4). These models, however, require a free parameter, $\dot{F}$, which determines the proportion of the total radiative energy, L_{bol}, of the AGN that is transferred as thermal energy, E_{gas}, to the surrounding gas (i.e. $\dot{F} = \dot{E_{gas}}/L_{bol}$). This is commonly referred to as the coupling efficiency. In the Di Matteo et al. (2005) models, $\dot{F}$ was tuned to a value of 5 % (see also Springel et al., 2005; Hopkins et al., 2006). In addition, the simulations suggest that the outflows should be visible on scales comparable with the host galaxies themselves, and also demonstrate that both the star formation rate (SFR) and SMBH accretion rate peak close to the time of coalescence of the two SMBHs (Springel et al., 2005, see Figure 1.5). Following the Di Matteo et al. (2005) results,

$\dot{F} = 5\%$ became a benchmark parameter in both theoretical and observational studies of single phase AGN-driven outflows. However, it is still not clear what the true coupling efficiency of the outflows should be.

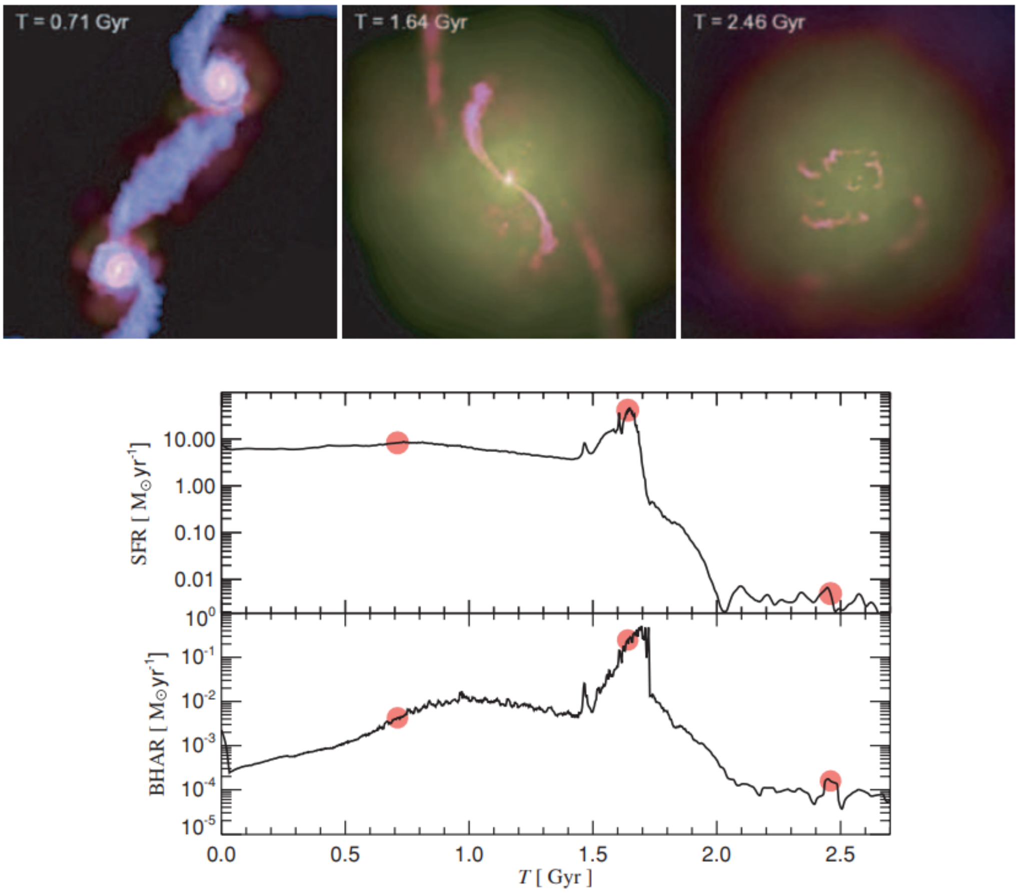

Figure 1.5: Merger of two spiral galaxies, including the effects of black hole growth and AGN feedback. The images show the gas distribution in the two spirals at three different times, where colour hue encodes temperature while brightness measures gas density. Each frame measures 50 h^{-1} kpc on a side. The bottom panels show the time evolution of the accretion rate onto the black holes (bottom) and the star formation rate (top). The red symbols in these panels mark the three times shown in the images on top. The first snapshot shows the system just after the first passage of the two discs. The second snapshot captures the system when the galaxies are coalescing, at which point the star formation and accretion rates peak. Finally, the third snapshot shows the system after the galaxies have fully merged and most of the mass has settled into a slowly evolving remnant. Credit: Springel et al. (2005)

Indeed, further theoretical estimates of $\dot{F}$ range from 0.1 % (Choi et al., 2012) to 15 % (Booth & Schaye, 2009), depending on the type of coupling energy (i.e. kinetic, thermal, momentum) and the various implementations of feedback employed in the simulations (see the review by Harrison et al., 2018). One particular implementation of feedback is the "multistage" model proposed by Hopkins & Elvis (2010). They argue that an initial shock-wave or strong wind of hot gas, driven by the SMBH, can disturb clouds of gas in its wake and increase their effective cross-section perpendicular to the AGN. This allows successive outflows to be driven more efficiently. In this scenario, the required coupling efficiency of the AGN to the outflow can be as low as $\dot{F} \sim 0.5$ %. Therefore, due to the wide range in the expected coupling efficiencies of the AGN-driven outflows from theoretical models, it is clear that comparison with the properties of AGN outflows directly determined from observations is crucial for testing the models.

1.3.3 Observations of outflows

Over the past four decades, warm ($\sim 10^4$ K) ionised outflows – detected using optical and infrared emission lines such as Hα, [OIII] and [NeIII] – have been shown to be a common feature of all types of AGN. Early evidence for AGN-driven outflows was provided by Heckman et al. (1981), through optical observations of a sample of 36 Seyfert and radio galaxies. They noted that [OIII]λ5007 emission-line profiles in the majority of the sample were asymmetric, with broad, blue-shifted wings extending to significant velocities with respect to the rest-frame of the host galaxies. These asymmetric blue wings to the emission-line (or absorption-line) profiles in AGN spectra are interpreted as evidence of outward flows of gas. An example of such a profile is shown in Figure 1.6. Outflows have since been observed in all types of AGN, from Seyfert galaxies (e.g. Whittle et al., 1988) to compact radio sources (e.g. Holt et al., 2008). Furthermore, disturbed [OIII] kinematics, consistent with outflows, are found in a large proportion of optically-selected AGN from the Sloan Digital Sky Survey (Mullaney et al., 2013; Zakamska & Greene, 2014).

Interestingly, outflow signatures are also detected in colder atomic and molecular gas phases. Outflows of neutral atomic gas are sampled by NaID absorption (e.g. Rupke et al., 2005a,b) or HI 21cm absorption (e.g. Morganti et al., 2005); and cold molecular gas is commonly sampled by transitions between the rotational energy levels of the carbon monoxide (CO) molecule (e.g. Feruglio et al., 2010; Cicone et al., 2014). However, while detecting the presence of outflows is relatively straightforward, determining their physical properties is extremely challenging. Most outflows are unresolved in imaging and spectroscopic data, meaning that only average properties can be derived. In addition, whereas simulations are able to access the entire bulk outflow, observers are often limited to only one particular gas phase depending on the emission/absorption lines available in observations, and the relationship between the three above phases remains uncertain. This thesis focusses predominantly on the warm, ionised outflows sampled by optical emission lines.

Determining outflow properties

In order to calculate the mass outflow rates, kinetic powers and coupling efficiencies of the warm outflows observationally, the outflow velocities, electron densities, reddenings, and radial extents of the outflows must be known.

As discussed above, warm outflows are generally characterised by asymmetric and/or blue-shifted components in high-ionisation optical emission lines (e.g. [OIII]λ5007Å; Rodríguez Zaurín et al. 2013; and [NeIII]$\lambda 15.56\mu$m; Spoon & Holt 2009). In general, components with velocity widths, FWHM > 500 km s^{-1}, and/or velocity shifts, $|\Delta v| > 250$ km s^{-1}, relative to the

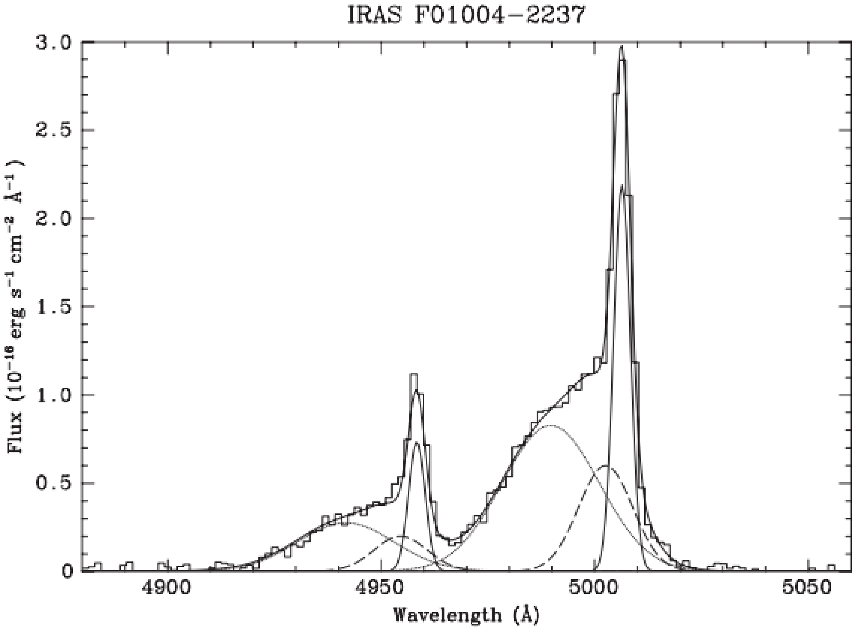

Figure 1.6: An example of the asymmetric, blue wings to the [OIII] emission lines in the optical spectrum of IRAS F01004–2237, which are interpreted as evidence for warm outflows in AGN. Credit: Rodríguez Zaurín et al. (2013).

host galaxy rest frame are considered clear evidence for outflows. However, the specific definitions vary from study to study, and these broad emission lines are often confined to the near-nuclear regions of active galaxies (e.g. Spoon & Holt, 2009; Rodríguez Zaurín et al., 2013).

The mass outflow rates, kinetic powers and coupling efficiencies are proportional to the emission-line luminosity, e.g. $L_{[OIII]}$, and inversely proportional to the electron density, n_e, of the observed region (see Chapter 4 for the full equations). The luminosity is measured using the observed flux, F, of a strong emission line (often [OIII], Hα or Hβ) which is then converted to luminosity using $F = \frac{L}{4\pi D^2}$, where D is the distance to the source. However, the measured fluxes can be affected by the reddening effect of dust, which leads to under-estimated emission-line luminosities if not corrected for. In the optical regime, the reddening can be estimated by the ratio of combinations of the hydrogen recombination series of emission-lines (Balmer series). However, extreme kinematics, such as those observed in outflow regions, can lead to large uncertainties on the reddening because the key line at optical wavelengths – Hα – is blended with the [NII] lines. This results in significant uncertainties on the calculated emission-line luminosities.

Similarly, the electron density is a challenging property to measure. In the optical regime, the electron density is traditionally measured using the nebular [OII](3729/3726) or [SII](6716/6731) emission-line doublet ratios. Unfortunately, these ratios are sensitive to only a narrow range of densities ($10^2 < n_e < 10^{3.5}$ cm^{-3}), and are also close together in wavelength, which makes separating the doublet components challenging in outflow regions (see Chapter 5 for more detailed discussion). Previous studies have attempted to quantify the properties of the warm outflows in this way, but the resultant errors on the density, combined with uncertainties on the reddening and other parameters, can lead to orders of magnitude uncertainties in the derived mass outflow rates and kinetic powers of the outflows (see Rodríguez Zaurín et al., 2013). The difficulties in obtaining accurate densities has meant that, in many studies, a density value is simply assumed for the calculations (e.g. Liu et al., 2013; Harrison et al., 2014; McElroy et al., 2015). The problem with this approach is that the value assumed for the density (typically n_e ~100 cm^{-3}) has a major effect on the resultant mass outflow rates and kinetic powers derived. This means that, while these studies have calculated large kinetic powers for the warm outflows and hence coupling efficiencies comparable with the benchmark value, $\dot{F} = 5$ %, required by the simulations, it is unclear whether this is correct or simply the result of assuming densities that are orders of magnitude lower than the true values (Harrison et al., 2018).

Another significant uncertainty across the literature is the total radial extent of the outflows, and in most cases only upper limits have been derived due to the outflows being unresolved in ground-based data. The mass outflow rates and kinetic powers are inversely proportional to the radius of the outflow. For the warm outflows in type II AGN, estimates range from just 0.12 kpc (Villar-Martín et al., 2016) to more than 10 kpc (Harrison et al., 2012, 2014; Liu et al., 2013; McElroy et al., 2015) based on ground-based Integral Field Unit (IFU) data. However, these larger radii have proven contentious, particularly due to the circular morphologies, and surprisingly small variations in velocity widths and shifts of the outflow regions. Therefore, it has been argued that these studies have failed to account properly for the smearing effect of atmospheric seeing (Villar-Martín et al., 2016; Husemann et al., 2016a). To remedy this, some groups have used spectro-astrometry – a technique which is less sensitive to beam-smearing – on IFU and long-slit data and report sub-bulge scale outflows ($R_{out} < 3.5$ kpc) for the entirety of their samples of type II AGN (e.g. Carniani et al., 2015; Villar-Martín et al., 2016). In addition, Husemann et al. (2016a) re-analysed the IFU data of Liu et al. (2013) and showed that the apparent large-scale radii reported for the outflows could indeed be explained by beam-smearing.

When the above uncertainties are propagated through the relevant equations, the resultant mass outflow rates and kinetic powers of the outflows vary over several orders of magnitude between the various studies: the reported mass outflow rates are in the range $0.1 < \dot{M} < 23000$ $\mathrm{M_{\odot} yr^{-1}}$; and kinetic powers in the range $10^{37.7} < \dot{E} < 10^{45.8}$ erg $\mathrm{s^{-1}}$ (Harrison et al., 2014; Villar-Martín et al., 2016). When compared with the respective AGN luminosities, the higher end of these ranges suggests it is possible for the observed coupling efficiencies to reach the $\dot{F} \sim 5 - 10\%$ level required by the hydrodynamical simulations of Di Matteo et al. (2005). However, it is still uncertain whether or not this conclusion is simply due to the aforementioned uncertainties on the properties of the outflows. Therefore, it is clear that alternative approaches must be taken to better quantify the electron densities, reddenings and radii of the warm outflows, in order to be able to determine the true importance of AGN-driven outflows.

1.4 Ultraluminous infrared galaxies and galaxy evolution

In order to investigate the properties of warm outflows in detail, a suitable sample of galaxies is required. One particularly interesting group for this work are the ultraluminous infrared galaxies (ULIRGs; Sanders & Mirabel 1996). ULIRGs are extremely luminous in the infrared (IR) part of the EM spectrum ($\sim 5 - 500\mu$m), emitting more energy in the IR ($L_{IR} > 10^{12}\,L_{\odot}$) than all other wavelengths combined. First detected by the Infrared Astronomical Satellite (IRAS) all-sky survey in 1983 (Houck et al., 1985), ULIRGs are the most rapidly evolving galaxies in the local universe, thought to represent the peaks of major mergers when the star formation rates and SMBH accretion rates are at their highest, close to the time of coalescence of the two SMBH from the merging galaxies (see Figure 1.5). Indeed, almost all ($> 90\%$) local ULIRGs show tidal features indicative of galaxy mergers (e.g. Veilleux et al., 2002). Furthermore, at least $\sim$40 – 70 % of the ULIRGs explored in past studies show evidence for AGN activity, based on optical (e.g. Kim & Sanders, 1998; Veilleux et al., 2002; Lee et al., 2011) and mid-infrared (e.g. Farrah et al., 2007; Veilleux et al., 2009; Risaliti et al., 2010; Nardini et al., 2010; Alonso-Herrero et al., 2012) diagnostics.

Major mergers, therefore, provide a mechanism to drive large amounts of gas and dust into the nuclear regions, which are needed to create the intense starburst and/or AGN activity that powers the high-IR luminosities.

Furthermore, the simulations predict that particularly powerful outflows are driven during coalescence of the nuclei, when the BH accretion rate is at its maximum. This is supported by the work of Rodríguez Zaurín et al. (2013), who found that ULIRGs with Seyfert-like AGN show evidence for more extreme kinematics – and hence more powerful outflows – than the general population of (non-ULIRG) AGN in the local universe.

While ULIRGs are relatively rare locally, with 118 objects detected at 60 μm within $z < 0.3$ based on the flux-limited 1 Jy survey of Kim & Sanders (1998), they are thought to represent local analogues of the population of IR-dominated galaxies detected at sub-mm wavelengths in the early Universe (Blain et al., 2002). A popular theory of galaxy evolution is the hierarchical model, in which galaxies grow by merging together over time. Therefore it has been suggested that ULIRGs are a transitional stage between the gas-rich spiral galaxies, and gas-poor elliptical galaxies observed in the local Universe (see Kormendy & Sanders, 1992). In this scenario, two (or more) merging gas-rich spiral galaxies pass through a ULIRG phase close to the peak of the merger, during which intense periods of star formation, AGN activity and jets/outflows remove gas and dust, before finally emerging as a gas-poor elliptical galaxy[1]. This scenario is observationally supported by the fact that merger remnants are found to show $R^{1/4}$ light profiles and have similar stellar kinematics to those of elliptical galaxies (e.g. Genzel et al., 2001; Tacconi et al., 2002; Dasyra et al., 2006). Therefore, ULIRGs, and the AGN-driven outflows within, are potentially important drivers of galaxy evolution.

---

[1] Note that it has also been suggested that ULIRGs first transition into quasars, before finally becoming elliptical galaxies (Sanders et al., 1988), however this is controversial (see Farrah et al., 2001).

1.5 Outstanding questions

Based on the above discussion of the literature, several outstanding questions remain. These are as follows.

- What are the true spatial extents of AGN-driven outflows?
- What are the true electron densities of AGN-driven outflows?
- What are the true mass outflow rates, kinetic powers and coupling efficiencies of the observed AGN-driven outflows and how do they compare to the values required by simulations of major mergers?
- Are previous studies missing something by concentrating only on the near-nuclear outflows?

In order to address these questions, high resolution optical imaging, along with wide-spectral-coverage optical spectroscopic observations, of a sample of local ULIRGs ($z < 0.175$) have been obtained. As mentioned above, ULIRGs are the most rapidly evolving galaxies in the local universe, and hydrodynamic simulations predict that they should drive particularly powerful outflows. Therefore, as an extreme population, they are particularly important for testing the importance of AGN-driven outflows in the evolution of galaxies.

This thesis is structured as follows: the main sample and data reduction processes are described in Chapter 2. A detailed study of Mrk 273 – one of the closest ULIRGs – is provided in Chapter 3, introducing some of the main concepts used in later analyses. Chapter 4 then provides an in-depth analysis of the properties of the near-nuclear outflows in the ULIRG sample, with particular focus on accurate calculations of the electron densities, mass outflow rates and kinetic powers of the warm near-nuclear outflows. Chapter 5 discusses and validates the technique used to determine the electron densities in Chapter 4. Chapter 6 then examines the properties of the spatially extended emission-line gas observed in a large fraction of the sample. Finally, Chapter 7 summarises the main results, and discusses the possible directions for future work.

Chapter 2

Observations and data reduction

2.1 Declaration

The data collection and reduction processes described in this chapter are also outlined in Spence et al. (2016) and Spence et al. (2018). As my research has contributed to the QUADROS project, a collaborative series of three papers, some overlap in the descriptions of the data collection and reduction exists with Rose et al. (2018). Unless clearly stated, the following is my own work.

2.2 Chapter introduction

This chapter outlines the data that were collected, reduced and analysed to produce this thesis. The main sample contains spectroscopic observations of 18 ULIRGs obtained using the 4.2m William Herschel Telescope (WHT) – operated by the Isaac Newton Group of Telescopes (ING) at the Observatorio del Roque de los Muchachos on the island of La Palma – and the 8.2m Very Large Telescope (VLT) – operated by the European Southern Observatory (ESO) at Paranal, Chile. The WHT data were collected, reduced and calibrated by myself, whereas the VLT data were collected, reduced and calibrated by Dr. Marvin Rose. In this chapter, I give an overview of the selection criteria and general properties of this sample, and describe the data reduction processes that have been applied. In addition, I describe datasets from the 10.4m Gran Telescopio Canarias (GTC), also on La Palma, and the 2.5m Hubble Space Telescope (HST), operated by NASA and located in low earth orbit, which have also been used in this thesis work. Finally, I provide an overview of previous observations, and indicate the slit locations used for each object.

2.3 WHT ULIRG sample

2.3.1 Sample selection

The analyses presented in this thesis make use of deep spectroscopic observations of a sample of local ULIRGs, obtained as part of a long-term project titled "Quantifying the AGN-Driven Outflows in ULIRGs" (QUADROS). The main QUADROS sample is based on the Kim & Sanders (1998) 1 Jy sample of 118 ULIRGs, and contains all of the objects classified by Yuan et al. (2010) as having Seyfert-like optical nuclear spectra, according to Baldwin, Phillips and Terlevich (BPT) diagnostic diagrams (Baldwin et al., 1981). This was to ensure that AGN are the dominant power sources in these objects. The equivalent widths of the key emission-lines were also required to be strong enough to allow accurate measurements to be made.

A further requirement was that the objects satisfied the following selection criteria:

- $z < 0.175$;
- $12 < RA < 02$ hr;
- $\delta > -25$ degrees.

The redshift limit was in place to ensure the targets were bright enough for the required observations, and that the necessary emission lines were not shifted out of the visible range. In particular, it was necessary to maximise the chances of spatially resolving the outflow regions – 0.1 arcsec corresponds to ∼0.25 kpc at z = 0.15 (Tadhunter et al., 2018). The RA limits were constrained by the proposal cycles of the WHT, and the declination limit was necessary to ensure that the ULIRGs were not contaminated by emission from the dusty Galactic centre. Note that objects with broad-line AGN were excluded from the sample because FeII emission from the BLR can potentially contaminate the [OIII] emission lines which are used to map out the nuclear outflow regions (Chapter 4).

After applying these criteria, 17 ULIRGs remained, of which deep spectroscopic observations were obtained for 15 of them. In addition to these, three other 1 Jy ULIRGs – F05189–2524, F14378–3651 and F19254–7245 – were observed to fill gaps in the observing schedule. These additional objects satisfied the spectral and redshift criteria, but fell outside of the *RA* and/or declination range of the rest of the QUADROS sample. Therefore the overall sample of 1 Jy ULIRGs with deep spectroscopic observations consists of 18 objects – 9 observed with VLT/XShooter, and 9 observed with WHT/ISIS. The full sample is referred to throughout as the “extended QUADROS” (e-QUADROS) sample. Overall, this sample is representative of the population of local ULIRGs containing warm, AGN-driven outflows. The basic properties of these objects are shown in Table 2.1.

Table 2.1: Properties of the extended QUADROS sample. Column (1): object designation in the IRAS Bright Galaxy Survey (Soifer et al. 1987); Column (3): optical redshifts measured from the QUADROS spectra; Columns (4) and (5): right ascension and declination of the IRAS source position as listed in the SIMBAD astronomical database; Column (6): IR luminosity from Kim et al. (2002), where available. "*" denotes IR luminosity is taken from Duc et al. (1997); Column (7): nuclear structure from Veilleux et al. (2002); Column (8): Interaction class from Veilleux et al. (2002), where available: III: pre-merger; IV: merger; V: old merger; tpl: Triple; Iso: Isolated. (a): the host galaxy redshift of F13428+5608 (Mrk 273) is taken from Rodríguez Zaurín et al. (2014). Unlike the other objects, a reliable redshift could not be obtained from the new spectrum due to the fact it did not pass through the centre of the system.

Object name IRAS (1)	Instrument (2)	z (3)	RA (J2000.0) (4)	Dec. (J2000.0) (5)	log L_{IR} ($L_\odot$) (6)	Nuclear structure (7)	IC (8)
F01004 – 2237	WHT/ISIS	0.11783 ± 0.00009	01 02 50	– 22 21 57	12.24	Single	III
F13428 + 5608 (Mrk 273)	WHT/ISIS	0.0373[a]	13 44 42	+ 55 53 13	12.10	Multiple	IV
F14394 + 5332E	WHT/ISIS	0.10517 ± 0.00017	14 41 04	+ 53 20 09	12.04	Multiple	Tpl
F17044 + 6720	WHT/ISIS	0.13600 ± 0.00014	17 04 29	+ 67 16 28	12.13	Single	IV
F17179 + 5444	WHT/ISIS	0.14768 ± 0.00015	17 18 54	+ 54 41 48	12.20	Single	IV
F23060 + 0505	WHT/ISIS	0.17301 ± 0.00007	23 08 34	+ 05 21 29	12.44	Single	IV
F23233 + 2817	WHT/ISIS	0.11446 ± 0.00010	23 25 49	+ 28 34 21	12.00	Single	Iso.
F23389 + 0303N	WHT/ISIS	0.14515 ± 0.00013	23 41 30	+ 03 17 27	12.09	Double	III
F12072 – 0444	VLT/XShooter	0.12905 ± 0.00013	12 09 45	– 05 01 14	12.35	Single	IV
F13305 – 1739	VLT/XShooter	0.14843 ± 0.00011	13 33 17	– 17 55 11	12.21	Single	V
F13443 + 0802SE	VLT/XShooter	0.13479 ± 0.00015	13 46 51	+ 07 47 18	12.15	Multiple	Tpl
F13451 + 1232W	VLT/XShooter	0.12142 ± 0.00013	13 47 33	+ 12 17 24	12.28	Double	III
F15130 – 1958	VLT/XShooter	0.11081 ± 0.00011	15 15 55	– 20 09 17	12.09	Single	IV
F15462 – 0450	VLT/XShooter	0.09969 ± 0.00003	15 48 57	– 04 59 34	12.16	Single	IV
F16156 + 0146NW	VLT/XShooter	0.13260 ± 0.00026	16 18 09	+ 01 39 21	12.04	Double	III
F05189 – 2524	WHT/ISIS	0.04275 ± 0.00007	05 21 01	– 25 21 45	12.07	Single	IV
F14378 – 3651	VLT/XShooter	0.06809 ± 0.00020	14 40 59	– 37 04 32	11.94*	Single	–
F19254 – 7245S	VLT/XShooter	0.06165 ± 0.00012	19 31 22	– 72 39 21	11.91*	Double	–

Table 2.2: Log of the spectroscopic observations for the extended QUADROS sample. Column (1): Object designation in IRAS BGS; Column (2): Date of observation; Column (3): Position angle of the spectroscopic slit; Column (4): Total exposure time per arm; Column (5): Range of airmass during observations; Column (6): Estimated 1D seeing measured from the FWHM of a telluric standard star, which was observed at the same time and under approximately the same conditions as the target. The error is deduced from the standard error on the mean of the seeing variation over the observation period, as measured by the RoboDIMM seeing monitor. Column (7): Galactic extinction in A_V from Schlafly & Finkbeiner (2011). Column (8): The pixel scale for the adopted cosmology.

Object name IRAS (1)	Date (2)	PA (degrees) (3)	Integration (s) (4)	Airmass (5)	Seeing$_{1D}$ FWHM (arcsec) (6)	GA$_V$ (mag.) (7)	Scale (kpc/") (8)
F01004 – 2237	09/2015	5	6000	1.59 – 1.68	1.43 ± 0.12	0.048	2.033
F13428 + 5608	06/2014	23	3000	1.15 – 1.19	1.20 ± 0.35	0.022	0.727
F14394 + 5332E	06/2014	130	6000	1.13 – 1.30	1.25 ± 0.07	0.031	1.849
F17044 + 6720	06/2014	145	6000	1.29 – 1.40	1.61 ± 0.07	0.081	2.300
F17179 + 5444	06/2014	105	6000	1.25 – 1.57	1.60 ± 0.06	0.082	2.471
F23060 + 0505	09/2015	325	5400	1.11 – 1.28	1.07 ± 0.11	0.173	2.813
F23233 + 2817	09/2015	282	6000	1.28 – 1.83	1.17 ± 0.15	0.331	1.972
F23389 + 0303N	09/2015	0	5400	1.11 – 1.14	1.44 ± 0.10	0.145	2.427
F12072 – 0444	05/2013	40	5200	1.07 – 1.11	0.73 ± 0.03	0.120	2.222
F13305 – 1739	05/2013	70	4800	1.12 – 1.25	1.16 ± 0.10	0.195	2.506
F13443 + 0802SE	05/2013	20	4800	1.18 – 1.21	0.74 ± 0.05	0.066	2.320
F13451 + 1232W	05/2013	20	4800	1.25 – 1.43	0.92 ± 0.07	0.092	2.120
F15130 – 1958	05/2013	113	4800	1.01 – 1.16	0.88 ± 0.14	0.385	1.917
F15462 + 0450	05/2013	30	4800	1.11 – 1.21	0.81 ± 0.02	0.590	1.776
F16156 + 0146NW	05/2013	30	4800	1.12 – 1.20	0.64 ± 0.02	0.235	2.262
F05189 – 2524	09/2015	340	2700	1.83 – 1.98	1.63 ± 0.05	0.080	0.808
F14378 – 3651	05/2013	35	4800	1.02 – 1.10	0.86 ± 0.10	0.198	1.255
F19254 – 7245S	05/2013	10	4800	1.49 – 1.53	1.01 ± 0.03	0.235	1.140

2.3.2 Observations

WHT/ISIS

Long-slit spectra for 50% of the e-QUADROS sample were obtained in June 2014 and September 2015 with the Intermediate dispersion Spectrograph and Imaging System (ISIS) dual-beam spectrograph[1] on the WHT. These observations were optimised to make accurate measurements of the trans-auroral [SII]$\lambda\lambda$4068,4076 and [OII]$\lambda\lambda$7319,7330 emission features, in order to facilitate estimation of the electron densities and reddening for the warm ionised gas (Holt et al., 2011; Rose et al., 2018) – crucial for the results presented in Chapter 4. The R300B and R316R gratings were used on the blue and red arms respectively, along with a dichroic cutting at 6100Å, to achieve spectral coverage of 3300 - 8800Å in the observed frame. This ensured that the key emission lines were contained in the spectral range that is relatively unvignetted.

Use of a 1.5" slit resulted in spectral resolutions of 5.4(5.6)±0.1 Å on the blue arm, and 5.1(5.4)±0.2(0.1) Å on the red arm for the 2014(2015) observations. These were obtained from the mean spectral FWHM of three prominent night-sky lines in each arm, which were measured using Gaussian fits in DIPSO. This corresponds to 272(283)±5 km s^{-1} at 5938 Å, and 222(236)±9(4) km s^{-1} at 6876Å, for the blue and red arms, respectively. In order to mimimise the effects of differential atmospheric refraction, the objects were observed either at low airmass or with the slit aligned along the parallactic angle for the centre of the observations. A 2x2 binning mode was used, resulting in spatial scales of 0.4 arcsec pix^{-1} and 0.44 arcsec pix^{-1}, and dispersions of 1.73 Å pix^{-1} and 1.84 Å pix^{-1} for the blue and red arms respectively. The spatial scale of the red arm was re-sampled during the reduction process (see section 2.3.3) to create

---

[1] http://www.ing.iac.es/astronomy/instruments/isis

a consistent spatial scale of 0.4 arcsec pix^{-1} across both arms. The total integration time per object was 5400 – 6000 seconds per arm, observed in two blocks of $\sim$ 1 hour, except for Mrk 273 and F05189 – 2524, which were observed in a single $\sim$1 hour block. At the midpoint of each pair of blocks, an A-type star was observed in order to facilitate removal of telluric absorption features from the target spectra. One exception to this was F23233 + 2817, for which the telluric standard was observed at the end of the $\sim$2 hour period, rather than the midpoint. This was due to an oversight at the telescope. No telluric standard star was observed for Mrk 273. In addition to these observations, several spectrophotometric standard stars were observed per night – 5 during the 2014 run and 4 during the 2015 run – in order to provide accurate flux calibration. Note that the spectrophotometric standard star observations were taken with a 5" slit whereas the telluric standard star observations were taken with the same slit width as the object observations (1.5").

VLT/XShooter

The second 50% of the e-QUADROS sample was observed during May 2013, using the XShooter multi-wavelength medium resolution spectrograph[2] in service mode on the Unit 2 telescope at the VLT facility. The observations are fully described in Rose et al. (2018), however a brief overview is provided here for completeness.

As with the WHT/ISIS observations, the science targets were observed with the slit position angles at the parallactic angle of the centre of the observations, or at low airmass. Unlike the WHT/ISIS observations, however, the telluric standards stars were observed immediately *after* the science observations for all targets, as opposed to the midpoint. To ensure similar extinction, the air masses of the telluric standard stars were chosen

---

[2] https://www.eso.org/sci/facilities/paranal/instruments/xshooter.html

to match those of the centre of the observations.

The slit configurations used were 1.3×11 arcsec on the UVB (ultraviolet to blue) arm and 1.2×11 on the VIS (visible) arm, leading to spectral resolutions of 72.7±1.5 km s^{-1} and 45.8±0.8 km s^{-1} respectively, calculated at the central wavelengths of the arms. The spectral coverage is 3000 – 5600Å on the UVB arm, 5600 – 10240Å on the VIS arm. The spatial scale was 0.16 arcseconds per pixel. Note that observations up to a wavelength of 24800Å were also made on the NIR (near-infrared) arm, however these observations were not directly used for the work within this thesis.

2.3.3 Data reduction – WHT/ISIS

The WHT observing runs provided raw data from the blue and red arms of the spectrograph, which consisted of: two-dimensional (2D) spectra of the science targets; 2D bias frames (zero-exposure time); 2D flat-field images (short observations of an internal uniformly lit field); 2D spectra of an arc lamp which produces a known emission line spectrum; 2D spectra of spectrophotometric standards stars; and 2D spectra of an A-type telluric standard star per science target (except for Mrk 273).

Before any meaningful analyses could be performed, these data needed to be reduced and combined to create fully calibrated data frames. To do this, the following reduction process was applied to the data for each target. Unless stated, each step was applied to both the blue and red science frames in the same way. The reduction process was performed using IRAF (Image Reduction and Analysis Facility) and also the STARLINK package FIGARO.

Median-combine images

For each arm, six two-dimensional (2D) spectra were taken per target (with the exception of F05189–2524 and Mrk 273, where only three were taken). These individual images were median-combined using the IMCOMBINE routine in IRAF. This improved signal-to-noise (S/N) and removed the majority of cosmic rays.

Subset

The quality of the data at the far ends of the 2D spectra produced by the two arms of the spectrograph was relatively poor due to the dichroic cut, and the quantum efficiency of the detector falling off. The design of the observations took this into account and the useful diagnostic emission lines were located outside of these regions. The overall useful wavelength range in the observed frame was $\sim$ 3600 – 8600 Å. It was therefore beneficial to remove the noisy data outside of the minimum and maximum of this range, using the IMCOPY routine within IRAF. The quality of the data within the vicinity of the dichroic cut ($\sim$ 6000 – 6200 Å) was also poor. These data were not removed, however, because an overlap between the blue and red arms was required for comparing the relative flux calibration at a later stage, and also for displaying the reduced spectra.

Transpose the data frames

The raw data frames were originally orientated with the spatial dimension on the x-axis and the spectral dimension on the y-axis. Several routines within FIGARO, however, require the axes to be transposed. Therefore, all data frames were transposed using the IMTRANSPOSE routine in IRAF.

Subtract bias

A bias voltage is applied to the CCD in the detector to mitigate the issue of negative counts. This bias level needs to be subtracted from all flat-field, standard star and target data before further processing. To do this, a number of bias frames (typically ∼15) were taken at the start of the observing run. These are images taken with the shutter closed and with zero exposure time to measure only the bias level. The bias frames were then median-averaged to reduce readout noise, creating a "master" bias frame for the blue and red arms. After ensuring there was no obvious structure across the master frame, the data visualisation application SAOIMAGE DS9 was used to measure the mean bias level across the useful region of the CCD. These were 1926(1932) and 1535(1523) for the 2014(2015) blue and red frames respectively. These constant values were then subtracted from all necessary data frames.

An alternative approach would have been to subtract the 2D bias frame itself, rather than a constant value, to capture any pixel-to-pixel variations or structure. If there was significant variation, subtracting a constant mean value could lead to significant under- or over-subtractions across the data frames. Therefore, to test the significance of the pixel-to-pixel variations, the histogram of the bias counts was measured for each object, using the bias strips at the edge of each 2D science frame. These are regions of the CCD that receive no light, equivalent to taking zero-exposure images with the shutter closed. The standard deviations of the distributions across all objects were extremely small, of the order ∼0.1% of the mean counts. Based on these probability distributions, 99 % of bias values across each CCD are expected to lie within just a few counts of the mean for all objects. The standard error on the mean across all objects was also of the order of 0.1%. Therefore, any pixel-to-pixel variations, and other large-scale variations, in the bias voltage could be considered negligible.

Flat field correction

Effects such as vignetting (loss of light off-axis), pixel-to-pixel variations (not all pixels are identical) and even dust grains on the CCD window or slit can affect the sensitivity of the system as a function of position across the images. This can be accounted for using flat-field images. These are images of an internal uniform light source (Tungsten lamp), taken using the same optical setup as the science observations. Three flat field images per arm were taken at the start of each night with the telescope pointing in the same position on the sky for the target observations. Further images were taken at the mid-point of each set of observations, with the exception of Mrk273, F05189–2524 and F23233+2817 when they were taken at the end.

Initially, only the frames from the start of the night were median-combined to create a master flat-field frame for the entire night. These were normalised by dividing by the mean count value – measured using SAOIMAGE DS9 over the same region across which the bias level was measured – and then divided into the target and standard star frames to correct for variations in the effective sensitivity. However, this did not work well for the targets observed towards the end of the night and resulted in significant fringing across the science frames. This was most likely due to variations in the optical setup as the night progressed – for example, flexure of the instrument and/or temperature-dependent variations in the wavelength of the dichroic cut. This subsequently led to inaccuracies in the flux calibration at a later stage of reduction. To rectify this, master flat-field frames were instead created for each individual target object. These "local" flat-fields were then applied to their respective science targets and standard stars. This approach worked significantly better.

Calibrate wavelength range

A key step of the reduction process was the wavelength calibration. This was achieved using observations of a copper-neon (CuNe) gas-discharge arc lamp, which creates a known emission-line spectrum. An example of one of the 2D arc frames for the blue arm is shown in Figure 2.1. Using the IDENTIFY routine in IRAF, the emission lines in the arc spectrum were manually identified by comparing it to the arc line atlas for the appropriate grating.[3] The interface for this process is shown in Figure 2.2 for reference. Once a suitable number of emission lines had been identified across the full wavelength range (20–30 lines worked well) and their wavelengths specified, a coordinate function was created using the FITCOORD routine. This was then applied to each appropriate science and standard star frame using the TRANSFORM command, resulting in wavelength calibrated spectra. Note that individual wavelength calibration curves were created for each target and associated standard stars.

To determine the accuracy of the wavelength calibration for each object, the wavelengths of 3–4 prominent night sky lines present in the science frames were measured, as given by the coordinate fit. These were

---

[3] http://www.ing.iac.es/astronomy/instruments/isis/calibration_info.html

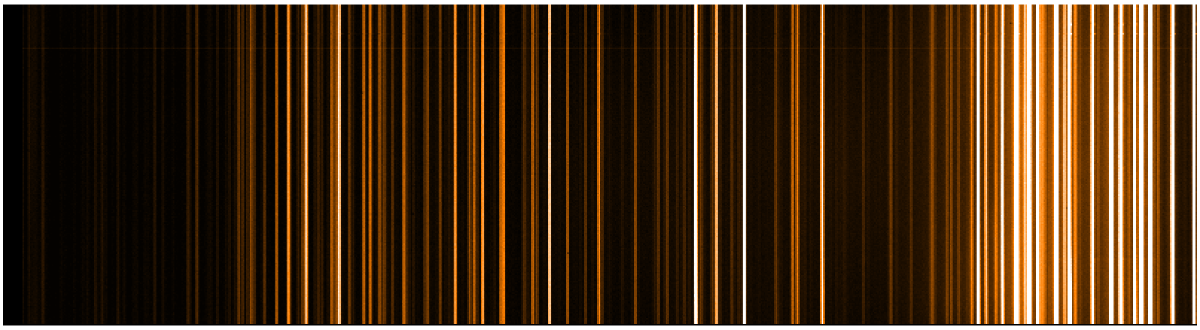

Figure 2.1: An example of an arc frame used for wavelength calibration. The spectrum is generated from a CuNe (copper-neon) gas discharge lamp.

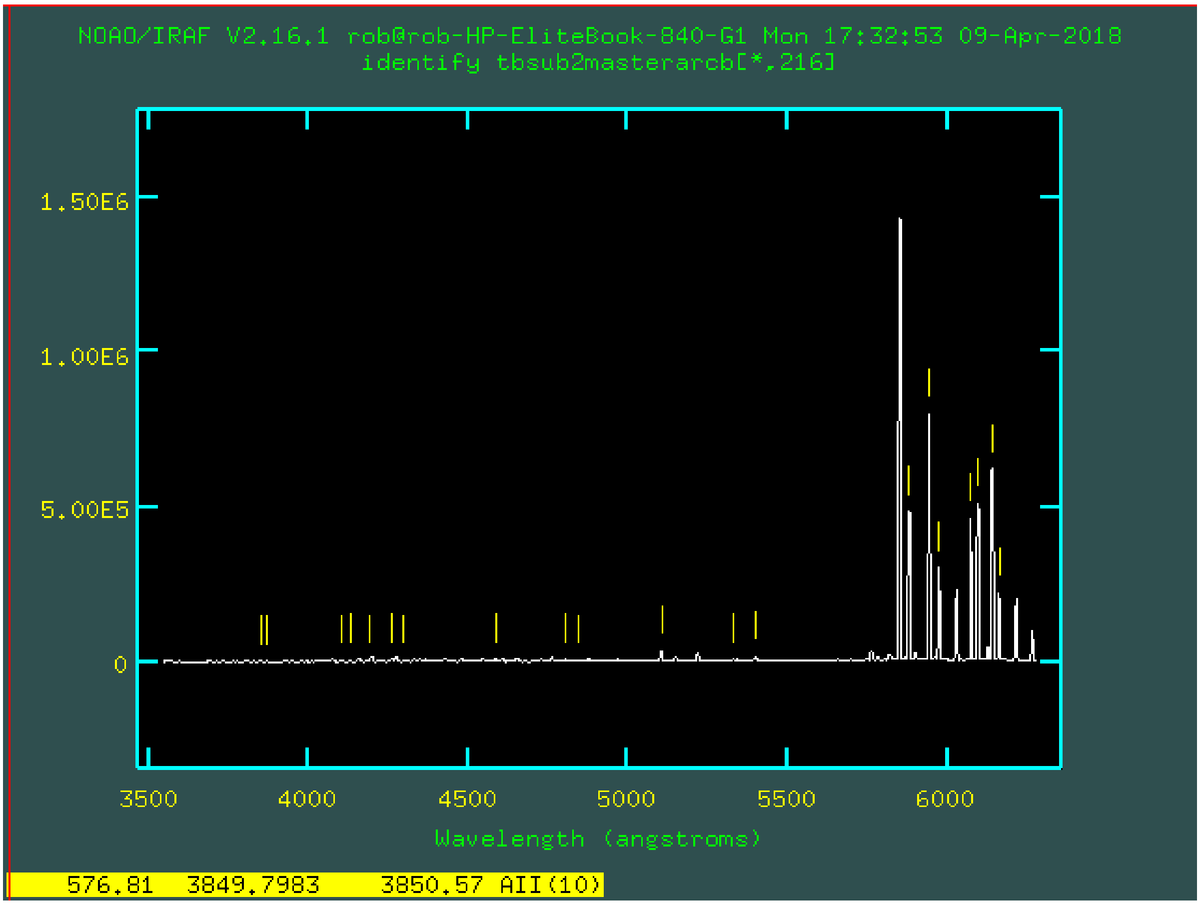

```
NOAO/IRAF V2.16.1 rob@rob-HP-EliteBook-840-G1 Mon 17:32:53 09-Apr-2018
identify tbsub2masterarcb[*,216]
```

```
576.81  3849.7983     3850.57 AII(10)
```

Figure 2.2: An example of the user interface for identifying emission lines. Each emission line was manually identified by comparing to an atlas of known emission-line spectra. The vertical yellow lines indicate where the wavelength has been specified by the user.

then compared to the known wavelengths of the lines.[4] For the 2015 observations, the wavelength calibration was accurate to within 0.3 Å. However, for the 2014 objects a systematic offset occurred between the wavelength given by the calibration and the known wavelengths. As this offset was consistent to within 1-σ across the entire wavelength range for each object, this could be corrected for by shifting the spectrum by the appropriate amount, using the IMSHIFT routine in IRAF (or ISHIFT routine within FIGARO). Alternatively, the FIGARO function LXSET could be used to manually set the correct wavelength range. Once corrected, the final wavelength calibration for the 2014 observations was estimated to be accurate to within 0.5 Å.

Straighten spectra

The slit of the spectrograph is not usually perfectly aligned with the y-axis of the detector, meaning the resultant imaged spectrum can appear to be tilted. If not corrected for, this would cause problems when extracting one-dimensional spectra. To correct for any residual tilt in the 2D spectra, they were straightened using the APALL routine within IRAF. This function extracts and traces the spectrum along the dispersion axis and shifts it to align the aperture. When “strip” is specified as the format, this produces a new 2D spectrum in which the dispersion axis of the spectrum is aligned with the edge of the image frame.

---

[4] http://www.eso.org/observing/dfo/quality/UVES/txt/sky/

Invert spatial axis (red only)

A subtlety of the raw data was that the detector of the red arm was installed in the opposite orientation (180°) to the detector of the blue arm. This resulted in the spatial axis of the 2D images on the red arm being reflected through the dispersion axis (x-axis after transposition). To correct for this, the IMCOPY routine within IRAF was used to perform a reflection through the dispersion axis on all of the ULIRG and standard star red frames.

Modify pixel scale (red only)

A further subtlety of the raw data was that the pixel scales of the blue and red detectors were different. Originally, the pixel scale of the blue CCD (name: EEV12; type: EEV4280) was 0.4 arcsec per pixel, whereas the pixel scale for the red CCD (name: REDPLUS; type: EEV4482) was 0.44 arcsec per pixel. This was an important detail to note, and would affect later aperture extractions if not adjusted. Therefore, to correct for this, a factor 1.1 dilation was performed on the spatial axis of all red science and standard star frames, using the ISTRETCH routine in FIGARO. This resulted in a consistent pixel scale between the blue and red frames of 0.4 arcsec per pixel, which was confirmed by comparing the spatial FWHM of the standard stars between the blue and red frames either side of the dichroic cut using DIPSO.

Align red and blue spectra

Next, it was important to align the frames to ensure that each row of the 2D blue spectra was spatially consistent with the same row of the 2D red spectra. This was required to ensure that emission lines fluxes could be compared across the dichroic. To do this, for each ULIRG a spatial slice of ∼20 Å was extracted from either side of the wavelength of the dichroic cut. DIPSO was then used to fit a Gaussian to the profile, and measure the central pixel value. For the two images to be aligned, the central pixels should be equivalent (within 1σ). If there was a discrepancy, the red frame was shifted by the appropriate amount using ISHIFT in FIGARO.

Calibrate flux

Arguably the most crucial step was the flux calibration, particularly the calibration accuracy across the full wavelength range of the observations. Consequently this was the most time-consuming stage of the reduction process.

To begin, each photometric standard star frame was reduced in precisely the same way as the science targets, i.e. subset, bias-subtracted, flat-fielded, wavelength calibrated, straightened and aligned. Initially a global flat field was applied for the flat-field correction. Then, using measurements from Oke & Gunn (1983), data files containing directly measured fluxes of each standard star as a function of wavelength were created.

Next, a 1D spectrum of each star was extracted. The SENSFUNC routine in IRAF was then used to create one-dimensional sensitivity functions for each standard star spectrum. The SENSFUNC routine takes the directly measured standard star flux data as input and fits a polynomial to the data points. An example of the user interface is shown in Figure 2.3, for reference. In general, a Legendre function with orders between 3 and 8 was specified, minimising the root mean squared (RMS) error and requiring the residuals of the fit to be less than 5%. Lower order functions were prioritised because using a high order can introduce unwanted variations in the output if sampling in the flux files is sparse; however, in some cases a high order was necessary to produce an acceptable fit. This process outputted a one dimensional calibration curve, with units of magnitude per count per second as a function of wavelength for each standard star.

To check the consistency between the functions of each star, a 1D spectrum of each standard star was extracted and each calibration curve was applied in turn. The resultant spectra were then divided into each other. If the sensitivity functions were 100 % consistent, these should have produced spectra with a value of exactly unity across the entire spectral range. However, due to slight variations in the calibration curves of the different stars, a 5% tolerance was accepted across the useful wavelength range. Once the sensitivity functions were consistent, these were mean-combined into "master" sensitivity functions – one for the blue arm and one for the red arm. These were applied to the science targets using the CALIBRATE routine in IRAF to convert the relative observed fluxes into absolute fluxes.

It was important to have a good relative flux accuracy between the blue and red frames, because a key part of this research involved measuring flux ratios of emission lines which fall either side of the dichroic cut. After the initial flux calibration, however, the relative flux calibration of the objects observed later in the nights was much poorer than those observed at the beginning of the night. In addition, the continuum for some of the objects showed unexpected "banding" across the flux-calibrated spectra.

It was hypothesised that this was due to the flat-fielding. As men-

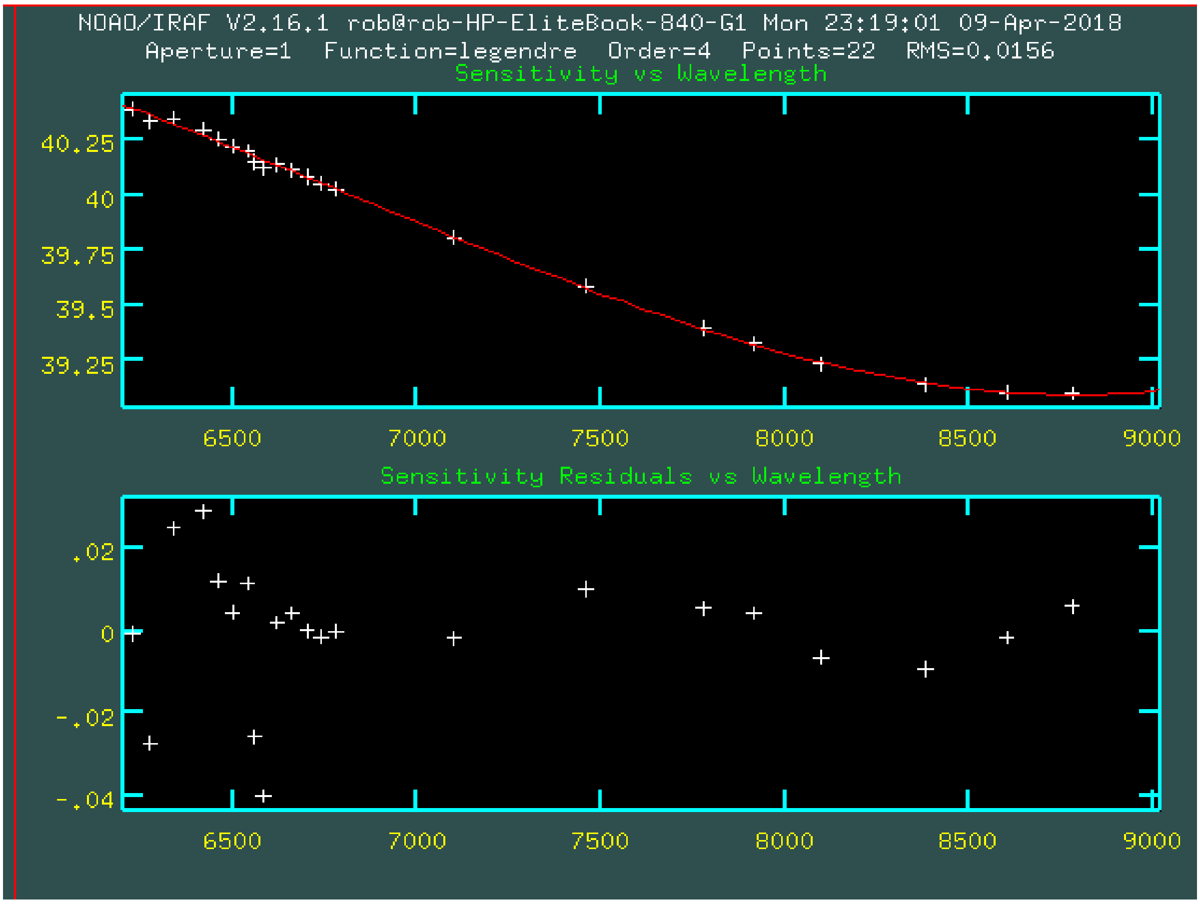

```
NOAO/IRAF V2.16.1 rob@rob-HP-EliteBook-840-G1 Mon 23:19:01 09-Apr-2018
Aperture=1   Function=legendre   Order=4   Points=22   RMS=0.0156
```

Figure 2.3: An example of the user interface for generating sensitivity functions. The upper plot shows the ratio of the directly measured fluxes and the tabulated fluxes of the standard star (white crosses) as a function of wavelength. The red line indicates the fit to the data points. The residuals are shown in the lower plot.

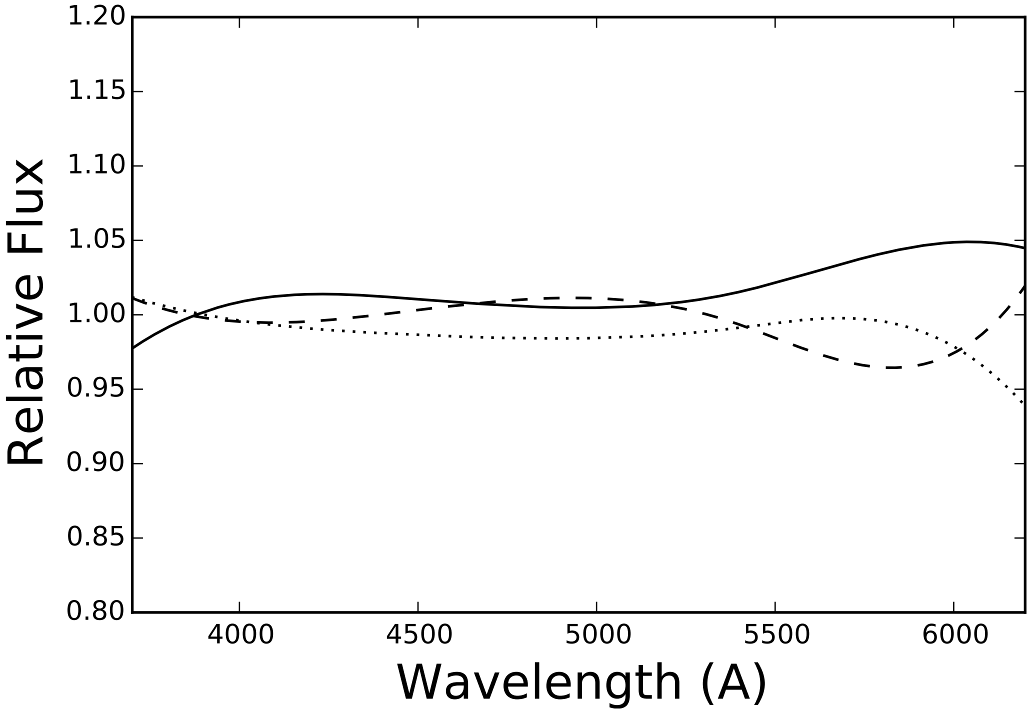

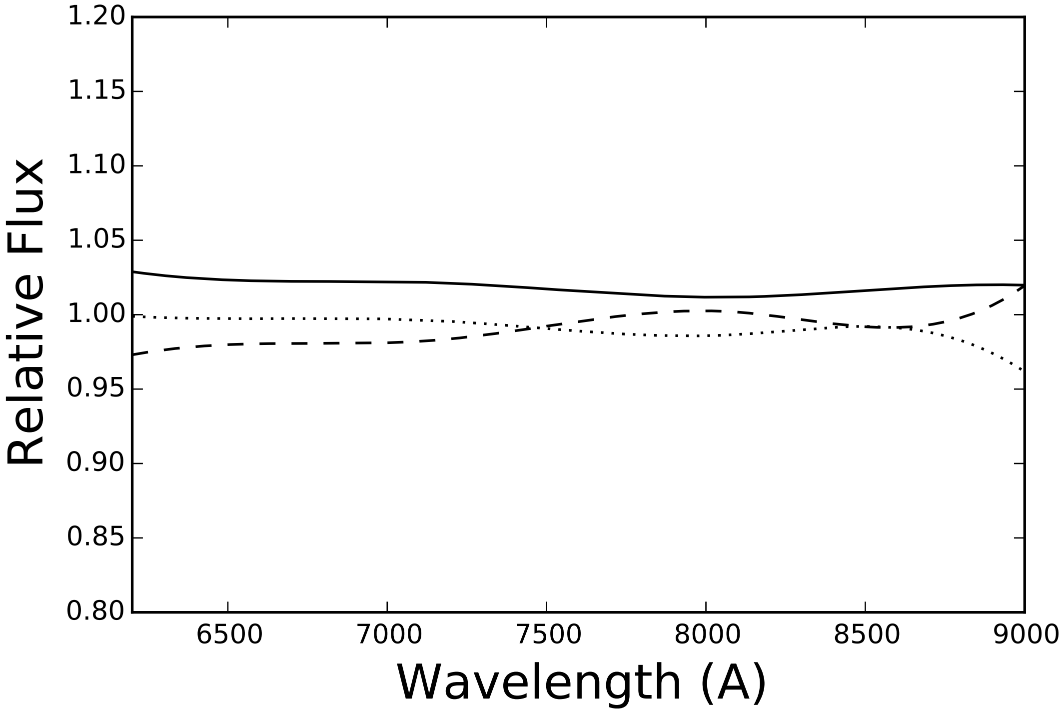

Figure 2.4: These plots show the comparison of the sensitivity functions derived from the three photometric standard stars used to calibrate F01004–2237. Each calibration curve is applied to a featureless spectrum of 1, and then normalised by the averaged sensitivity function. The calibration accuracy was better than 5% across the entire wavelength range.

tioned above, initially all of the objects were flat-fielded using a global flat-field frame, which was obtained from observations taken at the start of the night. If the optics of the telescope had varied as the night progressed (e.g. due to temperature changes), this could have led to the flat-field correction, and hence flux calibration curves, being inadequate for objects observed towards the end of the night. To test this, individual flat-field frames were created for each object and divided into the science and standard star frames, generating new calibration curves for each individual standard star, for each individual science target. Whereas the initial technique created one calibration curve per arm, which was applied to each ULIRG in turn, this new approach led to the creation of dedicated flux calibration curves for each object.

This improved the relative flux calibration, however several objects still showed significant “banding” throughout their spectra. After investigation, it was noticed that all of the affected objects had one particular standard star in common during the flux calibration process (SP1409). The flux spectrum for this star was extremely poorly sampled over visible wavelengths in the data file. Therefore the polynomial fit to this spectrum was likely introducing unwanted variations into the associated calibration curves, which was surfacing in the calibrated continuum of the ULIRG spectra. Once the sensitivity functions of this star were removed from the mean calibration curves, the significant “banding” of the spectra was reduced.

To estimate the uncertainty in the flux calibration across the full wavelength range for each object, the response curves of the individual spectrophotometric standard stars observed in each run were compared by applying each one to a featureless spectrum and normalising the result by that of the averaged curve. This is illustrated in Figure 2.4. The final flux calibration was better than ±5% for each ULIRG. In addition, the

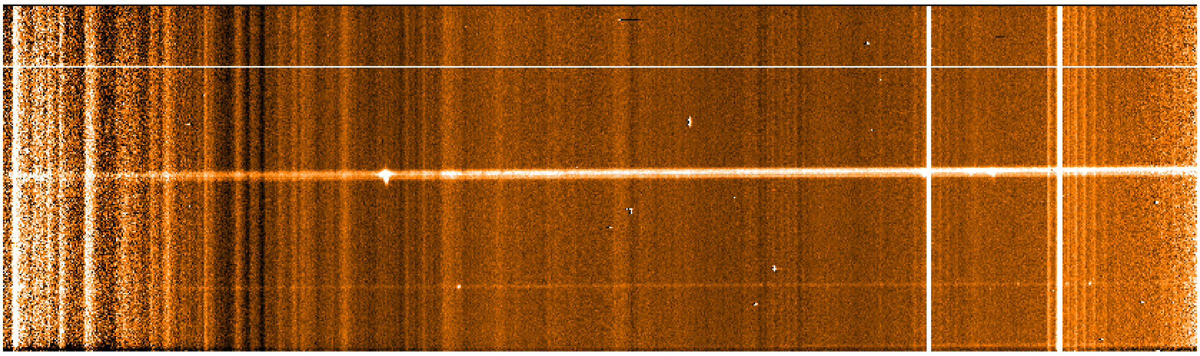

Figure 2.5: An example of a 2D science frame before the sky subtraction has been applied.

consistency between the fluxes across the dichroic cut in the final reduced spectra was excellent (see spectra in Chapter 4, Figures 4.1 to 4.4).

Subtract sky background

In order to measure only the light from the science targets, the sky background needed to be removed from the data frames. To do this, the SKYSUB routine within IRAF was used. This routine creates an average sky spectrum from extraction apertures either side of the nuclear region, which is then subtracted from each row of the 2D spectra. An example of a science frame before sky-subtraction is shown in Figure 2.5. The same data frame after the sky background has been subtracted is shown in Figure 2.6. Some residuals remain on the stronger sky lines; however, overall the sky background was well subtracted.

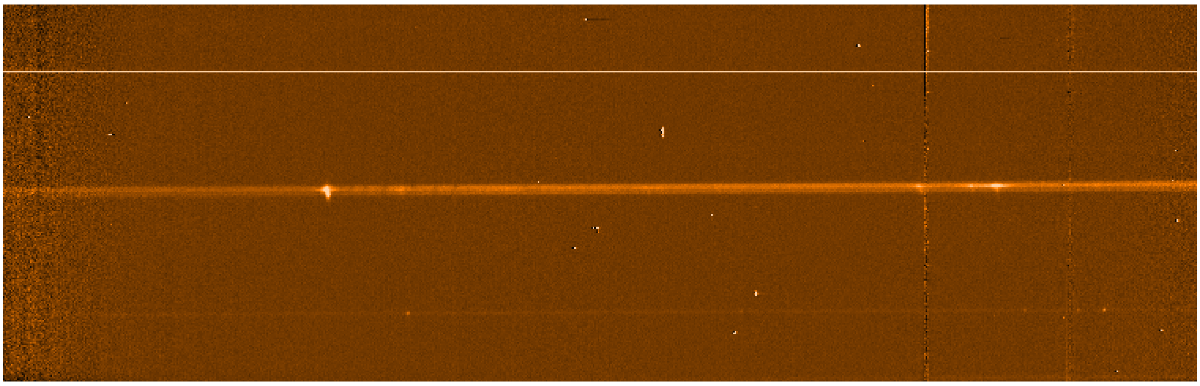

Figure 2.6: An example of the same 2D science frame as in Figure 2.5 after the sky background has been subtracted.

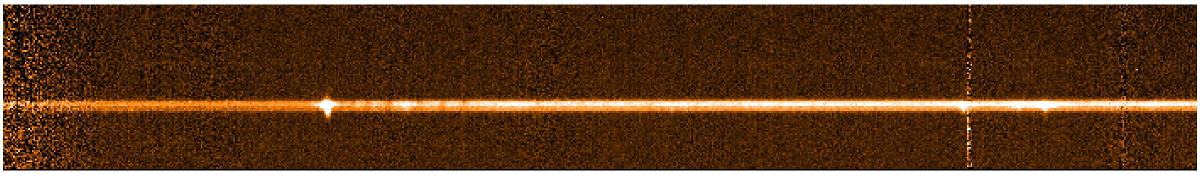

Figure 2.7: The same 2D frame as in Figures 2.5 and 2.6, after the spectrum has been cleaned of residual cosmics and bad pixels (the top and bottom edges of the frame have been trimmed).

Clean cosmic rays and bad pixels

Faulty pixels on the CCD can fail to detect the correct amount of incoming light, and lead to defects in the reduced spectra. These faults remain in the same location across all images, so are generally straightforward to fix. Equally, high energy particles (cosmic rays) can strike the CCD, producing bright spots on the impacted pixels. Most cosmic ray detections were removed by median-averaging multiple exposures. For any remaining bad pixels/cosmic ray detections, these can be manually cleaned up. To do this, the CLEAN routine in FIGARO was used to interactively fix any bad pixels by replacing the flux in the defective pixel with the average of the flux in adjacent pixels. "Before" and "after" images are shown in Figures 2.6 and 2.7.

Remove telluric absorption features (red only)

The red arm in particular is affected by telluric contamination from the Earth's atmosphere, mainly from water vapour, oxygen and OH molecules in the atmosphere. To correct for this, A-type stars were observed at the mid-point of each observing block to ensure identical conditions (with the exception of F05189–2524 and F23233+2817, for which the telluric standards were observed at the end of the block, and Mrk 273, for which no telluric standard was observed). For each target, the known stellar absorption features from the telluric standard star were removed using IRAF, the continuum subtracted and then normalised to create a relative flux spectrum. The resultant spectrum, containing only atmospheric absorption features, was then divided into the spectrum of the science target. An example of a telluric absorption spectrum is shown in Figure 2.8. To illustrate the effectiveness of the correction, Figure 2.9 shows the spectrum of F01004–2237 before the telluric correction was applied, overplotted with the spectrum after.

Once this reduction process was complete for all 9 QUADROS ULIRGs observed with WHT/ISIS, the emission line spectra could be extracted and analysed.

2.3.4 Data reduction – VLT/XShooter

The remaining 9 e-QUADROS ULIRGs, observed with VLT/XShooter, were reduced by Marvin Rose. Compared to WHT/ISIS, VLT/XShooter has a much broader wavelength coverage, containing UVB, VIS and NIR arms. A full description of this reduction process is presented by Rose et al. (2018), however for completeness the important details are outlined

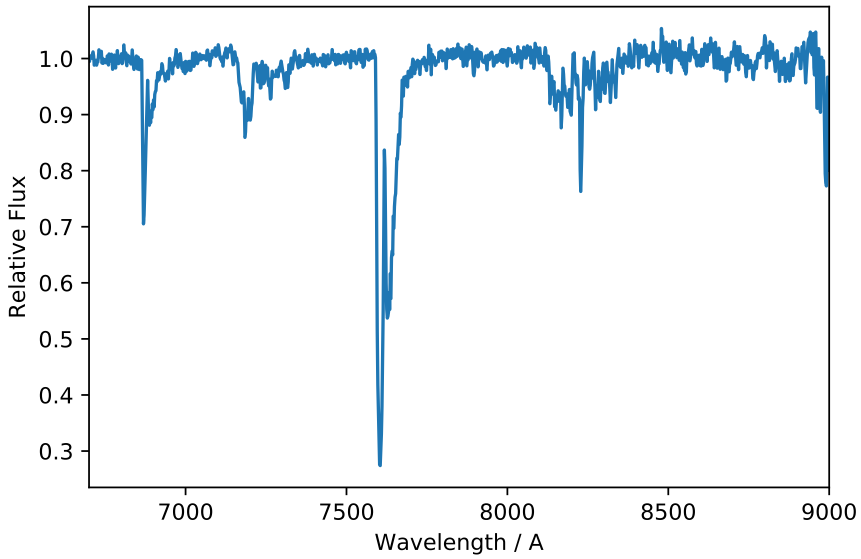

Figure 2.8: An example of the continuum-subtracted telluric spectrum, containing only the atmospheric absorption features. This was then divided into the target spectra to remove the unwanted features.

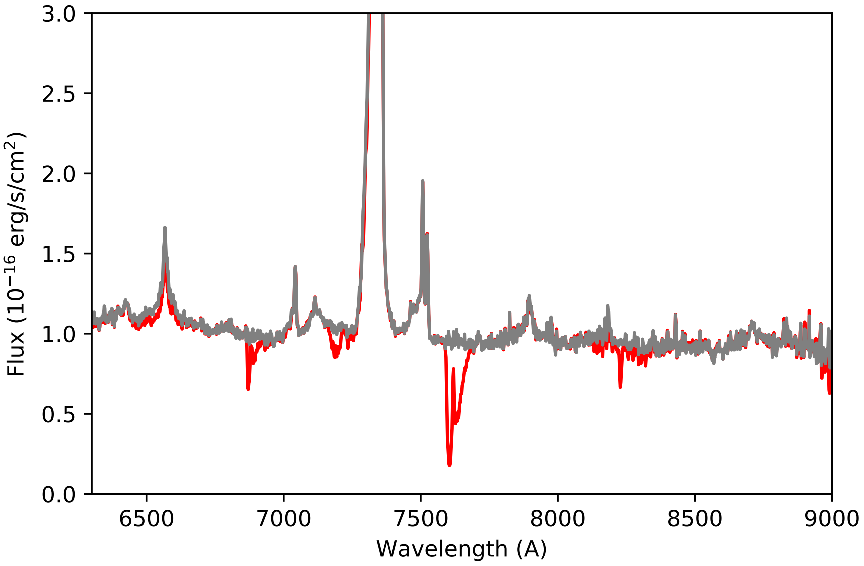

Figure 2.9: An example of the telluric-corrected spectrum of F01004–2237 (grey) overplotted onto the observed spectrum (red). This illustrates the effectiveness of the telluric correction technique.

here.

The data were initially reduced using the XShooter pipeline ESOREX (version 6.6.1) in physical mode (Freudling et al., 2013). This produced two-dimensional bias-subtracted, flat-field corrected, order merged and wavelength calibrated spectra, plus flux and telluric standard star spectra. The wavelength calibration was accurate to within 5 km s^{-1} in the UVB and VIS arms, and 10 km s^{-1} in the NIR arm. The relative flux calibration was accurate within 10% over the full wavelength range.

IRAF and FIGARO were then used to subtract the sky background and clean any bad pixels/cosmic rays, in a similar fashion to that described in the previous section for the WHT/ISIS reduction process.

Finally, the atmospheric absorption features were removed using the spectra of the telluric standard stars, as discussed previously.

2.3.5 HST/STIS data

In addition to the ground-based spectroscopy obtained with WHT/ISIS and VLT/XShooter, space-based spectroscopic observations were also available for four of the QUADROS ULIRGs (22% of the sample), observed with the Space Telescope Imaging Spectrograph (STIS)[5] installed on the HST, under the observing programs 8190 (PI: Farrah) and 12934 (PI: Tadhunter; Tadhunter et al. 2018). The observations were made with 0.1 – 0.2 arcsec slit widths. The space-based spectra have the advantage of higher spatial resolution, and reduced levels of stellar contamination from the host galaxy, due to the narrower slit widths. This was particularly advantageous for the work described in Chapter 4, which required the measurement of emission lines with relatively low equivalent widths.

Note that the STIS spectra were calibrated in units of surface bright-

---

[5] http://www.stsci.edu/instruments/stis/

ness, B_i, rather than flux, F_i. To convert these B_i values to fluxes comparable with the ISIS and XShooter units, the following equation was used:

$$B_i = \frac{F_i}{wm_s}, \tag{2.1}$$

where w is the slit width in arcseconds and m_s is the pixel scale of the detector in arcseconds. In this case, $w = 0.2$ arcsec and $m_s = 0.05$ arcsec. Therefore $F_i = B_i/100$.

2.3.6 GTC/OSIRIS data

Chapters 3 and 6 also make use of deep, high-resolution tunable filter (TF) imaging of a sample of thirty-two 1 Jy ULIRGs, seven of which overlap with the e-QUADROS sample. The GTC imaging was obtained with the Optical System for Imaging and low-Intermediate-Resolution Integrated Spectroscopy (OSIRIS)[6] instrument between 2012 and 2014 (the images were kindly made available by J. Rodriguez Zaurin, private communication). To sample the Hα emission for each ULIRG, the TF was centred on the redshifted wavelength of Hα. In addition, a medium-band continuum image was taken blue-ward of Hα. The OSIRIS images were bias and flat-field corrected in the usual way. For the flux calibration, a photometric standard star was observed using exactly the same setup as for the galaxy. A flux calibration factor was then derived using a customised PYTHON routine that generates a TF transmission curve for a given central wavelength and FWHM.

Any night sky lines contained within the bandwidth of the filter cause ring structures in the TF images. To remove such sky emission, a series of 1D polynomials were fitted in the x- and y-directions which gen-

---

[6] http://www.gtc.iac.es/instruments/osiris/osiris.php

erated a synthetic image containing only the sky emission. This image was then subtracted from the original, flux calibrated image of the source resulting in an image cleaned from any background and sky emission with the faintest visible structures having a surface brightness of $\sim 1.1 \times 10^{-17}\mathrm{erg\,cm^{-2}s^{-1}arcsec^{-2}}$.

2.4 Atmospheric seeing estimates

2.4.1 WHT/ISIS

All ground-based observations are affected by atmospheric seeing, which is the process in which turbulence in the atmosphere "smears" out light as it travels to the telescope. Accounting for this effect is crucial for studies in which accurate spatial information is required. The seeing is commonly estimated by measuring the full-width at half maximum (FWHM) of the intensity profile of the seeing disc, which can be measured using a point source, such as a star. Atmospheric seeing smears out what should be a point source over multiple pixels on the CCD, resulting in a fuzzy disc being imaged. Thus, the FWHM of this disc, derived from 2D Gaussian fits to the image, gives an estimate of the seeing.

Unfortunately WHT/ISIS does not provide acquisition images containing point sources which could be used to calculate the seeing. The RoboDIMM (Robotic Differential Image Motion Monitor) on La Palma does monitor the seeing conditions each night, providing 2D estimates, however it points continuously towards stars close to the zenith and so cannot provide specific estimates at the positions of the target objects on the sky. Instead, to estimate the FWHM of the seeing disc, the one-dimensional spatial FWHM of the telluric standard star, observed with each science target in the same position on the sky, was used.

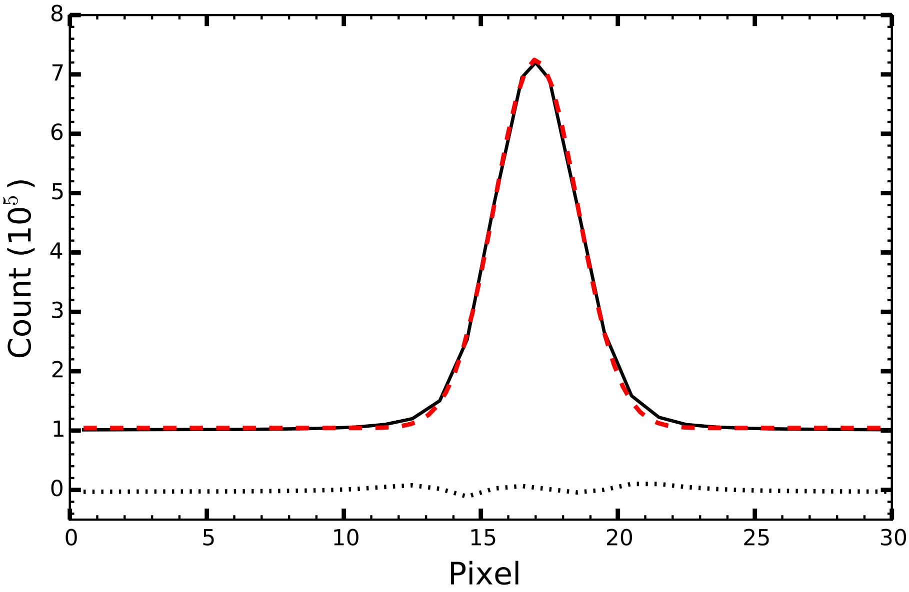

Figure 2.10: An example of the extracted spatial profile of a telluric star (black, solid), fitted with a single Gaussian (red, dashed). The black dotted line indicates the residuals of the fit.

To do this, spatial slices were extracted across a ~10Å wavelength range close to the wavelengths of the redshifted [OIII]λ5007 (a strong emission line commonly associated with AGN activity) in the 2D spectra of the telluric stars. The resultant 1D profiles were then fitted with a single Gaussian using DIPSO. The FWHM of this Gaussian fit was taken to be an estimate of the seeing. An example of this is shown in Figure 2.10.

The advantages of using this technique over the 2D seeing estimates from the RoboDIMM monitor are that it accounts for the integration of the seeing disc across the spectroscopic slit (see the discussion in Rose et al. 2018) and the measurement is taken at the same airmass as the object observations. The 1D seeing (FWHM) estimates obtained in this way ranged from 1.07 – 1.63 arcsec across the two nights of observations.

It is important to note that the exposure times for the telluric standard stars were short compared with those of the science targets (tens of seconds vs. tens of minutes). The seeing can, however, vary significantly over the total observation period for each target (1–2 hours). This means that the errors on the FWHM of the spatial profiles of the telluric standard stars provided by DIPSO are likely underestimations of the true uncertainty on the seeing. To account for this, the RoboDIMM measurements – taken every two minutes during the night – were used to provide an estimate of the variation in the seeing over the relevant observation periods. The standard errors on the means of the RoboDIMM measurements were calculated to provide percentage errors, and scaled with the FWHM measured from the telluric standard stars. In this way, a more realistic measure of the uncertainty in the seeing was created. The 1D seeing estimates, along with their associated uncertainties, for the individual objects are displayed in Table 2.2.

2.4.2 VLT/XShooter

Contrary to WHT/ISIS, the VLT/XShooter observations benefited from acquisition images of the target objects, meaning the FWHM of field stars present in these images could be used to estimate the FWHM of the seeing disc. This still suffers from the problem of short exposure times compared with the science exposures, and hence underestimation of the errors. In a similar way to the WHT/ISIS observations, variations in the seeing were provided by the DIMM channel of the MASS-DIMM instrument, and a better estimation of the uncertainty on the seeing could be calculated using the standard error on the mean of these measurements (Rose et al., 2018).

2.5 Slit locations and general descriptions

In this section, the slit locations for the spectroscopic observations are indicated, and general descriptions of the objects in the e-QUADROS sample are provided. Note that, in the following figures, north is upwards and east is to the left.

2.5.1 WHT/ISIS ULIRGs

The following object descriptions are adapted from Spence et al. (2018).

IRAS F01004–2237 (z = 0.11783)

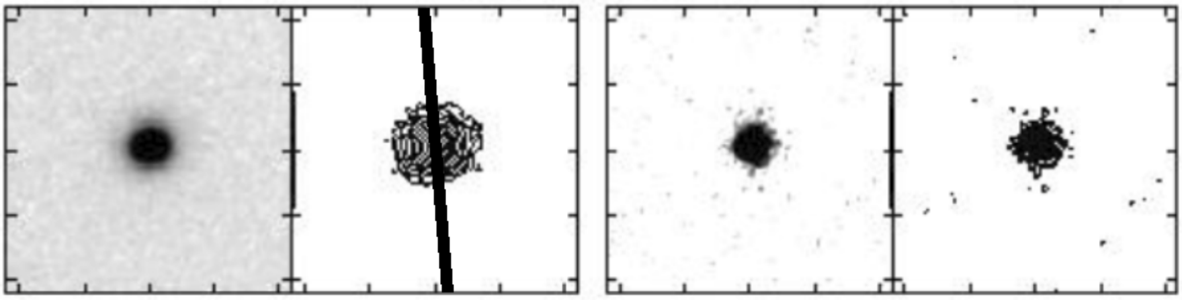

Figure 2.11: R-band (left) and K'-band (right) images and contour plots of F01004–2237, originally presented in Kim et al. (2002). The tick marks are separated by 5" and the thick vertical bar on the y-axis represents a distance of 20 kpc. Superimposed on the R-band contour plot is a black line indicating the slit position angle (5°) for the observations, as listed in Table 2.1.

The single nucleus, compact morphology of this system (Figure 2.11) suggests it is being observed at, or just after, the peak of a major merger (Surace et al., 1998). Historically it has been classified as both an HII galaxy and Seyfert II galaxy based on optical diagnostic line ratios – although the narrow components appear consistent with stellar photoionisation, the broad components are more consistent with ionisation by an AGN (Rodríguez Zaurín et al., 2013).

F01004–2237 is a particularly interesting object in the QUADROS sample. The optical spectra show that it has changed dramatically over the last decade – completely unexpectedly in the context of this study. Compared to previous spectra taken in 2005, the 2015 spectrum shows the appearance of unusually strong, broad helium emission lines (Tadhunter et al., 2017). A follow-up examination of an archival optical light curve revealed a significant flare in 2010, providing evidence for the first tidal disruption event (TDE) ever observed in a starburst galaxy (see §4.4).

IRAS F05189–2524 (z = 0.04275)

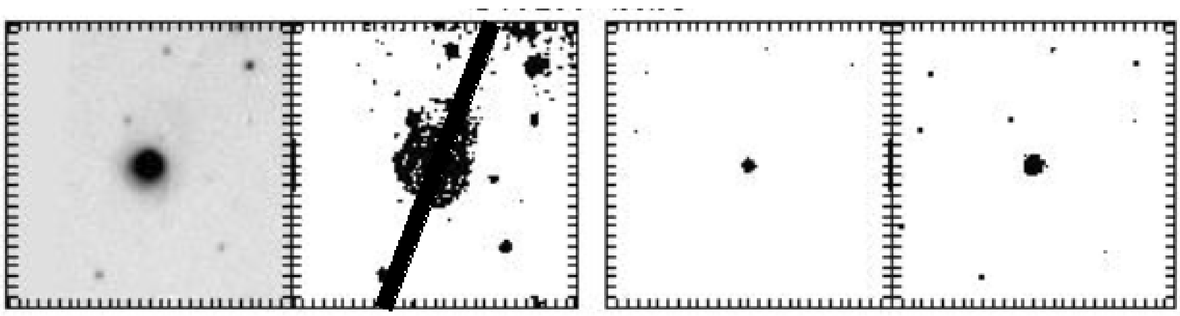

Figure 2.12: R-band (left) and K'-band (right) images and contour plots of F05189–2524, originally presented in Kim et al. (2002). The tick marks are separated by 5" and the thick vertical bar on the y-axis represents a distance of 20 kpc. Superimposed on the R-band contour plot is a black line indicating the slit position angle (340°) for the observations, as listed in Table 2.1.

F05189–2524 is a compact, late-stage merger surrounded by tidal debris (Veilleux et al., 2002, 2006, see Figure 2.12). In HST images it shows a complex nuclear structure, dominated by two bright knots separated by ∼0.25 arsec (Surace et al., 1998). It is not yet clear whether these two knots represent a true double nucleus, or a single nucleus bisected by a dust lane. A HST/STIS long-slit spectrum is available for this object, however, which cuts through both knots. This indicates that the AGN is associated with the more northerly of the two knots.

IRAS F13428+5608 (z = 0.0373)

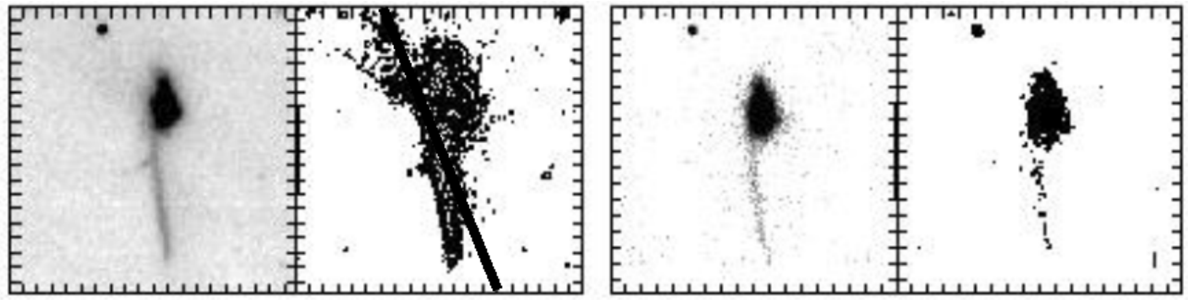

Figure 2.13: R-band (left) and K'-band (right) images and contour plots of F13428+5608 (Mrk 273), originally presented in Kim et al. (2002). The tick marks are separated by 5" and the thick vertical bar on the y-axis represents a distance of 20 kpc. Superimposed on the R-band contour plot is a black line indicating the slit position angle (23°) for the observations, as listed in Table 2.1.

F13428+5608, one of the closest ULIRGs (also known as Mrk 273), is a striking object well known for its ∼40 kpc tidal tail, shown in the and K'-band images in Figure 2.13. This object is discussed in detail in Chapter 3. Note that, unlike the rest of the e-QUADROS sample, in which the spectroscopic slits were centred on one of the object nuclei, the slit for Mrk 273 was positioned off-nucleus in order to sample the extended emission seen to the NE and SW of the nuclear region.

IRAS F14394+5332 (z = 0.10517)

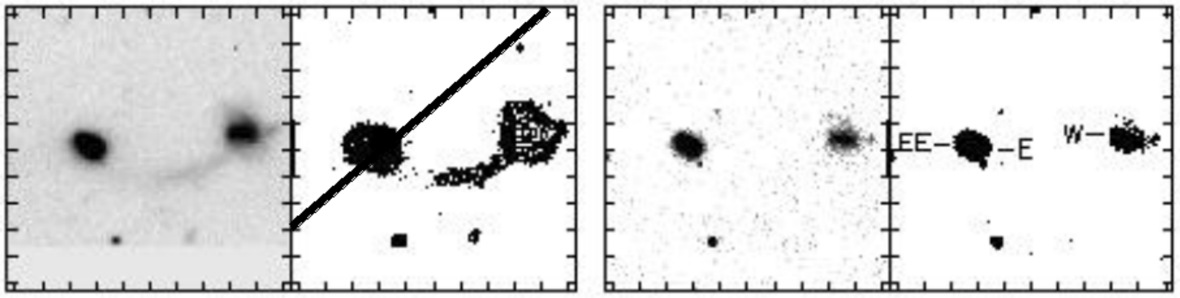

Figure 2.14: R-band (left) and K'-band (right) images and contour plots of F14394+5332, originally presented in Kim et al. (2002). The tick marks are separated by 5" and the thick vertical bar on the y-axis represents a distance of 20 kpc. Superimposed on the R-band contour plot is a black line indicating the slit position angle (130°) for the observations, centred on the Eastern (E) nucleus, as listed in Table 2.1.

F14394+5332 consists of two interacting galaxies separated by ~56 kpc and connected by a bridge of faint, diffuse emission (Kim et al., 2002; Tadhunter et al., 2018). The spectroscopic slit for the WHT/ISIS observations was placed on the more westerly of the two nuclei in the eastern galaxy (Kim et al., 2002) that contains the optical AGN nucleus (see Figure 2.14), and for which a powerful ionised nuclear outflow has been previously reported in Rodríguez Zaurín et al. (2013), based on the [OIII] emission lines (see also Lípari et al., 2003). Evidence for a molecular outflow is also reported in Veilleux et al. (2013), based on blueshifted OH 119μm profiles.

IRAS F17044+6720 (z = 0.13600)

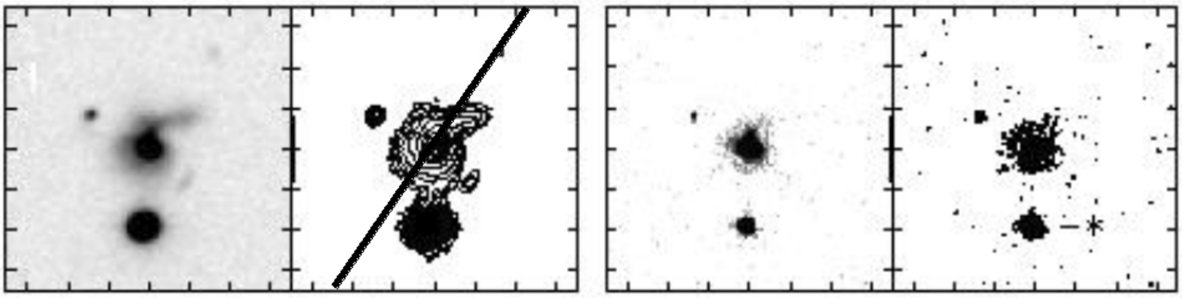

Figure 2.15: R-band (left) and K'-band (right) images and contour plots of F17044+6720, originally presented in Kim et al. (2002). The tick marks are separated by 5" and the thick vertical bar on the y-axis represents a distance of 20 kpc. Superimposed on the R-band contour plot is a black line indicating the slit position angle (145°) for the observations, as listed in Table 2.1. The "*" symbol represents a field star.

This is a highly disturbed system (see Figure 2.15), with two bright nuclear continuum condensations, a prominent series of dust features and a ~15 kpc tidal tail to the north (see Tadhunter et al., 2018). The extraction aperture for the WHT/ISIS observations was centred on the brightest nuclear continuum condensation, which also contains the AGN and warm outflow.

IRAS F17179+5444 (z = 0.14768)

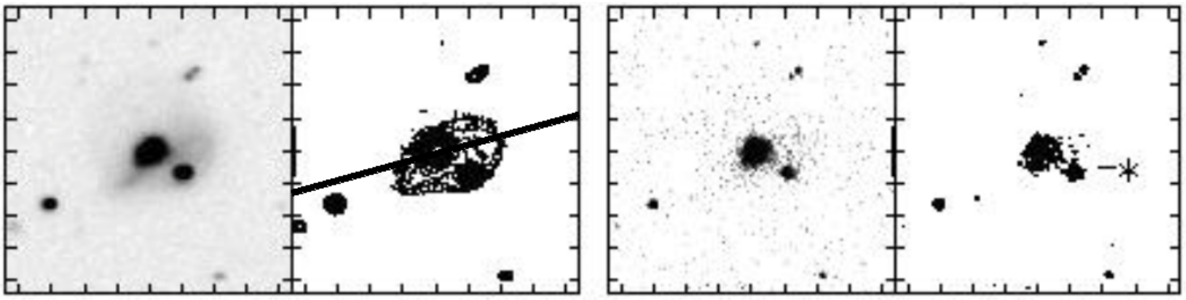

Figure 2.16: R-band (left) and K'-band (right) images and contour plots of F17179+5444, originally presented in Kim et al. (2002). The tick marks are separated by 5" and the thick vertical bar on the y-axis represents a distance of 20 kpc. Superimposed on the R-band contour plot is a black line indicating the slit position angle (105°) for the observations, as listed in Table 2.1. The "*" symbol represents a field star.

Although the continuum morphology of this single-nucleus object is complex due to a series of dust features that cross the nuclear regions, its [OIII] emission is dominated by a compact region associated with the brightest nuclear continuum condensation (Tadhunter et al., 2018); the spectroscopic extraction aperture for the WHT/ISIS observations was centred on this region (Figure 2.16). While evidence for warm ionised outflows from [OIII] emission is reported in Rodríguez Zaurín et al. (2013), Rupke et al. (2005c) found no evidence for significant outflows using the NaID absorption lines. Note that F17179+5444 is one of the few objects in the e-QUADROS sample that can be considered radio-loud, with $L_{1.4GHz} = 10^{25.23}$ W Hz^{-1}. To date, however, there have been no reports of jets associated with this radio emission.

IRAS F23060+0505 (z = 0.17301)

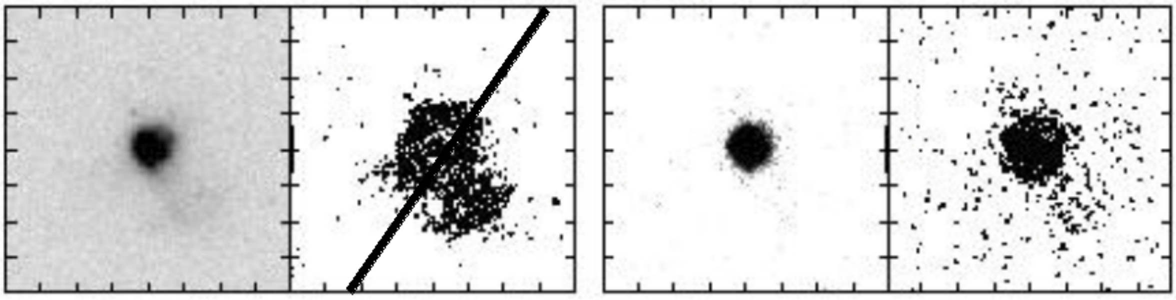

Figure 2.17: R-band (left) and K'-band (right) images and contour plots of F23060+0505, originally presented in Kim et al. (2002). The tick marks are separated by 5” and the thick vertical bar on the y-axis represents a distance of 20 kpc. Superimposed on the R-band contour plot is a black line indicating the slit position angle (325°) for the observations, as listed in Table 2.1.

F23060+0505 hosts the most powerful AGN out of the WHT/ISIS ULIRGs and would be classified as a quasar based on its [OIII] luminosity. Figure 2.17 shows it to be a single-nucleus system with a diffuse tidal feature to the south-west. Cicone et al. (2014) reported evidence for a massive molecular outflow in this object, based on CO emission. Broad-line region (BLR) components observed in this object (Veilleux et al., 1997; Rodríguez Zaurín et al., 2013) suggests that a moderately reddened type I AGN component is present in this source.

IRAS F23233+2817 (z = 0.11446)

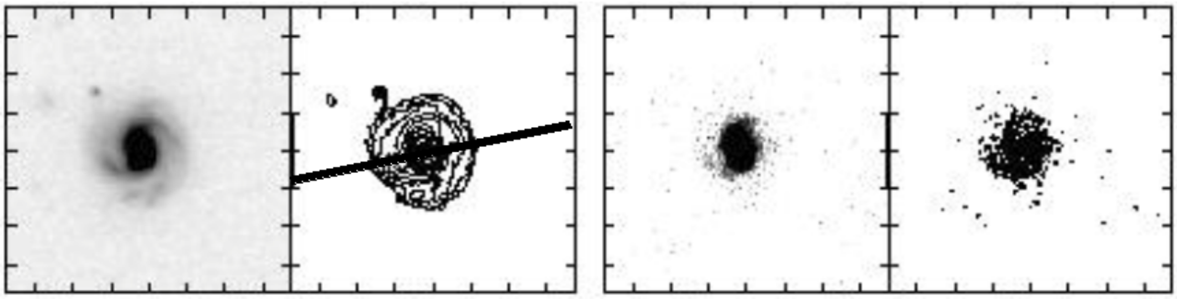

Figure 2.18: R-band (left) and K'-band (right) images and contour plots of F23233+2817, originally presented in Kim et al. (2002). The tick marks are separated by 5" and the thick vertical bar on the y-axis represents a distance of 20 kpc. Superimposed on the R-band contour plot is a black line indicating the slit position angle (282°) for the observations, as listed in Table 2.1.

Figure 2.18 shows F23233+2817 to have spiral-like morphology surrounding a very compact nucleus, with no visible tidal tails. F23233+2817 is one of few objects in the original 1 Jy sample with no obvious signs of interaction. Evidence for molecular outflows in this source based on OH 119μm is presented in Veilleux et al. (2013).

IRAS F23389+0303 (z = 0.14515)

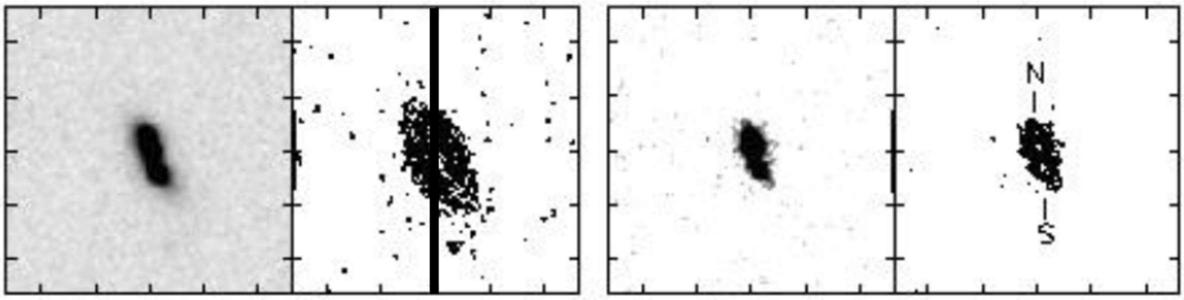

Figure 2.19: R-band (left) and K'-band (right) images and contour plots of F23389+0303, originally presented in Kim et al. (2002). The tick marks are separated by 5” and the thick vertical bar on the y-axis represents a distance of 20 kpc. Superimposed on the R-band contour plot is a black line indicating the slit position angle (0°) for the observations, as listed in Table 2.1. The slit was centred on the northern (N) nucleus.

F23389+0303 is a close binary, separated by 5.2 kpc (Kim et al., 2002; Veilleux et al., 2002), with a short tidal feature to the south (Figure 2.19). The spectroscopic extraction aperture was centred on the northern nucleus of the system. Evidence for blueshifted kinematics has been reported for neutral Na ID and OH 119μm in Rupke et al. (2005c) and Veilleux et al. (2013) respectively. F23389+0303 is another radio-loud object in the sample ($L_{1.4GHz} = 10^{25.63}$ W Hz^{-1}). A radio map of this object is presented in Nagar et al. (2003), showing two slightly resolved radio lobes separated by $\sim$ 830 pc.

2.5.2 VLT/XShooter ULIRGs

The following object descriptions are adapted from Rose et al. (2018).

IRAS F12072–0444 (z = 0.12905)

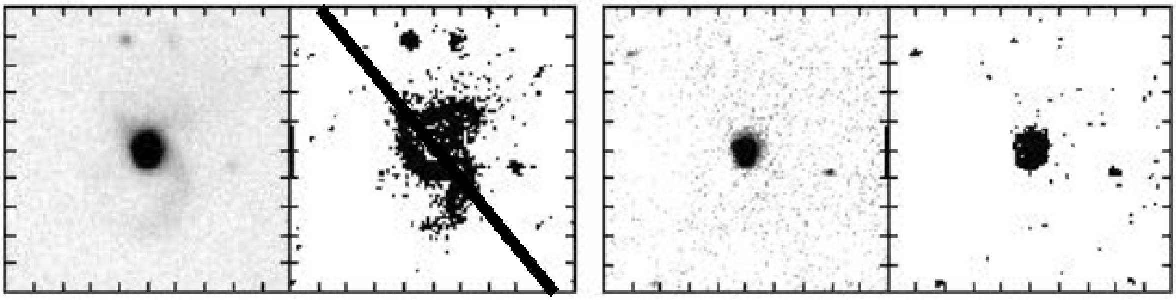

Figure 2.20: R-band (left) and K'-band (right) images and contour plots of F12072–0444, originally presented in Kim et al. (2002). The tick marks are separated by 5” and the thick vertical bar on the y-axis represents a distance of 20 kpc. Superimposed on the R-band contour plot is a black line indicating the slit position angle (40°) for the observations.

Although F12072–0444 appears to be a single nucleus system in the optical and near-IR images in Figure 2.20, high-resolution HST imaging reveals a double nucleus separated by ∼1 arcsec in the H-band (Veilleux et al., 2006). The spectroscopic slit for the VLT/XShooter observations was centred on the apparent single optical nucleus. The warm ionised outflow in this object was previously described by Rodríguez Zaurín et al. (2013), and evidence for a molecular outflow was detected by Spoon et al. (2013) and Veilleux et al. (2013) based on OH observations.

IRAS F13305–1739 (z = 0.14843)

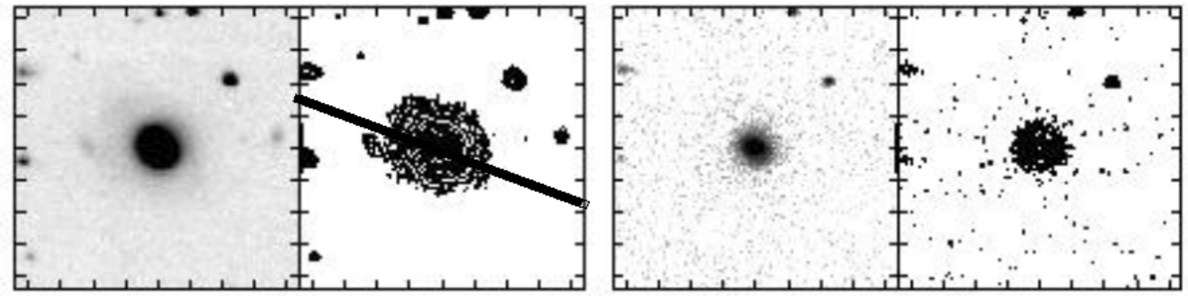

Figure 2.21: R-band (left) and K'-band (right) images and contour plots of F13305–1739, originally presented in Kim et al. (2002). The tick marks are separated by 5" and the thick vertical bar on the y-axis represents a distance of 20 kpc. Superimposed on the R-band contour plot is a black line indicating the slit position angle (70°) for the observations.

F13305–1739 appears as a single nucleus system in Figure 2.21. Evidence for an ionised outflow was discussed by Rodríguez Zaurín et al. (2013), however this object shows no evidence for molecular or neutral outflows based on OH and NaID absorption-line observations (Rupke et al., 2005c; Veilleux et al., 2013). F13305–1739 is the most luminous object in the QUADROS sample, and is classed as a type II quasar according to the criterion of Zakamska et al. (2003).

IRAS F13443+0802 (z = 0.13479)

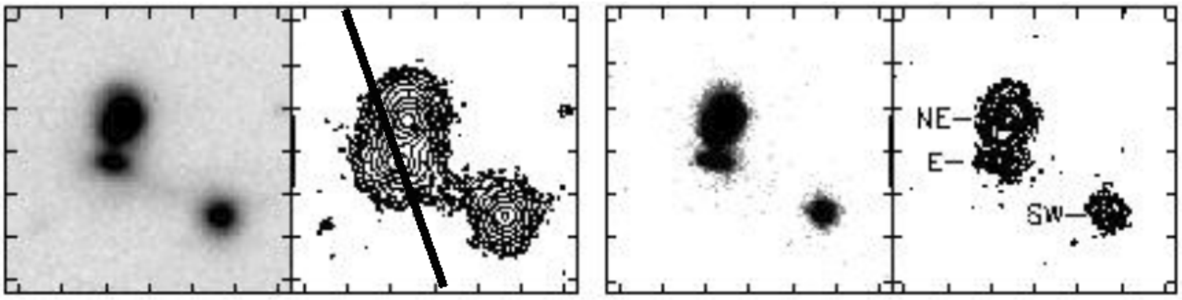

Figure 2.22: R-band (left) and K'-band (right) images and contour plots of F13443+0802, originally presented in Kim et al. (2002). The tick marks are separated by 5" and the thick vertical bar on the y-axis represents a distance of 20 kpc. Superimposed on the R-band contour plot is a black line indicating the slit position angle (20°) for the observations. The slit was centred on south-eastern (denoted E) nucleus

.

F13443+0802 is a triple system consisting of a close pair to the east (denoted NE and E in Figure 2.22) separated by ∼12 kpc and a third component (denoted SW) ∼37 kpc to the south west. A "Y-shaped" structure is apparent in optical HST imaging of the south-eastern component of the close pair (Tadhunter et al., 2018). The spectroscopic slit for the VLT/Xshooter observations was centred on this structure, which represents the location of the AGN. No evidence for a neutral outflow in this component was found by Rupke et al. (2005c) based on optical NaID absorption.

IRAS F13451+1232 (z = 0.12142)

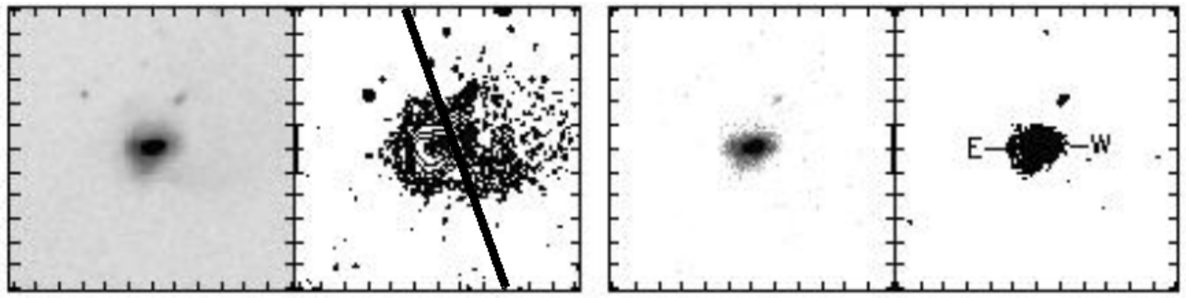

Figure 2.23: R-band (left) and K'-band (right) images and contour plots of F13451+1232, originally presented in Kim et al. (2002). The tick marks are separated by 5” and the thick vertical bar on the y-axis represents a distance of 20 kpc. Superimposed on the R-band contour plot is a black line indicating the slit position angle (20°) for the observations. The slit was centred on the western (W) nucleus.

F13451+1232 is a close double nucleus system separated by 2.1” (Kim et al., 2002; Tadhunter et al., 2018). The spectroscopic slit for the XShooter observations was centred on the western nucleus, which contains the AGN (see Figure 2.23). This object also qualifies as a type II quasar based on the Zakamska et al. (2003) criterion. Clear evidence for an emission-line outflow at optical wavelengths was presented by Holt et al. (2003), and evidence for neutral outflows has been detected in the HI 21cm and optical NaID lines (Morganti et al., 2005; Rupke et al., 2005c). In addition, a molecular outflow has been detected in CO emission (Dasyra & Combes, 2012; Morganti et al., 2013). F13451+1232 is also radio-loud, with $L_{1.4GHz} = 10^{26.30}$ W Hz^{-1}.

IRAS F14378–3651 (z = 0.06809)

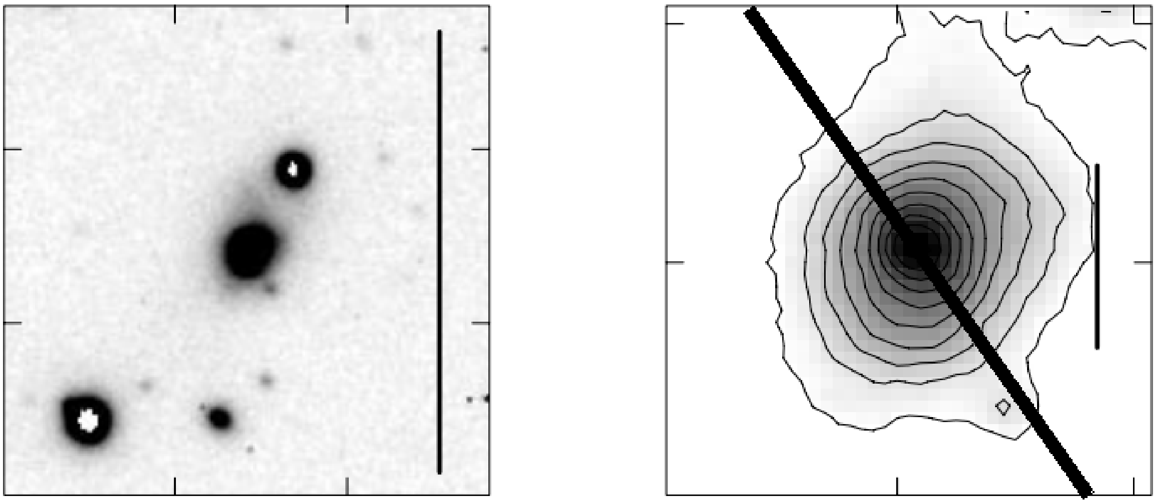

Figure 2.24: *R*-band image (left) and contour plot (right) of F14378–3651, originally presented in Duc et al. (1997). The tick marks in the left image are separated by 15" and the thick vertical bar represents a distance of 50 kpc. The tick marks in the right image are separated by 5" and the thick vertical bar represents a distance of 5 kpc. Superimposed on the contour plot is a black line indicating the slit position angle (35°) for the observations.

F14378–3651 shows a single, compact nucleus in Figure 2.24. An emission-line outflow was previously detected in Hα by Westmoquette et al. (2012), and clear evidence for a molecular outflow has been detected in OH (Sturm et al., 2011; Veilleux et al., 2013; González-Alfonso et al., 2017).

IRAS F15130+1958 (z = 0.11081)

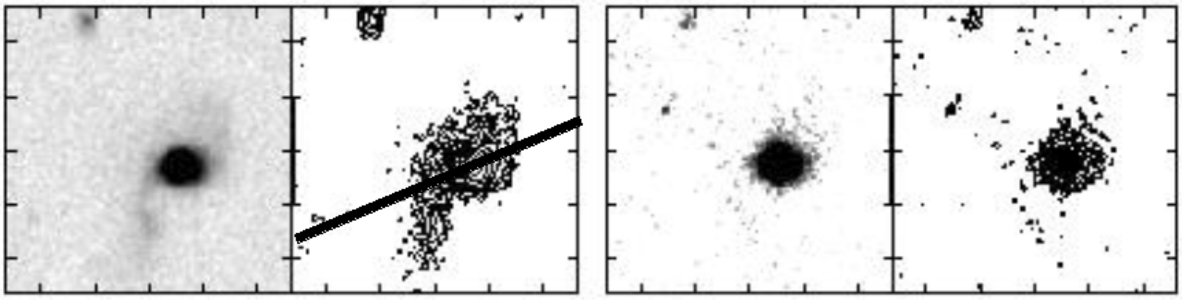

Figure 2.25: R-band (left) and K'-band (right) images and contour plots of F15130+1958, originally presented in Kim et al. (2002). The tick marks are separated by 5" and the thick vertical bar on the y-axis represents a distance of 20 kpc. Superimposed on the R-band contour plot is a black line indicating the slit position angle (113°) for the observations.

Figure 2.25 shows F15130+1958 to be a single-nucleus, compact source (also see Tadhunter et al., 2018), with tidal features to the north-west and south-east of the nucleus. The optical to near-IR spectrum of this object is unusual in that, while the blue end of the spectrum is relatively flat and shows clear Balmer absorption features characteristic of a young stellar population, the spectrum rises steeply from the red end of the optical into the near-IR. This shape is consistent with the presence of a moderately obscured type I AGN, however the expected broad-line region (BLR) component to Paα was not detected in the VLT/XShooter spectrum.

IRAS F15462–0450 (z = 0.09969)

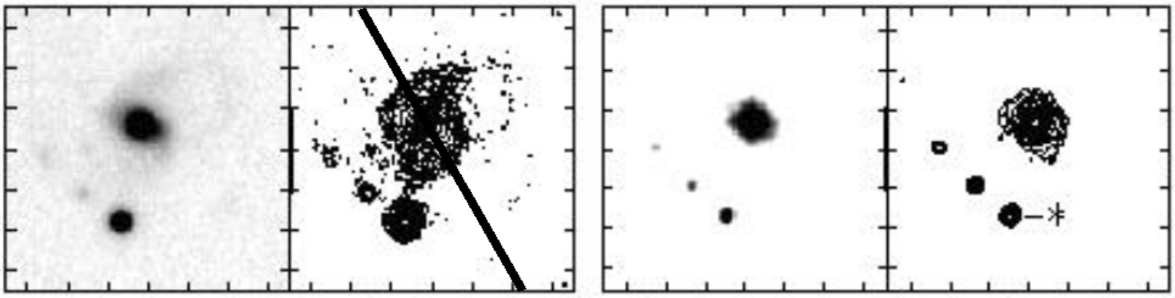

Figure 2.26: R-band (left) and K'-band (right) images and contour plots of F15462–0450, originally presented in Kim et al. (2002). The tick marks are separated by 5" and the thick vertical bar on the y-axis represents a distance of 20 kpc. Superimposed on the R-band contour plot is a black line indicating the slit position angle (30°) for the observations, as listed in Table 2.1.

F15462–0450 is a single nucleus system which shows strong BLR components to the hydrogen lines, indicating the presence of a type I AGN. Clear tidal features can be seen surrounding the nucleus in the left hand images of Figure 2.26. Evidence for a molecular outflow in this source was found by Veilleux et al. (2013) and Spoon et al. (2013) using OH absorption lines.

IRAS F16156+0146 (z = 0.13260)

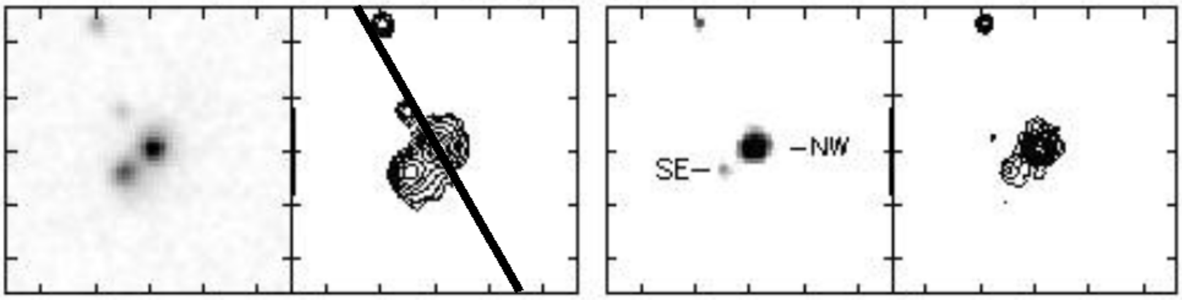

Figure 2.27: R-band (left) and K'-band (right) images and contour plots of F16156+0146, originally presented in Kim et al. (2002). The tick marks are separated by 5" and the thick vertical bar on the y-axis represents a distance of 20 kpc. Superimposed on the R-band contour plot is a black line indicating the slit position angle (30°) for the observations.

F16156+0146 shows two nuclei separated by ∼3.5 arcseconds (Figure 2.27). For the VLT/XShooter observations, the spectroscopic slit was centred on the NW nucleus, which contains the AGN.

IRAS F19254–7245 (z = 0.06165)

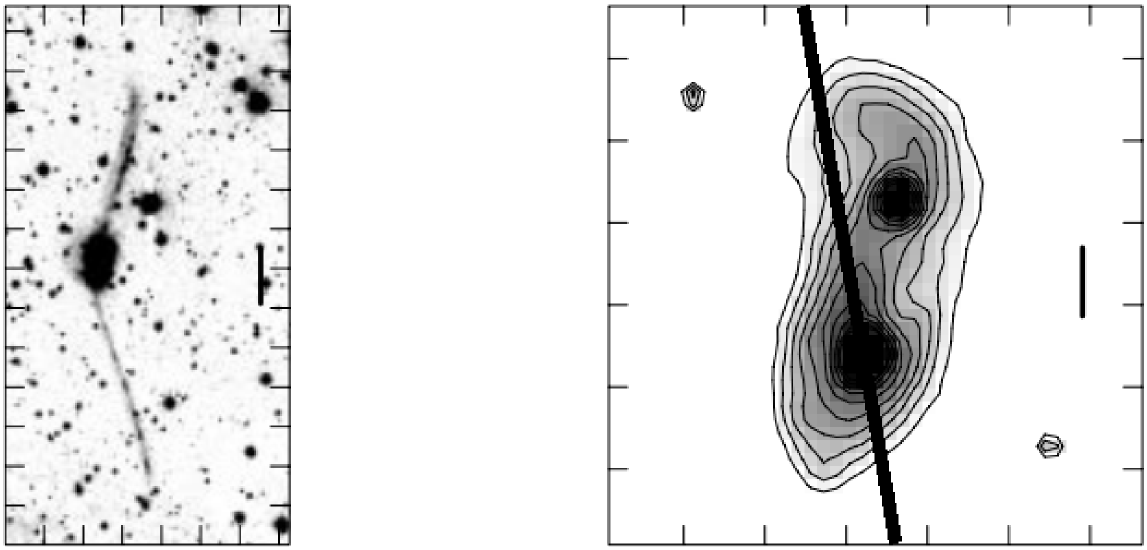

Figure 2.28: *R*-band image (left) and contour plot (right) of F19254–7245, originally presented in Duc et al. (1997). The tick marks in the left image are separated by 15" and the thick vertical bar represents a distance of 50 kpc. The tick marks in the right image are separated by 5" and the thick vertical bar represents a distance of 5 kpc. Superimposed on the contour plot is a black line indicating the slit position angle (10°) for the observations.

F19254–7245 (also known as the Superantennae Galaxy) is a well-studied merging system with two optical nuclei separated by 8.5 arcsec in the north-south direction (see Figure 2.28). The spectroscopic slit for the VLT/XShooter observations was centred on the southern nucleus, which contains the AGN. The southern nucleus also shows evidence for a molecular outflow based on OH absorption lines (Spoon et al., 2013). Evidence for a warm outflow is also seen in several optical emission lines (Colina et al., 1991; Mirabel et al., 1991; Westmoquette et al., 2012).

2.6 Chapter summary

This chapter has described the sample selection, data collection and reduction processes relevant to the work in this thesis. In addition, slit locations and general descriptions of each ULIRG in the main e-QUADROS sample have been provided. The following chapters present detailed analyses of these datasets, in an attempt to answer the questions posed in Chapter 1. The next chapter focusses on the properties of the extended ionised regions of one of the closest and most spectacular objects in the local Universe: Mrk 273.

Chapter 3

Case study: Markarian 273

3.1 Declaration

The work presented in this chapter was published in Spence et al. (2016), "*No evidence for large-scale outflows in the extended ionized halo of ULIRG Mrk 273*", Monthly Notices of the Royal Astronomical Society (MNRAS), in March 2016. The initial project proposal and data collection were contributed to by Javier Rodríguez Zaurín, Clive Tadhunter, Antonio Cabrera-Lavers, Henrik Spoon and Casiana Muñoz-Tuñon. Clive Tadhunter, Marvin Rose and Javier Rodríguez Zaurín were also involved in helpful discussions throughout the project. Unless stated otherwise, the text, figures, analysis, and interpretations presented in this chapter are my own work.

3.2 Chapter introduction

As discussed in Chapter 1, major mergers of two (or more) gas-rich galaxies are believed to be a key mechanism in driving galaxy evolution, forcing gas and dust towards the nuclear regions and triggering both starburst and AGN activity (e.g. Di Matteo et al., 2005). Hydrodynamical simulations indicate that this nuclear activity has the potential to drive surrounding gas out of the merging systems, heating and removing potentially star-forming material, and hence shaping their evolution.

Local ULIRGs are ideal laboratories for studying this process in detail, as they represent the phase in which the nuclear outflows are expected to have the most significant effects on the host galaxy. Many previous studies, however, have focused on a radius of only a few kpc from the nucleus and evidence for larger-scale outflows is still lacking, leading to significant uncertainties in quantifying the energetics of the outflows. Measuring the maximum radial extent of the AGN-driven outflows is complicated by atmospheric seeing, which can "smear" out the light in observations and lead to over-estimation of the outflow radii if not accounted for properly (e.g. Villar-Martín et al., 2016; Husemann et al., 2016a). Moreover, the extended gas at significant distances from the nuclear regions is likely to have low surface brightnesses. These extended components could be easily missed if the imaging and or/spectroscopic observations are not deep enough, leading to underestimation of the outflow radii. It is therefore important to determine the true spatial extents of these AGN-driven outflows and investigate the ultimate fate of the outflowing gas.

In order to address these issues, a deep imaging and spectroscopic survey of local ULIRGs (QUADROS) has been undertaken, with the goal of better quantifying the outflows (see Chapter 2 for details). As part of this study, Markarian 273 (Mrk 273), one of the closest ULIRGs to the Milky Way ($z = 0.0373, L_{IR} = 10^{12.10} L_{\odot}$), was observed. This merging system shows evidence for galaxy-wide emission line gas (Rodríguez Zaurín et al., 2014, hereafter RZ14), making it an ideal case study to investigate the size, origin and kinematics of these extended structures. The motivation for this chapter is to establish whether the extended gas is part of the AGN-driven nuclear outflow, which would provide direct observational evidence for the galaxy-wide outflows predicted by simulations (e.g. Di

Matteo et al., 2005; Springel et al., 2005; Johansson et al., 2009).

This chapter is structured as follows. In Section 3.3 I briefly describe Mrk 273 and give an overview of previous observations. I then describe the morphology and kinematics of Mrk 273 in Sections 3.4.1 and 3.4.2. Section 3.4.3 gives estimates of the electron density, reddening and gas mass in the extended regions of Mrk 273. I then examine the ionisation mechanism of the extended gas in Section 3.4.4, before discussing the implications of these results in Section 3.5.

3.3 A brief history of Mrk 273

3.3.1 Description

Mrk 273 (IRAS F13428+5608) is a well studied, visually striking object. Figure 3.1 shows an optical broad-band image taken with the HST. Mrk 273 can be considered a prototypical ULIRG, with a complex optical structure. The luminous nuclear region can be seen towards the upper centre of Figure 3.1, which contains three separate nuclei (RZ14). Stretching towards the south of the nuclear region (bottom of the image) is a spectacular tidal tail which extends over 40 kpc (∼130 million light-years) and provides strong evidence that Mrk 273 is a merging system formed of two (or more) colliding galaxies.

3.3.2 Previous observations

The nuclear regions of Mrk 273 show evidence for three nuclei: two detected at near- and mid-IR wavelengths (referred to as N and SW), separated by a distance of around 800 parsecs, and a third (referred to as SE) detected in [OIII] and radio emission (RZ14). The SW nucleus coincides with a strong hard X-ray point source, indicating that this nucleus

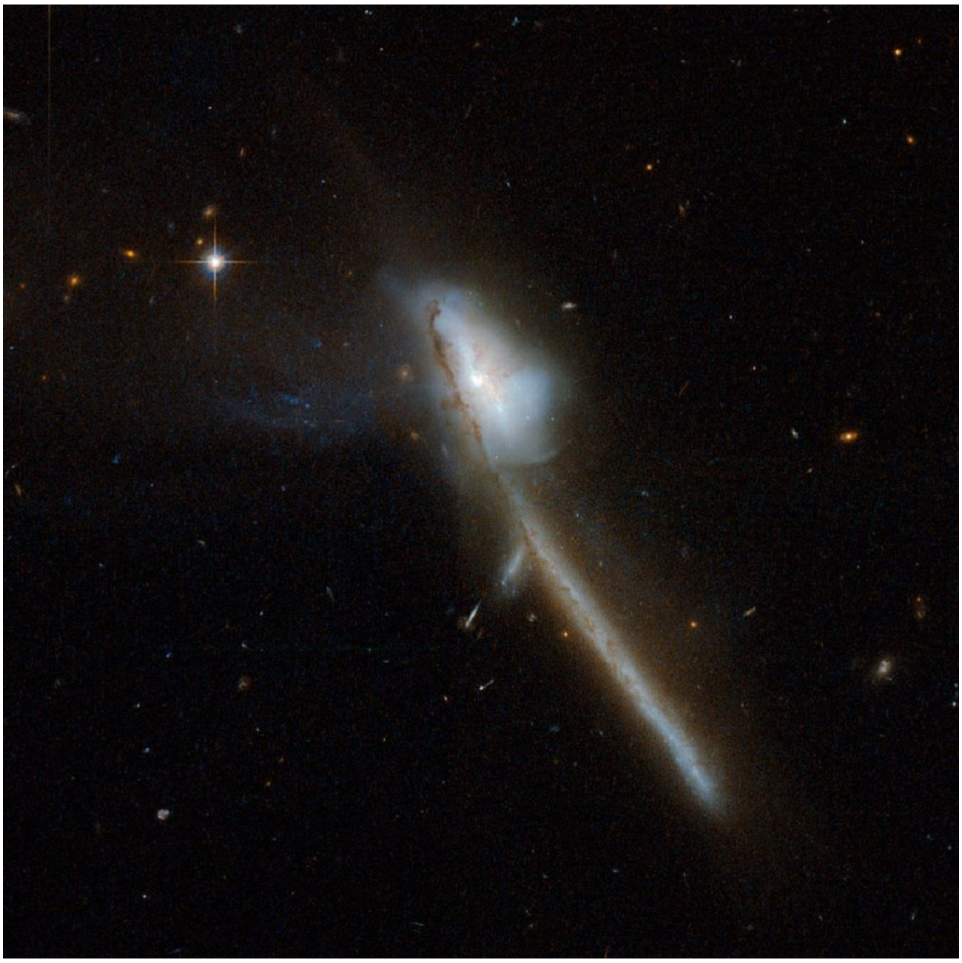

Figure 3.1: HST optical image of Mrk 273. Credit: NASA, ESA, the Hubble Heritage Team (STScI/AURA)-ESA/Hubble Collaboration and A. Evans (University of Virginia, Charlottesville/NRAO/Stony Brook University).

hosts an AGN. This was confirmed by U et al. (2013) using Keck integral-field observations. The N nucleus is the strongest radio source and also shows evidence for a buried AGN. In this nucleus, U et al. (2013) observed a rotating gas disk, and evidence for a molecular outflow based on H_2 emission. They also found that the SE nucleus, while first identified as a star cluster, emits strong [SiVI] emission consistent with AGN photo-ionisation. RZ14 then observed a strong, compact [OIII] structure in HST imaging coincident with this location, which supported the idea that the SE nucleus hosts a third AGN. This means that, in Mrk 273, it is likely that a rare, triple major merger (ratio of gas masses ∼1:1:1) is being witnessed in action.

While much attention has been paid in the past to the luminous nuclear regions of Mrk 273, the extended features that are faintly visible in Figure 3.1 have not been well studied. RZ14 attempted to fill this knowledge gap by obtaining further HST imaging and spectroscopic observations. These showed a loop of [OIII] emission extending ∼20 kpc to the east of the nuclear region, as well as highly disturbed emission line kinematics within a radius of 6 kpc (see also Rupke & Veilleux, 2013, hereafter RV13). The slits for these spectroscopic observations, however, did not sample the full extent of the extended halo, and the HST imaging did not probe the low-surface brightness features to the SW of the nuclear region.

This case study builds on the above work by combining new deep GTC/OSIRIS imaging[1] with a new WHT/ISIS long-slit spectrum, positioned to sample the off-nuclear emission to the NE and SW of the nuclear region (see Figure 2.13 for the slit location), in order to further investigate the kinematics and ionisation mechanisms of the extended halo of Mrk 273. The aim was to determine whether the extended halo surround-

---

[1] Note that the GTC imaging data were provided and reduced by Javier Rodriguez Zaurin through private communication.

ing the galactic core was formed from galaxy-wide outflows, or simply quiescent gas illuminated by the central AGN/starburst.

3.4 Results

This section presents the main results obtained from combined analyses of the deep imaging and the new long-slit spectrum.

3.4.1 Morphology

Firstly, the morphology of the merging system was examined. The deep line-free continuum image of Mrk 273 is presented in Figure 3.2a. This medium-band image was taken blueward of Hα using the OSIRIS red Order Sorter (OS) Filter f657/35 ($\lambda_{\mathrm{central}}$ = 6572Å; FWHM = 350Å). The exposure time was 270 seconds. This image traces the bulk stellar material of the system. The most luminous material is shown in white, with the lower surface brightness material ranging from light to dark blue as the surface brightness decreases. This image shows the impressive tidal tail to the south of the galaxy, which is a tell-tale sign that a merger has taken/is taking place. The tail is formed of debris from the primary merger event. Also present is a narrow dust lane along the tidal tail (clearly seen in the HST images presented in RZ14). This suggests that the disk of the main merging galaxy – and the plane of the primary merger – is being viewed close to edge-on (in all telescopic imaging a two-dimensional projection of a three-dimensional structure is observed).

Another notable feature is the appearance of a looped continuum structure extending >45 kpc to the north-east (NE) of the nuclear region, at an angle, $\theta \sim 130^{\circ}$, relative to the tidal tail. The diagram in Figure 3.3 indicates how this angle was measured. Assuming, based on the presence of the dust lane, that the tidal tail represents the plane of the main merger,

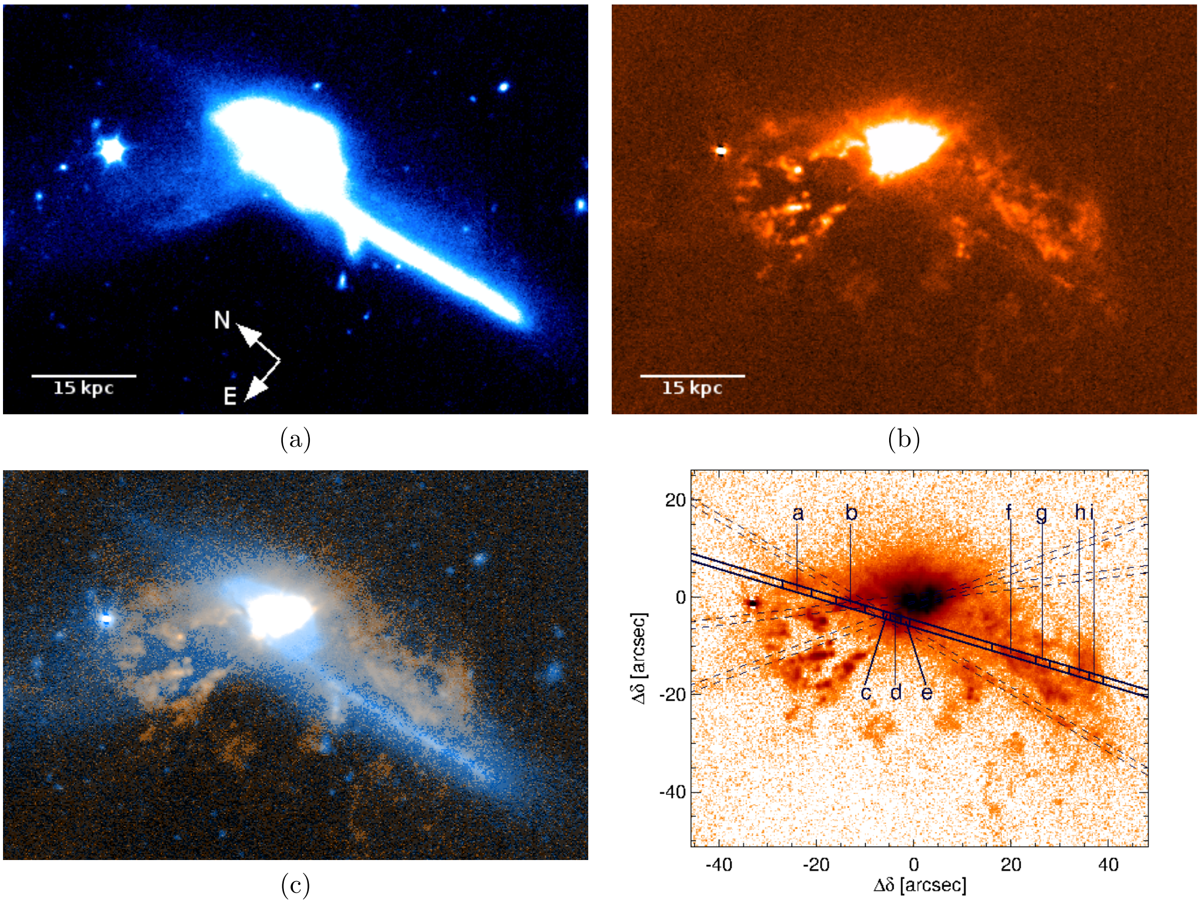

(a) (b)

(c) (d)

Figure 3.2: Images of Mrk 273 obtained with GTC/OSIRIS. **a)** Line-free continuum image showing the main tidal tail to the S and lower surface brightness diffuse emission to the NE and SW of the nuclear region. Note the extended loop to the NE. **b)** Continuum-subtracted Hα image, showing the bright knots to the NE. Also visible is the large amount of extended emission to the W of the tail. **c)** A composite colour image of the system. Blue and red/orange colours represent the continuum and Hα emission respectively. **d)** Hα image overplotted with the WHT/ISIS slit (PA 23) indicating the main apertures used for this work (solid), along with the locations of the other spectroscopic slits (PA 56, 70 and 180, dashed; Rodríguez Zaurín et al. 2010 and RZ14). Two further slits were shifted 1 arcsec to the N at PA 56 and 70, but are not plotted for clarity.

the NE structure could represent the tidal debris of a second merging galaxy which has approached/is approaching the nucleus at a large angle to the plane of the main merger. Combined with the presence of the third (SE) nucleus (RZ14), the morphology supports the conclusion that Mrk 273 is a triple merger system.

Finally, there is also significant continuum emission running parallel to and west of the main tidal tail, but much less emission to the east.

In comparison, Figure 3.2b shows a deep continuum-subtracted Hα image. To sample the Hα emission from the galaxy, the tunable filter was centered on 6810.7±2.0Å (i.e. the red-shifted Hα wavelength for the galaxy) and used with order sorter filter f680/43 ($\lambda_{\rm central}$ = 6802.1Å; FWHM = 432Å). These narrow-band observations had an effective band-pass of 17.7Å, sensitive to $|\Delta v_{\rm H\alpha}| <$ 400kms^{-1}. The exposure time was 1680 seconds. The resultant image traces only the line-emitting ionised gas. The most luminous gas is shown in white, with the lower surface brightness material in orange. Clearly visible is a spectacular nebula of ionised gas, stretching $\sim$ 40 kpc to the NE and SW of the nuclear region, with lower surface brightness regions also visible $>$ 45 kpc to the SE. It is this extended nebula that, if associated with the AGN-driven outflows, would provide direct evidence for the galaxy-wide outflows predicted by the hydrodynamical simulations. Note that this is the first time that the true scale of the spectacular halo surrounding Mrk 273 has been imaged.

It is notable that the Hα nebula to the NE stretches in a similar direction and with a similar spatial extent to the continuum loop, suggesting that the stellar material and ionised gas in this location are related. Note also that the inner ($<$ 20 kpc) higher surface brightness Hα knots were detected in [OIII] emission by RZ14. The substantial Hα emission observed to the west of the main tidal tail is also striking – little [OIII] emission was detected in this region in the previous HST imaging. This Hα emission

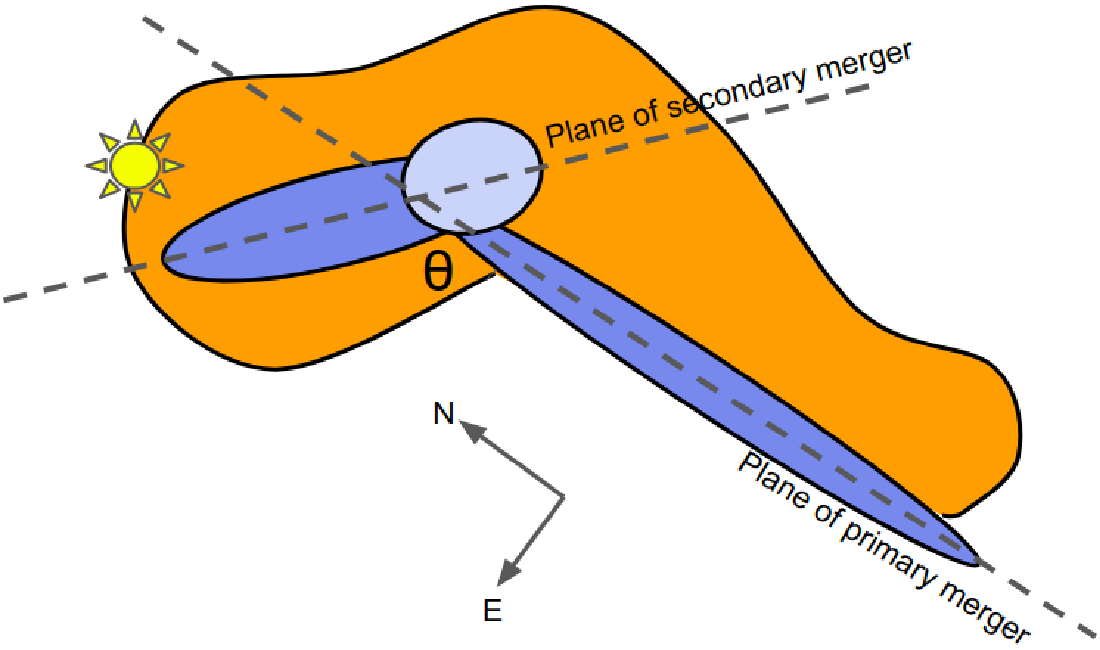

Figure 3.3: Diagram indicating the angle between primary and secondary merger planes. The central light blue region represents the nucleus, and the elongated dark blue regions represent the tidal tail to the south and the continuum "loop" to the NE. The surrounding orange region represents the ionised emission-line halo. θ is approximately 130°. The star to the NE indicates the location of a foreground star in the image. The relative scales are approximate.

is most prominent to the west of the main tail, again appearing to be related spatially to the continuum emission. The composite colour image in Figure 3.2c highlights this, showing the ionised gas (orange) overlying the continuum emission (blue).

3.4.2 Kinematics

Next, the kinematic properties of the gas sampled by the WHT/ISIS slit (PA = 23°; see Figure 3.2c) were analysed. To do this, multiple one-dimensional spectra were extracted along the spatial axis of the two-dimensional spectrum. Each 1D spectrum represented a different location within Mrk 273 and hence sampled various regions of the extended halo.

The most prominent emission lines ([OIII]λ5007, Hα and [NII]λ6583) within these spectra were then fitted with a Gaussian profile using DIPSO. From these fits, the radial velocities of the gas relative to the host galaxy rest frame (Δv), and also the velocity widths (FWHM) – which were taken to represent the level of turbulence present in the gas (i.e. the broader the emission lines, the more turbulent the gas) – were calculated.

The velocity shifts for each emission line quoted in this chapter are relative to the expected wavelengths for the host galaxy rest frame, which was calculated assuming $z = 0.0373$, as used by RZ14. The velocity widths quoted in this chapter, and subsequent chapters, have been corrected for instrumental broadening. The instrumental widths were estimated by calculating the weighted mean FWHM of three prominent sky lines at different wavelengths detected in each arm. For Mrk 273, the instrumental widths were 5.4±0.1Å and 5.1±0.2Å for the blue and red arms respectively. Assuming Gaussian profiles, the intrinsic widths of the emission lines (in km s^{-1}) were then determined using:

$$\mathrm{FWHM}_{\mathrm{intrinsic}} = \frac{\sqrt{\mathrm{FWHM}^2_{\mathrm{measured}} - \mathrm{FWHM}^2_{\mathrm{instrumental}}}}{\lambda_{\mathrm{observed}}} \times c, \tag{3.1}$$

and the associated errors propagated accordingly.

Figures 3.4 and 3.5 show the velocity widths (FWHM) and radial velocity shifts (Δv) measured using single Gaussian fits at different locations along the slit for the [OIII]λ5007, Hα and [NII]6583 emission lines. The reference point for the x-axis ($D = 0$ kpc) was chosen to be the centroid of the continuum emission along the slit, corresponding to the position of closest approach to the nucleus. This was because, unlike the rest of the e-QUADROS sample, the slit for Mrk 273 did not pass directly through the central nuclear region of the system. Instead, the slit was shifted ~2 kpc to the east. Intermediate to broad line widths (FWHM $>$ 500 km s^{-1}), indicative of high velocity gas associated with the powerful near-nuclear outflows, were detected in the region where the slit intersects the near-nuclear region. These velocities are consistent with previous studies (e.g. U et al., 2013; Rodríguez Zaurín et al., 2014). With the exception of one region with large error bars at $r \sim -8$ kpc, these broad lines appear to be confined to a narrow range along the slit ($0 \lesssim r \lesssim 5$ kpc). Taking the slit geometry into account, this corresponds to a maximum radial distance of $\sim$6 kpc from the centre of the nuclear region. While this is a relatively large radius compared with what is commonly measured for AGN-driven outflows in ULIRGs ($r \lesssim 2$ kpc; see Chapter 4 and also Rose et al. 2018 and Spence et al. 2018) it is still small compared to the typical radii of massive galaxies.

Outside the near-nuclear regions ($r > 6$ kpc), the widths of the Hα, [NII]λ6583 and [OIII]λ5007 emission lines are relatively narrow (FWHM $\lesssim$ 400 km s^{-1}), and the velocity shifts small ($|\Delta v| \lesssim$ 250 km s^{-1}). These would not be considered consistent with outflows based on the criteria of Rodríguez Zaurín et al. (2013). All emission lines in the extended regions of the PA 23° slit were well fit with single Gaussians and showed no signs of multiple kinematic components. Similarly quiescent kinematics were found in the extended regions in all other sampled slit locations: four from RZ14 and one from Rodríguez Zaurín et al. (2009), indicated by the dotted lines on Figure 3.2d. Therefore, despite extreme outflows with velocities up to 1500 km s^{-1} in the near-nuclear regions, kinematic analysis of the extended halo sampled by these various slit positions provides no obvious evidence to indicate that the outflow extends beyond a radius of $\sim$ 6 kpc.

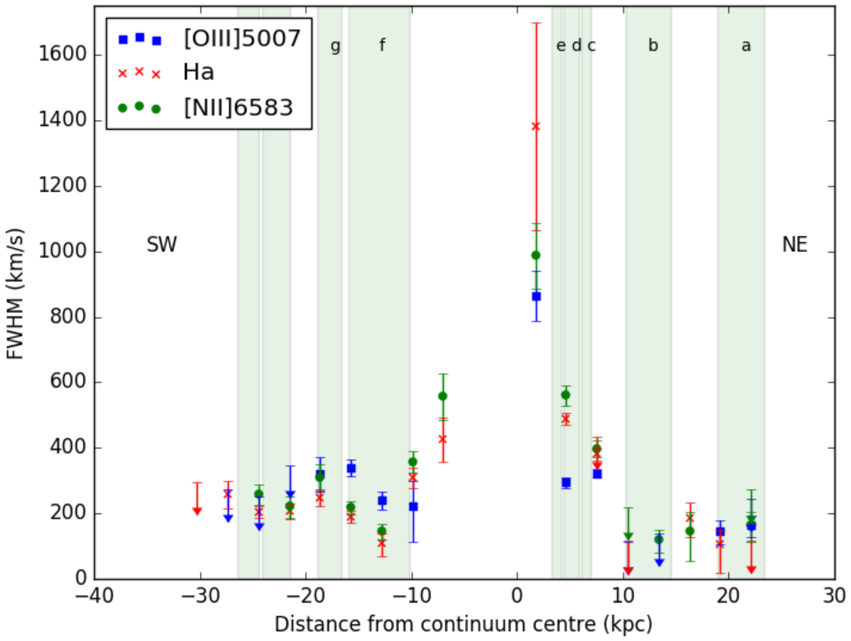

Figure 3.4: The velocity widths (FWHM) of the Hα, [NII]λ6583 and [OIII]λ5007 emission lines, corrected for instrumental width. Disregarding the aperture at ~-8 kpc due to large error bars, the gas was found to be quiescent (FWHM $\lesssim$ 350 km s^{-1}) outside the range $0 < r < 5$ kpc, corresponding to a radial distance of ~6 kpc from the nucleus. No complex kinematics were seen. The main apertures used to investigate the ionisation mechanisms (§3.4.4) are indicated by the shaded areas.

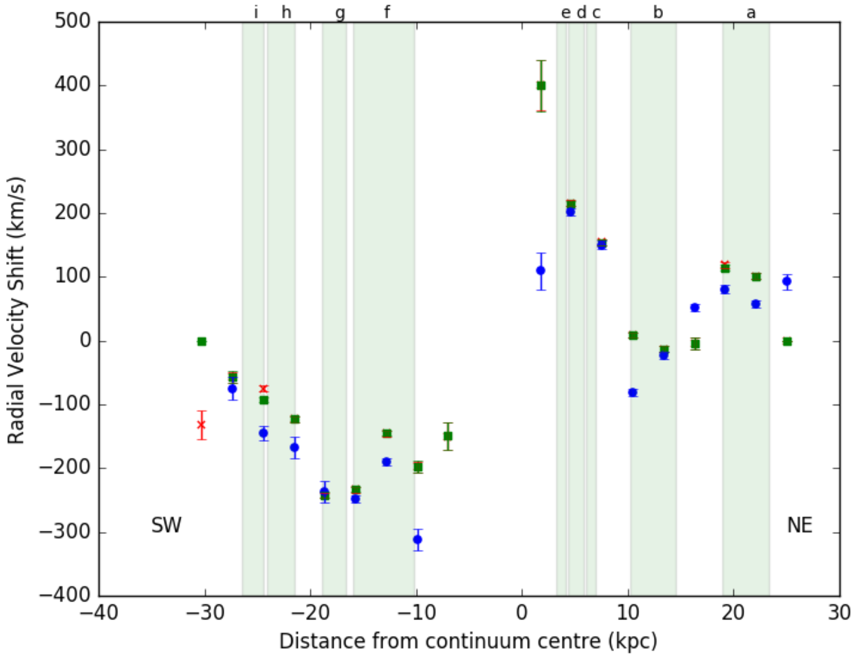

Figure 3.5: The velocity shifts relative to the continuum centre. Note there is an intrinsic uncertainty on these relative shifts due to the slit being offset from the system centre.

3.4.3 Density, reddening and gas mass

Another aim for this case study was to estimate the density, level of reddening and mass of gas contained in the extended regions of Mrk 273. These properties are generally difficult to measure accurately for high-velocity emission-line gas, due to blending of the required diagnostic emission lines, which causes significant degeneracies in the fits. However, because the emission-line gas in the extended halo is relatively quiescent, a reasonable estimate of the density and reddening was possible for these regions.

For this analysis, a total of 9 apertures across the slit (denoted *a* to *i*) were analysed, sampling the extended emission to the NE and SW of the nuclear region, along with the near-nuclear region. Figure 3.2d shows the location of these apertures relative to the Hα image. For clarity, apertures *a* and *b* are referred to as "NE", *c* to *e* as "near-nuclear" and *f* to *i* as "SW". The apertures are also indicated on the plots in Figures 3.4 and 3.5 for comparison with the kinematics. For each aperture, a 1D spectrum was extracted. The summed spectra for these regions are shown in Figure 3.6. DIPSO was used to fit a Gaussian to the relevant emission lines in order to measure their fluxes. Note that it was not necessary to first subtract the stellar continuum (which could contaminate the emission line fluxes) due to the fact that the slit was located off-nucleus, away from the central star-forming regions, and hence any stellar continuum emission was negligible.

To estimate the electron density of the ionised gas, the emission line profiles of the [SII]$\lambda\lambda$6716,6731 doublet in the extended apertures (*a, b, f, g, h* and *i*) were modelled using single Gaussians. The ratio of these two line fluxes is sensitive to electron densities between $10^2 < n_e < 10^{3.5}$ cm^{-3} – the higher the ratio, the lower the density. For the extended gas sampled by the PA 23° slit (excluding the near-nuclear apertures), an error-weighted mean ratio of [SII](6716/6731) = 1.4±0.1 was obtained. This ratio is consistent with the low density limit, indicating that the electron density of the extended ionised halo of Mrk 273 is low. Using the nebular modelling package FIVEL (De Robertis et al., 1987), a 3σ upper limit was placed on the density across the halo of $n_e \leq 430$ cm^{-3}, for an electron temperature of 10^4 K.

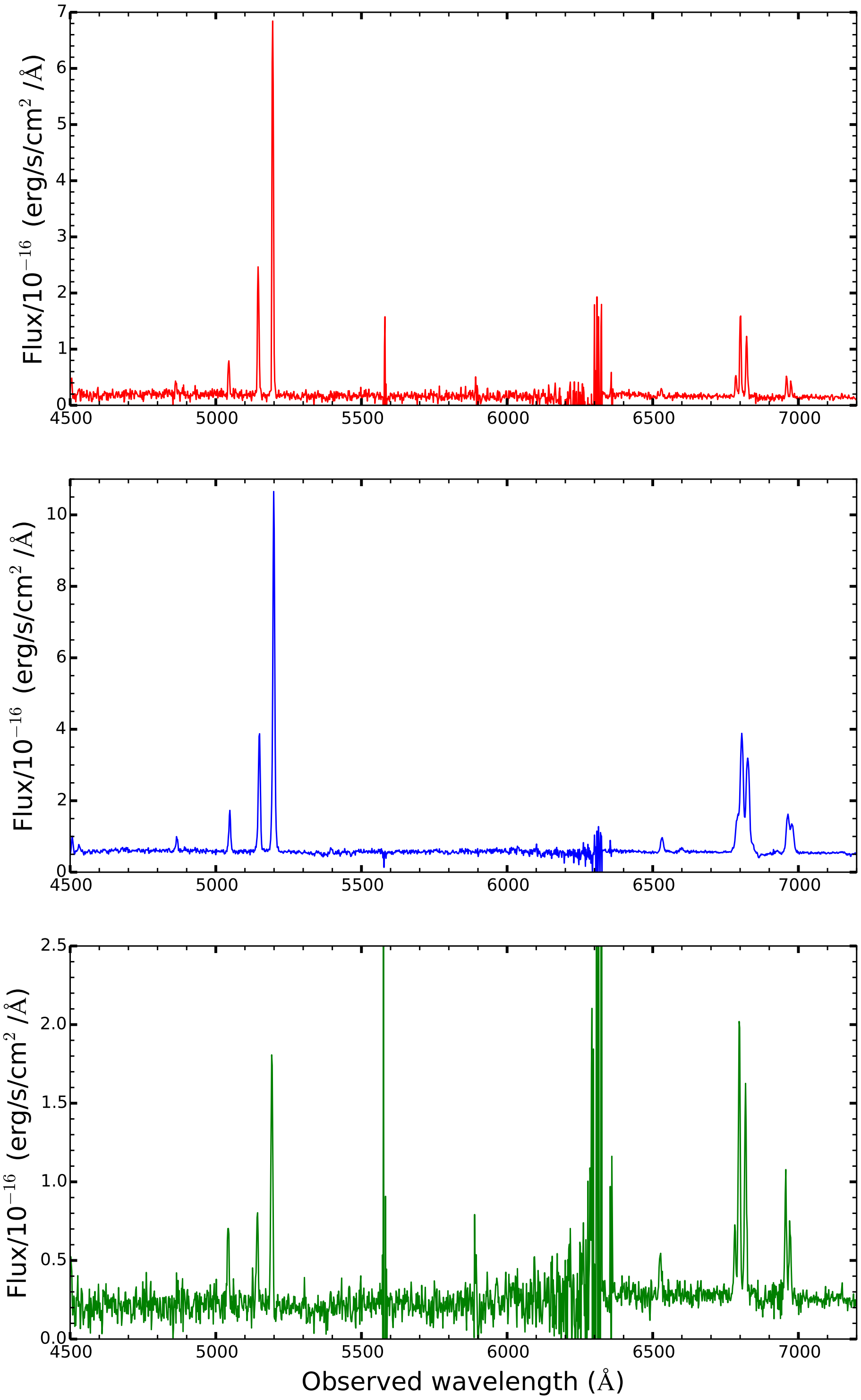

Figure 3.6: Top to bottom: the summed 1D spectra for the NE (red; a+b), near-nuclear (blue; c+d+e) and SW (green; f+g+h+i) regions. The feature at ∼5600Å is the residual of the strong night sky line at 5577Å. The feature at ∼6400Å is the region of poor quality data either side of the dichroic cut, which is particularly prominent in the SW spectrum due to the lower surface brightness in this region.

The detection of [OIII]λ4363 in aperture *b* also allowed an estimate of the electron temperature of the extended gas. This emission line ratio is sensitive to the temperature of the emitting clouds due to the significant difference in wavelength – the higher the ratio, the lower the temperature. A ratio of [OIII](4959+5007)/4363 = 85±20 was obtained. Using FIVEL, this corresponds to an electron temperature of $T = (1.37^{+1.8}_{-0.9}) \times 10^4 K$, for an electron density of 400 cm^{-3}.

An additional factor to consider when measuring emission-line fluxes is the reddening of the wavelength of the light caused by dust absorption. This would lead to an under-estimation of the true fluxes, particularly at the blue end of the spectrum. The effect of reddening is expected to be significant in the nuclear regions of Mrk 273 due to the large amounts of gas and dust present – signified by the high infrared luminosity (log(L_{IR}) = 12.10 L$_\odot$). The degree of reddening can be estimated using the ratio of Hα/Hβ, which is constrained by atomic physics to be 3.1 for case B recombination processes in AGN (Gaskell & Ferland, 1984). The uncertainties on the Balmer ratios for each individual aperture were too large to enable meaningful estimates of the reddening at each aperture location. Instead, an error weighted mean of Hα/Hβ = 3.1±0.1 was calculated for the extended apertures (*a, b, f, g, h* and *i*), indicating no significant dust extinction is present – on average – across the extended halo.

Following this, the mass of the gas contained in the extended ionised halo of Mrk 273 was estimated with the following equation:

$$M = \frac{L(H\alpha)m_p}{\alpha^{H\alpha}_{eff} h\nu_{H\alpha} n_e}, \tag{3.2}$$

where $L(H\alpha)$ is the emission-line luminosity of Hα; m_p is the proton mass; $\alpha^{H\alpha}_{eff}$ is the effective recombination coefficient of Hα, $\alpha^{H\alpha}_{eff} = 0.77\times10^{-13}$ cm^{-3}s^{-1} (Pequignot et al., 1991, $T_e = 10^4$ K); $h\nu_{H\alpha}$ is the energy of an

Hα photon and n_e is the electron density.

Due to the derived electron density being an upper limit, only a lower limit on the total warm gas mass of the extended halo ($r > 6$ kpc) could be estimated. This lower limiting gas mass was estimated using fluxes derived from the narrow-band GTC Hα emission-line image. By integrating the flux within a circular aperture of $r = 45$ kpc, and subtracting the flux within a circular aperture of $r = 6$ kpc, a flux of $L(H\alpha) = 1.02 \times 10^{41}$ erg s^{-1} was estimated for the extended halo of Mrk 273. Combining this with the upper limit on the density of $n_e \leq 430$ cm^{-3} led to a lower limit on the mass of warm gas contained in the quiescent, extended halo of $M_{\rm halo} \geq 8 \times 10^5\,{\rm M}_\odot$. For comparison, Cicone et al. (2014) estimated a total molecular gas mass for Mrk 273, based on CO(1-0) observations, of $M_{\rm mol} \sim 5\ \times 10^9\,{\rm M}_\odot$.

3.4.4 Ionisation mechanism

Despite the relatively small velocity shifts and widths measured in the extended regions of Mrk 273 compared to those usually attributed to outflows, it is also informative to investigate the ionisation mechanisms of the gas. This can be done by plotting diagnostic emission-line ratios on the Baldwin, Phillips & Terlovich (BPT) diagnostic diagrams (Baldwin et al., 1981; Veilleux & Osterbrock, 1987). The location of the points on these diagrams indicates the dominant source of ionisation for the sampled gas, based on the measured ratios. Comparing these ratios to shock and photo-ionisation models can potentially provide information about the acceleration mechanism of the gas.

The BPT diagrams are shown in Figures 3.7 and 3.8. Over-plotted on the left-most diagram ("[NII] plot") are two dividing lines. The solid line indicates the "extreme starburst line" derived by Kewley et al. (2001), which indicates the theoretical upper limit for star-forming galaxies. Any line ratios which fall above and/or to the right of this line must have been produced by AGN activity. The dashed line represents the semi-empirical upper boundary for star-forming (HII)regions derived by Kauffmann et al. (2003). Any ionised gas producing emission line ratios which fall below or to the left of this line are likely to be dominated by stellar processes rather than AGN activity. The area between these lines defines the composite region, in which it is difficult to distinguish highly star-forming galaxies from low luminosity AGN. Over-plotted on the second ("[SII] plot") and third ("[OI] plot") diagrams are the main AGN/HII dividing lines, as well as the AGN/LINER empirical dividing line derived by Kewley et al. (2006).

The BPT line ratios observed in both the NE nebula and near-nuclear regions (red squares and blue circles) are consistent with AGN photoionisation across all three diagnostic plots, according to their location on the three plots. Initially, this suggests that the gas in these regions of Mrk 273 is being illuminated by one (or more) of the central AGN.

The situation in the SW nebula (green triangles) is less clear. In the [NII] plot, the SW apertures fall close to or within the composite region of the plot, and on the [SII] and [OI] plots they apertures fall close to the AGN/LINER dividing line. One consistent feature across all three plots, however, is that there appears to be an obvious divide between the SW region and the NE and near-nuclear regions.

To further investigate the ionisation mechanism in the sampled regions of Mrk 273, the model grids of Groves et al. (2004) were overplotted onto the BPT diagrams in Figure 3.7. These grids indicate the theoretical emission-line intensities of a cloud irradiated by an AGN radiation field. The grids shown are for dusty, radiation-pressure dominated photoionisation models and are generated for values of the power-law index of the AGN radiation field, α, in the standard range -2.0 $< \alpha <$ -1.2 and ionisation parameter at the front of the cloud, U, (where $U = S/n_e c$; S = flux of ionising photons, n_e = cloud density, and c = speed of light) in the range $-4 < \log U < -1$. The other main dependency of the models is the metallicity, Z, of the gas cloud. Figures 3.7a and 3.7b are overplotted with grids for $Z = Z_{\odot}$ and $Z = 2Z_{\odot}$, respectively.

The emission line ratios for the NE and near-nuclear apertures show relatively poor consistency with the $Z = Z_{\odot}$ model, particularly on the [NII] plot. The consistency is better with the $Z = 2Z_{\odot}$ model. The ratios of the SW region are well explained by the photo-ionisation models, with the twice solar-abundance model providing the best fit. Previous studies on ULIRG metallicities, using optical line ratios, have shown that ULIRGs typically lie below the mass-metallicity relation followed by normal star-forming galaxies (e.g. Rupke et al., 2008; Kilerci Eser et al., 2014), and Pereira-Santaella et al. (2017) used far-infrared line ratios to estimate the metallicity of 19 local ULIRGs to be in the range $0.7 < Z_{\rm gas}/Z_{\odot} < 1.5$. Rodríguez Zaurín et al. (2013), however, found that the optical line ratios for a sample of local ULIRGs were best explained by $Z = 2Z_{\odot}$ photo-ionisation models, indicating that the metallicity is likely super-solar. The results presented here for Mrk 273 appear to support the higher metallicity case for both the near-nuclear and extended regions of Mrk 273.

A significant weakness of the standard BPT dividing lines, however, is that they do not take into account the possibility of a contribution to the emission-line fluxes from shock ionisation. Shocks, generated by both outflows and cloud-cloud interactions, have been shown to have the potential to produce similar emission-line ratios to LINER photo-ionised regions by enhancing the emission-line ratios of the low-ionisation species: [SII]$\lambda\lambda$6716,6731; [OI]λ6300 (e.g. Monreal-Ibero et al., 2006, 2010). When a higher density/pressure region of gas expands into a region of lower density/pressure, shock waves are produced. Across the shock wave, the pressure, density and temperature of the gas increases dramatically. In a galactic context, shock waves are produced when a radio jet, or high-velocity component of gas (i.e. outflows, tidal gas) expands into the surrounding ambient interstellar medium. These interactions can cause the gas temperature to rise to $T > 10^6$ K, ionising electrons from the constituent atoms. Once this hot gas cools and reaches $\sim 10^4$ K, it emits emission lines associated with warm ionised gas. Given the prevalence of fast outflows, and likelihood of cloud-cloud interactions, in ULIRGs, it is important to consider the potential contribution of shocks to the observed emission-line ratios.

Because this mechanism is not covered by the traditional dividing lines, shock model grids have been over-plotted onto all three diagrams in Figure 3.8. These pure shock grids were generated from the MAPPINGS III library of fast radiative shocks (Allen et al., 2008). The main tunable parameters of these models are the density of the pre-shock gas (i.e. before moving through the shock front), shock velocity, and magnetic field strength. While the density is a difficult property to measure accurately in high-velocity emission-line gas, an upper limit on the extended gas within the slit was determined using the [SII] doublet (see §3.4.3). Due to compression effects, related to the temperature and pressure differentials across the shock, as well as the magnetic field strength (which can limit compression), the density of post-shock gas can be a factor of 10 – 100 times larger than the density of the pre-cursor gas (Dopita & Sutherland, 1995). If it is assumed that the gas within the slit represents the post-shock gas (given that it must have been through the shock in order to be emitting the observed lines), this defines a range of pre-shock densities for the models comparable with the estimated post-shock density. The grids plotted on Figure 3.8, therefore, are the results for pure shock models for solar abundance gas with pre-shock densities of 1 cm^{-3} (Fig. 3.8a) and 10 cm^{-3} (Fig. 3.8b). The grids range in magnetic field strength ($1 < B < 100\,\mu$G) and shock velocity ($200 < v < 1000$ km s^{-1}).

Examining the plots, the NE and near-nuclear regions have a poor cross-plot consistency with the shock models, particularly for the lower density model. These results agree with the study of RZ14, who found that shock models generally failed to reproduce their observed line ratios across all areas of the nuclear region, as well as the extended filaments to the NE covered by their spectroscopic slits. The nebula to the SW of the nuclear region, however, was not covered by the spectroscopic observations presented in RZ14, therefore the dominant ionisation mechanism for this region of Mrk 273 is largely unknown. The SW nebula was covered by the WHT/ISIS spectra in apertures *f* through *i*. Examining Figures 3.7 and 3.8, the emission-line ratios in the SW apertures are relatively well explained by the higher density shock model with $200 < v_s < 400$ km s^{-1} across all three diagnostic diagrams, within the uncertainties. These shock velocities are comparable with the velocity widths and shifts measured in these apertures ($200 <$ FWHM < 400 km s^{-1}; $-250 < \Delta v < 0$ km s^{-1}, see Figure 3.4)

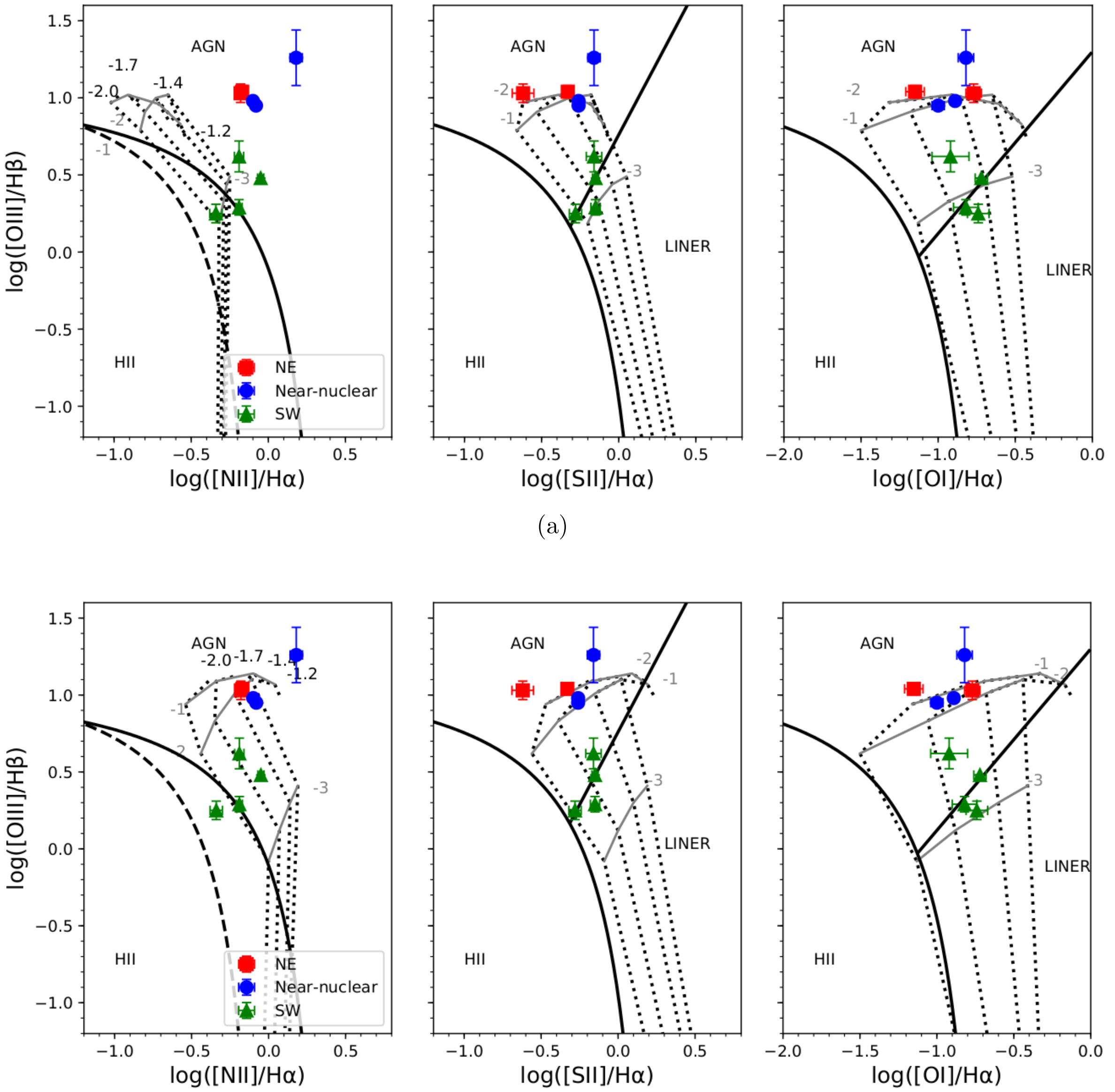

(a)

(b)

Figure 3.7: BPT diagrams overplotted with the Groves et al. (2004) dusty, radiation-pressure photo-ionisation model for (a) a solar abundance cloud, $Z = Z_{\text{sun}}$ and (b) a super-solar abundance cloud, $Z = 2Z_{\text{sun}}$. The dotted gridlines correspond to different values for the power law spectral index, α, of the ionising continuum ($-2.0 < \alpha < -1.2$). The solid, grey gridlines correspond to different ionisation parameters, ($-4 < \log U < 1$). The ionisation parameter increases from bottom to top.

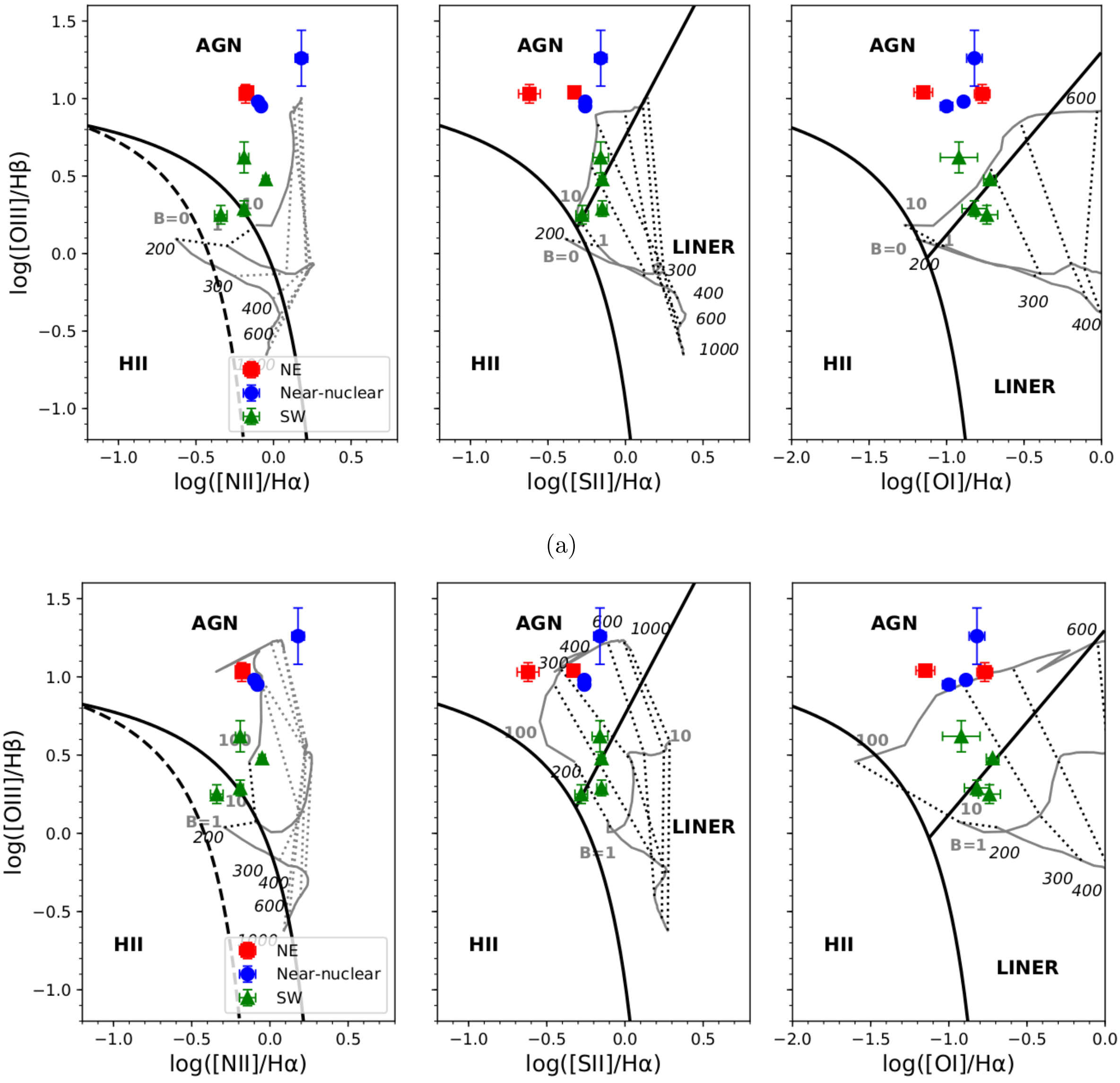

(a)

(b)

Figure 3.8: BPT diagrams overplotted with the Allen et al. (2008) pure shock model grids for (a): pre-shock density, $n_e = 1$ cm^{-3}; (b): pre-shock density, $n_e = 10$ cm^{-3}. The solid grey gridlines correspond to 4 possible values of magnetic field ($B = 0$, 1, 10 or 100 μG) and the dotted, black grid-lines correspond to 9 shock velocities ($v_s = 200, 300...1000$ kms^{-1}). v_s increases from bottom to top.

3.5 Chapter discussion and conclusions

In this chapter, results of a case study on the ULIRG Mrk 273 were presented. Newly obtained GTC/OSIRIS and WHT/ISIS observations were used to investigate the kinematics, physical conditions and ionisation mechanisms of the extended halo of warm ionised gas surrounding the nuclear regions of the merging system. Mrk 273 is a local ($z = 0.0373$) ULIRG which shows both extended emission-line structure ($r \sim 45$ kpc) and extreme nuclear kinematics, which made it an excellent target for investigating the connection between near-nuclear AGN-induced outflows and the wider host galaxy.

AGN feedback is expected to be important for the evolution of galaxies, yet observational evidence on the impact of these outflows on galaxy-wide scales (10s of kpc) is currently lacking. This raises the questions: to what extent do the AGN-driven outflows truly influence the outer regions of their host galaxies, and what is the ultimate fate of the outflowing gas?

Outflowing gas is generally identified by large velocity shifts and/or broad line widths (FWHM) in emission line profiles. Previous studies (RV13 and RZ14) have identified the presence of ionised outflows out to a radius of several kpc from the nuclear regions of Mrk 273. This is supported by the results of this chapter, which found relatively broad (FWHM > 500 km s^{-1}) emission line profiles in [OIII]λ5007, Hα and [NII]λ6853 out to a maximum radius of $\sim$ 6 kpc. In addition, the presence of a significantly larger-scale halo of more quiescent, narrow-line gas (FWHM $\lesssim$ 400 km s^{-1}) was highlighted, detected out to a radius of $\sim$45 kpc. Such an extended halo had not previously been imaged. One explanation for the origin of this galaxy-scale gas is that it represents a reservoir of gas which has accumulated from past/current outflows. Due to the narrow line widths, however, this scenario is only consistent with the observations if the turbulence in the outflow (responsible for broadening the emission line profiles) is somehow dissipated outside the near-nuclear regions. Assuming such a dissipation mechanism exists, the time-scale required for the “outflow reservoir” to accumulate can be estimated. For this, the mass outflow rate of RV13 was used, who found $\dot{M} = 10\ \mathrm{M_{\odot}yr^{-1}}$ for the inner warm outflow ($r < 4$ kpc). Taking their typical outflow velocity of 750 km $\mathrm{s^{-1}}$, it would take $\sim$60 Myr for this gas to reach the outer extent of the halo ($\sim$45 kpc), moving at constant velocity. Therefore the AGN would need to have a lifetime at least this long if the entire halo was to have formed in this way. Over this period, the accumulated mass would be $\sim 6 \times 10^{8}\ \mathrm{M_{\odot}}$ for a constant mass outflow rate of $10\ \mathrm{M_{\odot}yr^{-1}}$. This is a factor of $\sim$750 greater than the lower limit on the warm gas mass calculated in section 3.4.3; therefore, in order for the two masses to be consistent, the warm gas would have to either be extremely rarefied ($n_e \lesssim 1\mathrm{cm^{-3}}$), or in a colder phase not detected in emission lines.

On the other hand, the relatively quiescent kinematics of the extended gas are consistent with gravitational motions, given that the estimated total stellar mass of Mrk 273 ($7 \times 10^{10}\,\mathrm{M_{\odot}}$; Rodríguez Zaurín et al. 2010) is similar to that of the Milky Way, which has a typical rotational velocity of 200 – 250 km $\mathrm{s^{-1}}$. Therefore the most likely explanation for the formation of the large-scale ionised halo is due to the merger event(s) which originally triggered the nuclear AGN activity – violent collisions of gas-rich galaxies clearly have the potential to distribute gas over such scales. This hypothesis is supported by the looped structure observed in the stellar continuum image to the NE of the nuclear region, which is clearly a tidal feature. The Hα emission to the NE has a similar structure and extends in the same direction with a similar radius as the continuum loop. The fact that the distribution of these two components is similar suggests that the ionised component of the halo in this region is associated with the tidal debris, rather than an outflow. If warm outflows are expected to prevent star-formation (negative feedback) by suppressing the collapse of cold molecular material, then significant stellar continuum emission would not be expected to coincide with the ionised emission from an AGN-driven outflow to the extent observed in Mrk 273. However, it should be noted that, under the right conditions, positive feedback (e.g. shock-induced star formation) associated with outflows may occur (e.g. Maiolino et al., 2017).

To further investigate the origin of the extended gas, the ionisation mechanisms across different regions of the halo were analysed using BPT diagrams, Groves et al. (2004) photo-ionisation models and Allen et al. (2008) radiative shock models. The emission-line ratios measured to the NE and in the near-nuclear regions were consistent with AGN photo-ionisation, based on their location in the three BPT diagrams and comparison with photo-ionisation models (Fig. 3.7). The shock models (Fig. 3.8), on the other hand, were less successful at reproducing the measured ratios in these regions (see also RZ14). These results lead to the conclusion that the extended gas to the NE of the nuclear region consists of tidal debris which is being illuminated by one (or more) of the nuclear AGN, most likely from the northern nucleus.

The situation to the SW of the nuclear region is less clear, with the BPT diagrams indicating AGN photo-ionisation to be a less dominant mechanism, compared with the NE and near-nuclear region. The line ratios fall mainly in the composite/LINER region and can be explained by the Allen et al. (2008) radiative shock models across all three plots, demonstrating that radiative shocks have the potential to produce LINER-like emission-line ratios. These shocks can occur from tidal gas, disrupted by the major merger, interacting with the ambient interstellar medium, or through cloud-cloud collisions as the gas settles down following the merger (i.e. dissipation). The predicted shock velocities are in agreement with the measured velocity widths, shown in Figure 3.4, for the SW apertures. However, the Groves et al. (2004) photo-ionisation model is also able to reproduce the measured line ratios with a good level of consistency across all three BPT diagrams. Similarly to the NE region, the emission-line gas appears to be spatially related to the continuum emission along the tidal tail. Together, these results lend support to the conclusion that the warm gas to the west of the tidal tail consists of tidal debris which is being ionised either by low-velocity shocks (caused by cloud-cloud collisions as the gas settles after the merger), illumination from the AGN, or a combination of both mechanisms. Note that, if the SW gas were in fact a reservoir from past outflows, then the outflows in this location would most likely to be driven by intense star formation or supernovae in the tidal tail, stimulated by the merger. However this would not explain the asymmetry of the gas, as there would be no reason for the outflows to be preferentially directed to the west of the tidal tail.

The most conclusive result of this study is that the warm gas in the extended regions of Mrk 273 – covered by the spectroscopic slit – does not represent the outer part of the AGN-driven outflow detected in the near-nuclear regions. However, that is not to say that this will always be the case. Although the analysis presented in this chapter provides no obvious evidence for significant outflows outside of a radius of ∼6 kpc, based on the currently-observed kinematics of the emission lines, it is possible that the central AGN of Mrk 273 have not been active long enough to drive the outflows to larger scales. Over their lifetimes, supermassive black holes are expected to grow through accretion (and multiple phases of AGN activity) for a total of $10^7 - 10^9$ years (Marconi et al., 2004). Therefore, given more time, it may be possible that broad emission-line gas will become observable at > 6 kpc radii in the future.

Overall, this chapter has demonstrated the need for further detailed observations of emission-line gas in local ULIRGs in order to probe the true extent of AGN-induced nuclear outflows and discover their true impact on the evolution of their host galaxies. To this end, in Chapter 4 a detailed investigation into the warm gas in the nuclear regions of the e-QUADROS ULIRGs is presented. Chapter 6 then extends the analysis described in this case study to the large-scale emission-line gas seen in the rest of the e-QUADROS sample.

Chapter 4

Properties of the nuclear outflows

4.1 Declaration

The work presented in this chapter was published in Spence et al. (2018), "*Quantifying the AGN-driven outflows in ULIRGs (QUADROS) III: measurements of the radii and kinetic powers of 8 near-nuclear outflows*", Monthly Notices of the Royal Astronomical Society (MNRAS), in May 2018. The initial project proposal for this work was written by Clive Tadhunter and Javier Rodríguez Zaurín. In addition, I refer to work which was published in Tadhunter et al. (2017), "*A tidal disruption event in the nearby ultra-luminous infrared galaxy F01004–2237*", to which I contributed to the data reduction, emission-line analysis and scientific interpretation of the results. This publication was given a press release by the University of Sheffield. Unless stated otherwise, the text, figures, analysis and interpretations presented in this chapter are my own work.

4.2 Chapter introduction

In Chapter 3, I discussed the issues and lack of convincing observational evidence surrounding the true extents of ionised outflows in ULIRGs, and analysed the galaxy-scale ionised halo of Mrk 273 – concluding that these observations still do not provide evidence that this extended gas is part of the nuclear outflow. However, while a large proportion of local ULIRGs with optical AGN show evidence for warm outflows in their nuclear regions (e.g. Westmoquette et al., 2012; Rodríguez Zaurín et al., 2013), there remain significant uncertainties in the key properties of the outflows, such as the mass outflow rates, kinetic powers and coupling efficiencies. Observational measurements of these parameters are important for comparison with those required by hydrodynamical simulations in order to reproduce the observed correlations between the central SMBH and host galaxy properties (e.g. Di Matteo et al., 2005; Springel et al., 2005; Johansson et al., 2009, see also Chapter 1).

In the case of warm ionised outflows – which are observed via emission lines at optical wavelengths – these uncertainties arise predominantly from a lack of accurate diagnostics of the electron densities, radii and dust extinction of the outflowing gas (e.g. Rodríguez Zaurín et al., 2013; Rose et al., 2018; Harrison et al., 2018). Although much recent attention has been paid to galaxies at high redshifts, which show signs of AGN activity (e.g Nesvadba et al., 2008; Cano-Díaz et al., 2012; Harrison et al., 2012, 2014; Carniani et al., 2015, 2016; Perna et al., 2015), there is a limit to what can be learnt in detail about the co-evolution of black holes and galaxy bulges in such objects because of both their faintness, and the fact that many important diagnostic lines are shifted out of the optical/near-IR wavelength range.

To address these issues, the Quantifying ULIRG AGN-Driven Outflows (QUADROS) project has been undertaken to measure the outflow properties of local ULIRGs. This project concentrates on the nuclear regions of ionised outflows, and takes advantage of a technique pioneered by Holt et al. (2011) which uses the trans-auroral [SII]$\lambda\lambda$(4073/6725) and [OII]$\lambda\lambda$(3727/7330) emission-line ratios to simultaneously determine the densities and reddening. The QUADROS project has so far produced three publications. Paper I (Rose et al., 2018) presents deep VLT/XShooter spectroscopic observations of the nuclear regions of 7/15 QUADROS ULIRGs, plus two additional ULIRGs. Paper II (Tadhunter et al., 2018) presents *HST* Advanced Camera for Surveys (ACS) imaging of 8/15 objects with optical AGN.

This chapter presents WHT/ISIS spectroscopy of the nuclear regions of a further seven QUADROS ULIRGs, plus one additional ULIRG, and is published in paper III (Spence et al., 2018). Chapter 2 describes the sample selection, observations and data reduction. This chapter describes and presents the results of analysis of the nuclear spectra. In Section 4.3 I outline the aperture extraction and emission-line fitting processes. In Section 4.5 I provide measurements of the radii and kinematics of the outflows. I then use the trans-auroral line ratios to estimate the electron densities and reddening, and hence derive the mass outflow rates and kinetic powers of the warm AGN-driven outflows, which I compare with those derived in other studies of warm outflows in AGN in Section 4.6. Finally, I investigate the possible links between the warm outflows and the properties of the AGN for the whole e-QUADROS sample (Section 4.7).

In summary, this chapter aims to determine accurate radii, electron densities, reddenings, mass outflow rates, kinetic powers and ultimately coupling efficiencies of the AGN-driven outflows in the nuclei of local ULIRGs, in order to compare them to those required by hydrodynamical simulations. A cosmology with $H_0 = 73\,\mathrm{kms^{-1}Mpc^{-1}}, \Omega_0 = 0.27, \Omega_\Lambda = 0.73$ is assumed throughout.

4.3 Spectroscopic data

4.3.1 Aperture extraction

The ULIRGs in the QUADROS sample are known to exhibit strong AGN-induced outflows (Rodríguez Zaurín et al., 2013) that are concentrated in their nuclear regions. Therefore apertures of ∼5 kpc diameter were extracted, centred on the nuclei, following the approach of Rodríguez Zaurín et al. (2009). Guided by the pixel scale of the CCD and the cosmology-derived arcsecond-to-kpc conversion factors, 5±0.6 kpc apertures were extracted for all objects. This resulted in 8 nuclear spectra for analysis, which are shown in Figures 4.1 through 4.4. In the following sections, the described results were obtained by fitting the profiles of the emission lines detected in these nuclear spectra. It should be noted that the quality of the data in the vicinity (within ∼100 Å) of the dichroic cut at ∼6000Å (observed frame) is relatively poor (see Chapter 2). Fortunately this did not affect any of the key diagnostic emission lines.

4.3.2 Modelling the emission line profiles

This section describes the approach that was taken when modelling the nuclear emission lines, in order to extract the velocity shifts, FWHM and fluxes of the constituent components.

Prior to modelling the emission-line profiles, the spectra were corrected for Galactic extinction using the extinction function of Cardelli et al. (1989) and E(B-V) values of Schlafly & Finkbeiner (2011). They were then shifted to the galaxy rest frame using redshifts measured from the higher order Balmer stellar absorption features (3798, 3771 and 3750Å, where possible). One exception to this is F01004-2237, for which strong non-stellar continuum emission dominates over the stellar absorption features.

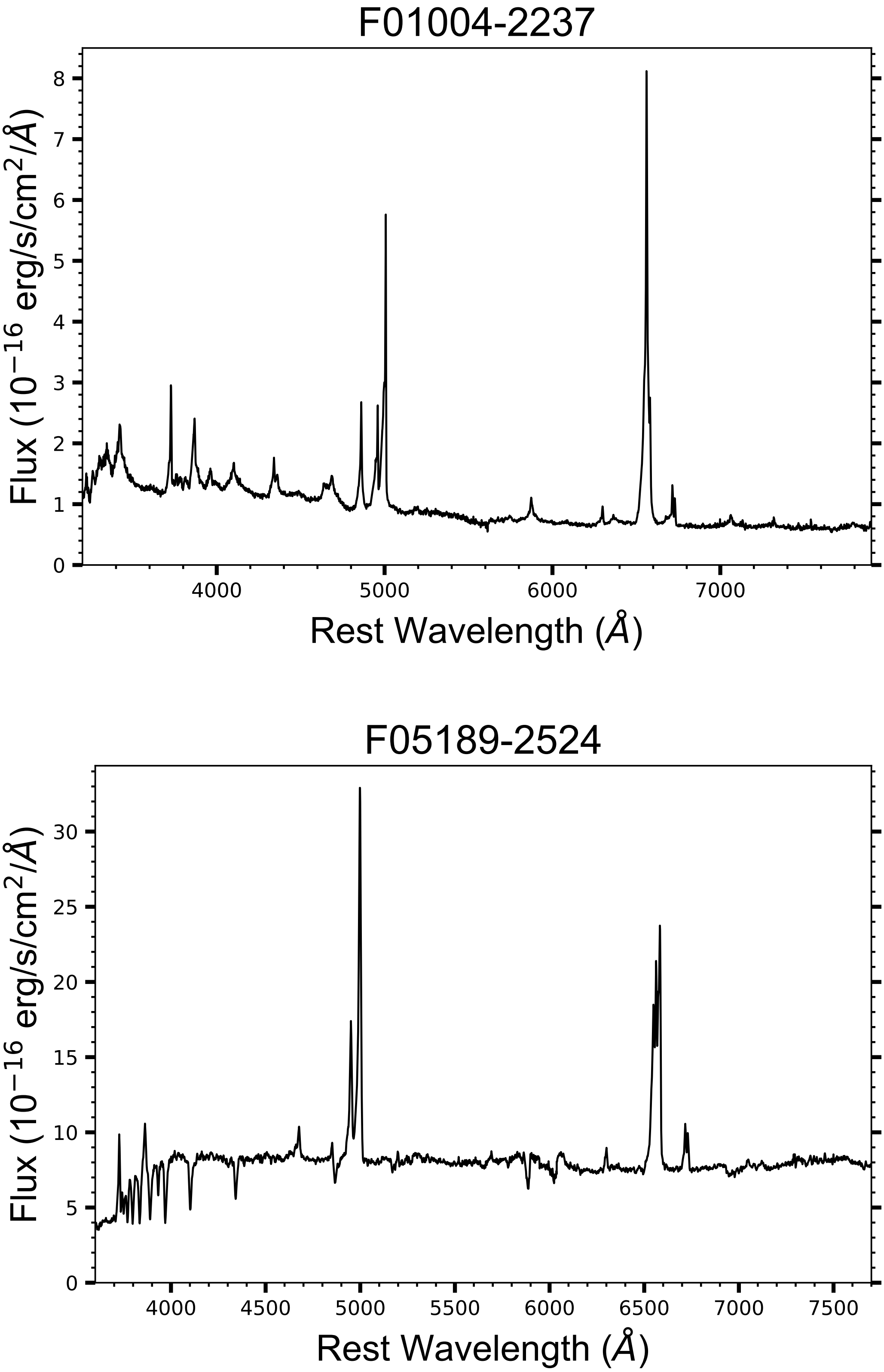

Figure 4.1: The rest-frame nuclear spectra for the ULIRGs considered in this study.

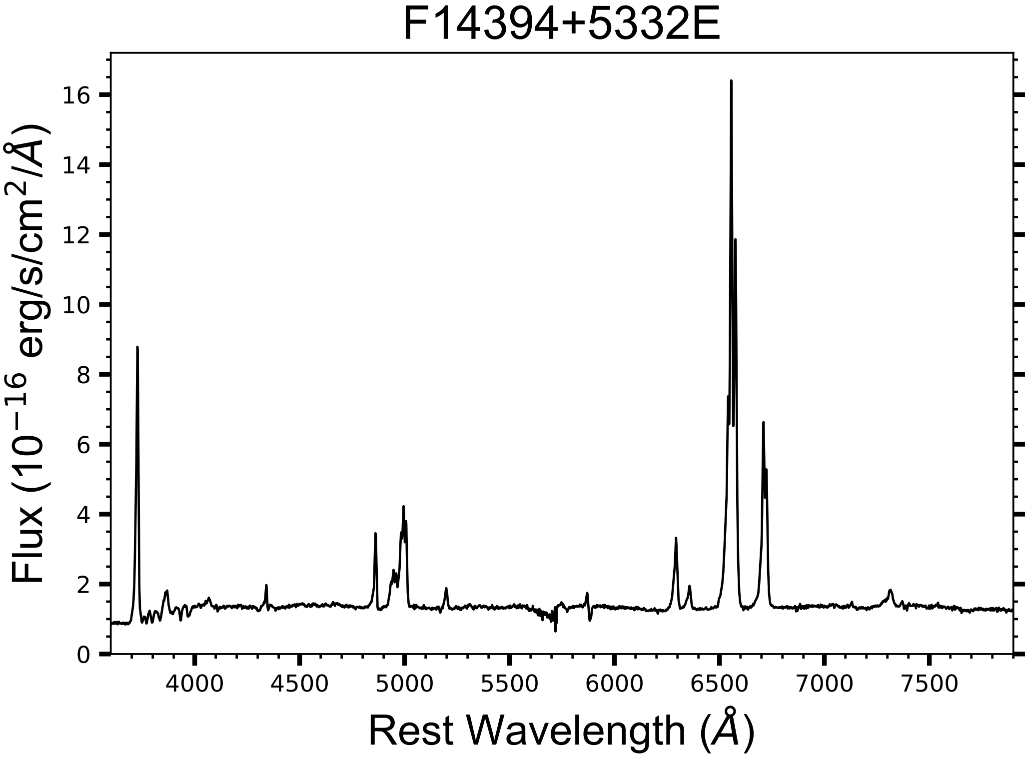

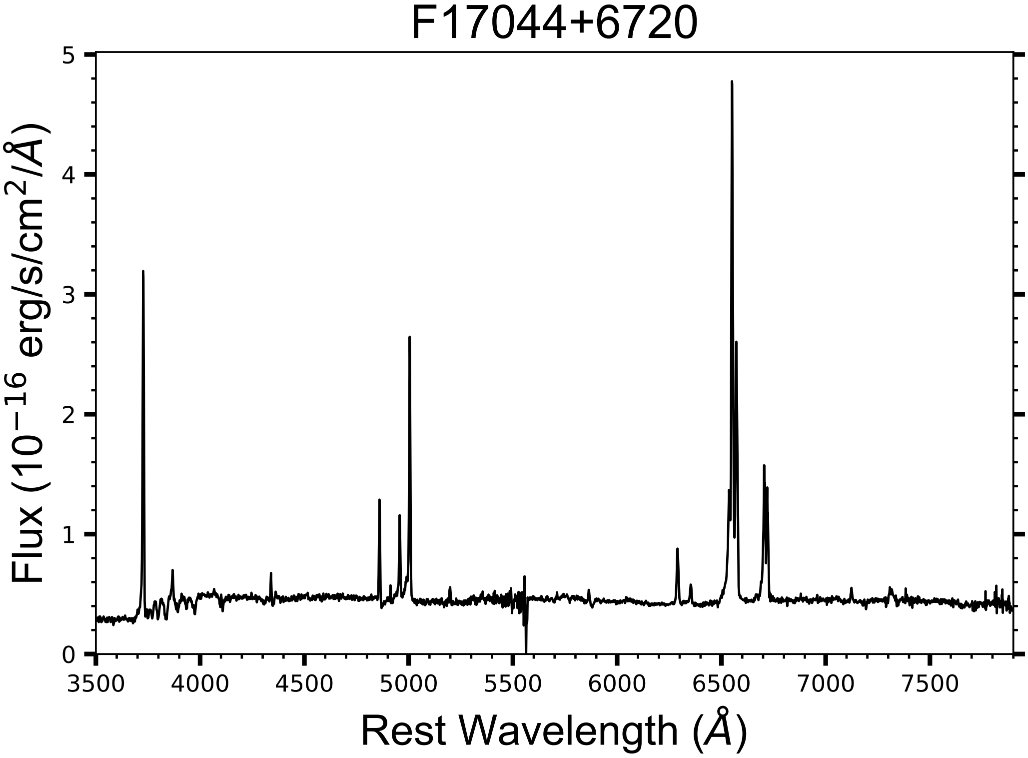

Figure 4.2: Continued from Figure 4.1.

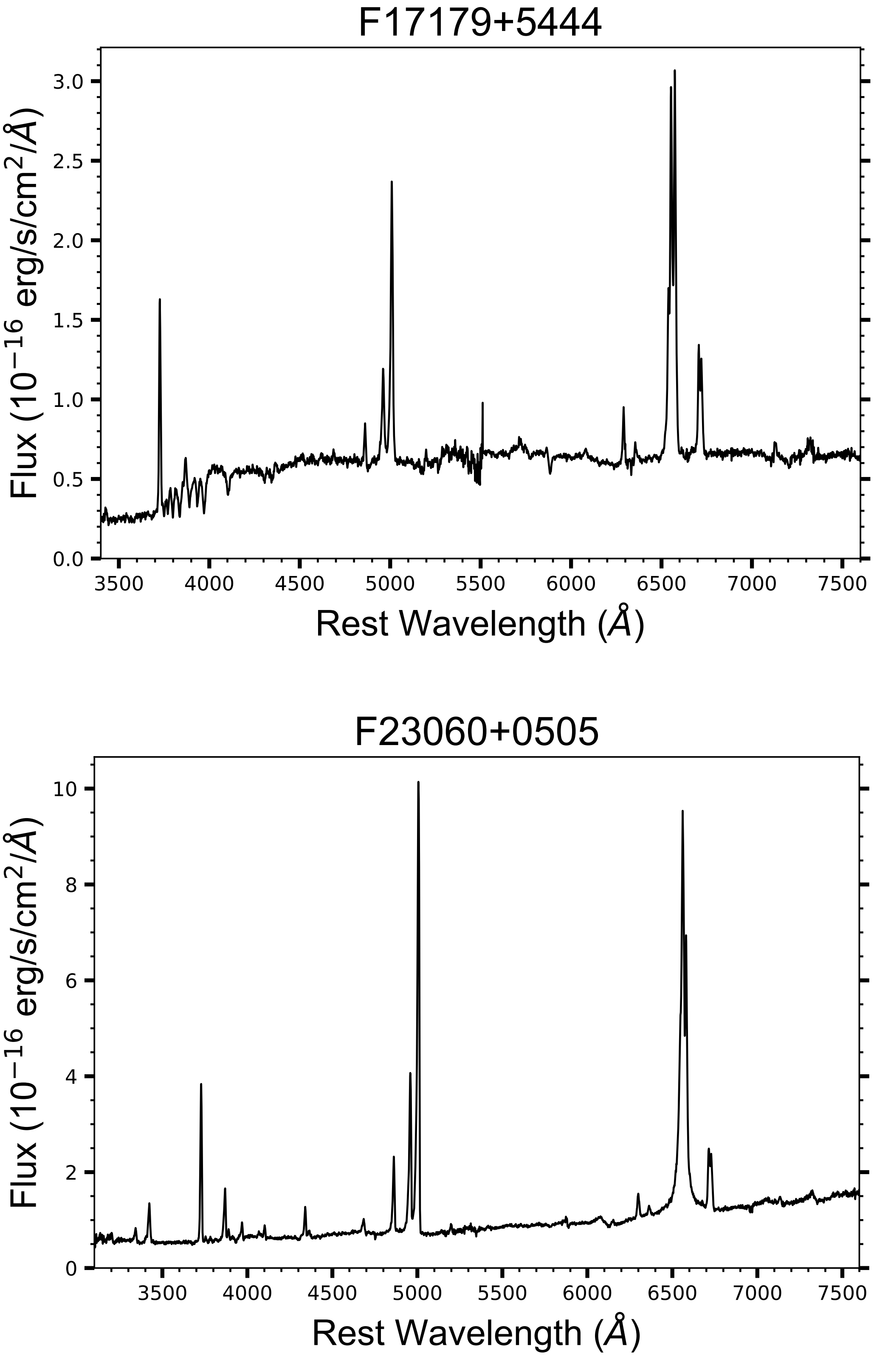

Figure 4.3: Continued from Figure 4.2.

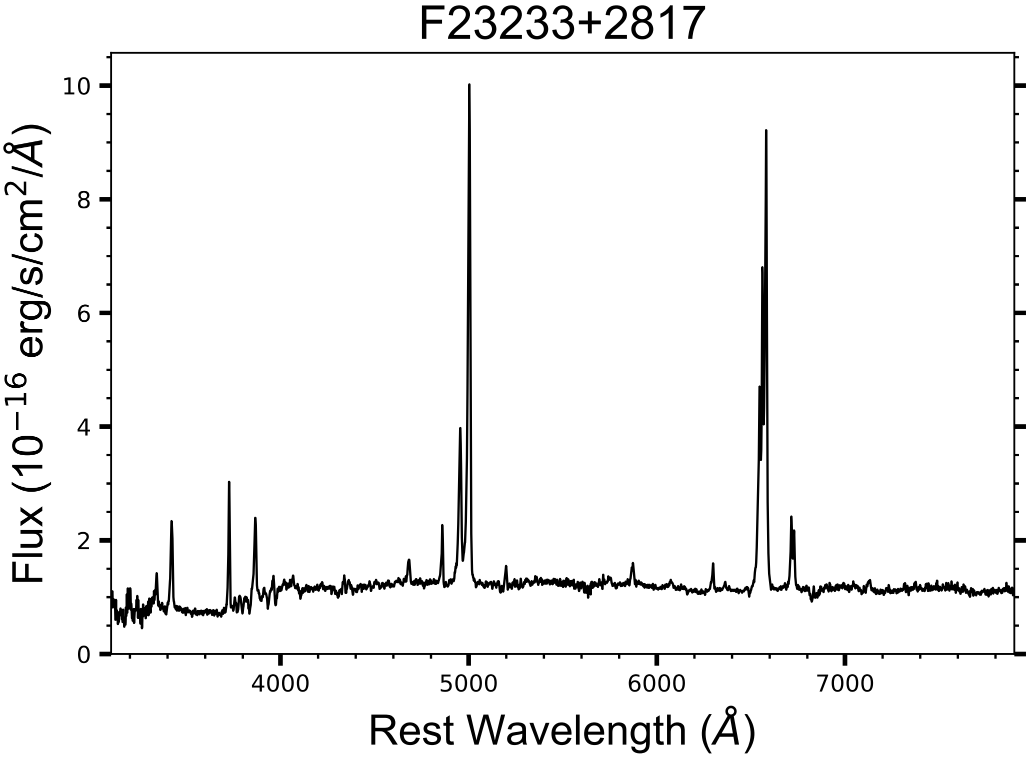

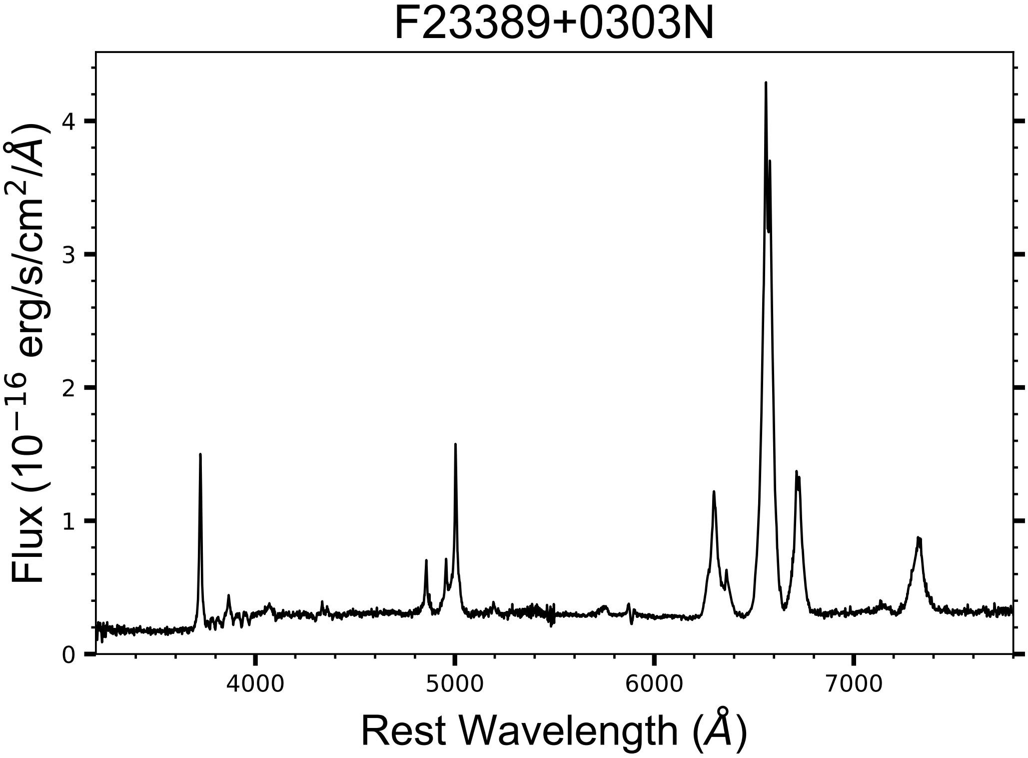

Figure 4.4: Continued from Figure 4.3.

In this case, the rest-frame was estimated using four narrow off-nuclear emission lines, detected in kinematically quiescent regions extending ∼10" (∼20 kpc) either side of the nucleus. The Galactic extinction magnitudes and redshifts are given in Chapter 2, Tables 2.1 and 2.2.

The spectra of six objects were then fitted with the spectral synthesis code STARLIGHT (Cid Fernandes et al., 2005), using the Bruzual & Charlot (2003) solar metallicity base templates in order to facilitate accurate stellar continuum subtraction. Note that emission lines and cosmetic defects (e.g. the noisy region around the dichroic cut) were masked out in the fitting process. The resultant continuum fit to the full optical spectrum of F17044+6720 is shown in Figure 4.5, for reference. A zoom on the part of the spectrum containing the Balmer absorption lines of F05189-2524 is also provided in Figure 4.6, illustrating the excellent consistency of the STARLIGHT fit with the estimated redshift and the stellar absorption line profiles. Note that no attempt was made to fit F01004-2237. The continuum of this object is highly complex due to the fact that its spectrum is dominated by the emission of a recent tidal disruption event (TDE; Tadhunter et al., 2017, see §4.4). Similarly, STARLIGHT struggled to fit the continuum in the red arm of F23060+0505 due to an underlying reddened type I AGN component. Therefore, the stellar continua were not removed in these cases.

The [OIII]λ5007 emission line is the strongest and cleanest high ionisation line associated with the out-flowing warm gas. For this reason, the emission line fitting procedure concentrated on this line. The approach was to fit the line profile, using DIPSO, with the minimum number of Gaussians required to give an acceptable fit. This was assessed both visually and by subtracting the fit from the line profile to assess the residuals. The [OIII] fits were constrained by setting the relative shifts between each component of [OIII]$\lambda\lambda$4959,5007 to be 47.92Å, and fixing the rela-

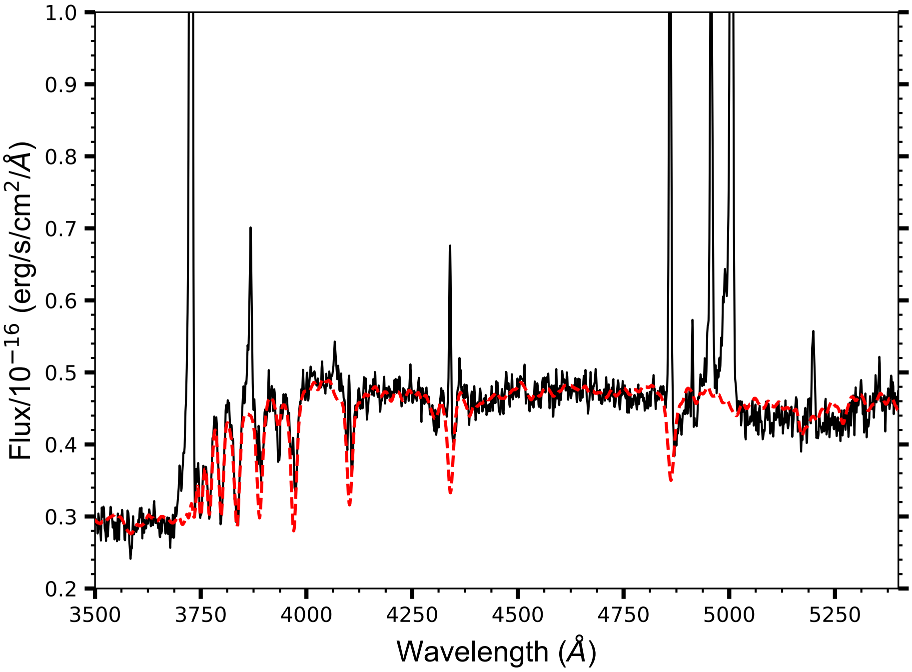

Figure 4.5: The nuclear spectrum of F17044+6720 (black, solid line), overplotted with the STARLIGHT fit to the stellar continuum (red, dashed line)

tive intensities according to those from atomic physics (1:2.99). At least two Gaussian components were required in all cases. The [OIII] fits are shown in Figure 4.8, along with their residuals. The velocity shifts and widths for each required component are shown in Table 4.1. The velocity widths have been corrected in quadrature for the spectral resolution. For consistency, the [OIII] components are labelled based on the line widths (FWHM) following Rodríguez Zaurín et al. (2013):

- Narrow (N): FWHM < 500 km s^{-1};
- Intermediate (I): $500 <$ FWHM < 1000 km s^{-1};
- Broad (B): $1000 <$ FWHM < 2000 km s^{-1};
- Very Broad (VB): FWHM > 2000 km s^{-1}.

The [OIII] kinematic models (i.e. relative widths and shifts with re-

Table 4.1: The [OIII] kinematics for the WHT/ISIS ULIRGs. Columns (3) and (4) give the FWHM and velocity shift of each kinematic component. Columns (5) and (6) indicate whether the [OIII] model worked for the Hα+[NII], [OII] and [SII] blends. Columns (7) and (8) give the observed [OIII]λ5007 and Hβ fluxes associated with each kinematic component.

Object IRAS (1)	Comp. (2)	FWHM kms^{-1} (3)	Δv kms^{-1} (4)	Hα + [NII] (Y/N) (5)	[OII]/[SII] (Y/N) (6)	[OIII]λ5007 flux (erg s^{-1} cm^{-2}) (7)	Hβ flux (erg s^{-1} cm^{-2}) (8)
F01004 – 2237	N	unresolved	63±25	N	N	(2.03±0.04)E-15	(4.71±0.02)E-16
	I	699 ± 32	-361 ± 35			(1.99±0.14)E-15	(6.10±0.09)E-16
	B	1586 ± 38	-1045 ± 60			(3.68±0.16)E-15	(1.55±0.10)E-15
F05189 – 2524	I	582 ±37	-505 ± 26	N	N	(2.48±0.04)E-14	(1.93±0.14)E-15
	B	1706 ± 24	-1072 ± 44			(1.91±0.05)E-14	(1.09±0.12)E-15
	I$_{H\beta}$	555 ± 76	-28 ± 55			-	(1.53±0.21)E-15
F14394 + 5332E	N1	408 ±11	17 ± 62	N	N	(1.61±0.03)E-15	-
	N2	288 ± 21	-701 ± 63			(9.01±0.44)E-16	-
	N3	242 ± 34	-1457 ± 66			(4.00±0.32)E-16	-
	B	1871 ± 19	-1000 ± 67			(7.02±0.10)E-15	-
	N$_{H\beta}$	420 ± 11	17 ± 63			-	(2.08±0.06)E-15
	I$_{H\beta}$	986 ± 42	-358 ± 93			-	(1.05±0.07)E-15
	B$_{H\beta}$	1927 ± 20	-1030 ± 69			-	(5.42±0.52)E-16
F17044 + 6720	N	218 ± 12	-1 ± 61	Y	Y	(1.46±0.01)E-15	(6.61±0.10)E-16
	B	1757 ± 60	-503 ± 85			(7.64±0.33)E-16	(1.58±0.24)E-16
F17179 + 5444	I	590 ± 12	58 ± 62	Y	Y[a]	(1.81±0.04)E-15	(4.12±0.18)E-16
	B	1530 ± 33	-242 ± 78			(1.43±0.05)E-15	(2.20±0.27)E-16
F23060 + 0505[b]	N1	147 ± 37	273±34	Y[c]	N	(4.09±0.45)E-15	(6.94±0.87)E-16
	N2	267 ± 35	-25 ± 38			(4.76±0.49)E-15	(9.60±1.02)E-16
	I	934 ± 32	-283 ± 44			(6.94±0.28)E-15	(8.07±0.59)E-16
	B	1399 ± 114	-1220 ± 146			(1.62±0.30)E-15	-
	BLR$_{H\alpha}$	2359 ± 69	393 ± 102			-	-
F23233 + 2817	N	239 ± 21	-92 ± 27	Y	Y[d]	(2.56±0.14)E-15	(6.50±0.58)E-16
	I	760 ± 13	-316 ± 31			(8.35±0.22)E-15	(6.61±0.92)E-16
	B	1892 ± 40	-785 ± 54			(4.71±0.19)E-15	(4.52±0.98)E-16
F23389 + 0303N	N	402 ± 16	-191 ± 27	Y	Y	(7.80±0.20)E-16	(3.60±0.13)E-16
	VB	2346 ± 38	-134 ± 36			(2.26±0.25)E-15	(7.81±0.25)E-16

[a] The [OIII] model worked for the trans-auroral [OII] blend, but not for the [SII]. In this case, a two component model with different widths and shifts was required for the strong blend. The broad component to the weak trans-auroral [SII] blend was not detected.

[b] Hβ was fit with just narrow and intermediate components. No broad component was required.

[c] The [NII] lines were well fit with the [OIII] model. Hα was fit with the narrow and intermediate components of the [OIII] model, however the broad component was dominated by a broad-line region component (FWHM > 2000 km s^{-1}).

[d] The [SII] blends did not require a broad component.

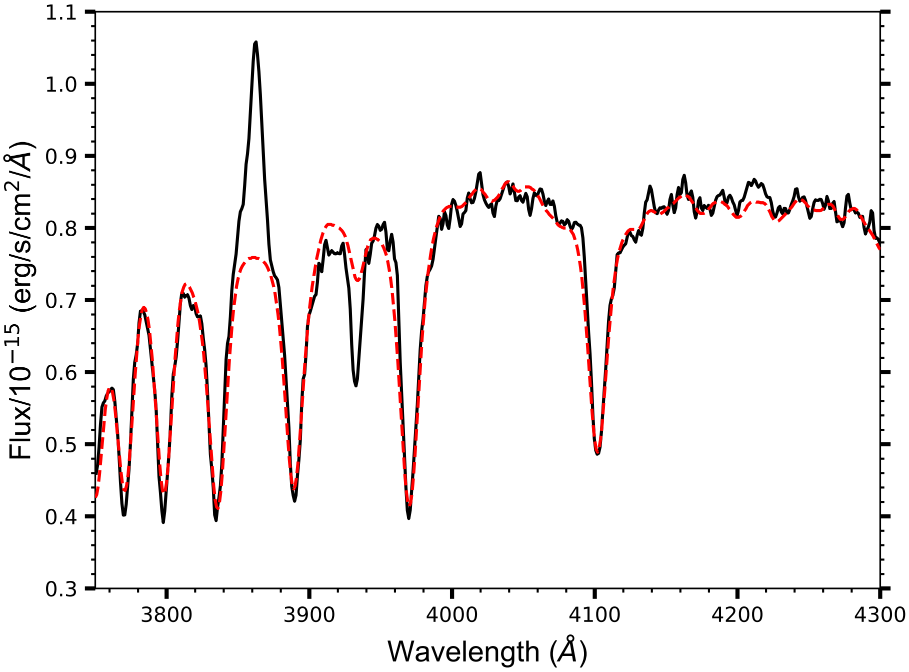

Figure 4.6: A zoom in on the higher order Balmer absorption features (Hδ–H11) in the nuclear spectrum of F05189–2524. Note that the [NeIII] emission line at 3869Å and the CaII K ISM absorption feature at 3933Å are not fitted by the model. The black solid line is the data, the red dashed line shows the STARLIGHT fit.

spect to the rest frame for each component) were then applied to the other diagnostic emission lines ([OII]λ3727, [SII]$\lambda\lambda$4068,4076, Hβ, [OI]λ6300, Hα, [NII]$\lambda\lambda$6548,6583, [SII]$\lambda\lambda$6716,6731 and [OII]$\lambda\lambda$7319,7330). This was important to ensure that comparisons between the kinematic components of the different emission lines could be made. Note also that the use of the various diagnostic emission line ratios in the following analyses requires the assumption that the flux of all of these emission lines originates from the same volume of gas. This assumption is discussed in Chapter 5.

The kinematic components were constrained according to the relevant atomic physics, as follows (see also Rose et al., 2018).

- The [SII](4068/4076) ratios were forced to fall within the range 3.01 $<$ [SII](4068/4076) $<$ 3.28.

- The [OII](7319/7330) ratios were fixed at 1.24.
- The [NII](6583/6548) ratios were fixed at 2.99.
- Where necessary, the ratios of the broad components of [SII](6716/6731) were fixed to the high-density limit value of 0.44 to ensure a physical fit.

The [OIII] models were successful for the majority of emission lines in 50% of the objects. An example of the application of the [OIII] model fits to all of the emission lines in F23389+0303N is shown in Figure 4.9.

For F01004–2237, F05189–2524, F14394+5332E and F23060+0505 the [OIII] model did not work for the other lines, and an alternative kinematic model was generated using [OII]λ3727, or [SII]$\lambda\lambda$6716,6731 in the case of F14394+5332E, which was then successfully applied to the remaining diagnostic lines.

F01004–2237, as mentioned above, appears to have recently undergone a tidal disruption event, strongly affecting its nuclear spectrum (see §4.4 for an aside about this serendipitous discovery). While the three-component [OIII] model worked for Hβ, the Hα + [NII] blend only required a two component fit to each line, with the [NII] narrow components very weak in this case. A two-component model (narrow + broad) was required to fit the [OII]λ3727 and [SII]λ6725 blends. Note that, although the red trans-auroral [OII]$\lambda\lambda$7319,7330 blend was detected in the WHT/ISIS spectrum, the blue trans-auroral [SII]$\lambda\lambda$4068,4076 blend was not detected due to severe contamination by TDE-related emission lines. It was, however, detected in the pre-TDE HST/STIS spectrum of F01004–2237 (shown in Figure 4.7, top). Therefore, given that there is good evidence that the slit losses for the HST/STIS and WHT/ISIS spectra were similar (Tadhunter et al., 2017), the density and reddening estimates presented in §4.5.2 for this source are based on comparing the total fluxes of the blue [SII] blend measured from the HST/STIS spectrum (single Gaussian fit) with those of the blue [OII], red [OII] (single Gaussian fit) and red [SII] blends measured from the WHT/ISIS spectrum.

In the case of F05189–2524, the full [OIII]$\lambda\lambda$4959,5007 profile was blueshifted by more than 500 km s^{-1} relative to the stellar rest frame, similar to the cases of PKS1549–79 (Tadhunter et al., 2001) and F15130–1958 (Rose et al., 2018). This behaviour was also seen to a lesser extent in F23233+2817 and F23389+0303N. However, for F05189–2524, an additional rest-frame intermediate component was required for the Balmer, [OI], [OII] and [SII] emission lines in the ground-based WHT spectrum. Although the blueshifted intermediate and broad components were also detected in Hβ, the broad component was not detected in the [OI], [OII] and [SII] lines which were fitted with a two-component model consisting of a rest-frame intermediate and a blueshifted intermediate component.

In the STIS spectrum of F05189–2524 (shown in Figure 4.7, bottom), only a single Gaussian could be fitted to the trans-auroral [OII] and [SII] lines to estimate the total emission-line fluxes. However, the relative shift of this component was within 3σ of the blueshifted intermediate component detected in the red [SII] and blue [OII] emission lines in the ground-based spectrum. It is therefore reasonable to assume that, due to the narrower slit used for the STIS observations, the measured total fluxes are representative of the outflow. This meant that the STIS fluxes could be used to estimate the densities and reddening for the outflow, rather than the ISIS fluxes (see §4.5.2).

The [OIII] profile of F14394+5332E was complex, requiring three narrow components (one rest-frame, two blueshifted) and a broad component (see also Rodríguez Zaurín et al., 2013). However, the two blueshifted narrow [OIII] lines were not detected in any of the other emission lines in this object. These were instead fitted with a three-component model (one nar-

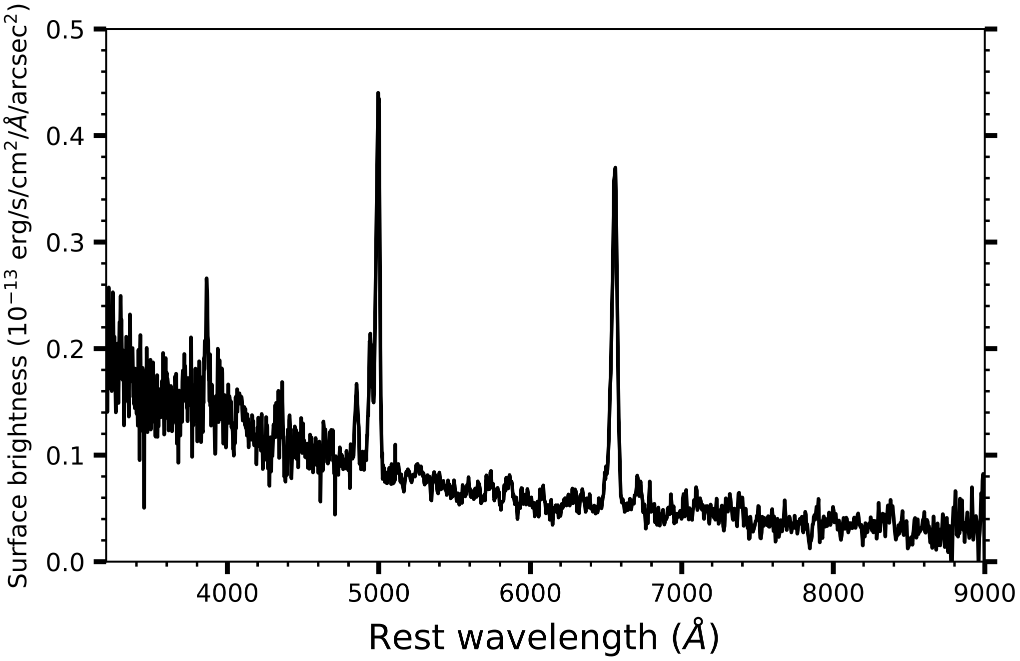

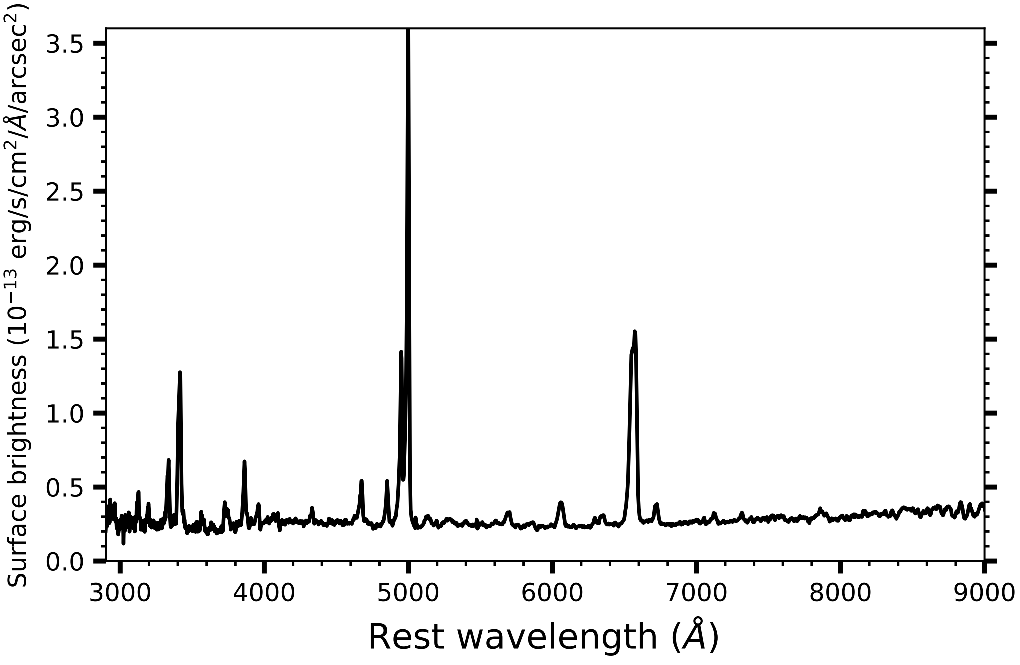

Figure 4.7: The HST/STIS nuclear spectra available for F01004–2237 (top) and F05189–2524 (bottom).

row, one intermediate and one broad component), with the exception of the [NII] doublet where no broad component was required. This was likely due to degeneracy with the broad component of Hα.

Finally, the [OIII] profile of F23060+0505 required four components: two narrow, an intermediate, and a broad. No broad component was detected in Hβ, nor for the [OI] and [OII] emission lines; and only the narrow components were detected in the [SII] blends, perhaps leading to an underestimation of the outflow density for this object using the trans-auroral line ratios (§4.5.2). However, a broad-line region (BLR) component (FWHM $= 2356 \pm 69\,\mathrm{km\ s^{-1}}$) was required in this case to fit the Hα+[NII] blend. As discussed by Rodríguez Zaurín et al. (2013), the presence of a moderately reddened type I AGN component in this source is confirmed by the relatively red shape of the long-wavelength end of its optical continuum spectrum (see Figure 4.4), and the detection of a broad Pα emission line at near-IR wavelengths (Veilleux et al., 1997).

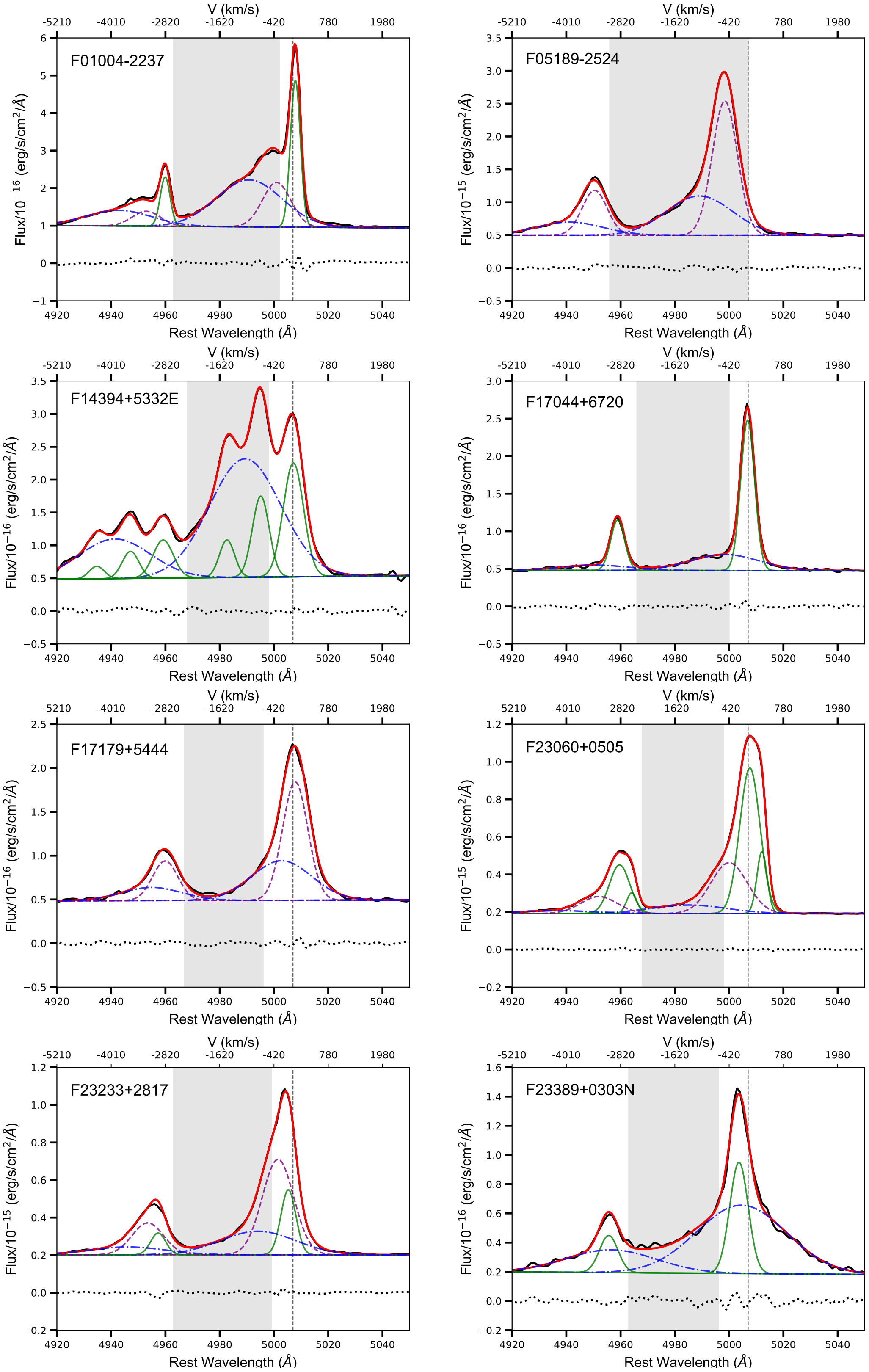

Figure 4.8: [OIII] profiles and fits for the WHT/ISIS ULIRGs considered in this study. The black solid line is the data, and the overall fit is shown by the red solid line. The individual components are coloured as follows: narrow (green, solid); intermediate (purple, dashed); broad (blue, dot-dashed). The residuals of the fit are shown below the profiles (black, dashed). The shaded regions show the velocity ranges extracted when determining the outflow radii.

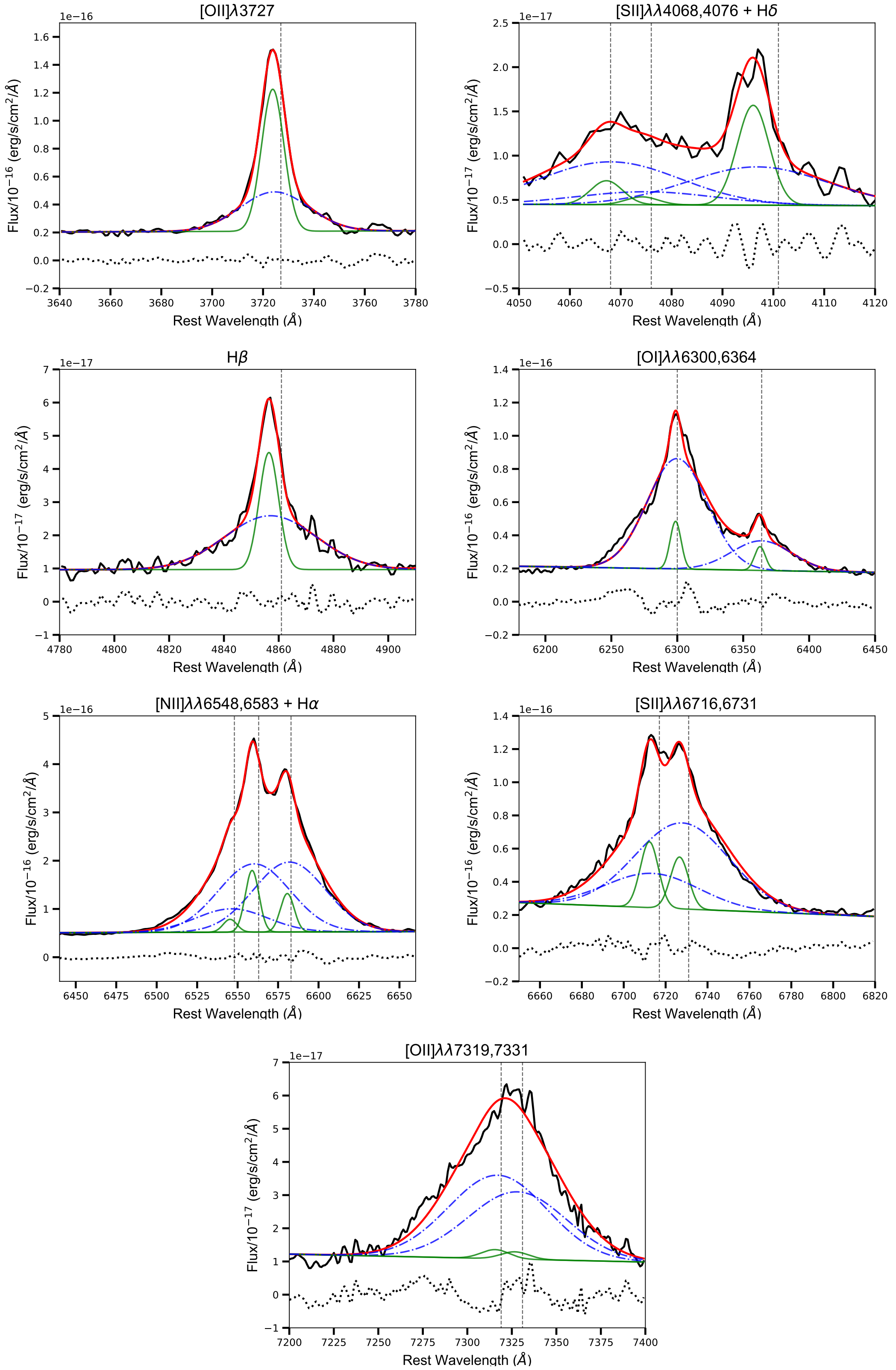

Figure 4.9: Emission line profiles and fits for all diagnostic lines for F23389+0303N. The black solid line is the data, and the overall fit is shown by the red solid line. The individual components are coloured as follows: narrow (green, solid); intermediate (purple, dashed); broad (blue, dot-dashed). The residuals of the fit are shown below the profiles (black, dashed).

4.4 Aside: a tidal disruption event in F01004–2237

While performing initial exploratory analysis of the reduced spectra, unusual features in the nuclear spectrum of F01004–2237 were noted. Unlike the other spectra, which were relatively flat (apart from the reddened type I component in F23060+0505) and showed clear high-order Balmer absorption features, there appeared to be a strong blue continuum component to the spectrum of F01004–2237, which washed out any Balmer absorption features. Not only this, but the helium emission lines, which are relatively narrow and weak in the other ULIRGs, were remarkably strong and broad. F01004–2237 is also one of the few ULIRGs in which Wolf-Rayet (WR) features have been detected at optical wavelengths in the past. Indeed, a prominent, broad emission-line blend of NIII and HeII at ∼4660Å was detected in the WHT/ISIS spectrum – an unmistakable WR signature (Armus et al., 1988). Wolf-Rayet stars are a rare type of luminous evolved star, whose spectra show strong, broad helium and nitrogen/carbon emission lines. The fact that these features were observable in the nuclear spectrum suggested that some part of the compact, central nucleus of the system was unobscured along the line of sight, allowing the star-forming regions at its core to be viewed. In addition, a relatively bright, compact core source was detected in HST images by Surace et al. (1998).

Upon comparison with a HST/STIS spectrum taken 15 years earlier, as part of a previous project, it became evident that the spectrum had changed significantly. The two spectra are shown in Figure 4.10. The most notable differences were the ∼4660Å feature – which had increased in flux by more than a factor of 5 since 2000 and developed extremely broad wings extending up to ∼5000 km s^{-1} redward of the narrow HeIIλ4686 component – and the appearance of new HeI emission-line features in the red spectrum. In addition, Hβ had increased by a factor of ~1.5. In comparison, the fluxes of the forbidden lines associated with the AGN (e.g. [OIII]) had not varied significantly. Furthermore, the ratios of the HeIIλ4686 and HeIλ5876 lines to Hβ were significantly larger than those found in typical quasars. While it is not unheard of for AGN spectra to vary (see Tadhunter et al. (2017) for examples), the variability shown by F01004–2237 was unprecedented in any known AGN. Taken together, these variations in the spectrum pointed towards some sort of transient event having occurred in the nucleus of F01004–2237.

However, because the two spectra were observed with different instruments, it was important to check that the respective fluxes were directly comparable before taking the analyses any further. The extraction aperture used for the HST/STIS spectrum was 0.2×0.2 arcsec. The extraction aperture used for the WHT/STIS spectrum, however, was 1.5×2.0 arcsec, corresponding to 75× the area of the STIS spectrum. Inevitably, this aperture included more emission from the extended regions around the nucleus than the STIS spectrum, which would manifest itself as stronger narrow-line emission in the WHT/ISIS spectrum compared with the HST/STIS spectrum. However, the fluxes of interest were those of the unusual broad features, which should not be significantly affected by this.

To check whether it was valid to directly compare the broad fluxes of the two spectra, the telluric standard star observed at the midpoint of the F01004-2237 observing blocks (CD-23448, an A3 type star) was used to estimate the slit losses for the WHT/ISIS observations. This was done by extracting an aperture of equivalent dimensions to the nuclear spectrum, and comparing the measured flux (corrected for Galactic extinction) at the central wavelength of the R-band (~6440Å) with the apparent R-band flux of the star. This was estimated using the J-band magnitude of

CD-23448, given by the Simbad Astronomical Database[1] as $m_J = 11.650$. This was converted to an R-band magnitude using the $V - R$ and $V - J$ colours of A3 stars ($V - R = 0.05$; $V - J = -0.02$ from Ducati et al. 2001) and converted from magnitude to flux using the Spitzer online converter[2]. The ISTAT routine in FIGARO was then used to measure the observed flux, f_{obs}, at the R-band central wavelength of the WHT/ISIS spectrum. This in turn was compared with the expected R-band flux, f_{exp}, for the telluric standard star. In this way, $f_{obs}/f_{exp} = 0.81$, giving a slit loss of 19%. This was comparable with the expected slit losses of 10 – 20% for the HST/STIS spectrum at a similar wavelength, therefore the fluxes of the 2015 and 2000 spectra could be compared.

Based on the changes observed between the HST/STIS and WHT/ISIS spectrum, Marvin Rose examined archival Catalina Sky Survey (CSS) optical data for this source, and the rest of the main QUADROS sample for comparison, over the period 2003 – 2015. The resulting V-band light curves for the 15 objects are shown in Figure 4.11. Whereas the light curves of the other 14 objects did not show significant variations over the $\sim$ 12 year period, the light curve of F01004–2237 (blue points) showed evidence for a significant increase in brightness around 2010, consistent with a transient event.

The cause of this event was then considered. Discussions with Justyn Maund and Paul Crowther – experts in supernovae and massive stars, respectively – ruled out supernovae as the cause. Although supernovae are expected to be common in ULIRGs because of their high star formation rates, the CSS light curve and post-flare spectrum were unlike any they had ever seen. In addition, the peak luminosity of the flare ($M_v <$ -20.1) would correspond to a super-luminous supernova, which are extremely

---

[1] http://simbad.u-strasbg.fr/simbad/

[2] http://ssc.spitzer.caltech.edu/warmmission/propkit/pet/magtojy/

rare.

Subsequently, the possibility of a tidal disruption event (TDE) was considered. Tidal disruption events are seen in post-starburst galaxies, in which strong, variable and broad HeI and HeII have been observed, however no TDE had ever been reported in a starburst galaxy such as F01004–2237 prior to this study. The V-band luminosity of the flare was consistent with post-starburst TDEs, and this, combined with the unusual features in the optical spectrum, led to the proposal that the tail end of an optical flare associated with a TDE had been serendipitously observed. Furthermore, the observations favour the scenario of a low-mass star being tidally disrupted and accreted by the central black hole.

Apart from providing the first observations of such an event in a ULIRG, this study provided key insight into the potential rate of TDEs in these objects. The rate of TDEs in the population of field galaxies is expected to be in the region of $\sim 10^{-5}$ – 10^{-4} yr^{-1} galaxy^{-1}. However, the detection of one TDE in a sample of 15 ULIRGs over a period of 10 years suggests the rate could be orders of magnitude higher than this – perhaps as high as 10^{-2} yr^{-1} galaxy^{-1}. This rate could be higher still considering the fact that the nuclear regions of the majority of the ULIRG sample are obscured by dust, rendering any optical TDEs unobservable.

For more information on this work, please refer to Tadhunter et al. (2017). It is also worth noting that, following this publication, observations of a mid-infrared "echo" associated with the optical flare, from archival WISE and NEOWISE data, were published by Dou et al. (2017), supporting these results.

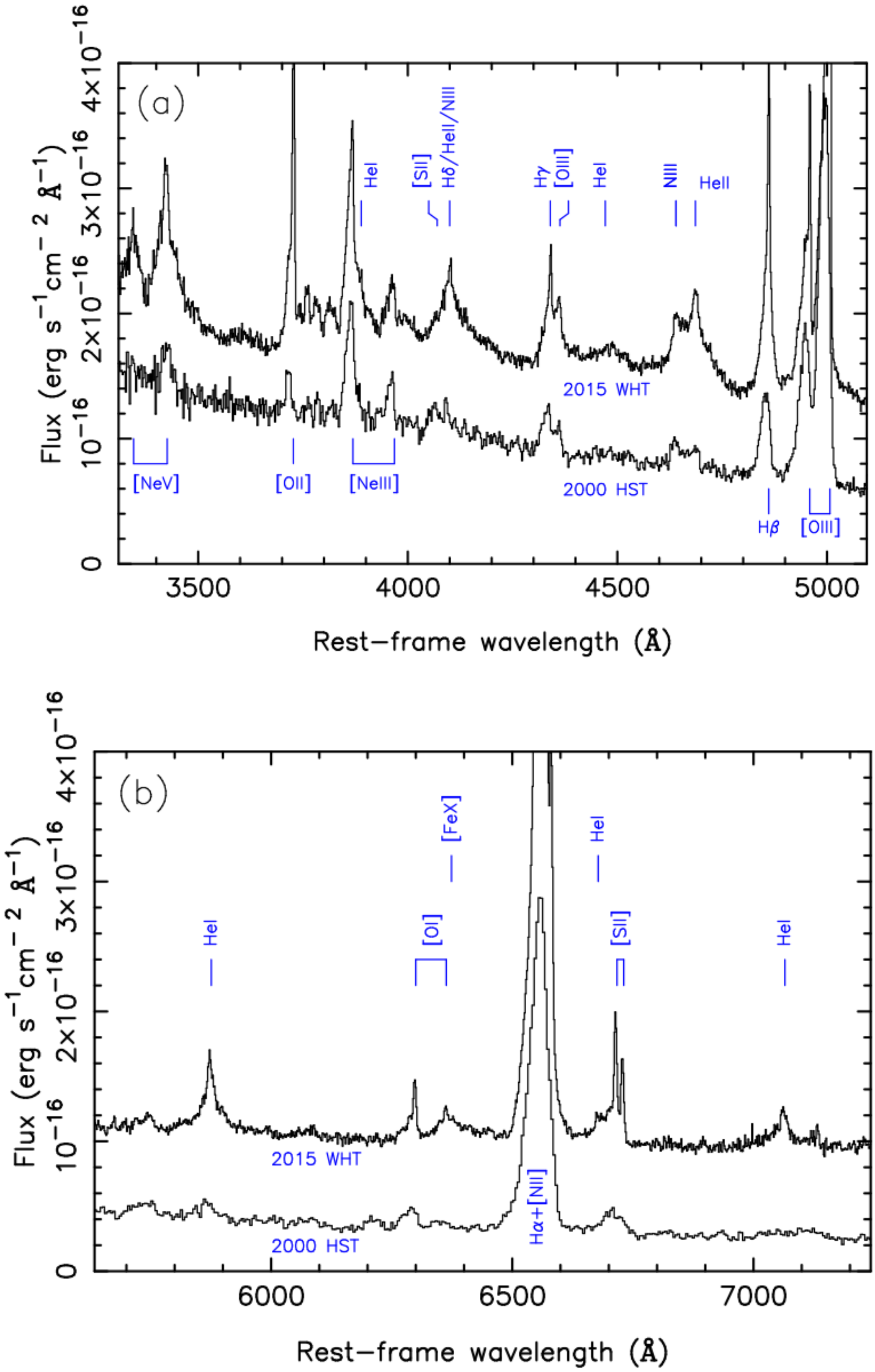

Figure 4.10: The spectra of F01004–2237 in (a) the blue; (b) the red. The top spectrum in each figure is the 2015 spectrum from WHT/ISIS, the bottom is the spectrum taken in 2000 from HST/STIS. The key emission lines have been identified. Reproduced from Tadhunter et al. (2017).

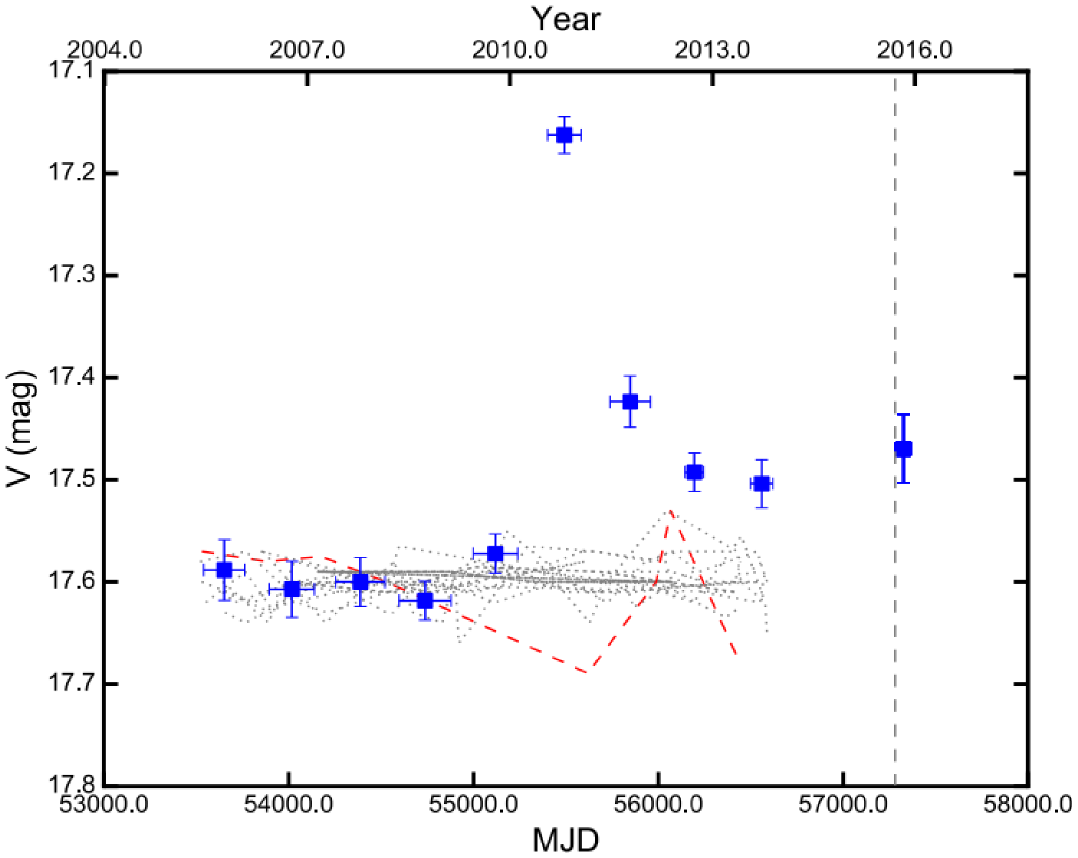

Figure 4.11: Catalina Sky Survey (CSS) light curves for F01004-2237 (solid blue points) and the other 14 sources in the main QUADROS sample (grey dotted lines and red dashed line). F01004-2237 shows a substantial flare in its V-band brightness (ΔM_v = $0.45 + / - 0.02$ mag) over the 10 years of the survey, unlike any of the other sources. The vertical dashed line indicates the date of the 2015 WHT/ISIS observations. Reproduced from Tadhunter et al. (2017).

4.5 Results – outflow properties

The ultimate aim of the QUADROS project was to better quantify the key properties of the AGN-induced outflows in the nuclear regions of local ULIRGs. The necessary calculations required accurate determinations of the outflow kinematics, radii, electron densities and intrinsic reddenings. In this section, the results of the kinematic models are presented.

4.5.1 Emission line kinematics and outflow radii

Firstly, the kinematics and radii of the nuclear outflows were measured. Table 4.1 gives the velocity shifts and widths (FWHM) of the kinematic components required to model the [OIII]λ5007 emission line for each object, using the fitting approach described in section 4.3.2. Blue-shifted intermediate/broad components were detected in all objects, indicating the presence of ionised nuclear outflows, consistent with the results of (Rodríguez Zaurín et al., 2013). The analyses focussed on the properties of these out-flowing components.

In order to properly quantify the outflow powers, it was also important to estimate their spatial extents along the slit. Currently, the true radial extents of AGN-induced outflows (R_{out}) in luminous type II AGN are highly uncertain, with R_{out} measurements ranging from just 0.06 kpc (Tadhunter et al., 2018) to >10 kpc (Harrison et al., 2012). To determine the radial extents of the WHT/ISIS ULIRGs, the out-flowing (broad, blueshifted) components of the [OIII] emission lines were isolated within the nuclear spectra. Guided by the Gaussian fits to the emission-line profiles, spatial slices between the 95th percentile (v_{95}) of the narrow [OIII]λ4959 component fit and 5th percentile (v_{05}) of the narrow [OIII]λ5007 component fit were extracted. In this way, *only* the out-flowing components were sampled, avoiding any significant narrow-line flux not associated with the outflow. In the case of F05189-2524, all components of [OIII] were significantly blue-shifted with respect to the stellar rest-frame. For this target, all of the [OIII]λ5007 flux blue-ward of the rest-frame was extracted. The velocity ranges over which the spatial profiles were extracted are given in Table 4.2, column 2, and indicated visually by the shaded regions in Figure 4.8.

The continuum was then removed by subtracting an average continuum profile created from two $\sim$ 30Å spatial slices, one taken blue-ward and the other red-ward of the [OIII]$\lambda\lambda$4959,5007 blend. The resultant spatial profile was then fitted with a Gaussian using DIPSO. In all cases, a single Gaussian was sufficient. To assess whether the outflow was resolved, the FWHM of this spatial profile was compared to the 1D seeing estimate, based on the spatial profiles of telluric standard stars (see Chapter 2). The outflow was considered spatially resolved if the difference between the spatial FWHM of the outflow and the FWHM of the seeing disc was greater than 3 times the estimated uncertainty in the difference (i.e. 3σ).

In the spatially resolved cases, the FWHM of the 1D seeing profile was subtracted from the spatial FWHM of the outflow in quadrature, converted to kpc using the pixel scale and angular scale on the sky consistent with the assumed cosmology, and then halved to find the radius. See §3.1 in Rose et al. (2018) for a full discussion of this technique.

Using the ground-based spectroscopy, the outflow regions were spatially resolved for three objects, with the other objects unresolved compared to the seeing. In the latter cases, the quoted radii are upper limits, derived by calculating the radius ($\mathrm{FWHM}_{[OIII]}$) at which the outflow would have been significantly resolved at the 3σ level compared to the 1D seeing (FWHM_{1D}):

$$\mathrm{FWHM}_{[\mathrm{OIII}]} < \sqrt{(\mathrm{FWHM}_{\mathrm{1D}} + 3\sigma)^2 - (\mathrm{FWHM}_{\mathrm{1D}})^2}. \tag{4.1}$$

Table 4.2: Radial extents of the broad, outflowing [OIII]λ5007 gas. Column (2): The velocity range over which the spatial slice was extracted. Columns (3) and (4) give the spatial FWHM for the outflow and 1D seeing disc (extracted from a standard star over the same wavelength range) respectively. Column (6) shows the calculated outflow radii using the WHT, and columns (7) and (8) show the radii measured using HST observations for comparison.

Object name IRAS	[OIII]λ5007 range (km s^{-1})	FWHM$_{[OIII]}$ (arcsec)	FWHM$_{1D}$ (arcsec)	Resolved WHT? (Y/N)	R$_{[OIII]}$ (kpc)		
					WHT/ISIS	HST/STIS	HST/ACS
(1)	(2)	(3)	(4)	(5)	(6)	(7)	(8)
F01004 – 2237	-2591 – -278	1.623 ± 0.017	1.430 ± 0.123	N	< 1.1	0.081 ± 0.010	–
F05189 – 2524[a]	-3016 – 0	1.774 ± 0.014	1.634 ± 0.052	N	< 0.3	0.074 ± 0.003	–
F14394 + 5332E	-2315 – -524	1.489 ± 0.010	1.248 ± 0.073	Y	0.75 ± 0.12	–	0.840 ± 0.008[b]
F17044 + 6720	-2453 – -422	2.044 ± 0.047	1.610 ± 0.069	Y	1.45 ± 0.18	–	1.184 ± 0.006
F17179 + 5444	-2327 – -614	1.796 ± 0.046	1.600 ± 0.060	N	< 1.0	–	0.112 ± 0.007
F23060 + 0505	-2375 – -524	1.469 ± 0.022	1.073 ± 0.110	Y	1.41 ± 0.19	–	–
F23233 + 2817	-2609 – -446	1.485 ± 0.014	1.167 ± 0.154	N	< 1.1	–	–
F23389 + 0303N	-2603 – -655	1.542 ± 0.018	1.441 ± 0.100	N	< 1.2	–	–

[a] The entire [OIII]$\lambda\lambda$5007,4959 profile for this component was blueshifted by > 500 km s^{-1}, i.e. only the outflowing component has been detected, so the spatial profile was extracted over the entire velocity range of [OIII]λ5007 blue-ward of the rest-frame.

[b] Note that the HST/ACS measurement assumes that the AGN is located in the dust lane that bisects the eastern nucleus of the system.

Table 4.2 gives the FWHM values of the spatial [OIII] and 1D seeing profiles for each object (columns 3 and 4), along with the estimated radii (columns 6 - 8). Two objects (F01004–2237 and F05189–2524) had space-based STIS spectroscopy available for comparison (column 7). Using the same spatial extraction technique, but considering the line spread functions instead of atmospheric seeing profiles, additional estimates for the outflow radii were calculated (see Rose et al., 2018). In these cases it was assumed that the emission features measured in the STIS spectra were dominated by the outflow components. For the [OIII] emission, $\mathrm{FWHM}_{[OIII]} = 0.108 \pm 0.004$ arcsec and $\mathrm{FWHM}_{[OIII]} = 0.193 \pm 0.003$ arcsec for F01004–2237 and F05189–2524, respectively. The line spread functions for each object were estimated to be $\mathrm{FWHM}_{lsf} = 0.080 \pm 0.002$ arcsec and $\mathrm{FWHM}_{lsf} = 0.059 \pm 0.002$ arcsec, respectively. Combining these measurements with the angular scale on the sky for each object (Table 2.2) gave compact radii for both objects, consistent with the WHT/ISIS upper limits.

Estimates of the outflow radii for a further three objects (F14394+5332E, F17044+6720 and F17179+5444) were also available from HST/ACS narrow-band imaging, presented in Tadhunter et al. (2018). The radius for F17179+544 was measured from fitting 2D Gaussians to the compact near-nuclear [OIII] structure in the image. For the other two objects, in which there was no compact [OIII] structure, a flux-weighted mean radius was estimated for the emission within a 5 kpc aperture. The HST imaging-based radius estimates are given in column 8. There is remarkable consistency between the HST/ACS estimates and the resolved WHT/ISIS estimates for F14374+5332E and F17044+6720. The ACS imaging estimate for F17179+5444 is also consistent with the upper limit from the

WHT spectroscopy.

Note that, while only an upper limit on the outflow radius could be determined for F23389+0303N, leading to lower limits on the mass outflow rates and kinetic powers in this case, estimates of the outflow properties based on the radius of the radio lobes (r = 0.415 kpc) from Nagar et al. (2003) are also presented. Although this involves the assumption that the outflows are jet-driven in this object, generally the emission-line outflows associated with compact radio sources of similar power to F23389+0303N are found to be co-spatial with the radio sources (e.g. Axon et al., 2000; Batcheldor et al., 2007; Tadhunter et al., 2014).

Overall, consistent with the VLT/XShooter and HST/ACS results of Rose et al. (2018) and Tadhunter et al. (2018) for their QUADROS ULIRGs, the outflows in the WHT/ISIS ULIRGs (with the exception of Mrk 273) are compact, with radii estimates in the range $0.07 < R_{out} < 1.5$ kpc.

4.5.2 Density and reddening

Next, the electron densities and intrinsic reddenings of the outflows were calculated. As discussed in Chapter 1 (see also Rose et al., 2018), previous attempts to calculate mass outflow rates and kinematic powers in AGN have been severely limited by the lack of accurate estimates of the electron density. For AGN, the most commonly used optical diagnostics are the [SII](6716/6731) and [OII](3729/3726) doublet ratios. However, these are only sensitive to relatively low densities ($10^2 < \mathrm{n_e} < 10^{3.5}\mathrm{cm}^{-3}$) and are therefore ineffective for the higher density clouds that are also expected to be associated with outflows. Furthermore, the highly blue- or redshifted, broad components can cause degeneracies in the fitting, due to severe blending of the emission-line profiles. These degeneracies can also affect the Hα + [NII] blend, leading to significant uncertainties in the intrinsic reddening calculated from the Balmer decrement.

For this reason, the WHT/ISIS observations were optimised for the trans-auroral [SII]$\lambda\lambda$4068,4076 and [OII]$\lambda\lambda$7319,7330 features. These emission line fluxes were combined with the [SII]$\lambda\lambda 6716, 6731$ and [OII]$\lambda\lambda 3726, 3729$ fluxes as follows:

$$\mathrm{TR([OII])} = F(3726 + 3729)/F(7319 + 7330); \text{and} \tag{4.2}$$

$$\mathrm{TR([SII])} = F(4068 + 4076)/F(6716 + 6731). \tag{4.3}$$

Combining the fluxes in this way gives a density diagnostic that does not suffer from the problems with degeneracies that affect the [SII](6716/6731) and [OII](3729/3726) diagnostics. This is because the total fluxes of the widely separated blends are compared, rather than the fluxes of the individual components within them. This technique, introduced by Holt et al. (2011), is also sensitive to a higher range of densities ($10^2 < n_e < 10^{6.5}\mathrm{cm}^{-3}$) because of the higher critical densities of the trans-auroral lines. Another advantage is that these diagnostics give a simultaneous estimate of the intrinsic dust reddening, E(B-V), of the emitting clouds. The trans-auroral emission lines are discussed further in Chapter 5.

The ideal scenario would be to resolve the individual trans-auroral kinematic components for all the ULIRGs. Unfortunately, the spectral resolution and signal-to-noise (S/N) for WHT/ISIS was lower than for the VLT/XShooter observations used in Rose et al. (2018). This means that the weaker [OII]$\lambda\lambda$7319,7330 and [SII]$\lambda\lambda$4068,4076 trans-auroral emission lines for the majority of the objects considered in this work were not sufficiently strong to allow the separation of narrow and broad/intermediate

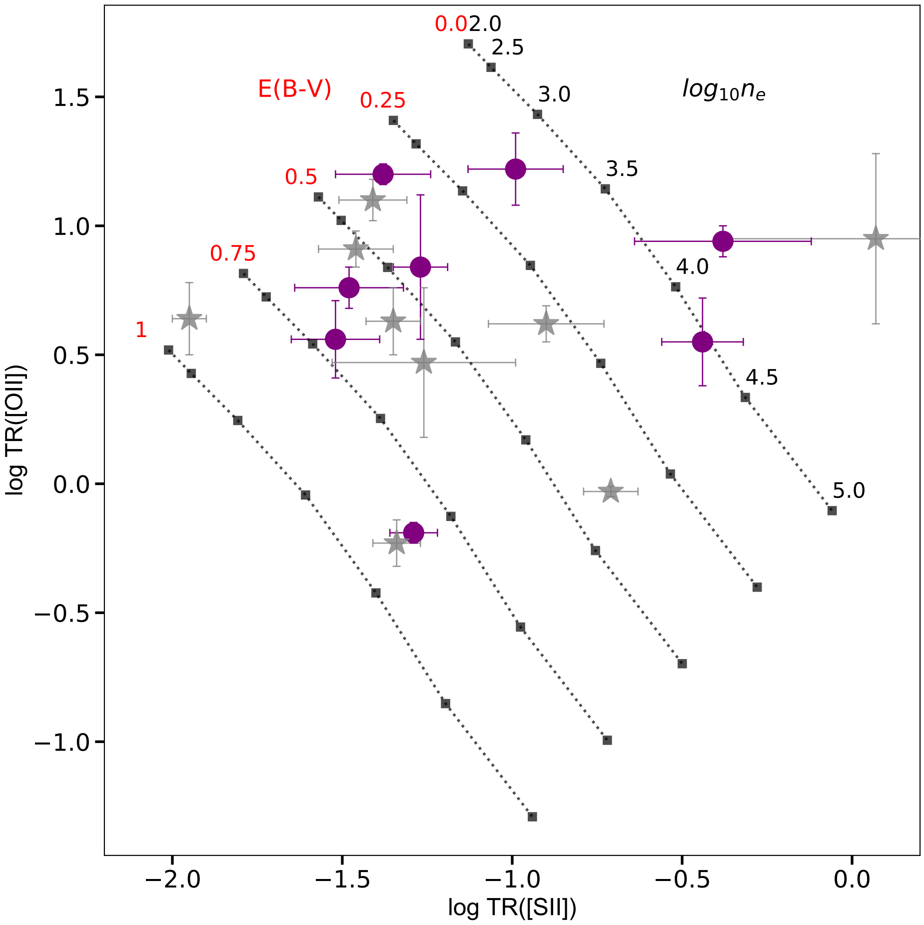

Figure 4.12: Trans-auroral line ratios for the total emission-line fluxes. The purple circles are the results from this work. Overplotted as grey stars are the results from Rose et al. (2018). The grid was generated by the photo-ionisation code CLOUDY (Ferland et al., 2013) and the Calzetti et al. (2000) reddening law.

components. In these cases, a single Gaussian profile was fitted in order to estimate the total emission line fluxes. Note that the densities derived from the total fluxes are generally lower than those derived from the broad component alone (see Figures 8 and 10 in Rose et al. 2018). Because the mass outflow rate and kinetic power depends on the inverse of the density, this could lead to the calculation of higher values for these outflow properties compared with Rose et al. (2018).

Figure 4.12 shows a plot of log TR([OII]) vs. log TR([SII]) for the total emission-line fluxes for the 8 objects considered in the WHT/ISIS sample

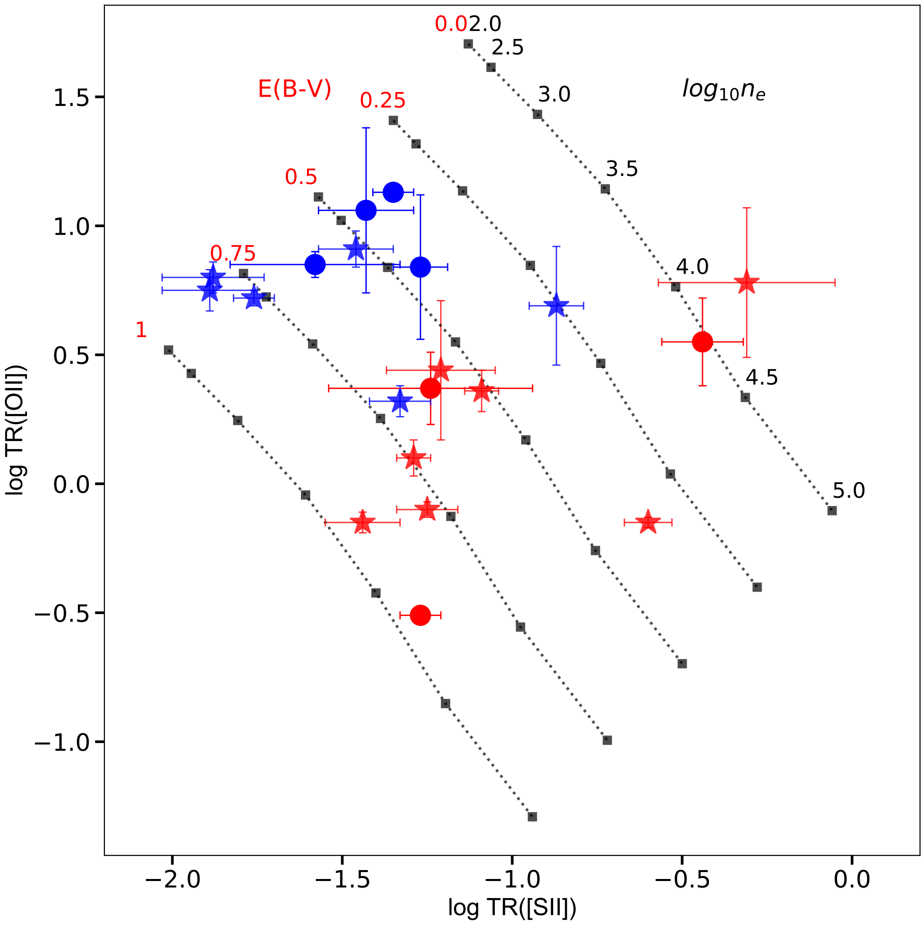

Figure 4.13: Trans-auroral line ratios for the narrow and broad component fluxes. The solid blue and red circles indicate the narrow and broad components, respectively, for the objects in this study. Over-plotted as blue and red stars are the narrow and broad ratios from Rose et al. (2018). The grid was generated by the photo-ionisation code CLOUDY (Ferland et al., 2013) and the Calzetti et al. (2000) reddening law.

(purple circles). All fluxes were measured from the WHT/ISIS spectra, with the exception of F01004–2237, for which the HST/STIS spectrum was used to measure the [SII]$\lambda\lambda$4068,4076 flux, and F05189–2524, for which the HST/STIS spectrum was used to measure all emission line fluxes. Also plotted are the measurements from Rose et al. (2018) for the VLT/XShooter sample (grey stars).

Over-plotted is a grid of predicted ratios generated by the photo-ionisation code CLOUDY (Ferland et al., 2013) and the Calzetti et al.

(2000) reddening law. The code was used to create plane-parallel, single-slab models, in which the photo-ionised gas was assumed to be radiation bounded and of solar abundance. The power-law shape of the ionising continuum was α = -1.5; $F_\nu \propto \nu^\alpha$ and the ionisation parameter was fixed to U = 0.005, however note that the trans-auroral ratios are not particularly sensitive to these parameters (Holt et al., 2011; Rose et al., 2018, see also Chapter 5). The electron density was varied in the range 2.0 < log n_e (cm^{-3}) < 5.0.

The densities based on the total fluxes fall in the range 2.5 < log n_e (cm^{-3}) < 4.5, with the median log n_e (cm^{-3}) = 3.10±0.29. The intrinsic dust reddening falls in the range 0.0 < E(B – V) < 1.0, with the median E(B-V) = 0.45±0.14. Table 4.3 gives the density and reddening values obtained using the total emission line fluxes for each object individually. These results are consistent with those obtained by Rose et al. (2018) using VLT/XShooter data for the rest of the ULIRGs in the QUADROS sample.

For the objects where narrow and intermediate/broad components of the trans-auroral emission lines could be resolved, the associated density and reddening estimates are also shown separately in Tables 4.4 and 4.5. Note that F23060+0505 is only included in the Table 4.4 because only the narrow components of the trans-auroral emission lines were detected. Similarly, F05189–2524 is only included in Table 4.5 because the whole trans-auroral emission line profiles were blue-shifted with respect to the rest frame, with no rest-frame narrow component detected. Therefore it was assumed that, in this case, all of the detected flux was associated with the outflow.

These narrow and broad flux ratios are plotted in Figure 4.13 (blue and red circles, respectively), along with the measurements from Rose et al. (2018) (blue and red stars, respectively). Some overlap between the narrow and broad components can be seen; however, considering the full e-QUADROS sample, the densities of the broad, out-flowing components are generally high ($3.5 < \log\, n_e(\mathrm{cm}^{-3}) < 4.5$, median $\log\, n_e(\mathrm{cm}^{-3}) = 3.8\pm0.2$). In comparison, the median density for the narrow components is an order of magnitude lower: $\log\, n_e(\mathrm{cm}^{-3}) = 2.8\pm0.3$.

Clearly, assuming a single low density ($\log\, n_e(\mathrm{cm}^{-3}) \sim 2$) for AGN-induced outflows, as is common in many outflow studies, is not justified and is likely to lead to some of the higher values of the mass outflow rates and kinetic powers in the literature.

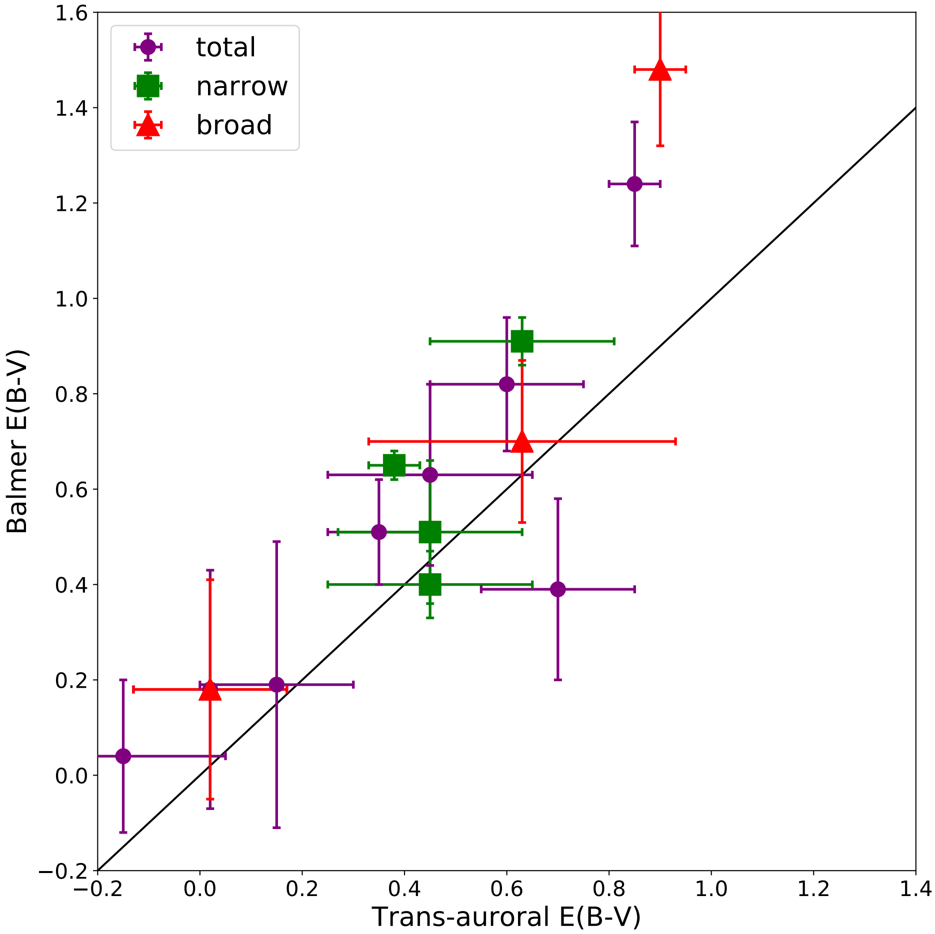

Figure 4.14: The reddening estimates obtained from the Balmer decrement and trans-auroral line ratios for the emission-line fluxes for the different kinematic components. The black solid line represents a one-to-one ratio. The two techniques are consistent to within 3σ.

Despite the previously mentioned degeneracies in the [NII] + Hα fits, as a check the intrinsic reddening, E(B-V), was determined based on the Hα/Hβ ratios for the individual components. The estimates are shown in column 6 of Tables 4.3 to 4.5. In general, the two techniques are consistent within 3σ. This is illustrated in Figure 4.14 for the total, narrow and broad fluxes. Interestingly, and consistent with Rose et al. (2018), no clear evidence is found to suggest that the outflowing gas is reddened more than the narrow-line gas associated with the host galaxy. Indeed, the narrow component ratios cover a similar range of reddening as the broad, outflowing components and are, on average, higher. Based on the reddening estimates derived from the Balmer decrements of the ULIRGs considered in this work, the calculated medians were $\mathrm{E(B\text{-}V)}_{\mathrm{narrow}} = 0.52\pm0.09$; median $\mathrm{E(B\text{-}V)}_{\mathrm{broad}} = 0.15\pm0.25$.

As a reference to compare with the trans-auroral estimates, the density of the gas emitting the narrow-line components was also measured using the [SII](6716/6731) doublet ratio, in which the narrow components are generally strong and well resolved. This technique is not appropriate for the broad components due both to degeneracies in the fit and the fact that in most cases the ratio of the broad components was constrained to the high-density limit during the fitting process. The estimated densities are presented in Table 4.4, Column 5. For the majority of objects the narrow-component ratios were less than 3σ from the low-density limit. For these a 3σ upper limit on the density is provided.

In all cases, the density estimates and upper-limits derived from the [SII](6716/6731) doublet ratios for the narrow components are lower than those derived from the ratios of both the total and broad trans-auroral fluxes, although in the case of F17044+6720 the two estimates are close. These results support the conclusion that the outflows have higher densities than the regions emitting the narrow components.

Table 4.3: The log n_e and E(B-V) values determined using the *total* trans-auroral emission-line fluxes. Column (5) shows the E(B-V) estimates obtained using the trans-auroral lines ratios. Column (6) shows the E(B-V) estimates obtained using the Hα/Hβ Balmer decrement.

Object name IRAS	log[SII]	log[OII]	log(n_e) (cm^{-3})	E(B-V)$_{\rm trans}$	E(B-V)$_{\rm Bal}$
(1)	(2)	(3)	(4)	(5)	(6)
F01004 – 2237	-0.38 ± 0.26	0.94 ± 0.06	$4.00^{+0.25}_{-0.30}$	-0.15 ± 0.20	0.04 ± 0.16
F05189 – 2524	-0.44 ± 0.12	0.55 ± 0.17	$4.25^{+0.25}_{-0.25}$	$0.02^{+0.15}_{-0.15}$	0.29 ± 0.25
F14394 + 5332E	-1.48 ± 0.16	0.76 ± 0.08	$2.90^{+0.30}_{-0.40}$	$0.60^{+0.15}_{-0.15}$	0.82 ± 0.14
F17044 + 6720	-1.38 ± 0.14	1.20 ± 0.04	$2.50^{+0.30}_{-0.50}$	$0.35^{+0.10}_{-0.10}$	0.51 ± 0.11
F17179 + 5444	-1.52 ± 0.13	0.56 ± 0.15	$3.05^{+0.30}_{-0.45}$	$0.70^{+0.15}_{-0.15}$	0.39 ± 0.19
F23060 + 0505	-1.27 ± 0.08	0.84 ± 0.28	$3.10^{+0.35}_{-0.50}$	$0.45^{+0.15}_{-0.20}$	0.63 ± 0.19
F23233 + 2817	-0.99 ± 0.14	1.22 ± 0.14	$3.10^{+0.30}_{-0.40}$	$0.15^{+0.15}_{-0.15}$	0.19 ± 0.30
F23389 + 0303N	-1.29 ± 0.07	-0.19 ± 0.03	$3.95^{+0.10}_{-0.10}$	$0.85^{+0.05}_{-0.05}$	1.24 ± 0.13

Table 4.4: The log n_e and E(B-V) values determined using the *narrow* emission-line fluxes. Column (4) shows the density estimates obtained using the narrow component of the trans-auroral emission lines, where detected. Column (5) shows the density estimates based on the narrow [SII]$\lambda\lambda$6716/6731 flux ratio for comparison. Columns (6) and (7) compare the E(B-V) estimates calculated using the trans-auroral [SII] and [OII] emission blends with those calculated using the Hα/Hβ decrement.

Object name IRAS (1)	log[SII] (2)	log[OII] (3)	$\log(n_e)_{\rm trans}$ (cm^{-3}) (4)	$\log(n_e)_{\rm [SII]}$ $\lambda\lambda$6716/6731 (cm^{-3}) (5)	E(B-V)$_{\rm trans}$ (6)	E(B-V)$_{\rm Bal}$ (7)
F01004 – 2237	–	–	–	< 2.60	–	0.75 ± 0.11
F05189 – 2524	–	–	–	$2.81^{+0.14}_{-0.14}$		0.47 ± 0.27
F14394 + 5332E	-1.58 ± 0.25	0.85 ± 0.05	$2.70\ ^{+0.35}_{-0.50}$	< 2.64	$0.63\ ^{+0.17}_{-0.18}$	0.91 ± 0.09
F17044 + 6720	–	–	-	$2.49^{+0.15}_{-0.18}$	–	0.65 ± 0.06
F17179 + 5444	–	–	–	–	–	–
F23060 + 0505	-1.27 ± 0.08	0.84 ± 0.28	$3.15\ ^{+0.30}_{-0.50}$	< 2.88	$0.45\ ^{+0.15}_{-0.18}$	0.51 ± 0.18
F23233 + 2817	–	–	–	< 2.55	–	0.52 ± 0.16
F23389 + 0303N	-1.43 ± 0.14	1.06 ± 0.32	$2.60\ ^{+0.60}_{-0.60}$	< 2.91	$0.45\ ^{+0.20}_{-0.20}$	0.40 ± 0.09

Table 4.5: The log n_e and E(B-V) values determined using the *broad* trans-auroral emission-line fluxes. Note that the results for F05189-2524 were obtained using HST/STIS data (also in Table 4.3.)

Object name IRAS (1)	log[SII] (2)	log[OII] (3)	$\log(n_e)$ (cm^{-3}) (4)	$\mathrm{E(B\text{-}V)_{trans}}$ (5)	$\mathrm{E(B\text{-}V)_{Bal}}$ (6)
F01004 – 2237	–	–	–	–	-0.20 ± 0.20
F05189 – 2524	-0.44 ± 0.12	0.55 ± 0.17	$4.25^{+0.25}_{-0.25}$	$0.02^{+0.15}_{-0.15}$	0.18 ± 0.24
F14394 + 5332E	-1.24 ± 0.30	0.37 ± 0.14	$3.55^{+0.45}_{-0.45}$	$0.63^{+0.22}_{-0.30}$	0.70 ± 0.21
F17044 + 6720	–	–	–	–	-0.35 ± 0.67
F17179 + 5444	–	–	–	–	0.11 ± 0.37
F23060 + 0505	–	–	–	–	1.10 ± 0.18
F23233 + 2817	–	–	–	–	-0.06 ± 0.45
F23389 + 0303N	-1.27 ± 0.06	-0.51 ± 0.03	$4.20^{+0.10}_{-0.10}$	$0.90^{+0.05}_{-0.05}$	1.48 ± 0.14

4.5.3 Bolometric luminosities

In order to compare the kinetic powers derived for the warm outflows with the total radiative powers of the AGN, their bolometric luminosities (L_{bol}) must first be determined. To do this, the [OIII]λ5007 emission-line luminosities were used, which have been shown to be reasonable indicators of AGN powers (Heckman et al., 2004; Dicken et al., 2014). Initially two approaches for determining L_{bol} were adopted: 1) the bolometric correction of Heckman et al. (2004): $L_{bol} = 3500 L_{[OIII]}$, where $L_{[OIII]}$ has not been corrected for dust extinction; and 2) the bolometric correction factors of Lamastra et al. (2009) which uses the reddening-corrected $L_{[OIII]}$. In the latter case, the correction factors are 87, 142 and 454 for reddening-corrected luminosities of $\log L_{[OIII]}$ = 38-40, 40-42 and 42-44 erg s^{-1}, respectively.

To determine the bolometric luminosities the total [OIII] fluxes were used, which involves the assumption that there is little contribution to [OIII]λ5007 from stellar photo-ionised regions. This is a reasonable assumption for the nuclear regions of the e-QUADROS ULIRGs, based on BPT diagnostic diagrams presented in Rodríguez Zaurín et al. (2013). The location of the diagnostic emission-line ratios on these diagrams indicate that the warm gas is dominated by AGN photo-ionisation. Although F05189–2524 was not included in the latter paper, further BPT analysis showed the line ratios for this object also to be consistent with AGN photo-ionisation.

The bolometric luminosities were determined using the measured [OIII]λ5007 fluxes. For technique (2), the luminosities were corrected for dust extinction using the total E(B-V) values from Column 5 in Table 4.3 and the extinction law of Calzetti et al. (2000). The calculated luminosities are shown in Table 4.6, where the estimates obtained using the corrections of

Heckman and Lamastra are compared in Column 6. The estimates are consistent to within a factor of ∼5 for most of the objects; however, for the three objects with the lowest dust extinction (F01004–2237, F05189–2524 and F23233+2817) the Lamastra estimates are over an order of magnitude lower than the Heckman estimates. Based on this, the Heckman corrections are likely the most appropriate for these cases due to the small amount of reddening. Therefore, the Lamastra estimates were dropped and only the Heckman-derived bolometric luminosities were used in the following analyses.

4.5.4 Mass outflow rates, kinetic powers and coupling efficiencies

The key parameters for quantifying the importance of AGN-driven outflows are the mass outflow rates, kinetic powers and coupling efficiencies. Following the arguments of Rose et al. (2018) the following two cases are considered, based on two different assumptions about the kinematics.

Using flux-weighted mean outflow velocities, ignoring projection effects

The mass outflow rate ($\dot{M}$) is given by:

$$\dot{M} = \frac{L(H\beta) m_p v_{out}}{\alpha_{eff}^{H\beta} h\nu_{H\beta} n_e R_{out}} \tag{4.4}$$

where v_{out} is the assumed velocity of the out-flowing gas, measured from the Gaussian fits, R_{out} is the outflow radius, L(Hβ) is the intrinsic (i.e. extinction-corrected) Hβ emission-line luminosity for the out-flowing gas (broad + intermediate components), n_e is the electron density derived from the trans-auroral emission line ratios, m_p is the proton mass, $\alpha_{eff}^{H\beta}$ is the Case B effective recombination coefficient of Hβ for T$_e$ = 10^4K

Table 4.6: [OIII]λ5007 luminosities and associated bolometric luminosities. Column (2): uncorrected [OIII] luminosity. Column (3): extinction-corrected [OIII] luminosity based on the E(B-V) values derived from the total trans-auroral flux ratios and extinction law of Calzetti et al. 2000. Column (4): the [OIII] bolometric luminosity based on the Heckman bolometric correction factor. Column (5): the [OIII] luminosity based on the appropriate Lamastra bolometric correction factor. Column (6): the ratio of the Heckman bolometric luminosity to the Lamastra bolometric luminosity.

Object name IRAS (1)	$L_{[OIII]-unc}$ erg s^{-1} (2)	$L_{[OIII]-corr}$ erg s^{-1} (3)	$L_{bol-Heck}$ erg s^{-1} (4)	$L_{bol-Lam}$ erg s^{-1} (5)	Heck/Lam (6)
F01004 – 2237	(2.5±0.1)E+41	(3.0±1.4)E+41	(8.8±0.4)E+44	(4.2±2.0)E+43	21
F05189 – 2524	(1.0±0.1)E+41	(1.1±0.5)E+41	(3.6±0.1)E+44	(1.6±0.7)E+43	23
F14394 + 5332E	(2.6±0.1)E+41	(3.1±1.4)E+42	(9.0±0.2)E+44	(1.4±0.6)E+45	0.64
F17044 + 6720	(9.9±0.2)E+40	(4.3±1.4)E+41	(3.3±0.1)E+44	(6.1±2.0)E+43	5.7
F17179 + 5444	(1.7±0.1)E+41	(3.2±1.5)E+42	(6.1±0.1)E+44	(1.5±0.7)E+45	0.41
F23060 + 0505	(1.3±0.1)E+42	(8.6±3.6)E+42	(4.6±0.4)E+45	(3.9±1.6)E+45	1.2
F23233 + 2817	(4.8±0.2)E+41	(8.9±4.0)E+41	(1.7±0.1)E+45	(1.3±0.6)E+44	13
F23389 + 0303N	(6.7±0.1)E+41	(2.3±0.4)E+43	(2.4±0.1)E+45	(1.1±0.2)E+46	0.22

($\alpha_{\rm eff}^{\rm H\beta} = 3.03 \times 10^{-14} {\rm cm^3 s^{-1}}$), taken from Osterbrock & Ferland (2006) and $h\nu_{H\beta}$ is the energy of an Hβ photon.

In this first scenario, the mean velocity shifts of the out-flowing components of [OIII] with respect to the galaxy rest-frames were taken to represent v_{out}. For those objects with two or more out-flowing components, flux-weighted means were calculated. For the radius the HST estimates were used where available from Table 4.2. In the three objects where this was not possible, the WHT/ISIS estimates were used, and for F23389+0303N the radial extent of the double-lobed radio source was used. To calculate L(Hβ) the observed fluxes were corrected using the appropriate E(B-V) values derived from the trans-auroral flux ratios.

The outflow kinetic power was then calculated using the following equation:

$$\dot{E} = \frac{\dot{M}}{2}(v_{out}^2 + 3\sigma^2) \tag{4.5}$$

where σ is the line-of-sight (LoS) velocity dispersion ($\sigma \approx$ FWHM/2.355) calculated using the full-width at half-maximum (FWHM) of [OIII] for the out-flowing gas component. Again, for those objects with more than one out-flowing component, the flux-weighted mean FWHM was used. This technique assumes that all of the emission-line broadening is due to turbulence in the gas and that v_{out} represents the true outflow velocity. Note that, in this method, the effects of projection on the measured velocities were not corrected for.

The outflow kinetic power is also expressed as a fraction of the AGN radiative power ($\dot{F}$) by dividing $\dot{E}$ by L_{bol} (derived using the Heckman correction). These values represent the coupling efficiencies of the outflows. The calculated values of v_{out}, FWHM, $\dot{M}$, $\dot{E}$ and $\dot{F}$ are presented in Table 4.7. In addition, for the objects where only upper limits on the outflow radius could be derived, the kinetic powers, mass outflow rates and coupling efficiencies given in Table 4.7 are lower limits.

Note that, unlike Rose et al. (2018), most of the estimates are based on density values derived from total trans-auroral fluxes (designated “T” in column 2). This is due to the lower spectral resolution and S/N for WHT/ISIS compared with VLT/XShooter. However, in two cases – F14394+5332E and F23389+0303N – estimates based on density values derived from the broad trans-auroral line fluxes alone (designated “B” in column 2) are presented. Moreover, in the case of F05189–2524, the total trans-auroral fluxes are representative of the broad, outflowing components. Overall, the estimates of the outflow properties based on the densities derived from the broad outflowing components in F14394+5332E, F05189–2524 and F23389+0303N are considered the most reliable.

In the cases where $R_{[OIII]}$ was resolved, the mass outflow rates were calculated in the range $0.06 < \dot{M} < 6$ $M_{\odot}yr^{-1}$ and kinetic powers in the range $1.8 \times 10^{40} < \dot{E} < 4.3 \times 10^{42}$ erg s^{-1}. Comparing the outflow kinetic powers with the bolometric luminosities of the AGN, coupling efficiencies in the range $4{\times}10^{-3} < \dot{F} < 0.5\%$ were calculated.

Using maximal outflow velocities to account for projection effects

The above estimates of the kinetic powers and coupling efficiencies are likely to underestimate the true values due to the fact that use of the mean outflow velocities of the out-flowing components does not take into account LoS projection effects, as discussed in Rose et al. (2018).

A more physical approach is to assume that the broadening of the emission lines is due entirely to different projections of the velocity vector of the expanding outflow with respect to the LoS, rather than due to turbulence. Therefore, the true velocity of the out-flowing gas is given by the extreme blue wing of the Gaussian profile. This corresponds to

Table 4.7: Outflow properties for the flux-weighted mean velocity case. Column (2): the trans-auroral fluxes used to calculate the density and reddening values employed in the calculations: T = total, B = broad/intermediate. In the case of F05189–2524, the whole profile was blueshifted with respect to the rest-frame and hence the total flux and broad flux were assumed to be equivalent. Column (3): the flux weighted mean velocity. Column (4): the flux-weighted mean FWHM. Column (5): the calculated mass outflow rate. Column (6): the calculated kinetic power. Column (7): the kinetic power expressed as a fraction of the bolometric luminosity ($\dot{E}/L_{bol}$).

Object name	Comp.	v_{mean}	FWHM	$\dot{M}$	$\dot{E}$	$\dot{F}$
IRAS	T/B	km s^{-1}	km s^{-1}	M$_\odot$ yr^{-1}	erg s^{-1}	%
(1)	(2)	(3)	(4)	(5)	(6)	(7)
F01004 – 2237	T	-826±52	1302±35	$0.5^{+1.0}_{-0.3}$	$(2.5^{+6.2}_{-1.9})\times10^{41}$	$(2.8^{+7.5}_{-2.1})\times10^{-2}$
F05189 – 2524	T,B	-688±31	949±32	$0.06^{+0.10}_{-0.04}$	$(1.8^{+3.4}_{-1.3})\times10^{40}$	$(5.1^{+9.8}_{-3.6})\times10^{-3}$
F14394 + 5332E	T	-990±89	1616±27	$5.5^{+16.9}_{-4.1}$	$(4.2^{+14.4}_{-3.2})\times10^{42}$	$0.47^{+1.65}_{-0.36}$
	B	"	"	$1.4^{+6.2}_{-1.3}$	$(1.1^{+5.3}_{-1.0})\times10^{42}$	$0.12^{+0.60}_{-0.11}$
F17044 + 6720	T	-503±85	1754±60	$0.3^{+1.2}_{-0.2}$	$(1.8^{+8.1}_{-1.3})\times10^{41}$	$(5.2^{+24.0}_{-3.7})\times10^{-2}$
F17179 + 5444	T	-241±78	1528±32	$3.2^{+26.0}_{-2.6}$	$(1.3^{+11.8}_{-1.1})\times10^{42}$	$0.22^{+1.96}_{-0.18}$
F23060 + 0505	T	-461±63	1023±48	$0.8^{+3.2}_{-0.6}$	$(1.9^{+9.5}_{-1.5})\times10^{41}$	$(4.0^{+22.8}_{-3.4})\times10^{-3}$
F23233 + 2817	T	-391±35	940±17	>0.04	$>6.6\times10^{39}$	$>4.0\times10^{-4}$
F23389 + 0303N[a]	T	-134±36	2345±37	>0.2	$>1.4\times10^{41}$	$>6.0\times10^{-3}$
	B	"	"	>0.1	$>1.30\times10^{41}$	$>5.4\times10^{-4}$
F23389 + 0303N[b]	T	-134±36	2345±37	$0.9^{+3.8}_{-0.6}$	$(8.9^{+37.7}_{-5.6})\times10^{41}$	$(3.8^{+16.4}_{-2.4})\times10^{-2}$
	B	"	"	$0.7^{+2.7}_{-0.4}$	$(6.2^{+26.3}_{-3.9})\times10^{41}$	$(2.6^{+11.4}_{-1.7})\times10^{-2}$

[a] These estimates were made using the upper limit on the outflow radius from the WHT/ISIS spectrum.

[b] These estimates were made using the radius estimate of the radio lobes (R = 415 pc) as a proxy for the outflow radius, taken from Nagar et al. (2003). This assumes that the outflows are jet-driven.

the gas travelling directly along the LoS. It follows that, in this scenario, the outflow kinetic power is given by dropping the turbulence term in equation (4.5), and taking the v_{05} shift of the Gaussian fit to the outflow component relative to the galaxy rest-frame to represent v_{out}, rather than the mean shift as before. Note v_{05} was used rather than v_{00} to avoid confusion with the continuum. The estimates derived using this method are presented in Table 4.8.

Under the maximal velocity assumption, and considering the estimates for the objects in which $R_{[OIII]}$ was resolved, mass outflow rates were calculated in the range $0.1 < \dot{M} < 20$ M$_{\odot}$yr^{-1} and kinetic powers in the range $9.3 \times 10^{40} < \dot{E} < 2.3 \times 10^{43}$ erg s^{-1}. These ranges are again consistent with those found in Rose et al. (2018) and the kinetic powers are a factor of $\sim 5\times$ higher than those obtained using the first method.

Comparing the outflow kinetic powers with the bolometric luminosities of the AGN, coupling efficiencies were calculated in the range $0.03 < \dot{F} < 2.5\%$. While the fraction of the AGN power contained in the outflow is naturally larger when using higher velocities, even in this maximal velocity case, the coupling efficiencies fall short of the threshold required ($\dot{F} \sim 5$ - 10%) by the Di Matteo et al. (2005) and Springel et al. (2005) models.

Initially, these results may suggest that the AGN-induced outflows alone do not contain the necessary energy to significantly impact their host galaxies. However, caution is required when comparing the $\dot{F}$ results with the predictions of theoretical models for AGN-induced outflows. As discussed in Harrison et al. (2018), it may not be appropriate to directly compare the $\dot{E}/L_{bol}$ (ϵ_f) values required by the models with the $\dot{F}$ values estimated for the warm outflows in the e-QUADROS ULIRGs: first, the $\dot{E}$ used in some of the models (e.g. Di Matteo et al., 2005; Springel et al., 2005) represents the thermal energy deposited in the near-nuclear gas by the AGN, rather than the kinetic power in the outflow; and second, not

Table 4.8: Outflow properties for the maximal velocity case using the v_{05} velocities. Column (2):the trans-auroral fluxes used to calculate the density and reddening values employed in the calculations: T = total, B = broad/intermediate. In the case of F05189–2524, the whole profile was blueshifted with respect to the rest-frame and hence the total flux and broad flux were assumed to be equivalent. Column (3): the v_{05} velocity. Column (4): the calculated mass outflow rate. Column (5): the calculated kinetic power. Column (6): the fraction of AGN bolometric luminosity contained within the outflow ($\dot{E}/L_{bol}$)

Object name IRAS (1)	Comp. T/B (2)	v_{05} km s^{-1} (3)	$\dot{M}$ M$_\odot$ yr^{-1} (4)	$\dot{E}$ erg s^{-1} (5)	$\dot{F}$ % (6)
F01004 – 2237	T	-1932±82	$1.0^{+2.2}_{-0.7}$	$(1.2^{+2.9}_{-0.9}) \times 10^{42}$	$0.14^{+0.35}_{-0.10}$
F05189 – 2524	T,B	-1494±58	$0.13^{+0.21}_{-0.09}$	$(9.3^{+17.0}_{-6.5}) \times 10^{40}$	$(2.6^{+4.9}_{-1.8})\times10^{-2}$
F14394 + 5332E	T	-2362±112	$13.2^{+37.4}_{-9.7}$	$(2.3^{+7.5}_{-1.8}) \times 10^{43}$	$2.6^{+8.6}_{-2.0}$
	B	”	$3.4^{+13.8}_{-3.0}$	$(6.0^{+27.4}_{-5.4}) \times 10^{42}$	$0.66^{+3.12}_{-0.60}$
F17044 + 6720	T	-1992±136	$1.2^{+3.8}_{-0.8}$	$(1.5^{+5.7}_{-1.0}) \times 10^{42}$	$0.42^{+1.69}_{-0.30}$
F17179 + 5444	T	-1539±105	$20.1^{+72.9}_{-14.9}$	$(1.5^{+6.5}_{-1.2}) \times 10^{43}$	$2.5^{+10.7}_{-1.9}$
F23060 + 0505	T	-1330±104	$2.2^{+8.1}_{-1.7}$	$(1.2^{+5.5}_{-1.0}) \times 10^{42}$	$(2.7^{+13.2}_{-2.2})\times10^{-2}$
F23233 + 2817	T	-1189±49	>0.11	>4.7 × 10^{40}	>9.5×10^{-2}
F23389 + 0303N[a]	T	-2126±67	>3.3	>4.4 × 10^{42}	>0.18
	B	”	>2.3	>3.2 × 10^{42}	>0.13
F23389 + 0303N[b]	T	-2126±67	$14.9^{+16.0}_{-7.3}$	$(2.1^{+2.6}_{-1.1}) \times 10^{43}$	$0.91^{+1.13}_{-0.48}$
	B	”	$10.4^{+11.1}_{-5.1}$	$(1.5^{+1.8}_{-0.8}) \times 10^{43}$	$0.63^{+0.79}_{-0.33}$

[a] These estimates were made using the upper limit on the outflow radius from the WHT/ISIS spectrum.

[b] These estimates were made using the radius estimate of the radio lobes (R = 415 pc) as a proxy for the outflow radius, taken from Nagar et al. (2003). This assumes that the outflows are jet-driven.

all of the kinetic power associated with an inner (e.g. accretion disk) wind generated by AGN may be transmitted to the cooler, larger-scale outflows that are observed in optical emission lines, due to radiative cooling, work against gravity and external pressure as the outflows expand. Indeed, some recent theoretical studies suggest that as little as 10% of the nuclear wind powers (or ∼0.5% L_{bol}) are transmitted to the large-scale outflows (Richings & Faucher-Giguère, 2018a). This is consistent with the direct observational comparisons that have been made between the kinetic powers of the inner high-ionisation wind and outer molecular outflow in the case of the ULIRG F11119+3257 (Tombesi et al., 2015; Veilleux et al., 2017). Such a low coupling efficiency is also consistent with the multi-stage outflow model of Hopkins & Elvis (2010). Therefore, the coupling efficiencies for the warm outflows presented here ($0.03 < \dot{F} < 2.5$ %) are in line with some of the most recent theoretical predictions.

4.6 Comparison to other outflow studies

4.6.1 Warm outflows

Astronomers have been attempting to measure the mass outflow rates and kinetic powers of warm outflows for over a decade. One of the motivations for the QUADROS project was the large inconsistencies between the results of various studies in the literature, due to differing methods, assumptions and predominantly a lack of knowledge about the radii and electron densities of the outflows. In this section, the results of the QUADROS project, obtained using the most accurate radii and density measurements available, are compared to a selection of these studies.

Table 4.9 compares the radii, mass outflow rates and kinetic powers of the QUADROS project (Rose et al., 2018; Tadhunter et al., 2018; Spence et al., 2018) with those deduced for AGN outflows by other groups using emission line data over the last 10 years. Instantly noticeable is the large range of values reported by the 10 studies. The outflow radii range from just 0.05 kpc to more than 10 kpc; the mass outflow rates range from 0.06 to over 20000 $M_{\odot}yr^{-1}$; and the kinetic powers range from $10^{37.7}$ to $10^{45.8}$ erg s^{-1} – over 8 orders of magnitude.

Considering the outflow radii, the QUADROS project calculated these for the nuclear regions through a combination of long-slit spectra and narrow-band imaging techniques, using the broad, blueshifted components of the [OIII]λ5007 emission line. The outflow radii, when corrected for the seeing, were found to be less than 1.5 kpc for the entire sample (with the exception of Mrk 273, however this object was not analysed in the same way – see Chapter 3). These extents are comparable to those found by the studies of Carniani et al. 2015 (C15) for a sample of 6 Type II quasars at high-redshift and Villar-Martín et al. 2016 (VM16) for a sample of 15 low redshift type II AGN. These studies report $R_{out} < 3.5$ kpc for the entirety of their samples. C15 and VM16 used spectro-astrometry on Integral Field Unit (IFU) and long-slit data, respectively – a technique which is less sensitive to seeing effects. Furthermore, Karouzos et al. (2016) used spatially resolved IFU measurements of a sample of 6 type II AGN and found outflow radii in the range $1.3 < R_{out} < 2.1$ kpc.

In comparison, Harrison et al. (2012, 2014), Liu et al. (2013) and McElroy et al. (2015) claim to detect outflows with radii up to 15 kpc, based on IFU data. Outflows of these extents would have been easily resolved in the QUADROS long-slit data, and it is strange that in a representative sample of ULIRGs containing optical AGN, only compact outflows were detected. A possible explanation for this is that the above IFU studies failed to properly account for the seeing. Indeed, the circular morphology of the outflow regions, and surprisingly flat FWHM and Δv variations with radius found by these authors, would be consistent with contamination from the seeing disc. In addition, Villar-Martín et al. (2016) show that, due to the large contrast in surface brightness between the central cores and the extended emission-line gas, the central emission can dominate even out to ∼10 times the FWHM of the seeing disc. This is especially critical for highly-luminous and/or high-redshift sources, such as those in the samples of the above studies. Furthermore, Husemann et al. (2016b) re-analysed the sample of Liu et al. (2013) and showed that beam-smearing could explain the apparent kpc-scale outflows observed. Therefore it is likely that the extended outflows reported in previous studies are, in fact, unresolved compared to the seeing and should be considered upper limits, rather than confirmed radii. Similarly, Perna et al. (2015) and Bischetti et al. (2017) assume radii of 11 and 7 kpc for their calculations, respectively, based on the extent of their detected [OIII] emission showing complex kinematics. Without carefully taking into account contamination by the seeing disc, these radii are likely unresolved and should also be considered upper limits.

By far the largest discrepancies, however, are in the calculated mass outflow rates and kinetic powers of the outflows. These vary over 8 orders of magnitude between the various studies. Referring to equations 4.4 and 4.5, the two most important parameters in calculating these values are the electron density, n_e, and outflow velocity, v_{out}.

Different studies have made varying assumptions on how v_{out} is determined from the emission-line profiles. The two scenarios explored in the QUADROS project are using (a) the mean shift of the emission-line component relative to the rest frame, which does not account for projection effects, and (b) the extreme 5^{th} percentile of the broad wing, i.e. the maximum velocity of the blue-shifted, expanding gas, which takes projection effects into account. However, even under this maximal velocity case, the mass outflow rates and kinetic powers deduced from the QUADROS analyses are relatively modest compared to other studies ($\dot{M} \leq 20\ \mathrm{M}_{\odot}\mathrm{yr}^{-1}$; $\dot{E} \leq 43.4$ erg s^{-1}).

This suggests that the largest factors in these discrepancies are the electron densities and reddenings of the emitting clouds. As discussed previously, both of these quantities are difficult to measure using traditional emission-line ratios, and have been poorly constrained in previous studies. For example, the large ranges in potential mass outflow rates and kinetic powers presented by Rodríguez Zaurín et al. (2013) arise, as they clearly state, from degeneracies in fitting the broad components of the [SII]$\lambda\lambda$6716,6731 blend – used to determine the density – and uncertainty of the reddening corrections applied to the Hβ luminosities – used to determine the gas masses, along with uncertain radii. Each parameter adds orders of magnitude uncertainty to the calculations.

Examining those studies which calculate orders of magnitude higher mass outflow rates and kinetic powers using a similar technique to this work, the typical assumed electron density is low, generally $n_e \sim 100$ cm^{-3} (e.g. Liu et al., 2013; Harrison et al., 2014; McElroy et al., 2015). This is below the lower boundary of the results for the e-QUADROS sample based on the trans-auroral line ratios, in which the electron densities for the broad, outflowing components were found to be typically 1 – 2 orders of magnitude higher ($200 \lesssim n_e \lesssim 56000$ cm^{-3}, median $n_e \sim 4500$ cm^{-3}). Indeed, the study which provides mass outflow rates which are most consistent with these results – Villar-Martín et al. (2016) – assumes an electron density of 1000 cm^{-3} for their calculations. Clearly, then, it is vital to have relatively accurate estimates of the electron densities of these outflows before calculating their mass outflow rates and kinetic powers. Any calculations made otherwise should be considered as conservative limits.

4.6.2 Neutral and molecular outflows

It is also informative to compare the mass outflow rates and kinetic powers deduced for the warm ionised outflow phase, to those of the colder neutral and molecular phases. Estimates for the neutral and molecular outflows of five of the ULIRGs in the e-QUADROS sample were available in the literature. These values are shown in Table 4.10.

Rupke et al. (2005c) estimated the properties of the neutral outflows in F05189–2524, F13451–1232 and F23389+0303N based on the NaID absorption line. An additional estimate for the neutral mass outflow rate of F13451–1232, determined using the HI 21cm line, was provided by Morganti et al. (2013). The neutral and ionised mass outflow rates are comparable in the case of F13451–1232, however the estimated neutral mass outflow rates are significantly higher for F05189–2524 and F23389+0303N – $> 5\times$ and $\sim 900\times$, respectively. The kinetic power in the neutral outflow, on the other hand, is two orders of magnitude greater than that of the ionised outflow in the case of F05189–2524; ~ 2 orders of magnitude lower in the case of F13451–1232, and comparable in the case of F23389+0303N.

Estimates for the molecular mass outflow rates in F05189–2524, F14378–3651 and F23060+0505 were provided by González-Alfonso et al. (2017) and Cicone et al. (2014). In all cases the molecular mass outflow rates are more than two orders of magnitude greater than those of the ionised outflows. González-Alfonso et al. (2017) also provided estimates for the kinetic powers of the molecular outflow for F05189–2524 and F14378–3651. In the former case, the molecular kinetic power is two orders of magnitude greater than that of the ionised outflow, and comparable with the kinetic power of the neutral outflow. In the latter case, the kinetic power measured for the molecular outflow is two orders of magnitude higher than the lower limit derived for the ionised outflow.

The larger mass outflow rates and kinetic powers for the cooler gas components are consistent with the idea that the gas has been accelerated in fast shocks, with the neutral and molecular gas then accumulating as the warm gas cools behind the shock fronts (Tadhunter et al., 2014; Zubovas & King, 2014; Morganti, 2015; Richings & Faucher-Giguère, 2018a).

Table 4.9: Comparison between the outflow properties deduced in various recent studies of warm, emission-line outflows in luminous AGN.

Study	Sample	N_{obj}	R_{out} (kpc)	$\dot{M}$ ($\mathrm{M_{\odot} yr^{-1}}$)	$\log(\dot{E})$ (erg $\mathrm{s^{-1}}$)	Method
(1)	(2)	(3)	(4)	(5)	(6)	(7)
This study	ULIRGs, $z < 0.2$, with optical AGN	8	0.08 – 1.5	0.06 – 6	40.3 – 42.6	mean v_{out}
			“ “	0.1 – 20	41.0 – 43.4	maximal v_{out}
Rose et al. (2018)	ULIRGs, $z < 0.15$, with optical AGN	9	0.05 – 1.2	0.004 – 3	38.7 – 42.2	mean v_{out}
			“ “	0.07 – 11	39.8 – 42.9	maximal v_{out}
Harrison et al. (2012)	ULIRGs, $1.4 < z < 3.4$, with radio AGN	8	4 – 15	–	43.9 – 45.5	energy conserving bubble
Liu et al. (2013)	Type II quasars, $z \sim 0.5$	11	> 10	2200 – 19000	44.6 – 45.5	clouds embedded in wind
Harrison et al. (2014)	Type II AGN, $z < 0.2$	16	1.5 – 4.3	3 – 70	41.5 – 43.5	similar to this study
			6	9000 – 23000	44.8 – 45.8	energy conserving bubble
Carniani et al. (2015)	Type II quasars, $z \sim 2.4$	6	0.4 – 1.9	10 – 700	–	conical outflow
Perna et al. (2015)	Type II quasars, $z \sim 2.4$	2	11	500 – 550	44.6 – 44.8	conical outflow
McElroy et al. (2015)	Type II quasars, $z < 0.11$	11	1.6 – 8.3	370 – 2700	42.7 – 44.3	similar to this study
Villar Martín et al. (2016)	Type II AGN, $0.3 < z < 0.6$	15	0.12 – 3.5	0.1 – 114	37.7 – 44.1	similar to this study
Bischetti et al. (2017)	Hyper-luminous quasars, $z \sim 2.5 – 3.5$	5	7	1700 – 7700	45.0 – 46.1	similar to this study

Table 4.10: A comparison between the ionised, neutral and molecular outflow phases, where estimates are available for the e-QUADROS sample. The sub-scripts are as follows: I = ionised; N = neutral; M = molecular. The measurements for the ionised outflows are taken from this work and Rose et al. (2018). The references for the neutral and molecular outflow measurements are denoted by the super-script letters.

Object name IRAS (1)	$\dot{M}_I$ $\mathrm{M_\odot yr^{-1}}$ (2)	$\dot{M}_N$ $\mathrm{M_\odot yr^{-1}}$ (3)	$\dot{M}_M$ $\mathrm{M_\odot yr^{-1}}$ (4)	$\log(\dot{E}_I)$ erg $\mathrm{s^{-1}}$ (5)	$\log(\dot{E}_N)$ erg $\mathrm{s^{-1}}$ (6)	$\log(\dot{E}_M)$ erg $\mathrm{s^{-1}}$ (7)
F05189 – 2524	$0.13^{+0.21}_{-0.09}$	117^a	$270^{+22\ b}_{-130}$	$40.97^{+0.45}_{-0.52}$	43.08^a	$43.2^{+0.1\ b}_{-0.2}$
F13451 – 1232W	$10.5^{+2.8}_{-2.3}$	7.6^a $16\text{–}29^c$	–	43.34±0.11	41.67^a	–
F14378 – 3651	>0.082	–	$180^{+180\ b}_{-33}$	>40.76	–	$43.1\pm0.2\ ^b$
F23060 + 0505	$2.2^{+8.1}_{-1.7}$	–	1500^d	$42.08^{+0.74}_{-0.78}$	–	–
F23389 + 0303N	$10.4^{+11.1}_{-5.1}$	$>49^a$	–	43.2±0.3	$>42.4^a$	–

[a] Rupke et al. (2005c)
[b] González-Alfonso et al. (2017)
[c] Morganti et al. (2013)
[d] Cicone et al. (2014)

4.7 Links between the warm outflow properties and AGN properties

Some observational studies have found evidence for correlations between the properties of the outflows and those of the AGN. For example, Fiore et al. (2017) found evidence of strong linear correlations between the mass outflow rates and AGN bolometric luminosities for both molecular and ionised outflows. Similarly, Cicone et al. (2014) showed evidence for a linear correlation between L_{bol} and the kinetic powers of molecular outflows. Given the assumption that the warm outflows observed in the e-QUADROS sample are AGN-driven (see §4.5.3), this has also been examined using the data presented in this chapter.

In Figure 4.15 the outflow kinetic power ($\dot{E}$) for the maximal v_{05} velocity case is plotted against the bolometric luminosity of the AGN for the full QUADROS sample. The red circles represent the results from Spence et al. (2018) and the blue stars represent the results of Rose et al. (2018). The best available estimate of the kinetic power was used for each object[3] and the most appropriate bolometric luminosity correction was taken as discussed in §4.5.3 in this chapter, and §3.3 in Rose et al. (2018).

Over-plotted are three lines corresponding to the fraction of the AGN luminosity contained in the kinetic power of the outflow ($\dot{F}$): 100% (solid), 5% (dashed) and 1% (dotted). Although the majority of the sample fall well below the 1% line, a significant number (∼35%) of the e-QUADROS ULIRGs fall close to, or above it. For reference, the results of Fiore et al. (2017) for 51 AGN are also over-plotted, for which they have claimed a significant correlation is present between L_{bol} and $\dot{E}$. Considering only the

---

[3] For this and the subsequent plots, the estimates of the outflow properties derived from the broad component fluxes of the trans-auroral emission lines were used where available. For the objects where the individual kinematic components were unresolved, the estimates derived from the total emission line fluxes were used.

e-QUADROS results, for which the outflow parameters have been measured in a precise and consistent manner, no significant linear correlation is found between the kinetic powers of the outflows and the AGN bolometric luminosities – a p-value of 0.47 means the null hypothesis that the two sets of data are uncorrelated cannot be rejected.[4] However, this apparent difference from the results of Fiore et al. (2017) is perhaps not surprising, given the small range of AGN luminosity covered by the e-QUADROS sample, and the relatively high degree of scatter.

Potential linear correlations between the AGN bolometric luminosities and other outflow properties such as the outflow velocities, radii and mass outflow rates, were also considered. These are plotted in Figure 4.16. In all three plots, the red circles, blue stars and grey crosses represent the results from Spence et al. (2018), Rose et al. (2018) and Fiore et al. (2017) respectively. No statistically significant correlation between L_{bol} and outflow velocity is found within the QUADROS sample (p = 0.49). Furthermore, little evidence is seen to support a significant correlation between L_{bol} and either $\dot{M}$ (p = 0.11) or radius (p = 0.76). Again, this lack of linear correlation could perhaps be explained by the high scatter and narrow luminosity range.

Interestingly, the e-QUADROS results fall within the scatter of the lower end of the $\dot{E}$ and $\dot{M}$ correlations of Fiore et al. (2017) shown in Figures 4.15 and 4.16c. However, this apparent agreement may be misleading: the lower outflow velocities[5] (see Figure 4.16a) and larger outflow radii (see Figure 4.16b) found by Fiore et al. (2017) may compensate for the lower gas densities (and hence larger total gas masses) assumed in their study.

---

[4] When calculating the Spearman rank-order correlation statistics, the upper/lower limits were included as if they were measured values.

[5] Note that, instead of v_{05}, Fiore et al. (2017) used the velocity of the peak of the broad component minus 2σ as the outflow velocity.

However, perhaps a lack of correlation between the AGN luminosities and outflow properties is to be expected. Zubovas (2018) argued that because AGN duty cycles are shorter than the dynamical times of the outflows, any observed outflows greater than around 0.1 kpc in extent are unlikely to have been originally driven by the current phase of AGN activity. Therefore, there is no reason to expect that the currently observed AGN luminosities should correlate with the observed outflow properties, and a high degree of intrinsic scatter is to be expected. The e-QUADROS results appear to be consistent with this conclusion.

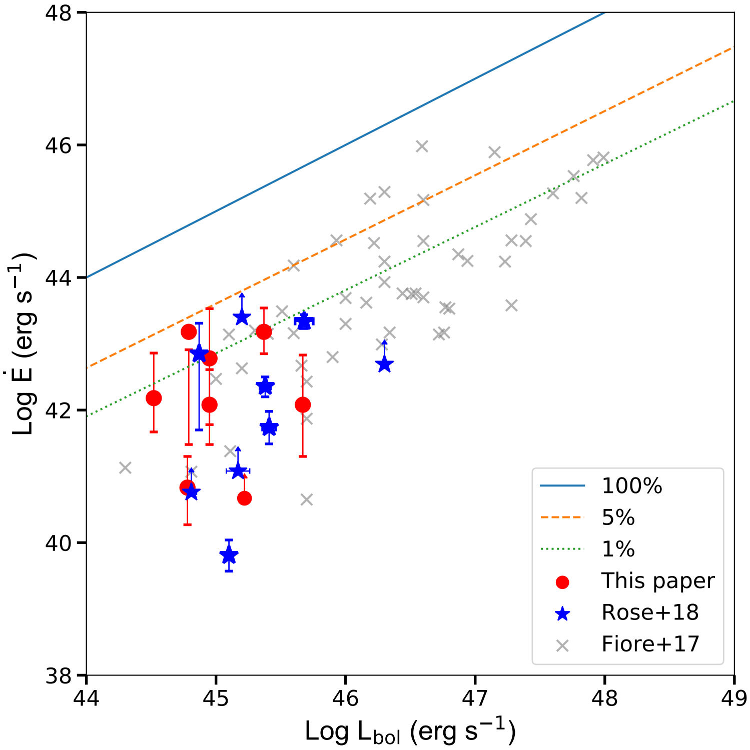

Figure 4.15: Outflow kinetic power vs. AGN bolometric luminosity for the maximal v_{05} velocity case. The bolometric luminosities were determined using the total emission line flux of [OIII]λ5007. The kinetic powers of the outflow were determined using the broad components of the Hβ emission line and the best available density estimates (i.e. using the broad trans-auroral fluxes where possible). The red circles and blue stars represent the results from this work and Rose et al. (2018) respectively.The over-plotted lines represent $\dot{F}$ = 100% (solid), 5% (dashed) and 1% (dotted). Also over-plotted for comparison are the warm, emission-line results of Fiore et al. (2017) for 51 AGN (grey crosses). Note that caution must be taken when directly comparing the e-QUADROS and Fiore et al. (2017) results due to the different methodologies employed for calculation of the outflow parameters. Figure from Spence et al. (2018).

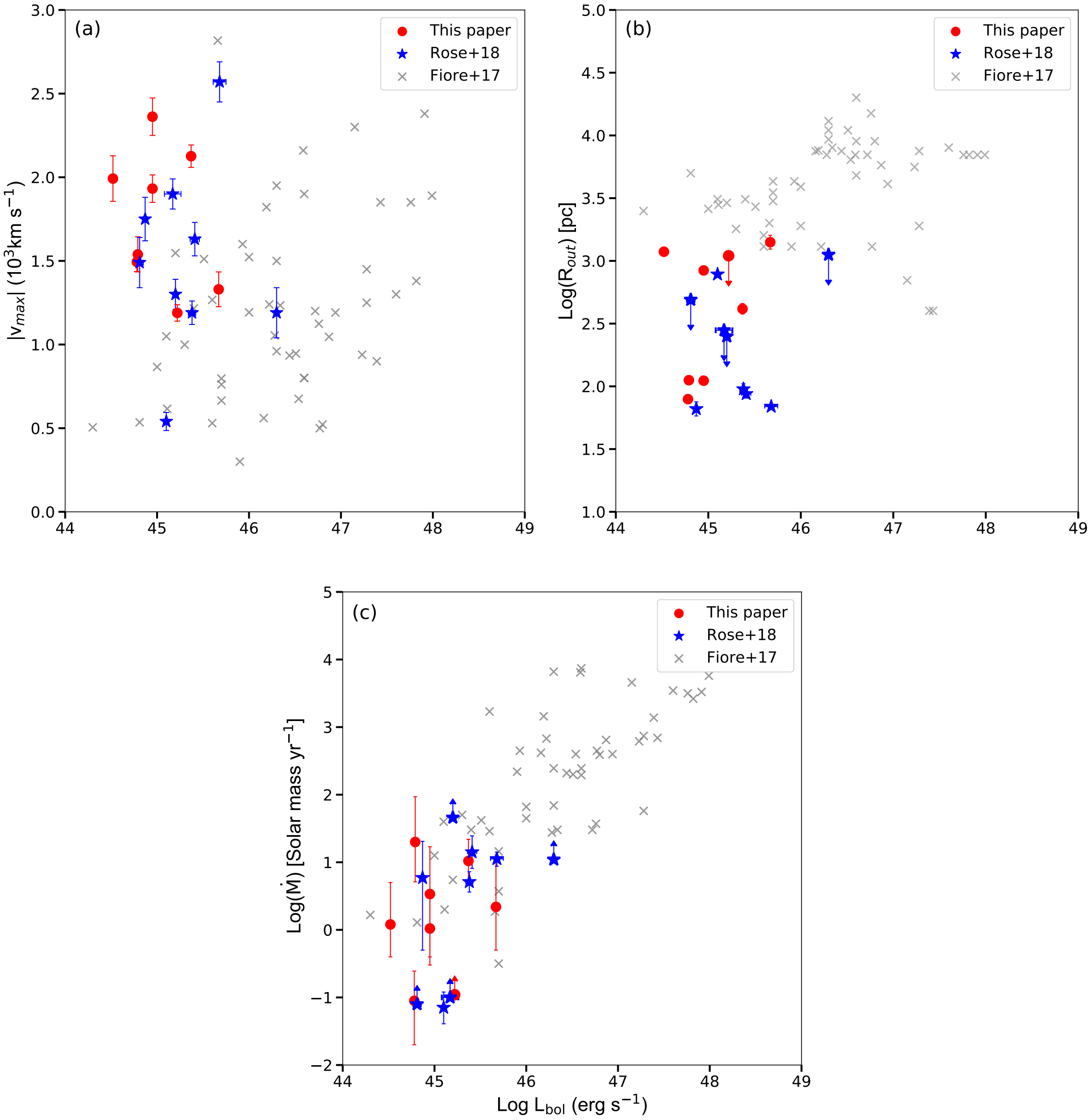

Figure 4.16: Plots of the outflow properties against log(L_{bol}) for the full QUADROS sample: (a) v_{05}; (b) log(R_{out}); (c) log($\dot{M}$). The points are as in Figure 9. Figure from Spence et al. (2018).

4.8 Chapter conclusions

This chapter presented the results of a study of warm outflows in 8 nearby ULIRGs with WHT/ISIS (Spence et al., 2018, QUADROS III), which strongly reinforce those obtained for 9 ULIRGs using VLT/Xshooter by (Rose et al., 2018, QUADROS I). After considering the effects of seeing, evidence that the ionised outflow regions are compact ($0.07 < R_{out} < 1.5$ kpc, median $R_{out} \sim 0.8$ kpc) was provided. In addition, it was found that the outflows can suffer a significant degree of reddening ($0 < E(B-V) < 1$, median E(B-V) $\sim$ 0.5), and have high densities ($2.5 < \log n_e(\mathrm{cm}^{-3}) < 4.5$, median $\log n_e(\mathrm{cm}^{-3}) \sim 3.1$).

The resultant mass outflow rates ($0.1 < \dot{M} < 20$ $\mathrm{M}_\odot$ yr^{-1}, median $\dot{M} \sim 2$ $\mathrm{M}_\odot$ yr^{-1}) and coupling efficiencies ($0.03 < \dot{F} < 2.5\%$, median $\dot{F} \sim 0.4\%$) are relatively modest, even under maximal velocity (v_{05}) assumptions for the outflow velocities. These values are only consistent with theoretical expectations if it is assumed that the inner winds transmit a modest fraction ($\sim$10%) of their energy to the large-scale outflows.

Considering the QUADROS sample as a whole, no evidence was found to indicate that the properties of the outflows are strongly correlated with the AGN bolometric luminosities. This lack of correlation may be due in part to the relatively narrow range in L_{bol} covered by the sample, coupled with the uncertainties in the L_{bol} values themselves. However, given that the key properties of the outflows (radii, densities, reddenings) have been accurately measured, it is more likely that there is a high degree of intrinsic scatter ($\sim$2 – 3 orders of magnitude) in $\dot{M}$, $\dot{E}$ and $\dot{F}$ for a given L_{bol}. This scatter could be due to different efficiencies in the coupling between the inner winds and the larger-scale ISM, perhaps related to different circumnuclear environments. Alternatively, it might reflect large-scale variability in the radiative outputs.

Indeed, in the case of F01004-2237 direct evidence for just such variability has been detected: this object has a high ionisation narrow-line spectrum characteristic of AGN, yet lacks a type I AGN BLR component, despite the fact that the recent detection of a TDE event in its nucleus demonstrates that the line of sight to its central supermassive black hole is relatively unobscured (Tadhunter et al., 2017).

Ultimately, the results of the QUADROS project further emphasise the importance of determining accurate radii, electron densities and reddening values for AGN-driven outflows. The dearth of reliable measurements of these parameters is likely to have been at least partially responsible for the lack of consistency between the results and conclusions of the various studies of AGN outflows in the past. This study, along with the rest of the QUADROS series, contributes the most accurate measurements to date of the properties of the warm nuclear outflows observed in the population of local ULIRGs, and helps constrain these quantities going forward. However, to gain a complete multi-phase understanding of the importance of AGN-driven outflows to galaxy evolution, this level of accuracy (and better) must also be achieved by future studies.

This chapter has provided a detailed investigation into the properties of the nuclear outflows, using the trans-auroral line ratios to derive the densities of the outflow regions. The next chapter examines the origin of these emission lines and validates the technique. It is then noted that, similarly to Mrk 273, many of the ULIRGs also show evidence for extended emission-line structures, stretching to tens of kiloparsecs from the nuclear regions. While some studies, which observe similarly extended gas, interpret this as evidence for galaxy-scale outflows, the results of Chapter 4 suggest that the AGN-driven outflows are ubiquitously compact, concentrated within a radius of a few kiloparsecs. Chapter 6 analyses the properties of these extended emission-line structures and investigates the hypothesis that they represent the outer parts of the AGN-driven outflows. The maximum possible contributions of the extended emission line structures to the overall mass outflow rates and kinetic powers are also estimated.

Chapter 5

Trans-auroral [SII] and [OII] as density diagnostics

5.1 Declaration

Some work presented in this chapter was published in Spence et al. (2018), *"Quantifying the AGN-driven outflows in ULIRGS III: measurements of the radii and kinetic powers of 8 near-nuclear outflows"*, Monthly Notices of the Royal Astronomical Society (MNRAS), in May 2018. This chapter expands on these results. Unless stated otherwise, the text, figures, analysis and interpretations presented are my own work.

5.2 Chapter introduction

The outflow velocities and emission-line luminosities presented in Chapter 4 were calculated using the [OIII] and Balmer lines. These values were then combined with density and reddening estimates derived from the trans-auroral emission line ratios ([OII]λ3727 and [SII]λ6725 nebular blends with the [OII]λ7330 and [SII]λ4073 trans-auroral blends) to calculate the mass outflow rates and kinetic powers of the AGN-driven outflows. Therefore, in order for these calculations to be valid, it is important that all of these lines are emitted by the same gas clouds. Due to this, an argument against the use of the trans-auroral lines to measure the densities of the outflows can be made, in that the higher critical density species ([SII]$\lambda\lambda$4068,4076 and [OII]$\lambda\lambda$7319,7330) may originate from dense clouds within a lower density outflow, whereas the other key lines (e.g. [OIII], Balmer) could instead originate from the low density gas (Sun et al., 2017).

In addition, because the trans-auroral lines arise from higher energy levels than the nebular lines, the trans-auroral line ratios used in Chapter 4 are potentially temperature-sensitive and hence might show a dependence on elemental abundances or ionisation mechanism. It is therefore important, in order to justify the use of these lines as a density diagnostic, to investigate the effects this may have on the density diagnostic grids used by Spence et al. (2018) and Rose et al. (2018).

Finally, the implications of a potential lower density component to the outflow which could contain the bulk of the mass and kinetic power of the outflow, but contribute little to the flux, are discussed.

5.3 Trans-auroral lines as a density diagnostic

Both singly-ionised [OII] and [SII] have three electrons in their outer energy shells. The energy level diagram for the ground configuration of these ions is shown in Figure 5.1. As indicated on the diagram, the nebular [OII]$\lambda\lambda 3726, 3729$ and [SII]$\lambda\lambda 6716, 6731$ doublets are emitted when electrons transition between the ^{2}D and ^{4}S levels. The upper levels have very similar excitation energies, so their relative intensities are largely insensitive to temperature. The upper levels do, however, have different transition probabilities meaning that the relative intensities will vary with density. However, the small wavelength separation between the individual components of the doublets can cause significant degeneracies when modelling the lines, leading to large uncertainties on the line ratios and subsequently the electron densities. In addition, due to their relatively low critical densities ($n_e \sim 10^3$ cm^{-3}), the [SII] and [OII] nebular doublets are suppressed in high density regions by collisional de-excitation and are therefore sensitive to only a narrow range of electron densities ($10^2 < n_e < 10^{3.5}$ cm^{-3}). At lower densities the intensity ratios are given by the ratio of the statistical weights of the transitions (∼1.5), whereas at higher densities the levels become saturated and the intensity ratio is determined by the Boltzmann distribution (∼0.4). This is indicated in Figure 5.2.

The alternative approach used in Spence et al. (2018) and Rose et al. (2018) is to use the ratios of the higher critical density trans-auroral transitions to the nebular transitions. With reference to Figure 5.1, the trans-auroral [OII]$\lambda\lambda$7319,7330 lines are emitted when electrons transition between the ^{2}P and ^{2}D levels. The trans-auroral [SII]$\lambda\lambda$4068,4076 lines are emitted when electrons transition from the ^{2}P to the ^{4}S ground state. The upper ^{2}P levels have higher critical densities than the ^{2}D levels from which the nebular lines originate. Consequently, when the electron density of the gas increases, the relative intensities of the trans-auroral emission lines increase with respect to the lower critical density nebular emission lines. These ratios are sensitive to a larger range of electron densities than the nebular doublets alone ($10^2 < n_e < 10^{6.5}$ cm^{-3}, Appenzeller & Oestreicher 1988), and can simultaneously measure both density and reddening due to the larger wavelength separation. Furthermore, this method requires only the total fluxes of the trans-auroral and nebular doublets rather than the individual doublet components, significantly reducing uncertainties in the emission-line fits and calculated densities and reddenings.

The trans-auroral density diagnostic diagram, pioneered by Holt et al.

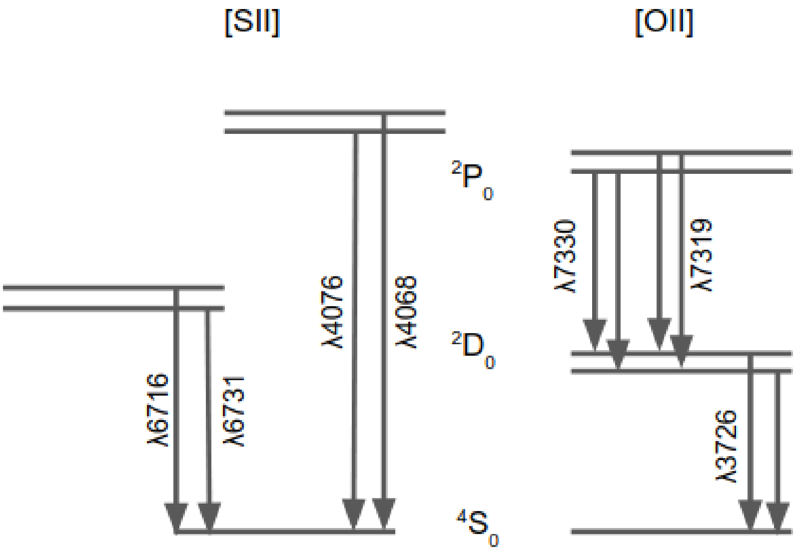

Figure 5.1: Energy-level diagrams of the $2p^3$ ground configuration of [OII] and $3p^3$ ground configuration of [SII].

(2011) and used by Rose et al. (2018) and Spence et al. (2018) to calculate accurate densities and E(B-V) values for the nuclear outflows in the e-QUADROS sample, is shown in Chapter 4, Figures 4.12 and 4.13. The zero-reddening grid-line was generated for radiation bounded, solar metallicity gas, fixing the spectral index of the ionising continuum to $\alpha = -1.5$ and the ionisation parameter to a value of $U = 0.005$. The strength of the ionising continuum effectively determines the temperature of the nebulae. Whilst the ^{2}P levels have higher energies than the ^{2}D levels – meaning that the trans-auroral ratios are also sensitive to temperature – Holt et al. (2011) found that the predicted ratios were not particularly sensitive to the photoionising power-law spectral index or ionization parameter used in the photo-ionisation models (see also Rose et al., 2018). This demonstrates that the electron density is the dominant diagnostic for a given radiation field. The zero-reddening grid-line was then reddened using the Calzetti et al. (2000) reddening law to produce the full diagnostic grid.

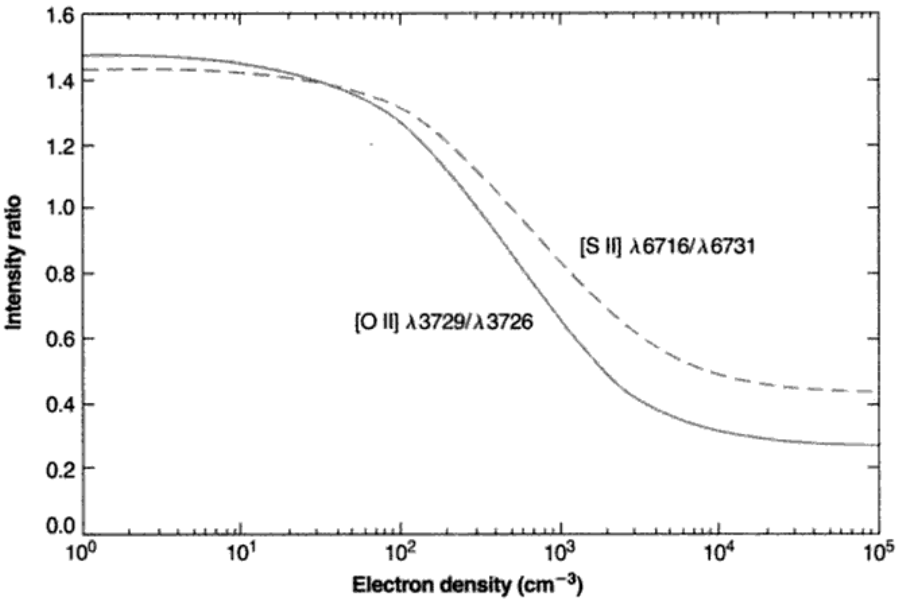

Figure 5.2: Calculated variation of the nebular [OII] (solid) and [SII] (dashed) doublet ratios for an electron temperature of 10^4K, from Osterbrock & Ferland 2006.

5.3.1 Abundance sensitivity

The effect of metal abundances on the trans-auroral diagnostic ratios, however, has not yet been explored. The presence of heavy elements affects the ability of the gas to cool – the higher the metallicity, the more efficient the cooling. Therefore the temperature of the nebula is dependent on the metallicity – lower metallicities permit higher electron temperatures, and vice versa (e.g. Stasińska, 2002). As the relative intensities of the trans-auroral line ratios to the nebular ratios are also sensitive to temperature, due to the large energy gap, it is important to determine, for a given radiation field, the effect that different abundances may have on the position of the diagnostic grid.

To explore this, new grid-lines were generated for the zero-reddening case using CLOUDY v17.00 for half solar, solar, and twice solar abundances. The ionising continuum was defined using the above values for the spectral index and ionisation parameter, for consistency. Figure 5.3 shows the original diagnostic grid published in Spence et al. (2018) (black), overplotted with the newly generated zero-reddening grid-lines for varying abundances (blue). Points of equivalent density have been highlighted with ellipses, in order to indicate the trend with abundance.

One thing to note is that the newly generated zero-reddening solar abundance line deviates from the original line for $\log n_e < 4$ cm^{-3}. This is likely due to the chemical composition tables having been updated between CLOUDY v13 and CLOUDY v17. Nevertheless, the result of interest is the general trend between the location of the predicted ratios and abundance, for a given ionising continuum. For electron densities of 10^4 cm^{-3} and greater, the trans-auroral ratios are largely insensitive to the abundance of the gas. At the lower density end ($\log n_e \leq 3$ cm^{-3}), there appears to be a trend for the TR([OII]) ratio to increase and TR([SII]) ratio to decrease with increased abundance. Therefore, if the abundances of the e-QUADROS outflows were super-solar then the calculated densities would be fractionally higher in Rose et al. (2018) and Spence et al. (2018) than those based on the solar diagnostic diagram. This in turn would lead to lower mass outflow rates and kinetic energies, and only increase the deficit between the observed properties of the AGN-driven outflows and those required by hydrodynamical simulations of major mergers. On the other hand, if the abundances were in fact sub-solar, fractionally lower densities and higher mass outflow rates and kinetic powers would be derived. The BPT analysis of Rodríguez Zaurín et al. (2013) suggests that the former case is more likely for the e-QUADROS ULIRGs.

However, on the whole, the variation caused by assuming different abundances is generally comparable with the size of the error bars on the measured ratios. Therefore, the main results of the QUADROS project (and those presented in Chapter 4) are unlikely to be affected by assuming slightly lower or higher model abundances compared with the actual outflow abundances.

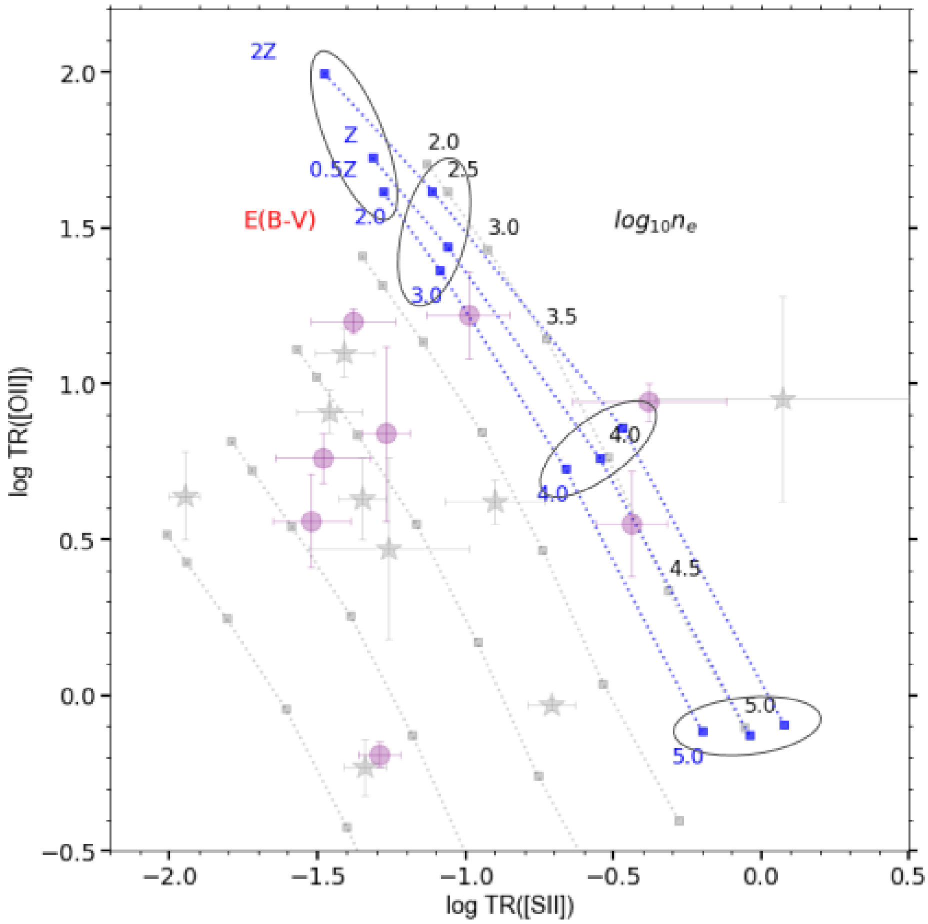

Figure 5.3: The trans-auroral diagnostic diagram from Spence et al. 2018 (black) overplotted with the newly generated grid-lines for abundances of half-solar, solar and twice-solar (blue). Points of equivalent density have been grouped with ellipses, to highlight the trend with abundances.

5.3.2 Shock model comparison

The locations of the nuclear optical emission-line ratios on the BPT diagrams for the e-QUADROS sample are consistent with AGN photo-ionisation being the dominant mechanism (Rodríguez Zaurín et al., 2013). However, there is significant overlap between the AGN photo-ionisation and shock models in many diagnostic diagrams (see Chapters 3 and 6), meaning that both mechanisms can produce similar flux ratios. Furthermore, the temperatures of shock ionised gas are expected to be significantly higher than those of AGN photo-ionised regions (Dopita & Sutherland, 1995; Villar-Martín et al., 1999; Veilleux, 2002). It is therefore important to investigate how the position of the trans-auroral ratios varies when they are generated by shock rather than AGN photo-ionisation models, to account for any possible effects on the densities derived assuming AGN photo-ionisation rather than shock ionisation. To explore this, zero-reddening grid-lines were generated using the shock models of Allen et al. (2008), assuming solar metallicity and a fixed magnetic field strength of 10μG. The pre-shock densities were varied between $0 < \log n_e$ (cm^{-3}) < 3, in order to be comparable with the AGN photo-ionisation densities of $2 < \log n_e$ (cm^{-3}) < 5 assuming a compression factor of 100, and shock velocities of 200, 600 and 1000 km s^{-1}.

The resulting grid-lines are shown in Figure 5.4, again over-plotted onto the original diagnostic grid from Spence et al. (2018). Comparison between the shock and photo-ionisation models is not straightforward, and is dependent on the compression factor. Points of equivalent density have been grouped together by ellipses, assuming a compression factor of 100. A clear result is that the trans-auroral ratios are relatively insensitive to the shock velocity. For the pre-shock gas (denoted *pc*) densities of $\log n_e^{pc}$ (cm^{-3}) < 2, the shock-derived trans-auroral ratios are comparable with those of the AGN photo-ionisation for the assumed compression factor. At the higher density end ($\log n_e^{pc}$ (cm^{-3}) > 2), the two models diverge more significantly. However, few densities measured in the QUADROS project fall significantly above $\log n_e$ (cm^{-3}) $= 4$ (referring to the AGN photo-ionisation grid). Therefore, the results of the QUADROS project are relatively unaffected by the ionisation mechanism of the gas, for the assumed compression factor of 100. Nevertheless, future studies should be aware of this potential issue when dealing with trans-auroral density measurements.

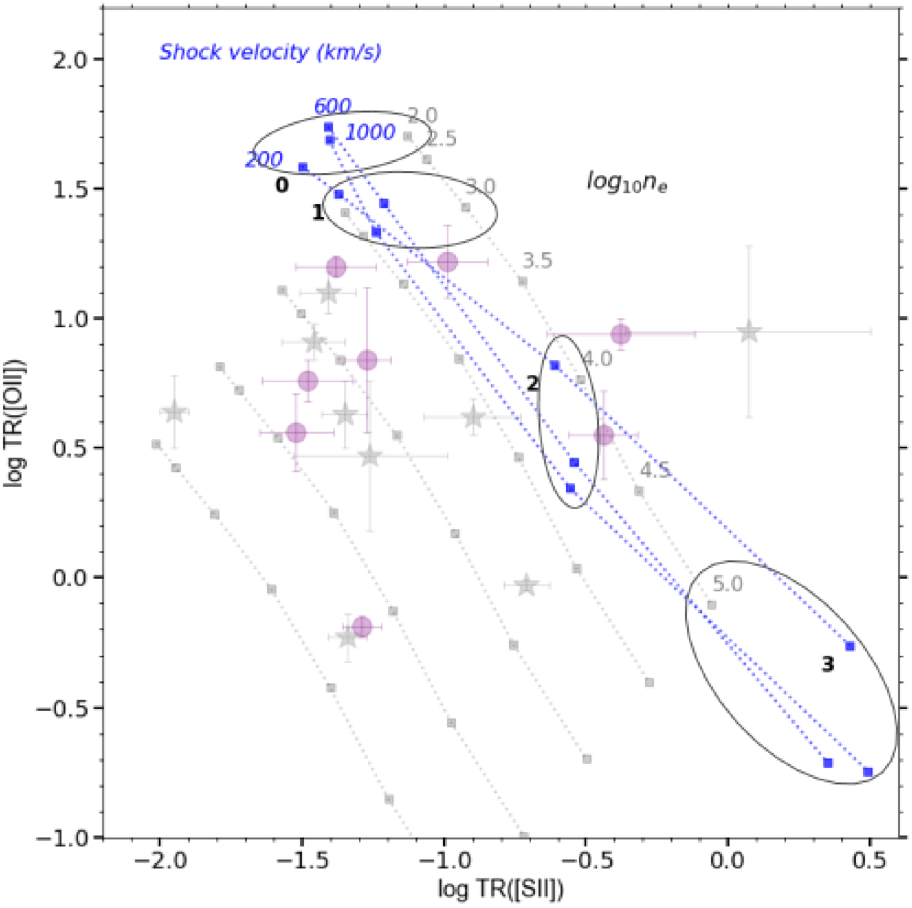

Figure 5.4: The trans-auroral diagnostic diagram from Spence et al. 2018 (black) overplotted with newly generated grid-lines using solar metallicity, dusty, radiation-pressure dominated shock models (Allen et al., 2008) for shock velocities of 200, 600 and 1000 km s^{-1} (blue). The magnetic field strength was set to 10μG. Points of equivalent density – assuming a compression factor of 100 – have been grouped with ellipses, to assist comparison with the AGN photo-ionisation grid.

5.4 Origin of the trans-auroral emission lines

It is also possible for the high critical-density trans-auroral transitions to originate from different gas components than the lower critical-density nebular transitions. If this were the case, then the densities derived in

Rose et al. (2018) and Spence et al. (2018) may not be representative of the outflow as a whole. However, as argued in Rose et al. (2018), any high density clumps would still be expected to radiate strongly in Hβ – which is used to estimate the gas mass – and the electron densities measured from the trans-auroral line ratios remain below the critical density, n_{crit}, of the [OIII]λ5007 line ($n_{crit} = 7 \times 10^5$ cm^{-3}), which is used to determine the outflow kinematics and radii. Therefore, depending on the ionisation level, the high density clumps might also be expected to radiate significant [OIII]λ5007 emission.

5.4.1 AGN photo-ionisation models

To investigate the origin of the key emission lines, theoretical AGN photo-ionised ratios of the high-critical density trans-auroral [OII] and [SII] blends to the [OIII]λ5007 and Hβ lines from a single, radiation bounded, solar abundance cloud were calculated and compared to those observed for the e-QUADROS sample. These models were generated using version 17 of CLOUDY, last described by Ferland et al. (2013). Figure 5.5 plots the following ratios:

$$\log([\mathrm{OII}]/[\mathrm{OIII}]) = \log([\mathrm{OII}]\lambda\lambda7319, 7330/[\mathrm{OIII}]\lambda5007); \tag{5.1}$$

$$\log([\mathrm{SII}]/\mathrm{H}\beta) = \log([\mathrm{SII}]\lambda\lambda4068, 4076)/\mathrm{H}\beta). \tag{5.2}$$

These ratios can be used to test whether the ratios measured from the spectra are consistent with the expected ratios from the photo-ionisation models. If the measured ratios differ significantly from the theoretical values, then the conclusion would be that the trans-auroral lines ([OII], [SII]) do not originate from the same source as the other key diagnostic

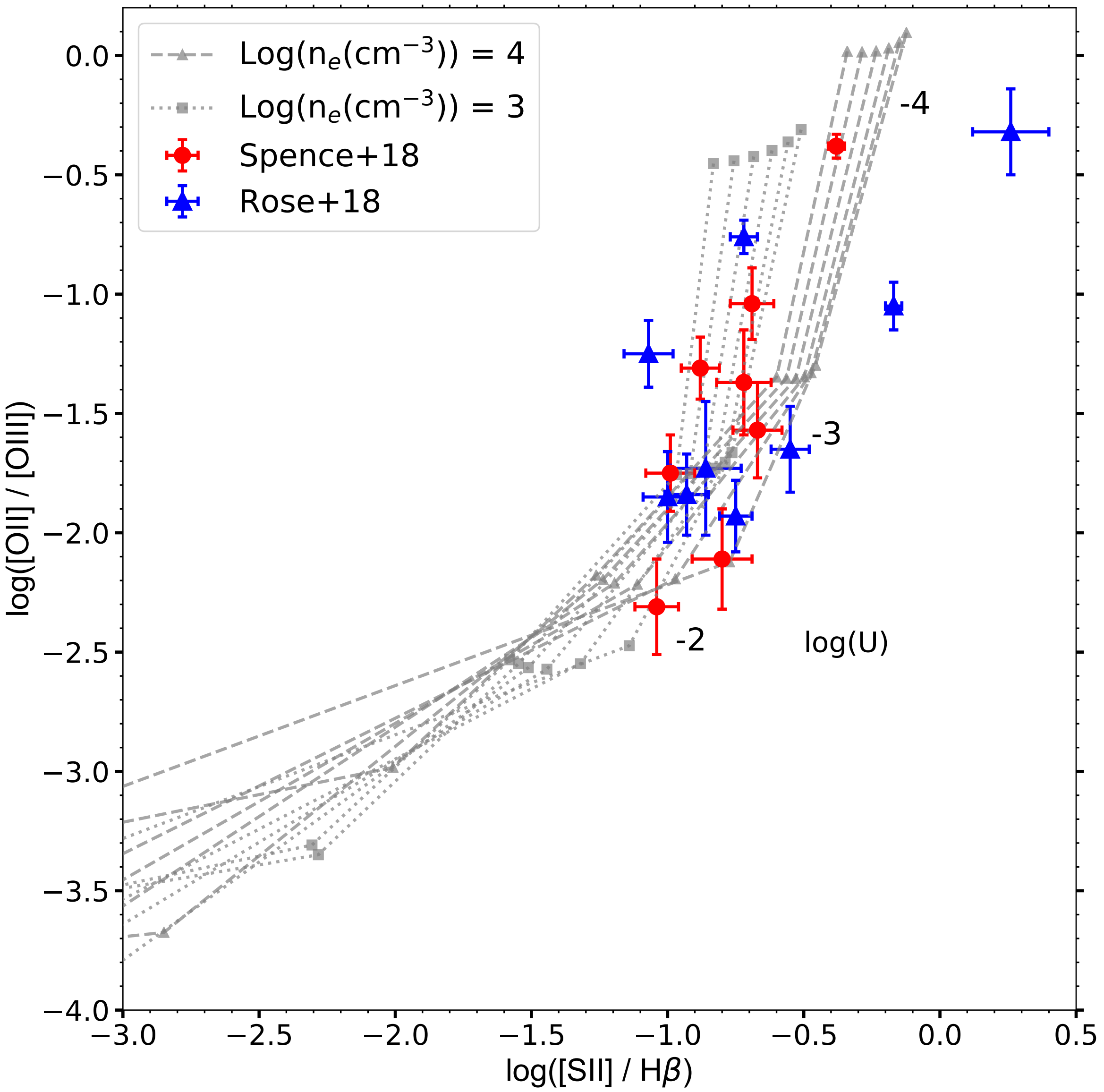

Figure 5.5: Theoretical photo-ionisation grids modelled with CLOUDY for the emission-line flux ratios of log([OII]$\lambda\lambda$7319,7330/[OIII]λ5007) against log([SII]$\lambda\lambda$4068,4076)/Hβ). The dotted lines correspond to a density of 10^3 cm^{-3}. The dashed lines correspond to a density of 10^4 cm^{-3}. The separate lines within these bands correspond to different values of the ionising power-law spectral index in the range -2 $< \alpha <$ -1, and the ionisation parameter, log(U), is indicated by the numbers. Over-plotted are the total flux ratios from Spence et al. 2018 (red circles) and Rose et al. 2018 (blue triangles), respectively.

lines (e.g. [OIII], Hα). In Figure 5.5, the ratios measured from Spence et al. (2018) (red circles) are presented along with those of Rose et al. (2018) (blue triangles) for the e-QUADROS sample, using total emission-line fluxes. Over-plotted as dotted and dashed lines are the theoretical grids generated by CLOUDY for densities of 10^3 cm^{-3} and 10^4 cm^{-3} respectively. The grids vary in ionisation parameter, U, and ionising power-law spectral index, α ($F_\nu \propto \nu^\alpha$), over the respective ranges: -4 <log(U) < -1 and -2 < α < -1, appropriate for AGN ionising radiation fields.

The measured ratios show good consistency with those predicted by the AGN photo-ionisation models. While the displacement between the two grids is not particularly large, the positions of the ULIRGs on the respective grids are consistent with the densities derived from the trans-auroral line-ratio analysis. In particular, all 8 ULIRGs considered in Spence et al. (2018) (red circles) fall in the range of densities expected from the trans-auroral emission line estimates: $10^3 < n_e < 10^4$ cm^{-3}.

66% of the ULIRGs from Rose et al. (2018) (blue triangles) also fall in this range; however in this case the scatter is larger, with three points falling off the grids. The anomalous point to the top right of the grid corresponds to F15462–0450. This object is an un-reddened type I AGN, for which the wing of the broad Hδ emission from this AGN overlaps with the trans-auroral [SII]λ4073 blend, potentially leading to a higher degree of uncertainty in the flux of this blend and the line ratios derived from it. A further object (F13451+1232W) falls to the right of the log n_e (cm^{-3}) = 4 grid, indicating higher densities. However, this is consistent with the fact that this object shows the highest estimated density of the whole e-QUADROS sample (log n_e (cm^{-3}) = 4.5$\pm$0.2). Finally, one object (F14378–3651) falls to the left of the log n_e (cm^{-3}) = 3 grid, consistent with the relatively low density estimated for this object based on the total trans-auroral emission-line fluxes in Rose et al. (2018): log n_e (cm^{-3}) $\sim$

2.

Furthermore, as a consistency check, the ionisation parameter, U, defined as the ratio of ionizing photon flux to the gas density, has been directly estimated for each ULIRG using the following equation:

$$U = \frac{L_{ion}}{c4\pi R_{out}^2 n_e h\nu_{ion}} \tag{5.3}$$

where c is the speed of light, R_{out} is the radius of the outflow, n_e is the electron density of the gas, ν_{ion} is the average ionizing photon frequency (ν_{ion} = 1.02 × 10^{16}Hz for α = -1.5, Robinson et al. 2000) and L_{ion} is the AGN ionizing luminosity. For these estimations, $L_{ion} = 0.56L_{bol}$ is assumed, based on the results of Netzer & Trakhtenbrot (2014) for AGN with non-rotating, 10^7 $M_\odot$ black holes. Using equation (6), and the electron densities derived from the total emission line fluxes, the e-QUADROS ULIRGs should be expected to cover $-1.3 < \log(U) < -3.4$. Given the assumptions, this is consistent with the range of $\log(U)$ covered by the line ratios in Figure 5.5. Note that the assumed black hole mass lies at the low end of the range estimated for ULIRGs (Veilleux et al., 2009), and therefore the values calculated for U may be over-estimated by up to a factor of 10 in some cases. Nevertheless, these results support the idea that the bulk of the flux of all of the diagnostic emission lines originates from the same dense gas structures.

5.4.2 Shock models

For comparison, grids were also generated using the solar abundance shock models of Allen et al. (2008). A significant amount of overlap is present between AGN photo-ionisation models and shock models for the BPT ratios of optical emission lines (see Chapter 3, section 3.4.4), which can make it challenging to determine the dominant ionisation mechanism for the ionised gas. The acceleration mechanism of AGN-driven outflows is still poorly understood, and acceleration due to shocks, radiation pressure or gentle acceleration by a hot, low-density wind have all been proposed (King & Pounds, 2015). Therefore, if it could be established that the outflowing clouds are shock ionised this would also support the idea that they are shock accelerated[1].

Figure 5.6 shows the measured line ratios of Rose et al. (2018) and Spence et al. (2018), over-plotted with the theoretical grids for pure shock models with pre-cursor densities, n_e^{pc}, of 10 cm^{-3} (brown, dashed grid) and 100 cm^{-3} (black, dotted grid). Note that these models do not include emission from the pre-cursor gas itself. These pre-cursor densities were chosen to be consistent with the densities of the AGN photo-ionisation models plotted in Figure 5.5, assuming that if the observed line-emitting clouds are ionised by shocks, then the measured line ratios are produced by the cooling post-shock ionised gas. In this way, the density of the cooling post-shock gas is expected to be a factor of 10–100 greater than the initial pre-shock density due to compression as the gas passes through the shock front (Dopita & Sutherland, 1995).

The shock models are able to explain ∼65% of the measured ratios within one error bar (1σ), and 100% of the data within two error bars (2σ). While the AGN photo-ionisation models provide a better fit to the observed data – which may suggest that the bulk of the fluxes of the key emission lines are produced by AGN photo-ionisation – overall, these results are consistent with the key line fluxes having a common origin.

---

[1] On the other hand, if they proved to be AGN photo-ionised this would not rule out shock acceleration, since the gas could have first been shock accelerated, cooled down, then photo-ionised by the AGN.

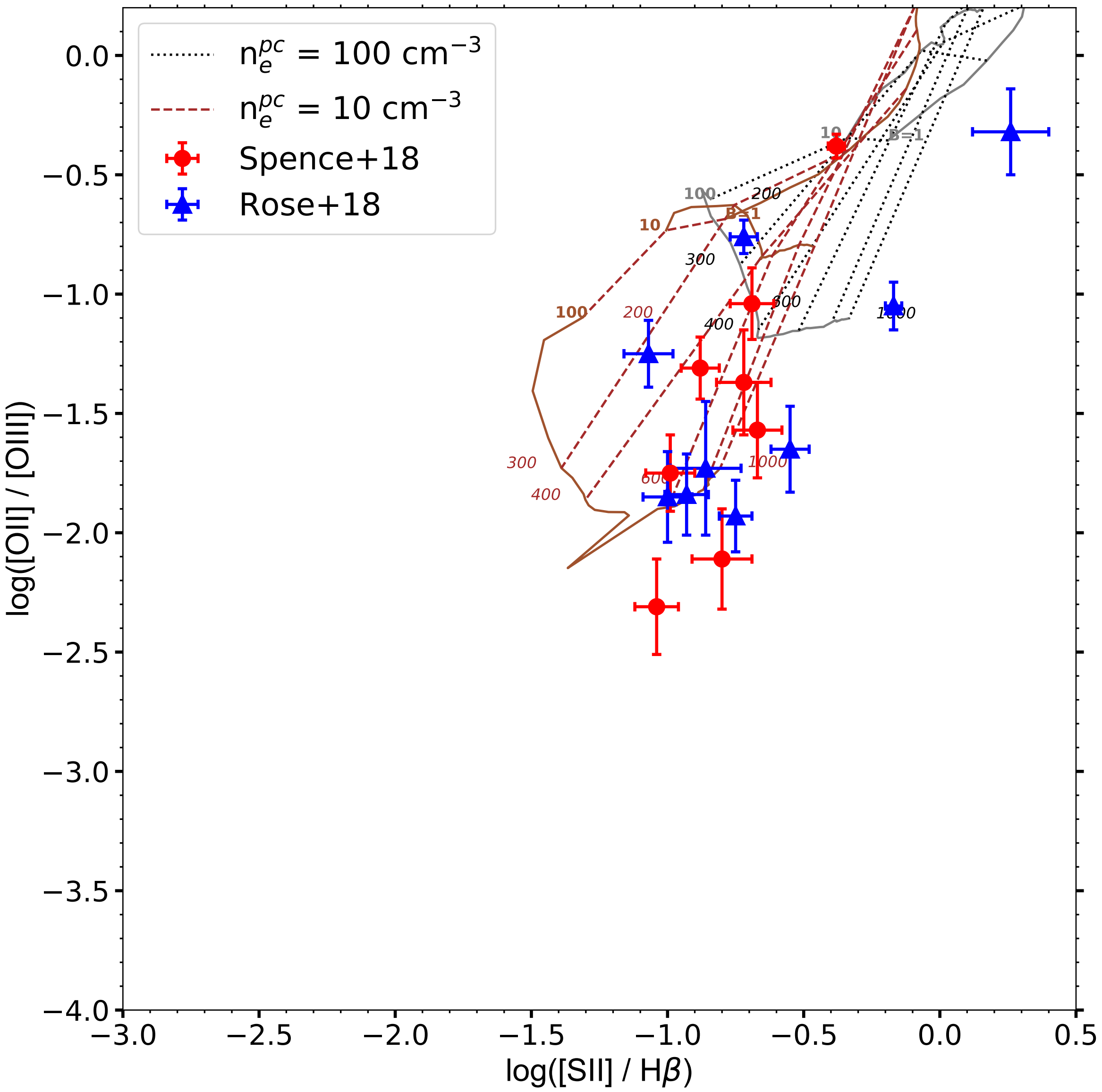

Figure 5.6: Theoretical shock grids for the emission-line flux ratios of log([OII]$\lambda\lambda$7319,7330/[OIII]λ5007) against log([SII]$\lambda\lambda$4068,4076)/Hβ), taken from Allen et al. (2008). The brown dashed grid corresponds to a precursor density of 10 cm^{-3}, corresponding to a post-shock density of 10^3 cm^{-3} for a compression factor of 100. The black-grey dotted grid corresponds to a precursor density of 100 cm^{-3}, corresponding to a post-shock density of 10^4 cm^{-3} for a compression factor of 100. The separate lines within these grids correspond to different shock velocities and magnetic field strengths, as labelled. Over-plotted are the total ratios from Spence et al. (2018) (red circles) and Rose et al. (2018) (blue triangles), respectively.

5.4.3 Possibility of high mass, low luminosity components

Whilst the bulk of the measured fluxes have been shown to originate from the same dense gas structures within the outflows, it is not possible to rule out the idea that there exists a lower density, higher filling factor gas component that has a higher gas mass but makes a relatively minor contribution to the emission-lines fluxes. This could lead to the trans-auroral diagnostics severely underestimating the true mass outflow rates and kinetic powers. To see this, consider the case in which the outflow contains two gas components (comprised of fully ionised pure hydrogen gas, for simplicity) with different densities: a higher density component with electron density n_h, volume filling factor f_h, mass M_h and Hβ luminosity $L(H\beta)_h$; and a lower density component with electron density n_l, volume filling factor f_l, mass M_l and Hβ luminosity $L(H\beta)_l$

Following arguments made in Spence et al. (2018)[2], this leads to the expressions for the ratio of the volume filling factors:

$$\left(\frac{f_h}{f_l}\right) = \left(\frac{L(H\beta)_l}{L(H\beta)_h}\right)\left(\frac{M_h}{M_l}\right)^2, \tag{5.4}$$

and the ratio of the electron densities:

$$\left(\frac{n_h}{n_l}\right) = \left(\frac{f_l}{f_h}\right)\left(\frac{M_h}{M_l}\right). \tag{5.5}$$

Therefore, it is possible for the low density component to be 10× more massive than the high density component ($(M_h/M_l) = 0.1$) yet contribute 10% or less of the Hβ luminosity of the high density component (i.e. $^{L(H\beta)_l}/_{L(H\beta)_h} \leq 0.1$), provided that the volume filling factor and density contrast satisfy $(f_h/f_l) \leq 10^{-3}$ and $(n_h/n_l) \geq 10^2$ respectively. The volume filling factor, f is calculated as follows:

---

[2] Derivation by Clive Tadhunter.

$$f = \frac{L_{H\beta}}{n_e^2 \alpha_{eff}^{h\beta} h v_{H\beta} V} \tag{5.6}$$

where V is the volume occupied by the gas. Assuming V for each ULIRG in the sample is approximated by the volume of a sphere with radius R_{out}, typical volume filling factors, f_h, for the warm outflows range from $10^{-6} < f_h < 10^{-3}$. Therefore such a high filling factor contrast is feasible. This raises the question as to whether a significant proportion of the mass of the outflow resides in lower density low-surface-brightness components. Indeed, low surface brightness ionised emission, extended on scales >10 kpc, is detected in many of the ULIRG spectra.

5.5 Chapter conclusions

In this chapter, the robustness of using trans-auroral [OII]$\lambda\lambda$7319,7330 and [SII]$\lambda\lambda$4068,4076 blends as a density and reddening diagnostic was confirmed. The advantage of using ratios of these lines instead of ratios of the standard nebular [SII](6716,6731) and [OII](3729/3726) transitions is that only the combined fluxes of the emission-line blends are required, rather than the individual doublet components. This significantly reduces degeneracy in fitting the emission-line profiles, and drastically reduces the uncertainties in the QUADROS results compared to previous studies.

Holt et al. (2011) showed that the density grids are largely insensitive to model parameters such as the power-law index of the ionising continuum, α, and the ionisation parameter, U. Here, that work was expanded on to show that, for the range of densities measured in the QUADROS project, the grids are also largely insensitive to the abundance and ionisation mechanism of the gas. These results indicate that electron density is the dominant diagnostic for the presented combination of ratios.

In addition, photo-ionisation models were used to show that the ratios of trans-auroral to nebular lines measured from the e-QUADROS spectra are consistent with what would be expected from AGN photo-ionisation of single clouds. In comparison, shock models do not explain the observed ratios with such a high degree of consistency, adding support to the conclusion that the densities derived by the QUADROS project are representative of the AGN-driven nuclear outflows. Overall, these results support the use of the trans-auroral line ratios as a robust density diagnostic for AGN-driven outflows.

In the next chapter, the properties of the extended low-surface-brightness gas detected in a sub-sample of the e-QUADROS ULIRGs is examined. It is then determined – motivated by the arguments presented above – whether a significant amount of the total mass and kinetic power of the outflows could be contained in these off-nuclear structures.

Chapter 6

Properties of the large-scale emission-line gas

6.1 Declaration

The analyses I present in this chapter have been performed using data from the full e-QUADROS sample, some of which were reduced by Marvin Rose (see Rose et al. 2018). This work is currently unpublished. Unless stated otherwise, the text, figures, analyses and interpretations are my own.

6.2 Chapter introduction

In Chapter 4 I examined the AGN-driven outflows in the nuclear regions of the e-QUADROS ULIRGs. These were found to be relatively dense and compact. Analyses of the energetics showed that, while some of the outflows have the potential to contain a significant fraction of the total AGN power, in general they fall short of the coupling efficiencies required by most hydrodynamical models of galaxy mergers.

The maximum radii of these observed outflows are, however, highly uncertain. Deep emission-line imaging of a sub-sample of 1 Jy ULIRGs, obtained with the GTC (Rodriguez Zaurin, private communication), reveals that many ULIRGs in the e-QUADROS sample contain significant low-surface-brightness emission with galaxy-scale extents. Indeed, faint emission-line structures can be seen in many of our long-slit spectra extending beyond the luminous, nuclear regions. In Chapter 3, analysis of one of the closest and most obvious examples of this – Mrk 273 – was presented (see also Spence et al., 2016). Whilst in that case the available evidence led us to conclude that the wider, galaxy-scale halo of ionised gas was not part of the nuclear outflow, the question remains as to whether this is true for all of the ULIRGs containing extended emission-line gas.

This question is motivated by the results of hydrodynamical simulations of major mergers, which suggest that outflows should be prevalent across galaxy-wide scales (Di Matteo et al., 2005; Springel et al., 2005), not just in the inner few kiloparsecs as the results provided in Chapter 4 indicate. It is therefore important to consider the possibility that the faint extended emission in the deep imaging and spectroscopic data may in fact represent extended, AGN-driven outflows. As discussed in Chapter 5, it is possible for low-density, high filling factor components of the outflows to contribute little to the emission-line flux, but contain a significant amount of mass and kinetic energy. Therefore, these extended components could potentially account for the small coupling efficiencies which arise when considering only the nuclear outflows. Furthermore, it is necessary to reflect on the criteria used to determine whether a particular gas structure is outflowing, and whether this is currently too restrictive.

In summary, this chapter investigates the radial extents, mass outflow rates and kinetic powers of any AGN-driven outflows detected outside the near-nuclear regions, and determines whether they could significantly affect the evolution of the host galaxies. We want to answer the question: are we missing something by only concentrating on the near-nuclear outflows? The chapter is structured as follows. In Section 6.3 I briefly motivate the project. Section 6.4.1 explains how I chose the extraction apertures for each object, and provides individual object descriptions of the 2D spectra. The results for the extended gas kinematics, estimated electron densities, mass outflow rates and kinetic powers are then presented in Section 6.5. Section 6.6 provides a short discussion of the main results, and general conclusions.

6.3 Project background

The radii of AGN-driven outflows has been a topic of debate in the observational literature over the past decade. As discussed in Chapters 1 and 4, measurements of this parameter based on emission-line outflows in the AGN population vary significantly, ranging from just 0.06 kpc (see Rose et al., 2018; Tadhunter et al., 2018; Spence et al., 2018) to over 10 kpc (see Harrison et al., 2012; Liu et al., 2013). The search for such AGN-driven outflows is motivated by hydrodynamical simulations of major mergers, which require feedback from the AGN in order to reproduce observational trends (e.g Di Matteo et al., 2005; Johansson et al., 2009). This feedback is achieved via AGN winds and outflows, which blast gas away from the galactic centre and regulate galaxy growth. The visualisations from the simulated mergers, which include black hole growth and trace the dynamic distribution of gas, indicate that AGN have the potential to blow out the gas to scales similar to those of the host galaxies themselves, and in some cases unbind it completely.

Furthermore, hydrodynamical simulations of major mergers performed by Debuhr et al. (2012) show that, when AGN winds are included, the mass of gas at distances larger than 10 kiloparsecs can be more than a factor of 20 greater than without. However, while these theoretical papers (e.g. King, 2005) discuss in detail the total *energy* required to be transferred to the winds in order to reproduce observed results, the theoretical *radii* of the outflows are not generally quantified. This leads to the general, yet somewhat undefined, expectation that AGN-driven outflows on scales of tens of kiloparsecs should be commonly observed – often referred to as "large-scale" outflows within the literature (e.g. King et al., 2011).

6.4 Spectroscopic data

6.4.1 Aperture extraction

12 of the 18 (60%) e-QUADROS ULIRGs show clear evidence in their long-slit spectra for extended emission line regions that extend well beyond the near-nuclear outflows discussed in Chapter 4. The analysis of F13428+5608 (Mrk 273) was presented as a stand-alone project in Chapter 3 (see also Spence et al., 2016). Analyses of the extended apertures in the remaining 11 ULIRGs with extended emission-line regions are presented in this chapter.

The spectra of the extended apertures were extracted for each object using the EXTRACT function in FIGARO, based on visual inspection of the 2D spectra. The number of apertures extracted for each object ranged from 1 to 7, depending on the level of structure visible off-nucleus. The 2D spectra are shown in Figures 6.1 through 6.19, covering the wavelength range of [OIII], and in three cases Hα+[NII], in order to indicate the extended structures.

The distances these apertures correspond to, relative to the continuum centre of each object, are shown in Tables 6.1 and 6.2, column (3). The continuum centre was measured by extracting two spatial slices, one from each end of the 2D spectrum. These were then fitted with a single Gaussian to determine the centroid. The continuum centre was then taken to be the mean of the two measurements.

One of the main difficulties when measuring faint extended emission is dealing with contamination from the nuclear region due to the seeing disc. Even at distances several times greater than the FWHM of the seeing disc, the nuclear emission can dominate (see discussion in Villar-Martín et al. 2016). In an attempt to minimise contamination from the nuclear emission due to the seeing disk, the apertures were extracted at least three times the HWHM (FWHM/2) of the seeing disc away from the continuum centre. However, some contamination may still occur beyond this limit.

6.4.2 Individual object descriptions

Below, the key characteristics of the extended emission-line structures based on the 2D spectra of the objects showing extended emission lines are outlined, along with the aperture locations.

F01004–2237

F01004–2237 (Fig 6.1) shows evidence for low surface brightness off-nuclear [OIII] emission out to a radius of ∼25 kpc to the north of the galaxy, and ∼15 kpc to the south (slit PA = 5°). Three apertures were extracted in order to sample this: two to the south (apertures a and b) and one to the north (aperture c). From visual inspection, the FWHM of the extended emission lines appear narrow, and the velocity shifts small, relative to the host galaxy rest-frame.

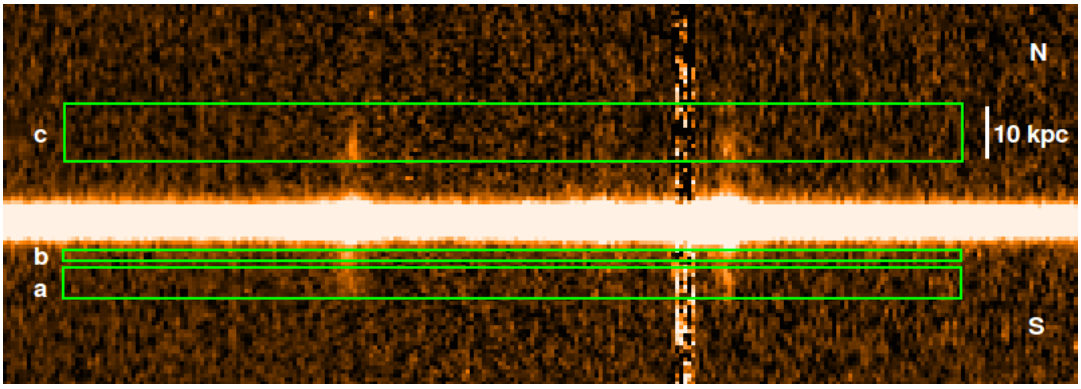

Figure 6.1: The 2D spectrum of F01004–2237 (PA 5°), indicating the locations of the main extended apertures used in these analyses. The scale is indicated by the white bar (10 kpc).

F13305–1739

A clear rotation curve is visible in the extended narrow [OIII] emission of F13305–1739 (Fig. 6.2), along with off-nuclear features (slit PA = 70°). The bright features to the east and west of the nucleus, covered by apertures a, b and c, appear narrow and are likely associated with quiescent gas undergoing gravitational motions. However, some broader, lower surface-brightness emission is also detected to the east of the nucleus, out to a radius of ∼12 kpc. This is sampled by aperture d.

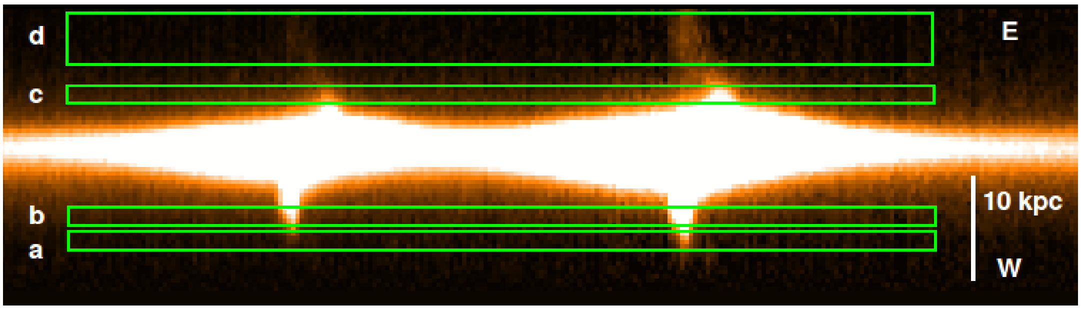

Figure 6.2: The 2D spectrum of F13305–1739 (PA 70°), indicating the locations of the main extended apertures used in these analyses. The scale is indicated by the white bar (10 kpc).

F13443+0802SE

Figure 6.3 shows the [NII]+Hα emission line blend of F13443+0802SE (slit PA = 20°). This object is compact but shows faint emission extending ∼3-4 kpc to the north of the nucleus, sampled by aperture a. In addition, a significant ionised gas structure is observed extending ∼10 kpc from the continuum centre, where the slit cuts through the southern nebula of the north-western nucleus (see Figure 6.5). This structure is also faintly visible in [OIII], and is sampled by aperture b. The FWHM of this structure appears relatively narrow, however it shows a significant velocity gradient. Figure 6.4 shows the optical HST image.

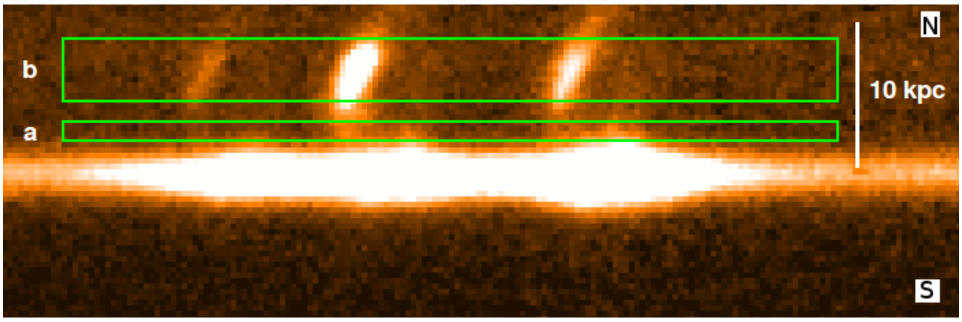

Figure 6.3: The 2D spectrum of F13443+0802SE (PA 20°), indicating the locations of the main extended apertures used in these analyses. The scale is indicated by the white bar (10 kpc).

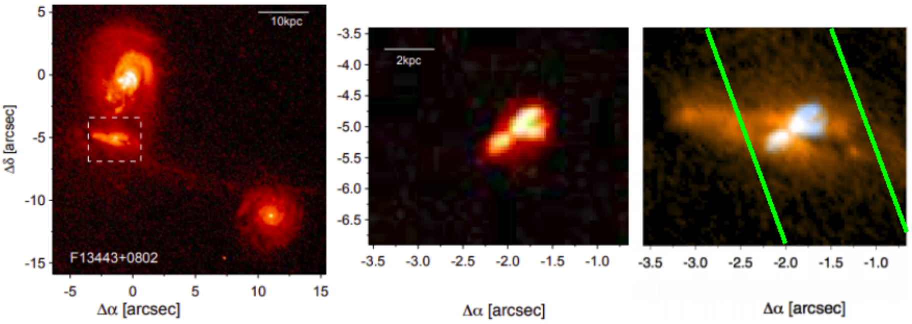

Figure 6.4: Left to right: HST-ACS continuum, continuum-subtracted [OIII], and [OIII] (blue) + continuum (orange) combined images of F13443+0802SE. North is up, east is left. The AGN nucleus is centred at 0,0. The approximate location of the spectroscopic slit is indicated by the solid green lines. Reproduced with permission from Tadhunter et al. (2018).

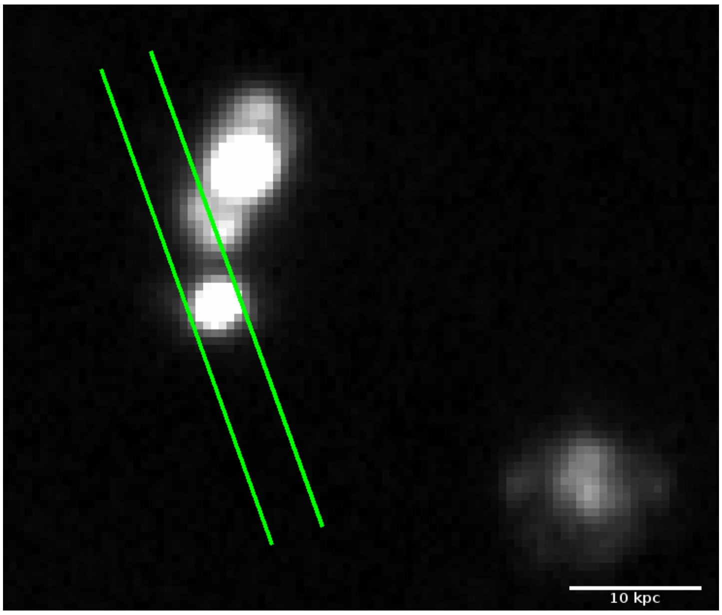

Figure 6.5: GTC narrow-band Hα image of F13443+0802SE. The scale is indicated by the white bar, which represents 10 kpc. North is up, east is left. The location of the spectroscopic slit is indicated by the solid green lines.

F13451+1232W

F13451+1232W is a kinematically complex double-nucleus system, and shows multiple emission-line structures out to a radius >10 kpc to the north, and ~5 kpc to the south of the western nucleus. The HST images presented by Tadhunter et al. (2018) (see Figure 6.6) clearly indicate a linear [OIII] structure to the north of the nucleus at a radius of ~2 kpc. The slit cuts through the edge of this structure. Unfortunately, in the spectra such inner extended structures overlap with the nuclear emission due to smearing by the seeing disc. In the case of F13451+1232W, however, the compact nucleus is spatially unresolved in the spectrum (Tadhunter et al., 2018). This enabled the removal of the broad nuclear outflow emission using the unblended blue wing of [NII]λ6548 from the central nuclear emission profile.

To do this, a 1D spatial slice was taken over a wavelength range of 7318 to 7322Å in the observed frame (corresponding to a velocity range of

-860 to -1030 km s^{-1} in the blue wing of [NII]λ6548), and the continuum removed using averaged spatial slices taken either side of the Hα+[NII] emission-line blend. This 1D profile was then "grown" into a 2D spectrum using the GROWX function in FIGARO, containing only emission from the nuclear outflow.

Similarly, a 1D spectrum was extracted for the nucleus between the central four pixels (0.64"), under the assumption that the flux in this aperture was dominated by the spatially unresolved near-nuclear outflow. The continuum was then subtracted by fitting a second-order polynomial function to the spectrum using the CREGS and PF functions in DIPSO. The residual spectrum was normalised to the mean flux over the wavelength of the extracted wing of [NII], and "grown" into a 2D spectrum using the GROWY function in FIGARO. The two "grown" spectra were then multiplied to create a 2D spectrum containing only the profile of the nuclear seeing disc across the entire wavelength range. This was then subtracted from the original spectrum, leaving behind the underlying extended emission.

Unfortunately, the [OIII] emission lines fell in a noisy region of the spectrum. Therefore, to guide the aperture selection the Hα+[NII] blend was used instead, as shown in Figure 6.7 (slit PA = 20°). The off-nuclear structures can be clearly seen, and are covered by 7 apertures (a to g).

Apertures a, f and g sample the low-surface-brightness emission $\sim$5–10 kpc to the north and south of the nucleus, as seen in the 2D spectrum. The emission to the north appears blue-shifted relative to the host galaxy rest-frame, but relatively narrow. Apertures b and c sample the higher-surface-brightness emission $\sim$1–4 kpc to the south of the nucleus, which appears consistent with the host galaxy rest-frame, with similar FWHM to the extended gas in apertures f and g. Apertures d and e sample the emission $\sim$1–3 kpc to the north of the nucleus, including the coherent

[OIII] structure shown in Figure 6.6, which is smeared into the slit by the seeing.

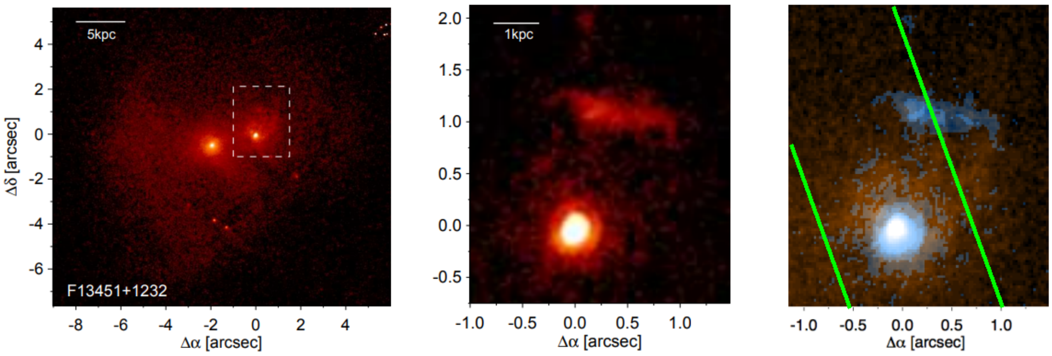

Figure 6.6: Left to right: HST-ACS continuum, continuum-subtracted [OIII], and [OIII] (blue) + continuum (orange) combined images of F13451+1232W. North is up, east is left. The AGN nucleus is centred at 0,0. The approximate location of the slit is indicated by the solid green lines. Reproduced with permission from Tadhunter et al. (2018).

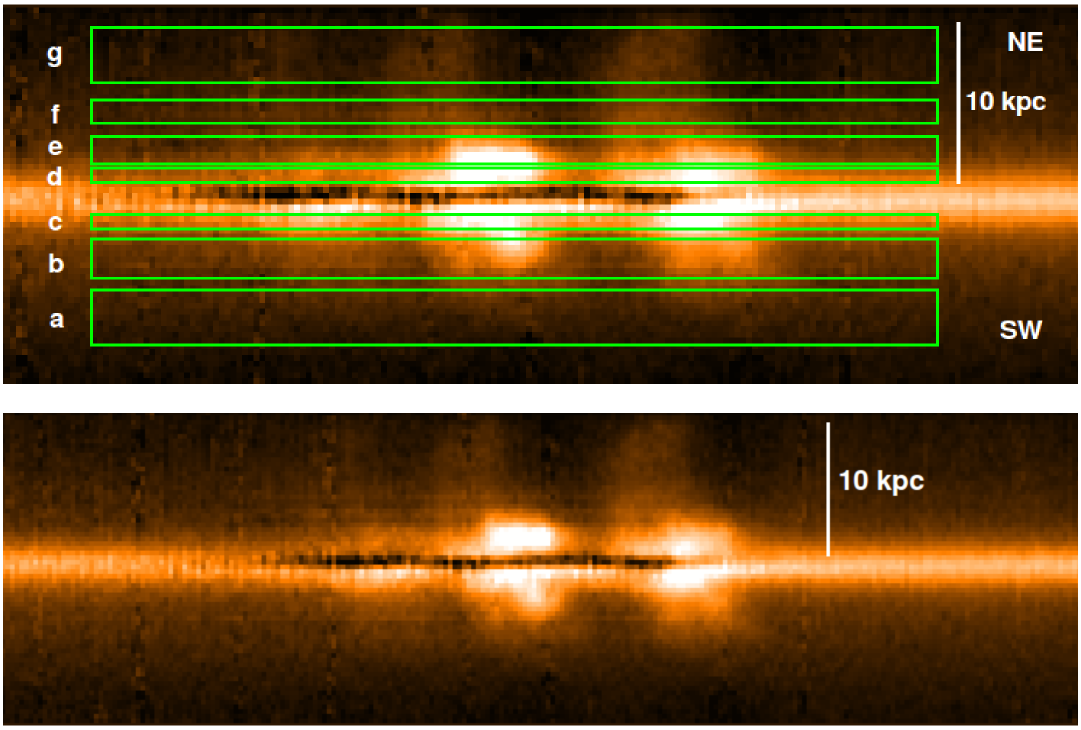

Figure 6.7: The 2D spectrum of F13451+1232W (PA 20°), indicating the locations of the main extended apertures used in these analyses. The scale is indicated by the white bar (10 kpc). The bottom panel is a repeat of the top panel without the green boxes, for clarity.

F14378–3651

The [OIII] emission of F14378–3651 is shown in Figure 6.8 (slit PA = 35°). The 2D spectrum shows a narrow, rest-frame component extending ∼5 kpc to the south of the nucleus. This is covered by a single aperture a. The quiescent nature of the structure, however, suggests it is unlikely to be part of the outflow.

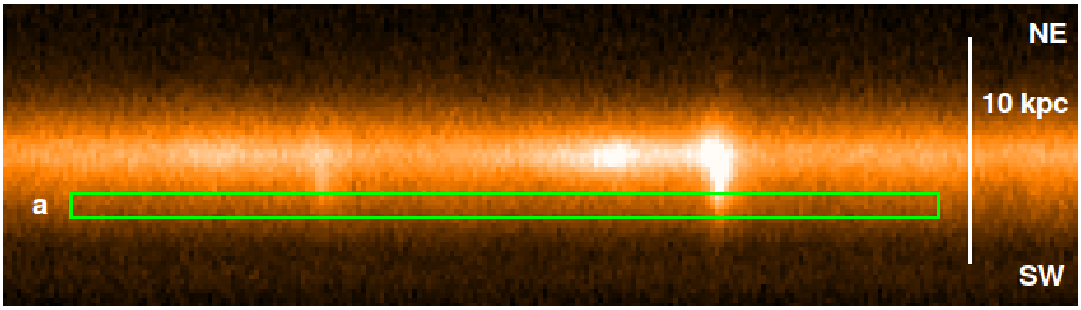

Figure 6.8: The 2D spectrum of F14378–3651 (PA 35°), indicating the location of the main extended aperture used in these analyses. The scale is indicated by the white bar (10 kpc).

F14394+5332E

The 2D spectrum of F14394+5332E (Figure 6.9) shows extended [OIII] emission to the SE, and possibly the NW, of the nucleus, out to a radius of ∼10 kpc from the continuum centre (slit PA = 130°). This corresponds to two loops of ionised emission seen in Hα imaging (Figure 6.11). Two apertures have been extracted to sample this, one to the NW (aperture a) and one to the SE (aperture b) of the nucleus. While aperture a may be dominated by the nuclear seeing disc, the extended emission is clearly seen in aperture b. The radial velocity of the extended component is close to the galaxy rest frame, and this component also shows a narrow FWHM. Emission-line loops or bubble structures such as those seen in F14394+5332E are often assumed to be outflows. The spectroscopic observations are particularly useful for testing whether this is, in fact, the case. The nuclear outflow is shown in HST imaging presented in Figure 6.10.

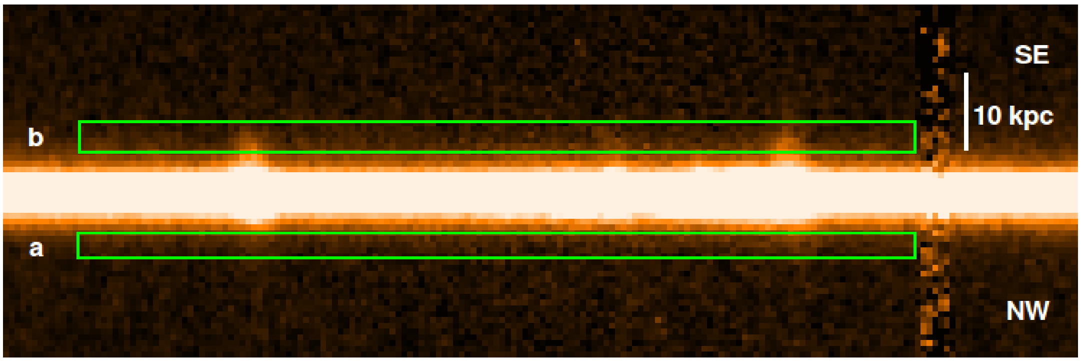

Figure 6.9: The 2D spectrum of F14394+5332E (PA 130°), indicating the locations of the main extended apertures used in these analyses. The scale is indicated by the white bar (10 kpc).

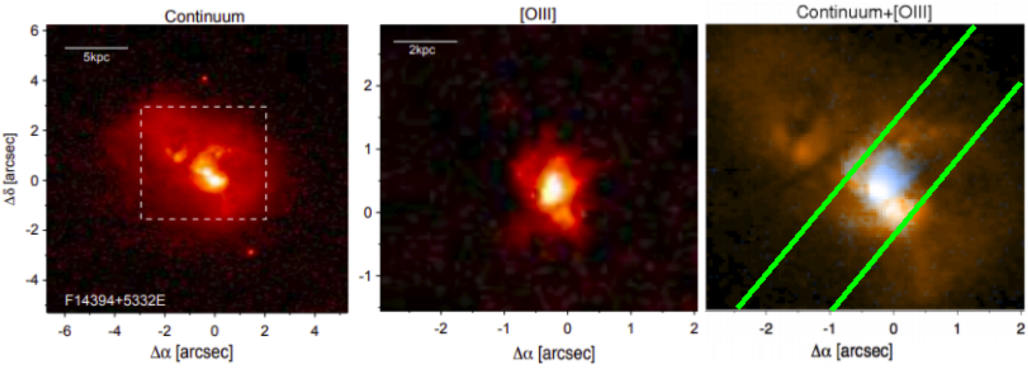

Figure 6.10: Left to right: HST-ACS continuum, continuum-subtracted [OIII], and [OIII] (blue) + continuum (orange) combined images of F14394+5332E. North is up, east is left. The AGN nucleus is centred at 0,0. The approximate location of the slit is indicated by the solid green lines. Reproduced with permission from Tadhunter et al. (2018).

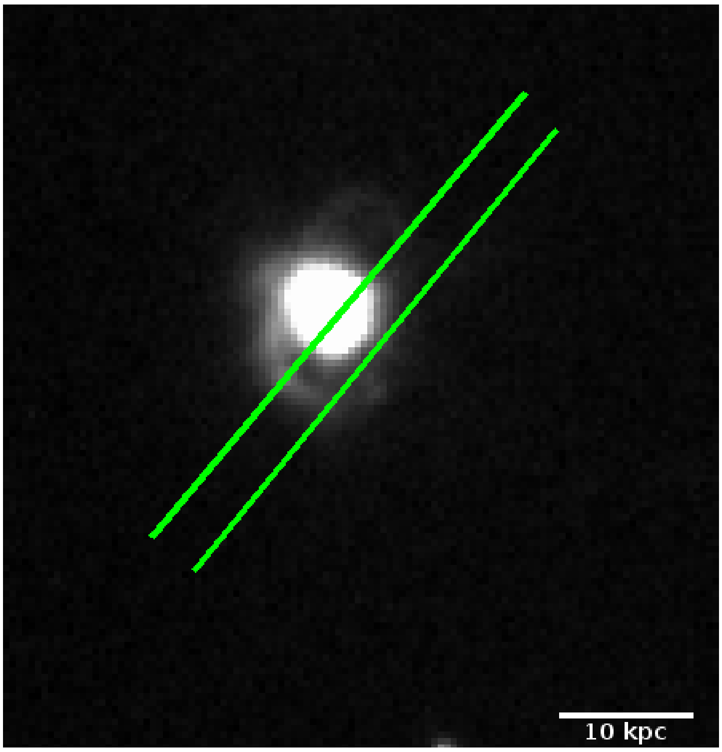

Figure 6.11: GTC narrow-band Hα image of F14394+5332E. The scale is indicated by the white bar, which represents 10 kpc. North is up, east is left. The approximate location of the spectroscopic slit is indicated by the solid green lines.

F15462–0450

F15462–0450 is a single nucleus ULIRG, with a narrow [OIII] emission feature extending ~7 kpc to the south visible in the 2D spectrum (slit PA = 30°). This is covered by aperture a, shown in Figure 6.12. A GTC narrow-band Hα image, along with the approximate position of the slit, is shown in Figure 6.13. The aperture corresponds to the radius at which the slit cuts through an arc-like structure to the south of the nucleus. This structure, however, has a radial velocity close to rest-frame, with a narrow FWHM. It is therefore unlikely that this represents part of the outflow.

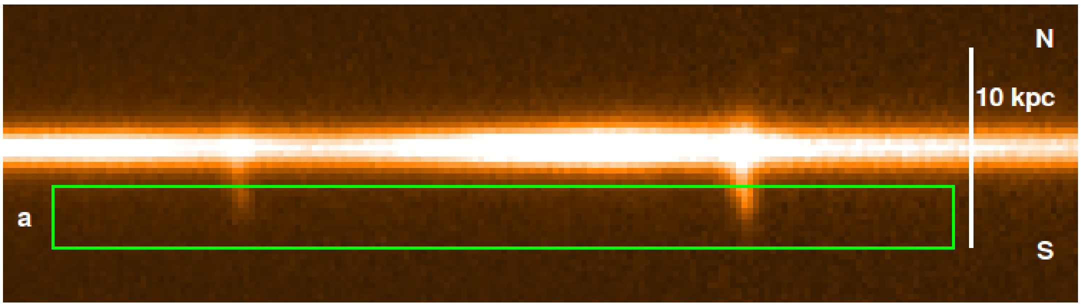

Figure 6.12: The 2D spectrum of F15462–0450 (PA 30°), indicating the location of the main extended aperture used in these analyses. The scale is indicated by the white bar (10 kpc).

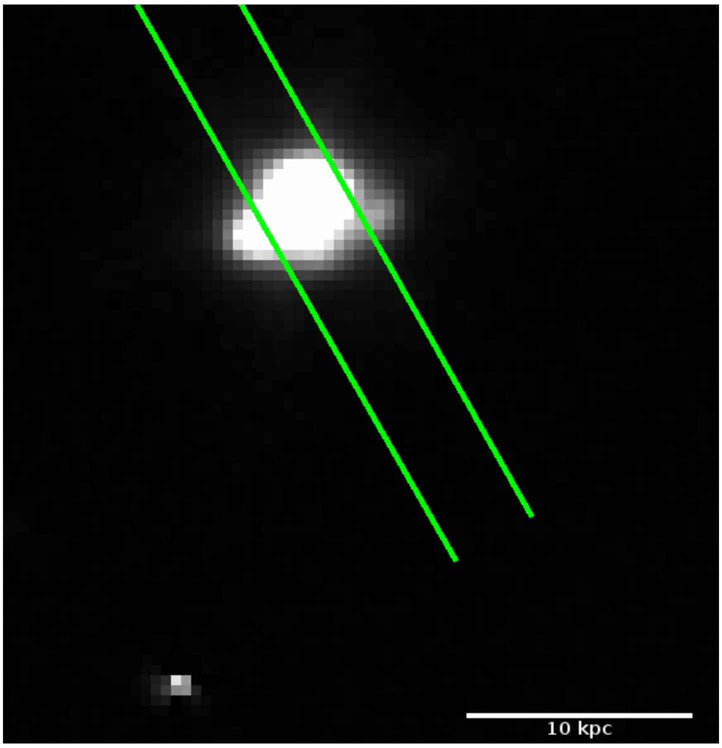

Figure 6.13: GTC narrow-band Hα image of F15462–0450. The scale is indicated by the white bar, which represents 10 kpc. North is up, east is left. The approximate location of the spectroscopic slit is indicated by the solid green lines.

F17044+6720

Optical imaging of F17044+6720 shows a spectacular system of condensations in an elongated structure that extends 10 kpc to the NW of the nucleus (see Tadhunter et al., 2018, and Figure 6.14). The WHT/ISIS spectrum cuts close to these condensations, and the extended emission to the NW of the continuum centre is sampled by aperture a (Fig. 6.15; slit PA = 145°). From a visual inspection, the FWHM appears narrow and no significant blue- or red-shifts are present. A narrower emission-line feature is also visible to the SE, covered by aperture b, extending to ∼5 kpc from the continuum centre. Figure 6.16 shows the Hα image of F17044+6720 taken with the GTC, overlaid with the slit location. Interestingly, no signs of the extended broad, blue-shifted feature to the NW of the nucleus described in Tadhunter et al. (2018) are seen. However, note that the PA of the slit used for that study (PA = 160°; Rodríguez Zaurín et al., 2013) was different to the one used here.

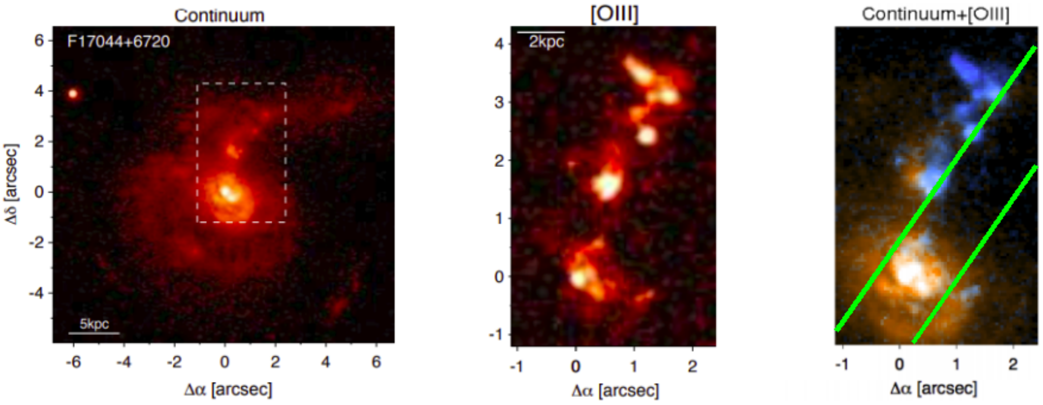

Figure 6.14: Left to right: HST-ACS continuum, continuum-subtracted [OIII], and [OIII] (blue) + continuum (orange) combined images of F17044+6720. North is up, east is left. The AGN nucleus is centred at 0,0. The approximate location of the spectroscopic slit is indicated by the solid green lines. Reproduced with permission from Tadhunter et al. (2018).

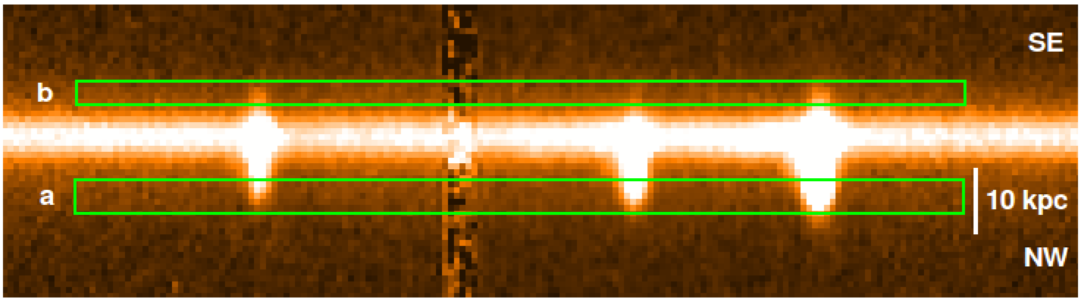

Figure 6.15: The 2D spectrum of F17044+6720 (PA 145°), indicating the locations of the main extended apertures used in these analyses. The scale is indicated by the white bar (10 kpc).

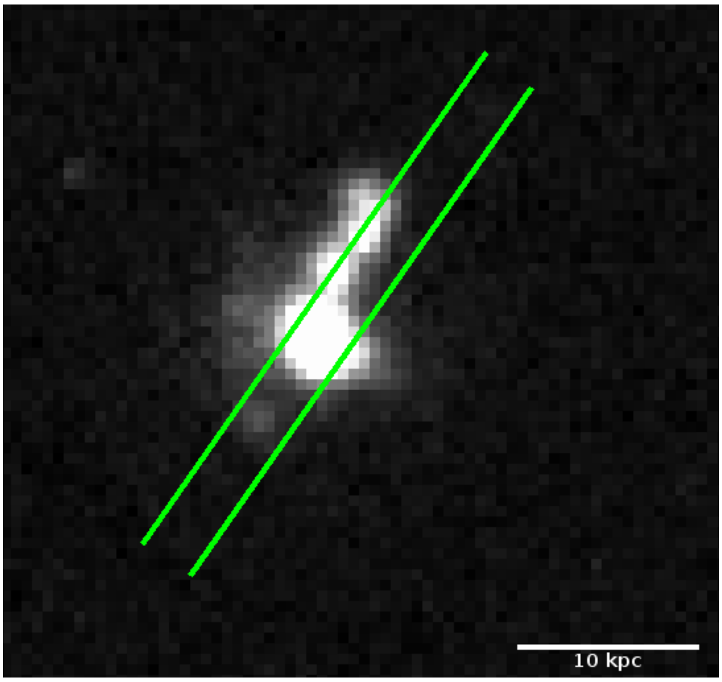

Figure 6.16: GTC narrow-band Hα image of F17044+6720. The scale is indicated by the white bar, which represents 10 kpc. North is up, east is left. The approximate location of the spectroscopic slit is indicated by the solid green lines.

F19254–7245S

F19254–7245S, also known as the Superantennae galaxy, shows complex emission-line structures off nucleus. These are indicated in Figure 6.17, which shows the [NII]+Hα emission blend in the 2D spectrum (slit PA = 10°), overplotted with the chosen apertures. Extended emission-line features are visible to a radius of ~7 kpc to both the north and the south of the nucleus. Apertures a, b, f and g cover the most extended features, which show evidence for a velocity gradient as well as narrow, split components to the emission lines (see also Bendo et al., 2009; Westmoquette et al., 2012). These could represent an accelerating, biconical outflow. In addition, a bright, narrow feature is seen ~1–3 kpc to the south, sampled by apertures c and d. To the north, a broader feature is visible, sampled by aperture e. However, due to the high luminosity of the nuclear region, the apertures closest to the nucleus are likely to be contaminated by the seeing disc.

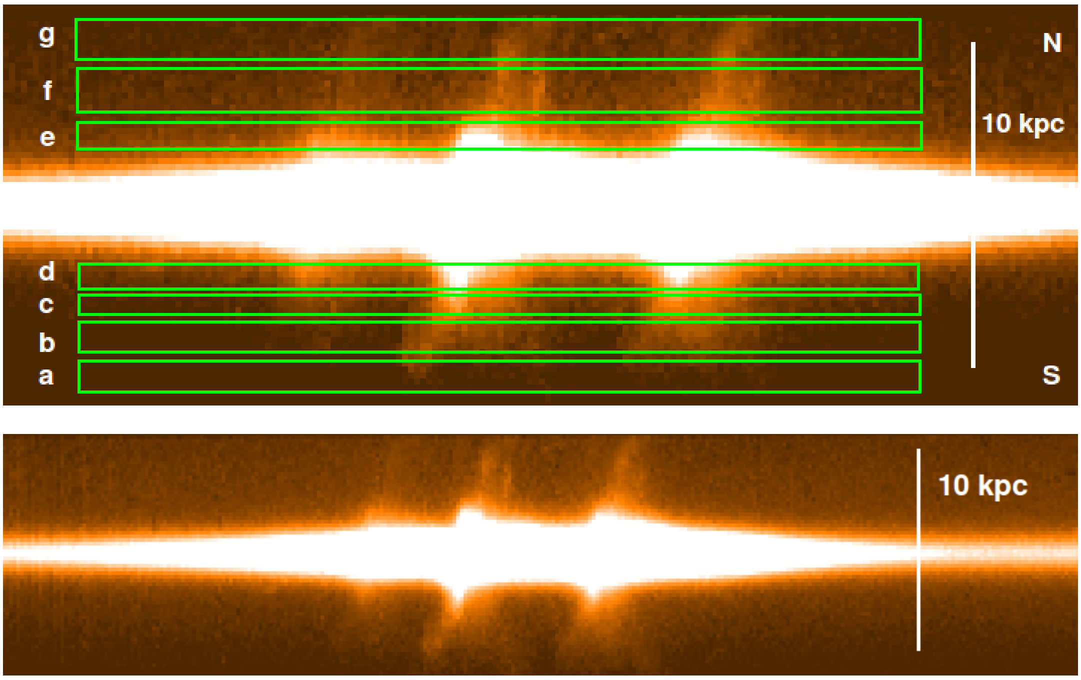

Figure 6.17: Top: the 2D spectrum of F19254–7245S (PA 10°), indicating the locations of the main extended apertures used in these analyses. The scale is indicated by the white bar (10 kpc). Bottom: the spectrum is reproduced to clearly show the extended structures.

F23060+0505

Figure 6.18 shows the [OIII] + Hβ emission for F23060+0505 (slit PA = 325). To the north of the nucleus, significantly split components are visible in [OIII] – indicative of outflows – out to a radius of ∼8 kpc. This is covered by aperture b. Aperture a covers any low-surface-brightness emission to the south of the nucleus, although this region is likely to be dominated by the nuclear seeing disc.

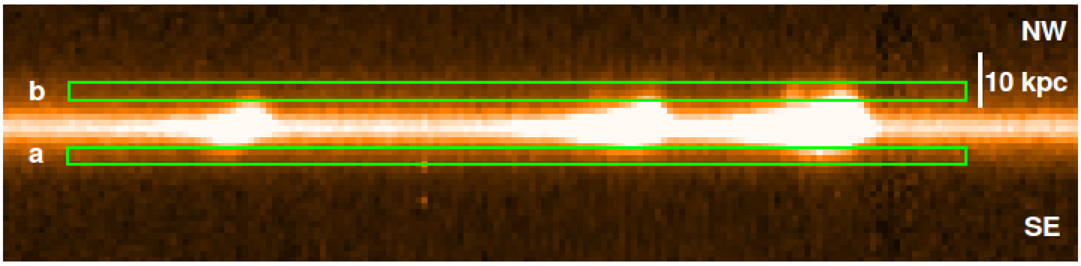

Figure 6.18: The 2D spectrum of F23060+0505 (PA 325°), indicating the locations of the main extended apertures used in these analyses. The scale is indicated by the white bar (10 kpc).

F23389+0303N

Figure 6.19 shows the [OIII] + Hβ emission of F23389+0303N (slit PA = 0°). Two apertures were chosen for this object: aperture b samples the emission ∼5 kpc to the south of the northern nucleus, which is associated with the southern nucleus; aperture a samples the low surface brightness component extending out to a radius of ∼20 kpc to the south of the northern nucleus. The kinematics, however, appear undisturbed with radial velocities close to the galaxy rest frame.

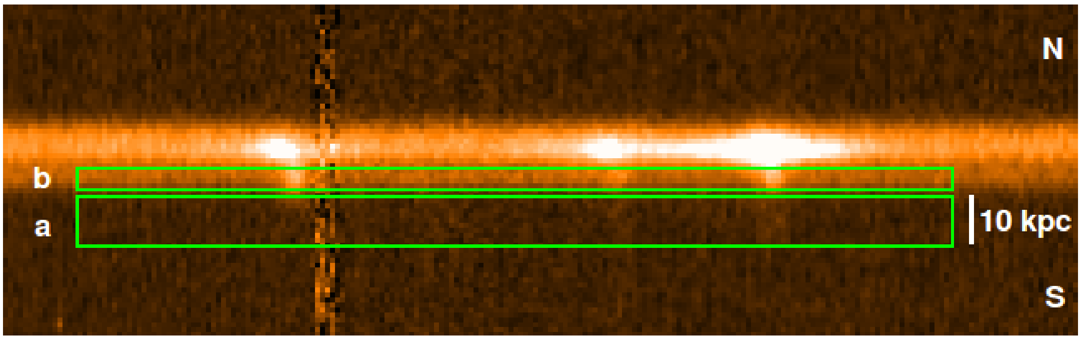

Figure 6.19: The 2D spectrum of F23389+0303N (PA 0°), indicating the location of the main extended aperture used in these analyses. The scale is indicated by the white bar (10 kpc).

6.5 Results

6.5.1 Gas kinematics

The kinematics of the emission-line gas detected in the extended apertures of each ULIRG were examined, in order to determine the radial velocity shifts relative to the host galaxy rest frame, Δv, and velocity widths, FWHM.

Outflows are generally characterised by blue-shifted emission-line components with large velocity shifts and/or widths, or alternatively by split lines showing both a blue- and redshifted component. However the exact criteria are somewhat arbitrary, which can make the identification of outflows difficult. In previous chapters, the criteria of Rodríguez Zaurín et al. (2013) were used to define an outflow to be any emission-line component showing FWHM or velocity shifts greater than 500 km s^{-1}. However, a lower velocity cut is supported by the hydrodynamical simulations of Debuhr et al. (2012). Their results showed that, when AGN-driven outflows were included in galaxy merger simulations, they were able to drive gas particles away from the galaxy at velocities, $v_{out} \sim 300 - 1000$ km s^{-1}. In contrast, no particles were accelerated to velocities higher than 300 km s^{-1} when the AGN-driven outflows were switched off (i.e. governed only by gravitational motions). Therefore, taking 350 km s^{-1} to be the velocity cut between outflowing and quiescent gas may be more appropriate[1].

Tables 6.1 and 6.2 give the velocity widths and shifts of the extended apertures for the sub-sample (11/18) of e-QUADROS ULIRGs which show evidence for off-nuclear emission-line gas. In addition, Figures 6.20 to 6.23 show the velocity shifts and widths across the 2D spectra as a function of distance from the continuum centre. Note that for this analysis additional

---

[1] Note 350 km s^{-1} is proposed rather than 300 km s^{-1} in order to avoid any confusion between lower outflow velocities and higher velocity gravitational motions.

Table 6.1: The extended [OIII] kinematics for the e-QUADROS ULIRGs. Column (2): aperture designation as given in Figures 6.1 through 6.19; column (3): radial width and direction of the aperture, relative to the continuum centre; column (4): components required by the fit, labelled according to the criteria of Rodríguez Zaurín et al. (2013). The subscript "*SD*" highlights components obviously dominated by the nuclear seeing disc; column (5): FWHM of each component, corrected for spectral resolution in quadrature; column (6): velocity shifts given relative to the host galaxy rest frame. calculated using the redshifts in Chapter 2, Table 2.1. Note the "Hα" superscript indicates where the model has been generated using Hα due to weak [OIII].

Object name IRAS (1)	Aperture (2)	T_{ap} (kpc) (3)	Component (4)	FWHM (km s^{-1}) (5)	Δv (km s^{-1}) (6)
F01004–2237	a	8.9 to 15.4 S	N	266 ± 123	-65 ± 36
	b	5.7 to 8.1 S	N	230 ± 145	-47 ± 22
			B_{SD}	1815 ± 299	-293 ± 114
	c	12.2 to 23.6 N	N	328 ± 77	26 ± 20
F13305–1739	a	7.8 to 9.5 W	N	89 ± 18	-99 ± 12
	b	5.5 to 7.5 W	N	99 ± 13	-111 ± 11
			B_{SD}	1081 ± 114	-166 ± 40
	c	4.3 to 5.8 E	N1	124 ± 15	167 ± 12
			N2	404 ± 32	115 ± 16
			B_{SD}	1357 ± 55	-9 ± 25
	d	7.8 to 12.5 E	N	229 ± 23	-68 ± 15
F13443+0802SE	a	2.3 to 3.7 N	N	315 ± 41	42 ± 21
			I_{SD}	712 ± 117	-89 ± 60
	b	4.9 to 9.3 N	N	359 ± 51	-50 ± 30
F13451+1232W$^{H\alpha}$	a	4.7 to 8.1 SW	N	492 ± 26	249 ± 17
	b	2.1 to 4.0 SW	N1	217 ± 17	83 ± 12
			N2	241 ± 15	323 ± 11
	c	0.6 to 1.3 SW	N1	369 ± 22	140 ± 9
			N2	460 ± 35	296 ± 45
	d	1.3 to 2.1 NE	N1	176 ± 29	-104 ± 18
			N2	375 ± 19	179 ± 14
	e	2.1 to 4.0 NE	N1	362 ± 36	-62 ± 30
			N2	357 ± 17	236 ± 14
	f	4.7 to 6.1 NE	N1	308 ± 57	-107 ± 45
			N2	284 ± 37	145 ± 43
	g	7.2 to 10.6 NE	N1	213 ± 40	-110 ± 25
			N2	157 ± 31	75 ± 20

Table 6.2: Continued from Table 6.1.

Object name IRAS (1)	Aperture (2)	T_{ap} (kpc) (3)	Component (4)	FWHM ($km\ s^{-1}$) (5)	Δv ($km\ s^{-1}$) (6)
F14378–3651	a	2.0 to 3.0 SW	N	114 ± 21	25 ± 13
F14394+5332E	a	6.7 to 9.6 NW	N	377 ± 99	123 ± 49
			B_{SD}	1818 ± 318	-535 ± 190
	b	6.7 to 9.6 SE	N	357 ± 34	-24 ± 10
F15462–0450	a	2.0 to 7.1 S	N	103 ± 14	153 ± 12
F17044+6720	a	6.4 to 12.0 NW	N	171 ± 54	44 ± 28
	b	5.5 to 8.3 SE	N	176 ± 73	53 ± 33
F19254–7254S	a	4.8 to 5.8 S	N1	190 ± 47	-315 ± 26
			N2	363 ± 54	114 ± 25
	b	3.4 to 4.6 S	N1	136 ± 34	-283 ± 18
			N2	419 ± 39	-38 ± 25
	c	2.7 to 3.3 S	N1	82 ± 28	-247 ± 14
			N2	373 ± 35	-68 ± 24
	d	1.6 to 2.5 S	N1	113 ± 24	-225 ± 15
			N2	196 ± 34	-35 ± 20
			B_{SD}	1728 ± 65	205 ± 34
	e	1.6 to 2.5 N	N1	143 ± 55	218 ± 31
			N2	245 ± 30	-47 ± 18
			B_{SD}	1565 ± 78	-117 ± 33
	f	3.0 to 4.3 N	N	355 ± 47	-19 ± 24
	g	4.6 to 5.7 N	N	289 ± 65	41 ± 31
F23060+0505	a	4.5 to 6.8 SE	I_{SD}	667 ± 17	-81 ± 29
			B_{SD}	1710 ± 506	-918 ± 307
	b	4.5 to 9.0 NW	N1	334 ± 27	200 ± 14
			N2	355 ± 38	-427 ± 25
F23389+0303N	a	11.2 to 20.9 S	N	445 ± 82	-62 ± 38
	b	5.3 to 9.2 S	N	380 ± 45	-71 ± 19

apertures were extracted alongside those described in section 6.4, in order to allow a finer sampling of the velocity field. To do this, 1–3 pixel apertures were extracted at regular intervals across the 2D spectrum of each ULIRG, and the [OIII] profiles (or Hα in the case of F13451+1232W) fitted using DIPSO. The direction of the apertures relative to the continuum centre is indicated on each plot. The horizontal blue dashed line indicates a velocity of 350 km s^{-1}. In the following analyses, any component with a FWHM and/or velocity shift greater than one error bar from this cut is considered to be a potential outflow component. In addition, any components showing velocity splitting by more than 350 km s^{-1} are considered as potential outflows.

Note that it is also important to consider the effects of atmospheric seeing when dealing with extended emission lines. The FWHM of the seeing disc of each ULIRG was estimated in Chapter 4 (see Table 2.2). The point spread function of the seeing is generally approximated as a Gaussian, but with extended wings[2]. The main "sphere of influence" of the nuclear seeing disc is indicated on the plots in Figures 6.20 to 6.23 by the dotted black lines. The radius of the sphere of influence is taken to be 3 times HWHM$_{1D}$ (3×HWHM $\sim 3.5\sigma$). For a Gaussian (normal) distribution, the flux drops to 0.2% of its peak value at a radius of 3.5σ from the centre. While the seeing is not strictly Gaussian, the above approximation can be used as a guide to distinguish smeared nuclear components from truly extended components. Referring to Figures 6.20 to 6.23, in general the broadest emission is contained within these regions. While some contamination outside of this radius is still possible due to the more extended wings of the seeing profile (especially for those objects with particularly bright nuclei), the nuclear seeing disc is symmetric about the nucleus. Therefore symmetry can also be taken into account when

---

[2] More accurately represented by a Moffat distribution.

determining whether the extended features are real or not.

Based on the above kinematic criteria, the velocity profiles of F01004–2237, F13443+0802SE, F14378–3651, F15462–0540, F17044+6720 and F23389+0303N show little evidence for extended outflows outside of the influence of the nuclear seeing disc. The extended components in these cases generally have narrow line widths (FWHM < 350 km s^{-1}) and small velocity shifts ($|\Delta v| < 200$km s^{-1}) relative to the host galaxy.

The extended, narrow components seen in the spectra of F01004–2237 and F23389+0303N are likely associated with large-scale structures of gas in the merging systems, however no imaging is available to confirm this. In the other four cases (F13443+0802SE, F14378–3651, F15462–0540 and F17044+6720) the spectroscopic slits cut through coherent structures which can be seen in GTC and/or HST imaging (see Section 6.4.1). Such arcs, loops and bright condensations are often taken to represent expanding outflows when observed near AGN, so it is interesting that they in fact appear to be kinematically quiescent.

At first sight, the remaining ULIRGs (F13305–1739, F13451+1232W, F14394+5332E, F19254-7245S and F23060+0505) show potential for extended outflows based on their [OIII] kinematics. For example, while the 2D spectrum (Fig 6.2) and velocity plots (Fig. 6.20) of F13305–1739 shows a clear rotation curve – implying a settled structure (i.e. disk) undergoing gravitational rotation – across the extended nebula, broad components (FWHM $>$ 1000 km s^{-1}) are detected out to a significant distance (r $\lesssim$ 8 kpc) to both sides of the continuum centre. However due to the large contrast between the high flux of the broad nuclear emission and the low-surface brightness extended structures (F13305–1739 is classified as a type II quasar), it is highly likely that these broad components represent contamination by the seeing disc, particularly given the symmetric nature of the velocity distribution. In addition, the FWHM and velocity shifts of the diffuse gas detected between 8 – 12 kpc to the north are small (FWHM $= 229 \pm 23$ km s^{-1}; $\Delta v = -68 \pm 15$ km s^{-1}), consistent with gravitational motions.

The HST [OIII] image of F13451+1232W (Figure 6.6) shows a coherent arc-like structure to the north of the nucleus, of which the eastern edge is smeared into the slit by the point spread function. This can be seen as a bright blob of [OIII] in the 2D spectrum, covered by apertures d and e. [OIII] is weak elsewhere in the spectrum; however, looking at the Hα emission, a more extensive low-ionisation halo becomes apparent, detected out to ∼10 kpc to the NE and ∼8 kpc to the SW. For this reason, the kinematics for this object shown in Figure 6.21 are measured using the Hα emission rather than the [OIII]. Also note that in this case the nuclear component was removed from the spectrum. Two narrow components – indicating split emission lines – are required across the majority of the system, separated by $150 < \Delta v < 300$ km s^{-1}. In apertures a, c, d and e the FWHM of at least one component exceeds 350 km s^{-1}.

F14394+5332 is one of the most interesting objects based on optical imaging, because it shows two ionised loop/bubble structures: one to the north-west and one to the south-east of the eastern nucleus (see Figure 6.11). The presence of these structures is often considered as evidence for outflows. To investigate this, the spectroscopic slit cuts the edge of the north-western structure, and goes through the middle of the south-eastern structure. The apertures to the SE require only a single, narrow Gaussian component (FWHM < 350 km s^{-1}), with radial velocities close to the host galaxy rest-frame, ruling this structure out of being part of the high-velocity outflow. An underlying broad blue-shifted component, however, is required for the [OIII] profile at a radius of ∼8 kpc to the north-west of the continuum centre, where the slit cuts close to the north-western loop. This component, however, is not obvious in the 2D spectrum, and the

FWHM and Δv values are consistent with the broad nuclear component. Therefore, despite the apparent asymmetry in the spatial distribution of this component, it is not clear in this case whether this is a genuinely extended broad component, or simply contamination from the nuclear outflow due to the binning of the aperture.

F19254–7245S (also known as the Superantennae galaxy) has extremely complex off-nuclear emission-line features, with evidence of velocity splitting by $\Delta v > 350$ km s^{-1} in its 2D spectrum (Figure 6.17). There is an approximately rest-frame narrow component (N1) detected across the entirety of the 2D spectrum, which appears to become more red-shifted as the radial distance increases to the south of the continuum centre (see Figure 6.22). In the southern region, over the range $-5 < r < -2$ kpc, a second narrow component appears (N2) which appears to become increasingly blue-shifted (relative to the host galaxy) as the radial distance increases. It is possible that these split components provide evidence for an accelerating outflow to the south of F19254–7245S. Broad emission lines (FWHM > 1000 km s^{-1}) are present throughout the nuclear region, and broad components are also detected at ∼2–3 kpc north and south of the continuum centre. These more extended broad components are, however, consistent with the broad nuclear components, and due to the high contrast in flux between the nuclear regions and the low-surface-brightness components, are likely to be due to contamination from the seeing disc. Finally, the extended narrow emission ∼6 kpc to the north provides little evidence for extended outflows.

Broad- and intermediate-width emission lines (FWHM > 500 km s^{-1}) are observed throughout the nuclear region of F23060+0505 (see Figure 6.23). These broader components are also seen to the SE in aperture a, suggesting that the emission in this region is dominated by the nuclear seeing disc. Split components, however, are seen in [OIII] in the 2D spectrum of F23060+0505 (Figure 6.18), sampled by aperture b. These components extend to a radius of ∼8 kpc to the NW of the nucleus, with a velocity separation of 627±39 km s^{-1} and FWHM ∼350 km s^{-1}.

Including Mrk 273 (see Chapter 3), only 4 out of the 18 ULIRGs (22%) in the e-QUADROS sample show evidence of outflows extending more than a few kiloparsec from the nuclei. Based on the kinematic analysis, the best extended outflow candidates from this Chapter are:

- F13451+1232W: emission-line splitting of $150 < \Delta v < 300$ km/s km s^{-1} is observed in this object. In addition, the FWHM of at least one component exceeds 350 km $^{-1}$ in four out of seven of the main apertures, extending to a radius of ∼8 kpc from the continuum centre.

- F19254–7245S: emission-line splitting ($\Delta v > 350$ km s^{-1}) is observed out to a radius of ∼5 kpc to the south of this system. Large velocity widths ($360 <$ FWHM < 420 km s^{-1}) are also observed to the south of the nucleus, extending ∼6 kpc.

- F23060+0505: emission-line splitting ($\Delta v > 600$ km s^{-1}) is observed at radii $4.5 < R < 9.0$ kpc to the north-west of this object.

Note, however, that while these objects show more extreme kinematics than would be expected from the gravitational motions of a stable dynamical structure (i.e. a settled disk) for typical ULIRG masses, it is difficult to rule out that the observed kinematics are caused by gas falling back into the merger remnant before it has settled into a stable structure. Given that local ULIRGs are predominantly associated with major mergers, this is not an unlikely scenario. For example, along any line of sight, the superposition of the velocity components of two (or more) gas clouds falling in from opposite sides of the galaxy on nearly radial orbits with a gravitationally-induced radial velocity of a few 100 km s^{-1} could lead to line widths or splittings >350 km s^{-1}, such as those seen here.

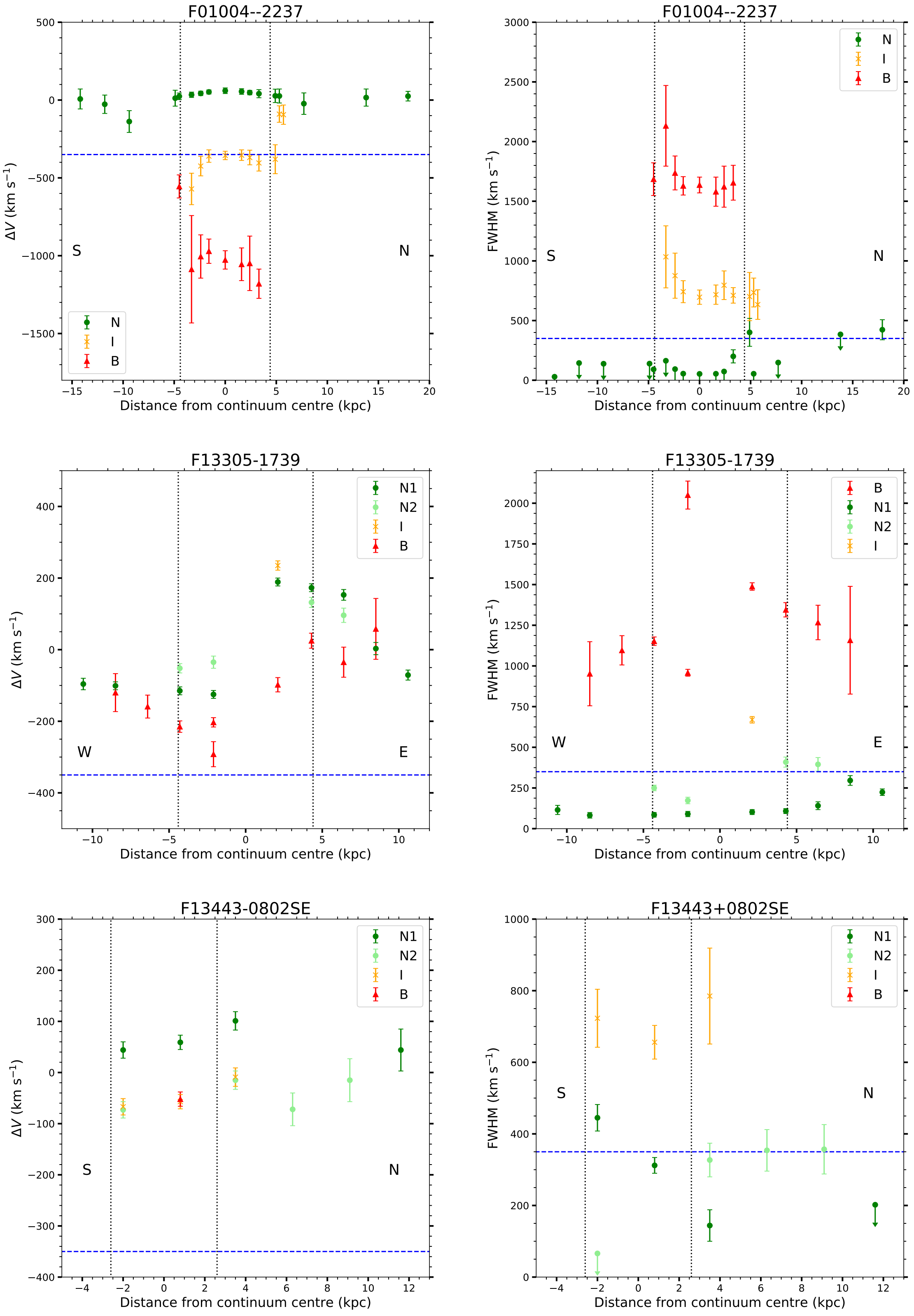

Figure 6.20: Velocity distributions of the extended gas. The left-hand plots show the velocity shifts relative to the continuum centre. The right-hand plots show the FWHM, corrected for spectral resolution. The dashed blue line indicates the velocity cut at 350 km s^{-1}. The dotted black lines indicate the seeing "sphere of influence" (see text).

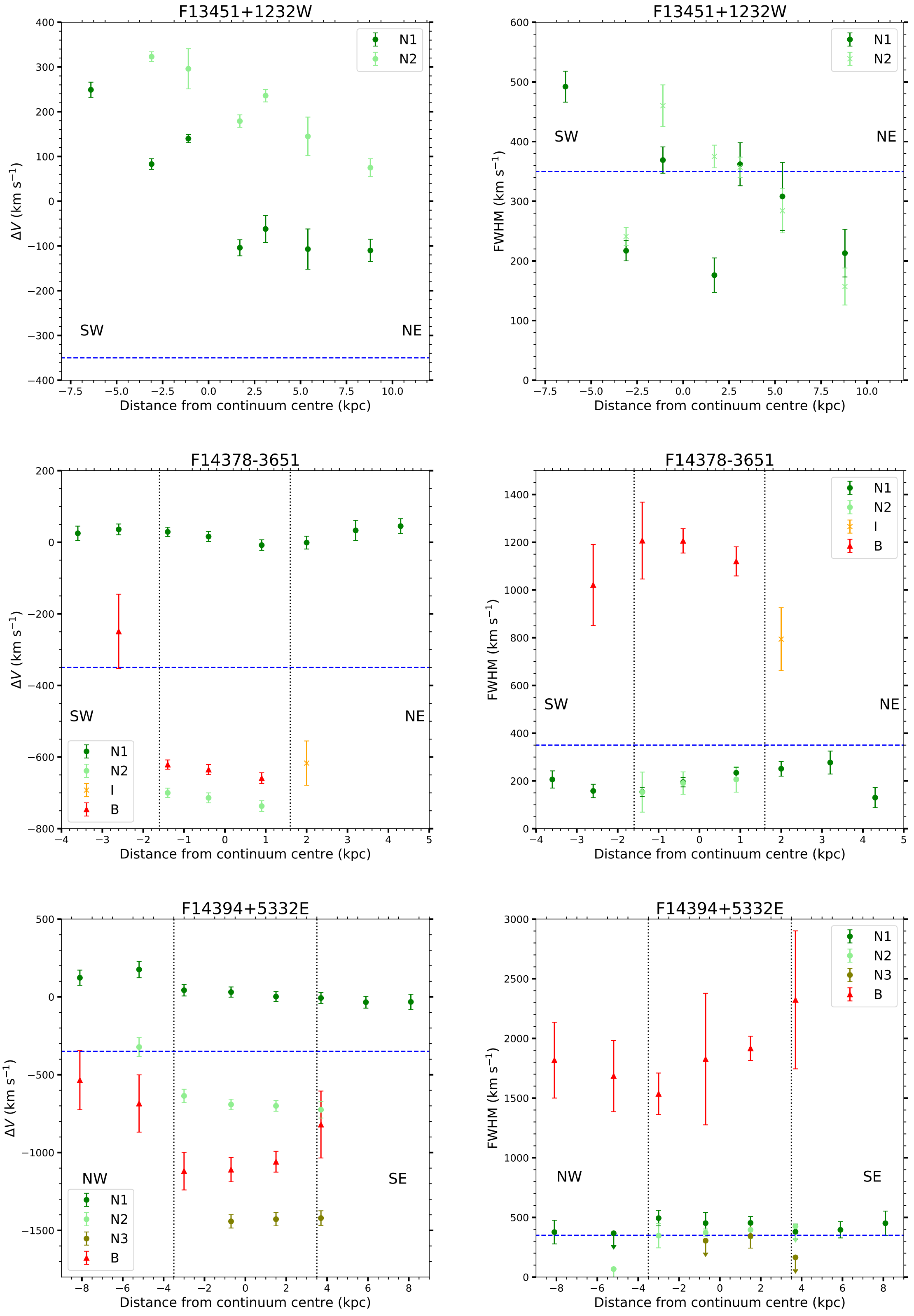

Figure 6.21: Continued from Figure 6.20. Note that the kinematics for F13451+1232W were measured using Hα.

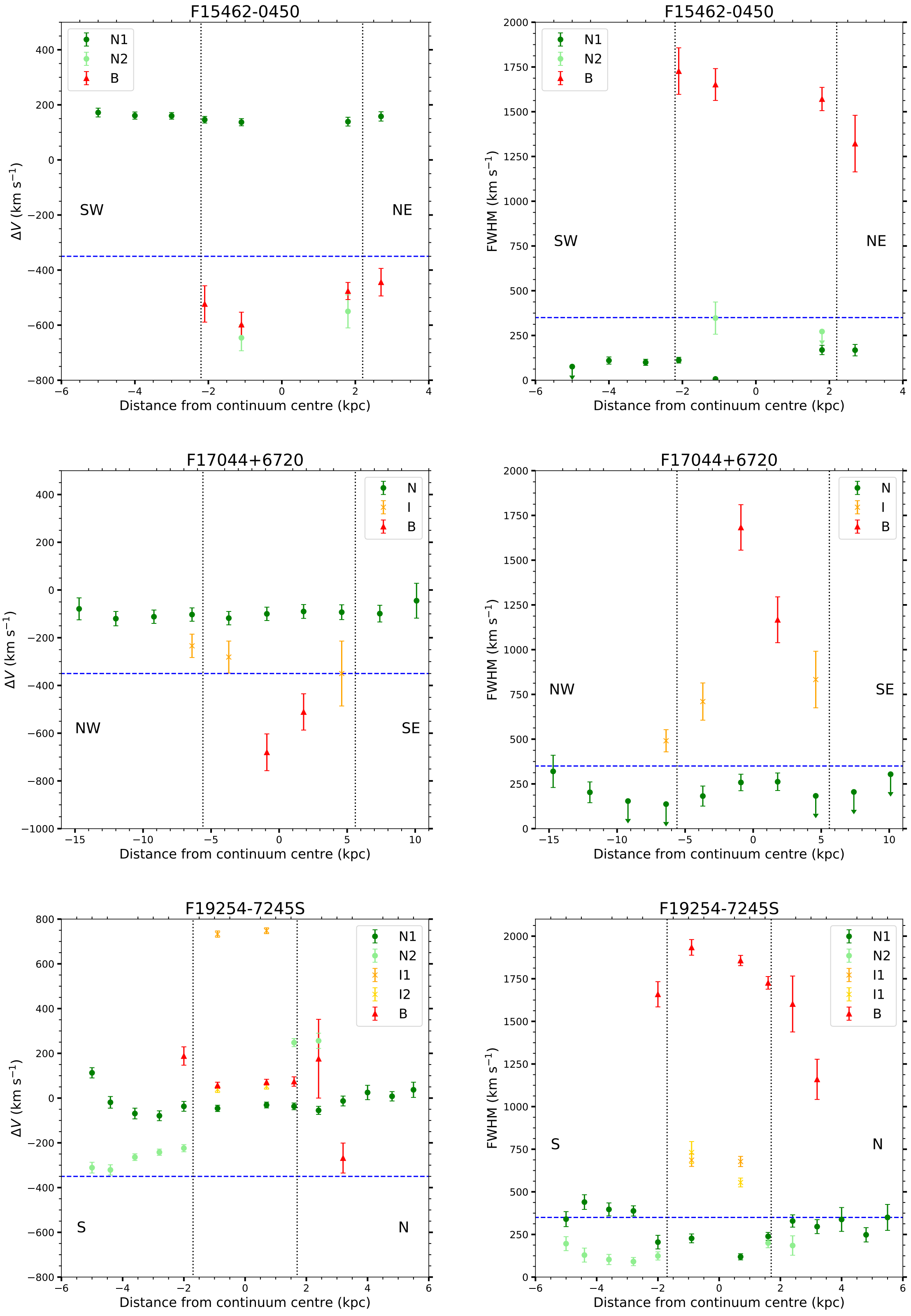

Figure 6.22: Continued from Figure 6.21.

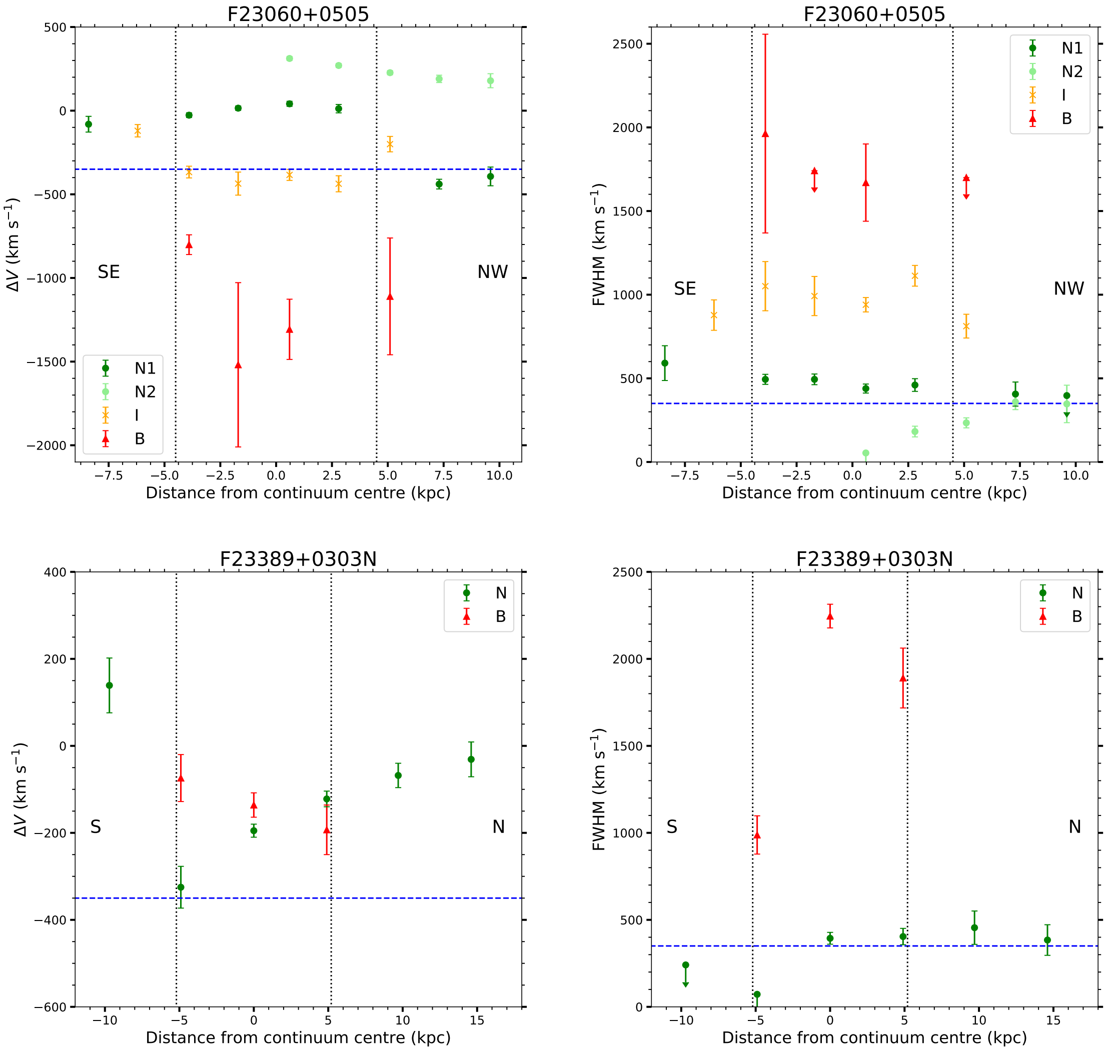

Figure 6.23: Continued from Figure 6.22.

6.5.2 Electron densities

Whilst kiloparsec-scale outflow signatures, based on the kinematic criteria, were observed in only a small number of the sample, it is nevertheless informative to estimate the potential mass outflow rates for the extended gas sampled by the apertures for all objects considered in this chapter. To do this, estimates of the electron densities were required. The uncertainties around this parameter were extensively discussed in Chapter 4.

Unfortunately, the high critical density trans-auroral [SII] and [OII] emission lines were not clearly detected in the off-nuclear spectra, therefore the traditional [SII]$\lambda\lambda$6716,6731 and [OII]$\lambda\lambda$3726,3729 doublets were used to measure the electron densities. The spectral resolution of the WHT/ISIS spectra was not good enough to resolve the [OII] doublet; however, this doublet was resolved in some cases in the higher resolution VLT/Xshooter spectra.

Despite the emission-lines in the off-nuclear regions being narrower, and the kinematics generally less complex, than the nuclear regions of the e-QUADROS ULIRGs, in most cases the uncertainties on the fluxes of the doublet components were still too large to allow accurate estimation of the electron densities for each individual aperture. This is due to the non-linear relationship between the ratios and electron densities (see Chapter 5, Figure 5.2). To get around this, an error-weighted mean [SII] and/or [OII] ratio was calculated using the total fluxes of all available extended apertures. Even then, an acceptable estimate of the electron density (i.e. a ratio more than 3σ from either the upper/lower density limit) was obtained for only 6/11 (54%) of the targets. For the remaining five targets, only 3σ upper limits could be placed on the electron density. The calculated densities or limits for each ULIRG are shown in Table 6.3. These were calculated using the TEMDEN function within IRAF, for an electron temperature of 10^4 K. Note that using error-weighted means requires the assumption that the electron density is the same across all the sampled regions which is unlikely to be true.

In general, the electron densities measured using the total fluxes for the extended gas are similar to those calculated for the nuclear outflows using the total trans-auroral emission line fluxes. Excluding upper limits, the electron densities fall in the range $2.3 < \log n_e$ (cm^{-3}) < 3.5, median[3]

---

[3] This is likely to overestimate the true median given that upper limits have been neglected.

$= 2.8 \pm 0.3$ cm^{-3}. In comparison, the electron densities based on the total trans-auroral fluxes for the nuclear regions of the WHT/ISIS ULIRGs fall in the range $2.5 < \log n_e$ (cm^{-3}) < 4.5, median $= 3.1 \pm 0.3$ cm^{-3}. These are, however, generally lower than the electron densities derived using only the broad components of the nuclear trans-auroral line ratios: $3.5 < \log n_e$ (cm^{-3}) < 4.5, median $= 3.8 \pm 0.2$ cm^{-3} (Spence et al., 2018; Rose et al., 2018, and Chapter 4).

Interestingly, the ULIRG with the highest off-nuclear electron density is F23060+0505, with an error weighted mean of $\log n_e = 3.47^{+0.30}_{-0.21}$ cm^{-3}. This weighted mean is dominated by the flux of the split components in aperture b, so can be considered representative of the potential outflow. Compression of gas by shock waves, generated as the outflow accelerates through the surrounding interstellar medium, leads to increased densities in post-shock regions (e.g. Zubovas et al., 2013). In this way, outflowing regions are expected to have higher densities than quiescent regions. The estimated density for F23060+0505 is consistent with the higher densities measured for the nuclear outflows, presented in Chapter 4 (see also Rose et al., 2018; Spence et al., 2018).

Conversely, F15462–0450 is the ULIRG with the lowest off-nuclear electron density. An upper limit of $\log n_e < 1.78$ cm^{-3} was placed using the [OII] emission-line doublet. This is significantly lower than the densities derived for any of the nuclear outflows in the e-QUADROS sample. Combined with the quiescent kinematics measured for the extended gas, it is unlikely that an extended outflow exists in this source.

6.5.3 Ionisation mechanisms

The mechanism by which AGN-driven outflows are initially accelerated is still largely unknown – theoretically the observed outflows can be driven

Table 6.3: The log n_e values determined using the error-weighted mean ratios of the total fluxes of the [SII]λ6725 blend and/or [OII]λ3727 blend, where available, across all extended apertures. All limits are 3σ.

Object name IRAS (1)	[SII](6716/6731) (2)	[OII](3729/3726) (3)	$\log(n_e)_{[SII]}$ (cm^{-3}) (4)	$\log(n_e)_{[OII]}$ (cm^{-3}) (5)
F01004–2237	0.98 ± 0.10	–	2.82 ± 0.18	–
F13305–1739	–	0.64 ± 0.04	–	$2.25^{+0.12}_{-0.16}$
F13443+0802SE	–	1.24 ± 0.20	–	$2.83^{+0.16}_{-0.22}$
F13451+1232W	1.30 ± 0.03	–	$2.08^{+0.10}_{-0.13}$	–
F14378–3651	$1.38^{+0.41}_{-0.30}$	–	<4.32	–
F14394+5332E	1.60 ± 0.25	–	<3.05	–
F15462–0450	$1.39^{+0.08}_{-0.07}$	$0.59^{+0.05}_{-0.04}$	<2.43	<1.78
F17044+6720	1.33 ± 0.19	–	<3.22	–
F19254–7245S	1.25 ± 0.06	0.86 ± 0.08	$2.25^{+0.16}_{-0.20}$	$2.30^{+0.16}_{-0.25}$
F23060+0505	0.65 ± 0.09	–	$3.47^{+0.30}_{-0.21}$	–
F23389+0303N	1.51 ± 0.08	–	<2.19	–

via energy and/or momentum propagated by shock waves (see King & Pounds, 2015), or via radiation-pressure on dust (see Fabian, 2012). One way to potentially determine this observationally is through examining the ionisation mechanism for the gas using diagnostic emission-line ratios. This can potentially determine the gas acceleration mechanism if clear distinctions can be made between shock ionisation and AGN photo-ionisation.

The ionisation mechanisms across the various extended apertures have been analysed using BPT diagnostic diagrams, and the ratios compared to those predicted by both photo-ionisation (Groves et al., 2004) and shock models (Allen et al., 2008). These diagrams are shown in Figures 6.24 through 6.34. In each of these figures the diagrams are overplotted with the following grids: top) solar abundance, pure shock model with pre-shock density set at 1 cm^{-3}; middle) solar abundance, pure shock model with pre-shock density set at 10 cm^{-3}, and bottom) dusty, radiation-pressure-dominated photo-ionisation model for a cloud of twice solar metallicity gas. The two shock models were chosen to ensure that the pre-shock densities were consistent with the range of post-shock densities calculated from the [SII] and [OII] doublets, given a compression factor of 10–100 (Dopita & Sutherland, 1995). The twice solar metallicity photo-ionisation model was chosen based on the results of Rodríguez Zaurín et al. (2013), who found that twice solar photo-ionisation models provided the best fit to the data for the nuclear outflows in ULIRGs. The individual results for each ULIRG are outlined below. The line ratios are measured using the total line fluxes within the apertures.

F01004–2237

The three main apertures extracted for F01004–2237 all lie in similar locations on the BPT diagrams in Figure 6.24. The ratios are consistent with the HII/AGN composite region in the [NII] and [SII] plots, but fall in the LINER region in the [OI] plot. This trend was also observed in Mrk 273 (Spence et al., 2016, see also Chapter 3) and is explained by the shock ionisation models. In particular, the measured ratios fall in the $200 < v < 300$ km s^{-1} region of the shock grids across all plots, consistent with the FWHM measured in Table 6.1: $230 <$ FWHM < 330 km s^{-1}. In comparison, the AGN photo-ionisation model does not reproduce the ratios consistently between the three plots. Low-velocity shocks are therefore the most likely source of ionisation in the extended regions of F01004–2237. However, given the quiescent nature of the kinematics, these shocks are probably driven by the dissipation of gas as it settles into a stable configuration after a major merger event (as in Mrk 273, Chapter 3), rather than an outflow.

F13305–1739

The four main apertures extracted for F13305–1739 are all consistent with AGN photo-ionisation based on the traditional BPT dividing lines in Figure 6.25. The AGN-photo-ionisation model also provides the best fit to the data for all regions covered by the spectroscopic slit. This supports the conclusion that the extended ionised gas observed in the spectrum of F13305-1739 is simply part of the large-scale structure of the galaxy, which is being illuminated by the AGN. Note that this object hosts one of the highest luminosity AGN in the e-QUADROS sample and therefore might be expected to photoionise the ambient gas out to large radii.

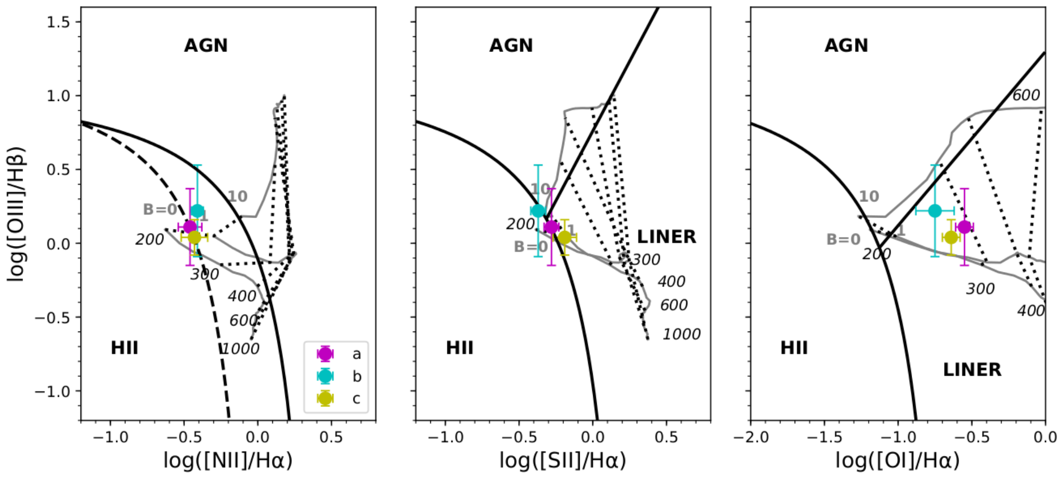

(a) Pure shock model for pre-shock density, $n_e = 1$ cm^{-3}.

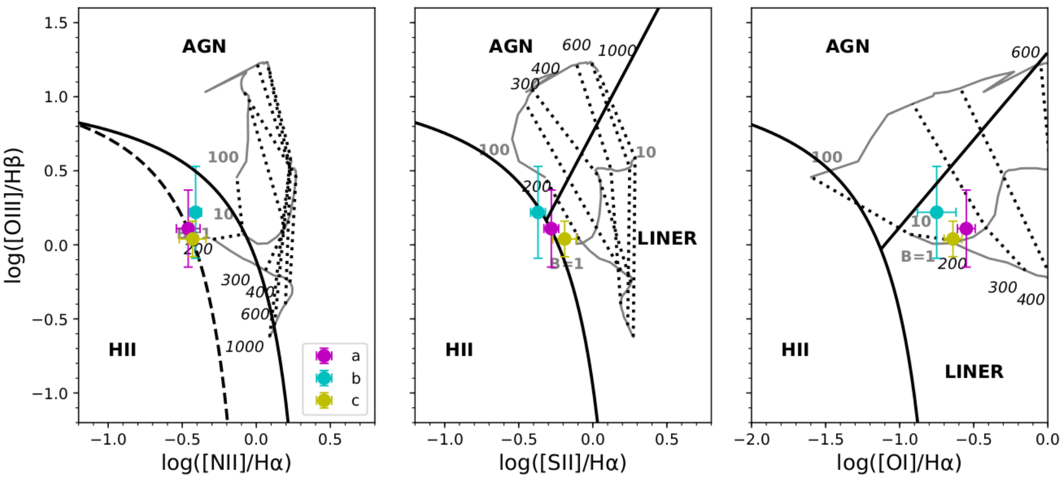

(b) Pure shock model for pre-shock density, $n_e = 10$ cm^{-3}.

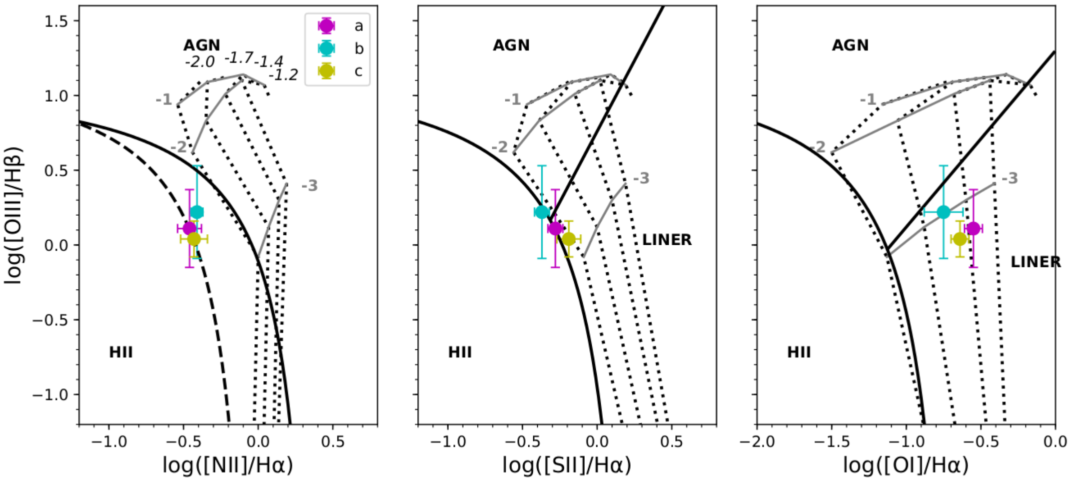

(c) AGN photo-ionisation model for a twice solar metallicity cloud.

Figure 6.24: BPT diagrams for F01004–2237, overplotted with AGN photo-ionisation and shock models. See Chapter 3, Figures 3.7 and 3.8 for model details.

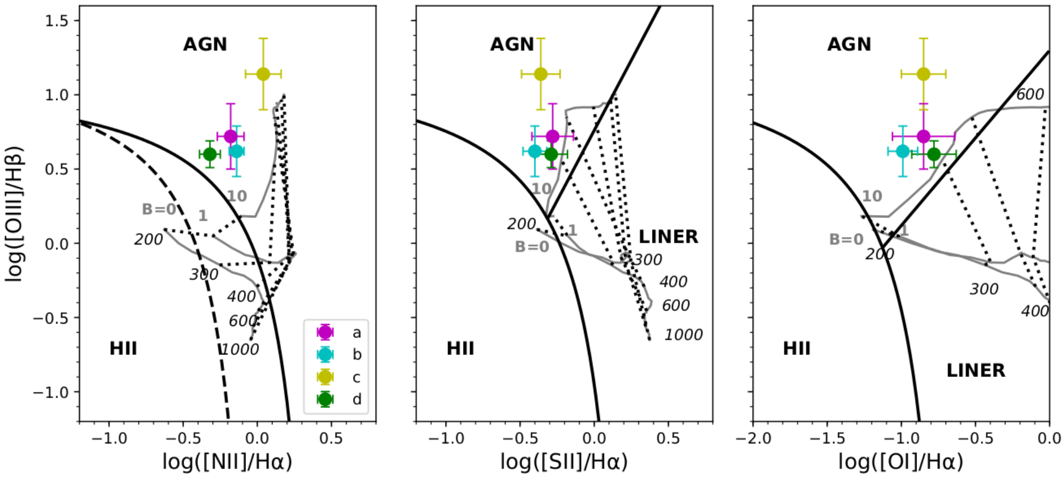

(a) Pure shock model for pre-shock density, $n_e = 1$ cm^{-3}.

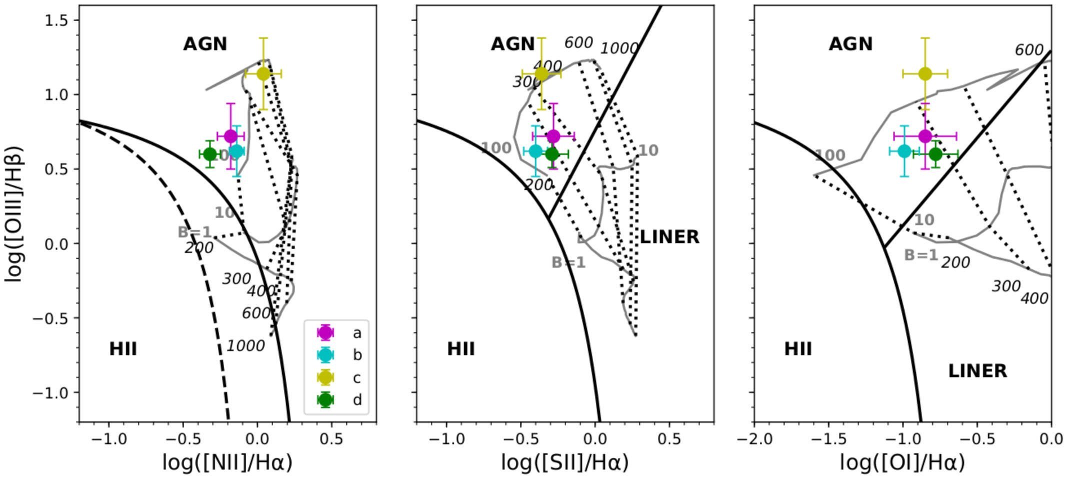

(b) Pure shock model for pre-shock density, $n_e = 10$ cm^{-3}.

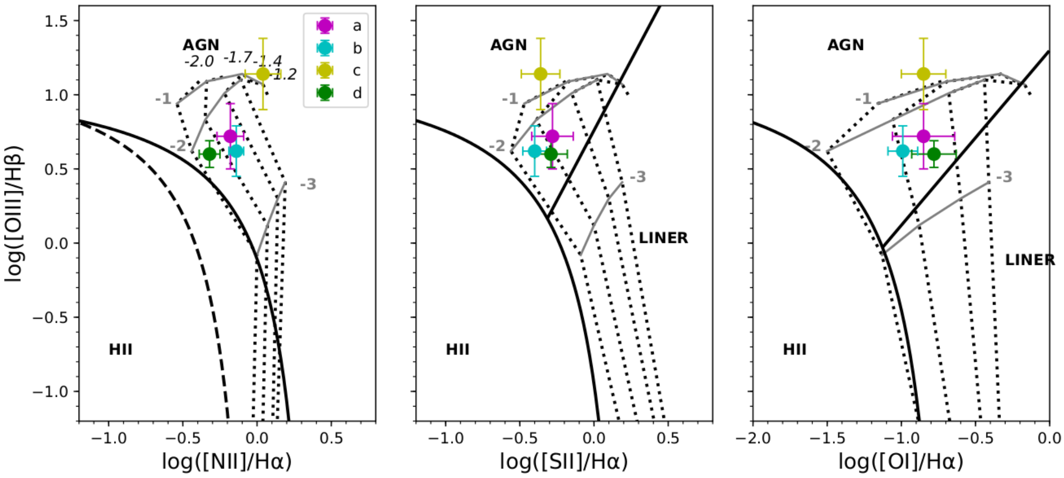

(c) AGN photo-ionisation model for a twice solar metallicity cloud.

Figure 6.25: BPT diagrams for F13305–1739, overplotted with AGN photo-ionisation and shock models. See Chapter 3, Figures 3.7 and 3.8 for model details.

F13443+0802SE

Figure 6.26 shows the BPT line ratios for the two extracted apertures in F13443+0802SE. Unlike the previous two ULIRGs in which all apertures showed similar line ratios, the two apertures in this object are significantly different. The aperture closest to the continuum centre (aperture a) falls in the AGN region of the diagram. In comparison, the more extended aperture b falls in the composite/HII region across all diagrams. Both apertures show reasonable consistency with the shock models at low velocities, but could also be explained by the AGN photo-ionisation model given the uncertainties or, in the case of aperture b, a combination of stellar and AGN photo-ionisation. Therefore it is unclear in this case what the dominant mechanism might be for these apertures.

F13451+1232W

[OIII] is generally weak in the extended regions of F13451+1232W, however its flux was measured in 6/7 of the main apertures. These are shown in Figure 6.27. The points fall mainly in the AGN region on the [NII] plot, with the two southern apertures falling close to the composite region. All apertures fall close to the AGN/LINER dividing line in the [SII] and [OI] plots. The data are remarkably consistent with the AGN photo-ionisation model for all apertures, but could also be explained reasonably well by the higher pre-shock density model. It is difficult to distinguish the dominant mechanism in this case.

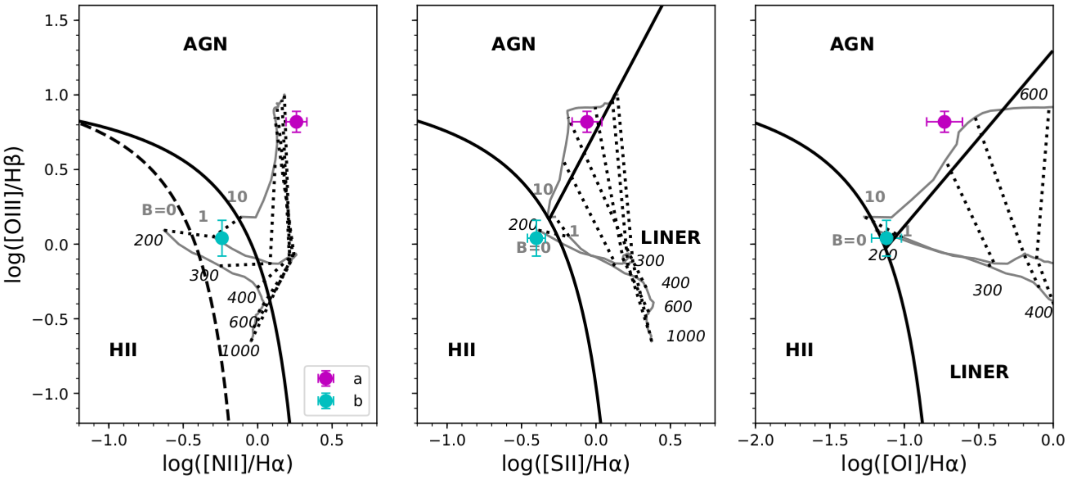

(a) Pure shock model for pre-shock density, $n_e = 1 \text{ cm}^{-3}$.

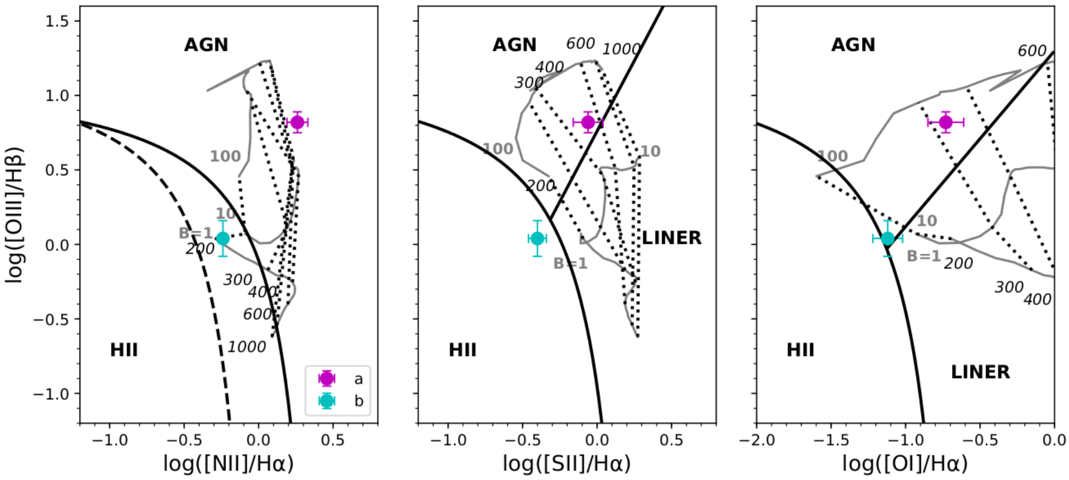

(b) Pure shock model for pre-shock density, $n_e = 10 \text{ cm}^{-3}$.

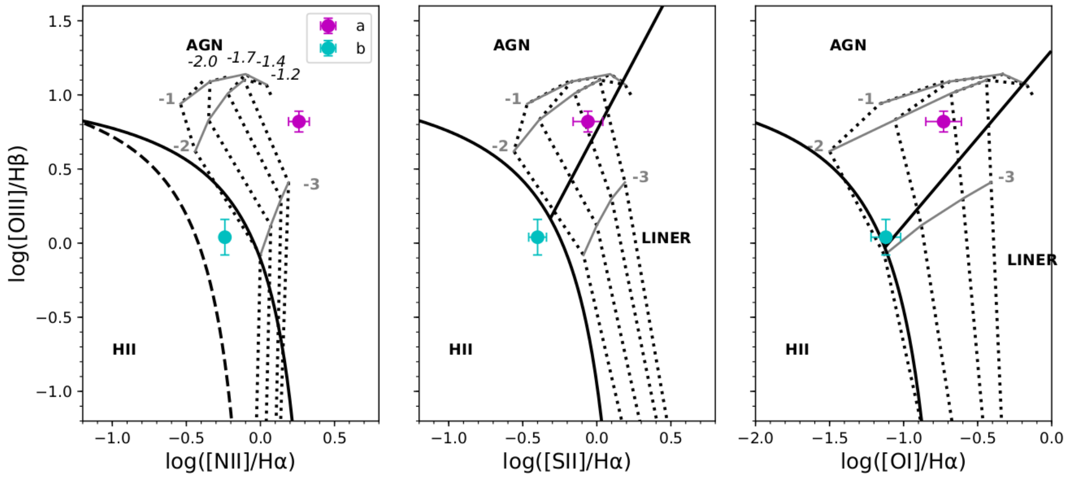

(c) AGN photo-ionisation model for a twice solar metallicity cloud.

Figure 6.26: BPT diagrams for F13443+0802SE, overplotted with AGN photo-ionisation and shock models. See Chapter 3, Figures 3.7 and 3.8 for model details.

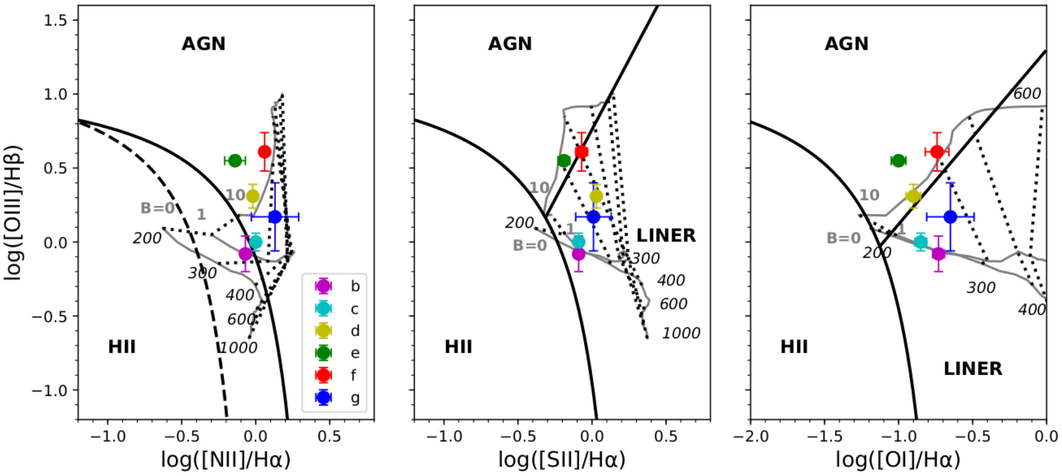

(a) Pure shock model for pre-shock density, n_e = 1 cm^{-3}.

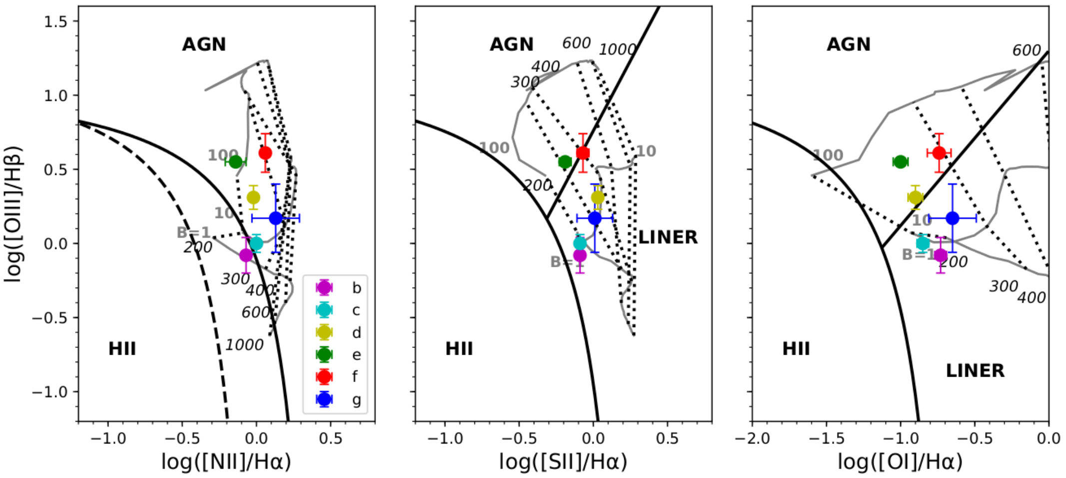

(b) Pure shock model for pre-shock density, n_e = 10 cm^{-3}.

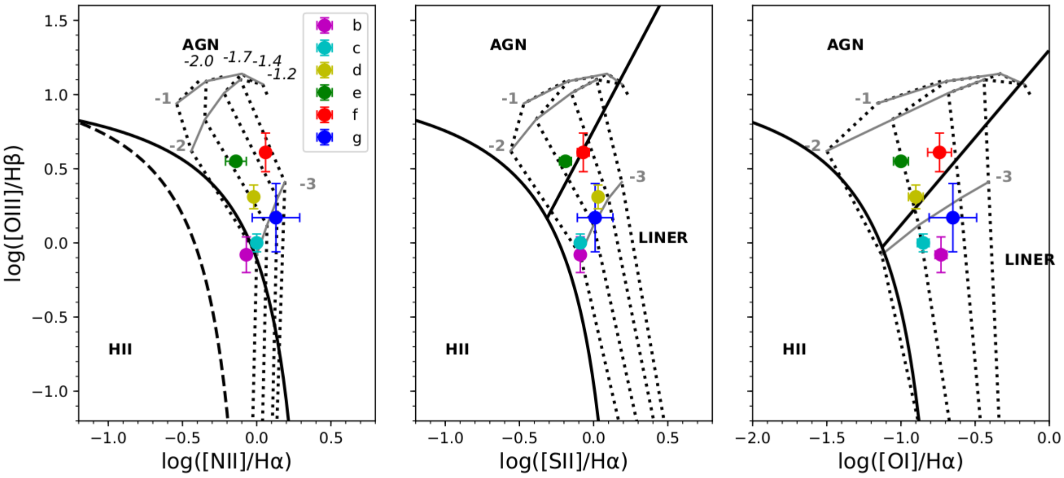

(c) AGN photo-ionisation model for a twice solar metallicity cloud.

Figure 6.27: BPT diagrams for F13451+1232W, overplotted with AGN photo-ionisation and shock models. See Chapter 3, Figures 3.7 and 3.8 for model details.

F14378–3651

Only one aperture was extracted for F14378–3651. The location of this aperture on the BPT diagrams is shown in Figure 6.28. The line ratios fall in the AGN region on the [NII] plot, and close to the AGN/LINER dividing line in the [SII] and [OI] plot. The ratios could be explained by both the AGN photo-ionisation model and the shock models, therefore it is unclear in this case what the dominant ionisation mechanism might be.

F14394+5332E

Two apertures were extracted for F14394+5332E, one to the NW (aperture a) and one to the SE (aperture b) of the continuum centre. Interestingly, the line ratios of the two apertures are markedly different. The BPT ratios (Figure 6.29) for the NW aperture fall in the AGN/LINER regions. The SE ratios, however, fall close to the composite region on the [NII] plot, and close to the join between the AGN, LINER and HII dividing lines on the [SII] and [OI] plots. Aperture a could be explained by either the AGN photo-ionisation or shock models. However, the predicted shock velocity for aperture b ($\sim$200 km s^{-1}) is lower than the FWHM measured in Table 6.2: 357 ± 34 km s^{-1}. Therefore this aperture is most likely ionised by the AGN, or a combination of stellar and AGN photo-ionisation.

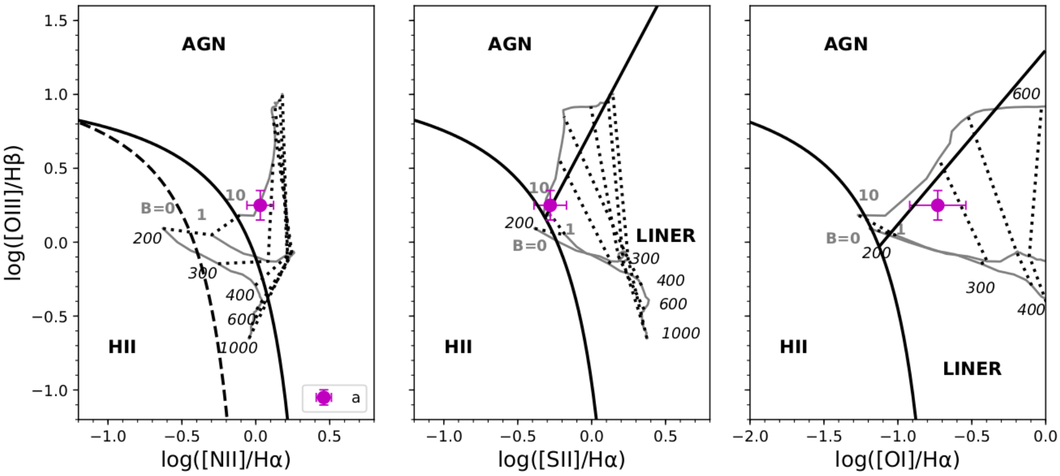

(a) Pure shock model for pre-shock density, $n_e = 1$ cm^{-3}.

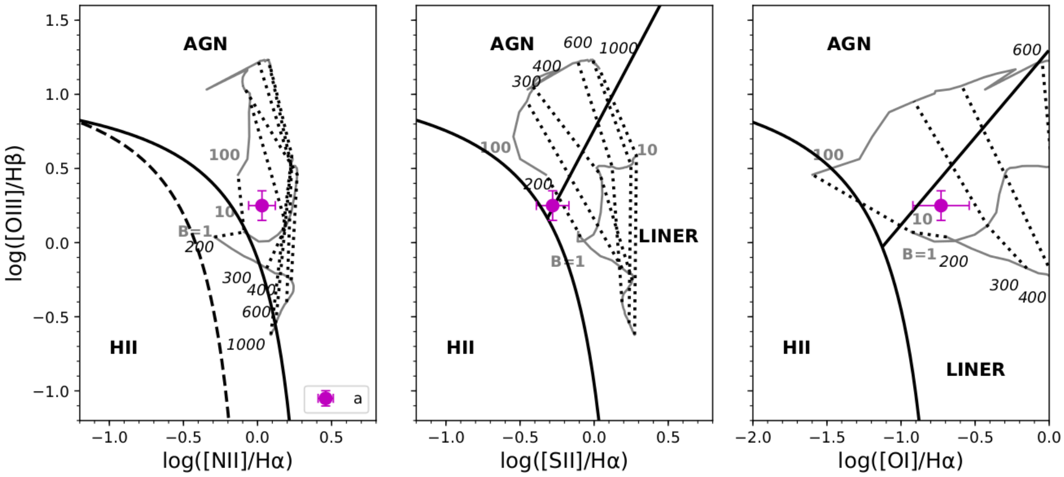

(b) Pure shock model for pre-shock density, $n_e = 10$ cm^{-3}.

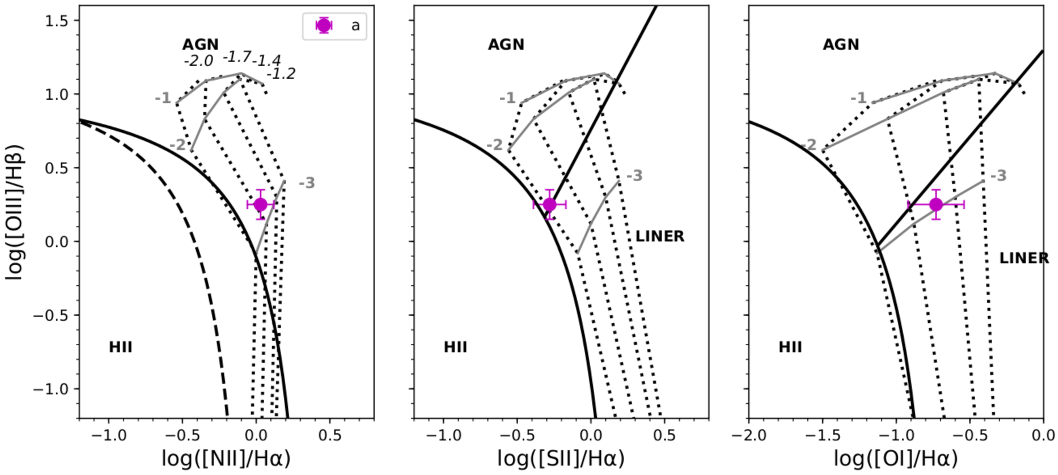

(c) AGN photo-ionisation model for a twice solar metallicity cloud.

Figure 6.28: BPT diagrams for F14378–3651, overplotted with AGN photo-ionisation and shock models. See Chapter 3, Figures 3.7 and 3.8 for model details.

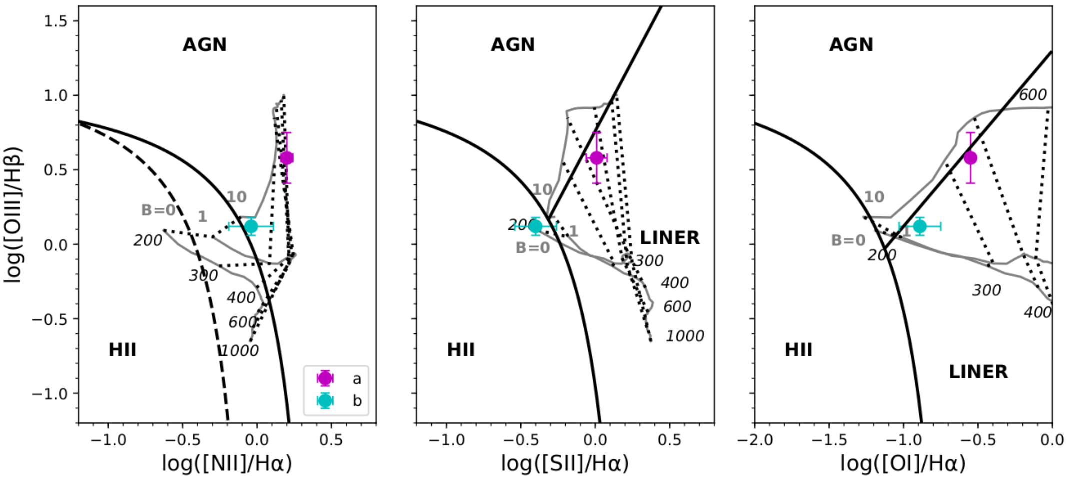

(a) Pure shock model for pre-shock density, $n_e = 1$ cm^{-3}.

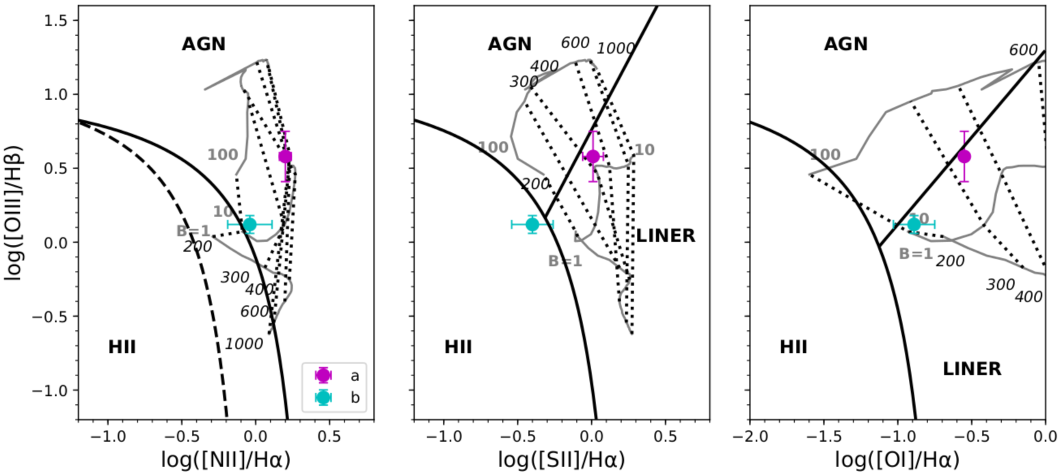

(b) Pure shock model for pre-shock density, $n_e = 10$ cm^{-3}.

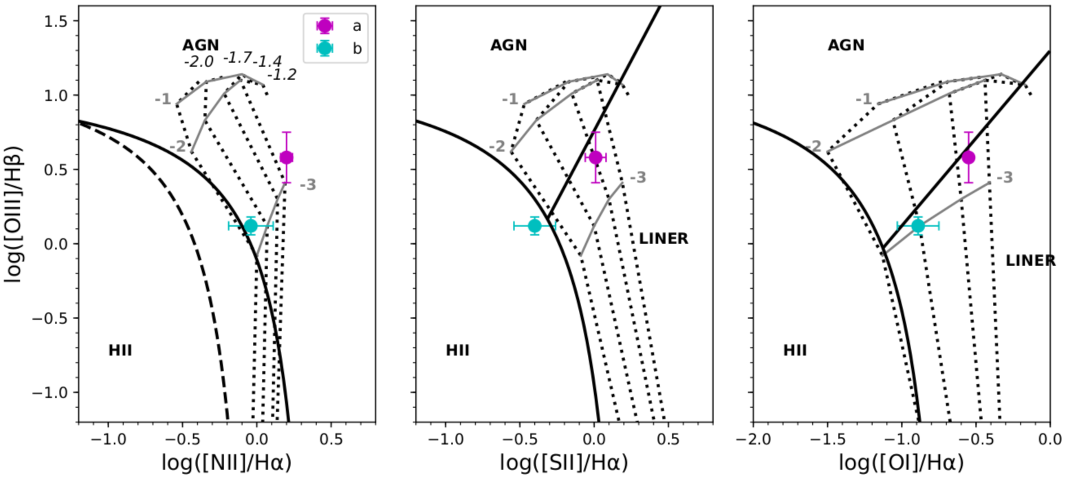

(c) AGN photo-ionisation model for a twice solar metallicity cloud.

Figure 6.29: BPT diagrams for F14394+5332E, overplotted with AGN photo-ionisation and shock models. See Chapter 3, Figures 3.7 and 3.8 for model details.

F15462–0450

The BPT diagrams for the single aperture extracted for F15462–0450 are shown in Figure 6.30. The aperture falls on the AGN/composite dividing line in the [NII] plot, the HII region in the [SII] plot, and the join between all three regions on the [OI] plot. The dominant photo-ionisation mechanism is therefore inconclusive from these results. The line ratios show poor consistency with the AGN photo-ionisation model. They are, however, reasonably consistent with the lower pre-shock density shock model at low velocities (FWHM = 103±14 km s^{-1}; $\Delta v = 153 \pm 12$ km s^{-1}). The extended halo in this object therefore appears to be ionised either by some combination of stellar photo-ionisation and low velocity shocks, or a mixture of AGN and stellar photo-ionisation.

F17044+6720

Figure 6.31 shows the BPT diagrams for F17044+6720. Based on their locations on the plots, the northern aperture a – which samples the spectacular extended, bright condensations seen in optical imaging – is consistent with AGN photo-ionisation, and the southern aperture b is more consistent with HII/LINER photo-ionisation. In terms of the theoretical models, aperture a is inconsistent with the shock models, but somewhat consistent with the twice solar photo-ionisation model. The measured [NII] flux, however, is weaker than expected, and could indicate lower abundances. Aperture b, on the other hand, is best explained with the lower density shock model with a shock velocity ∼200 km s^{-1}, consistent with the measured FWHM of 176±73 km s^{-1}.

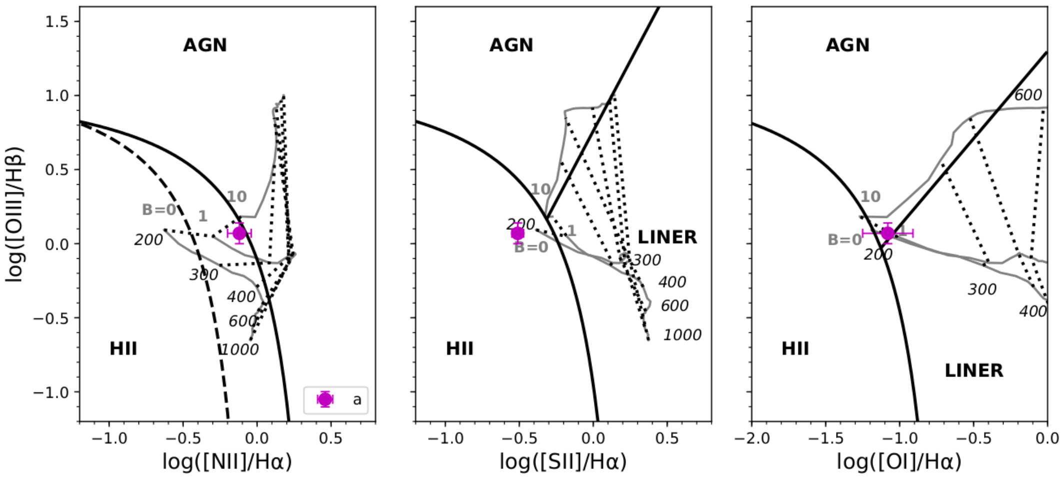

(a) Pure shock model for pre-shock density, $n_e = 1$ cm^{-3}.

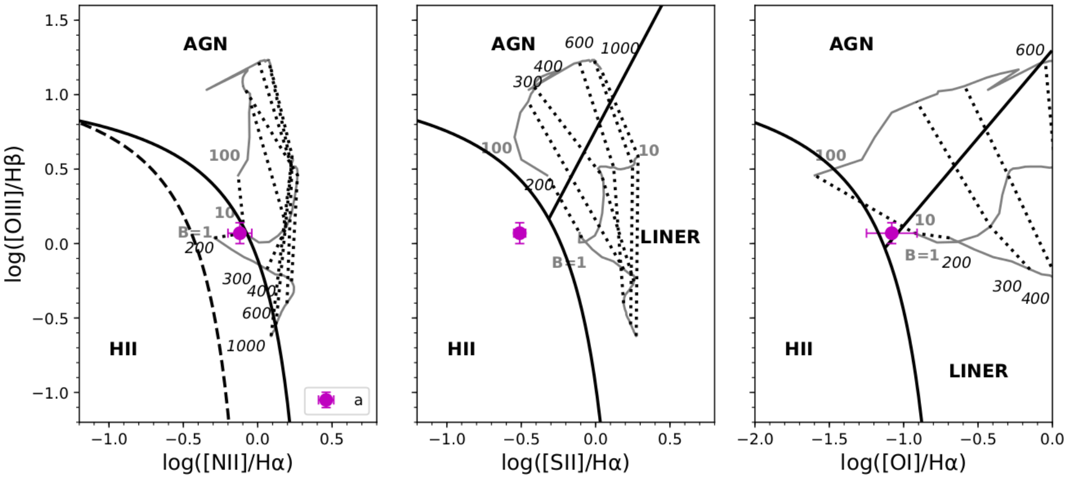

(b) Pure shock model for pre-shock density, $n_e = 10$ cm^{-3}.

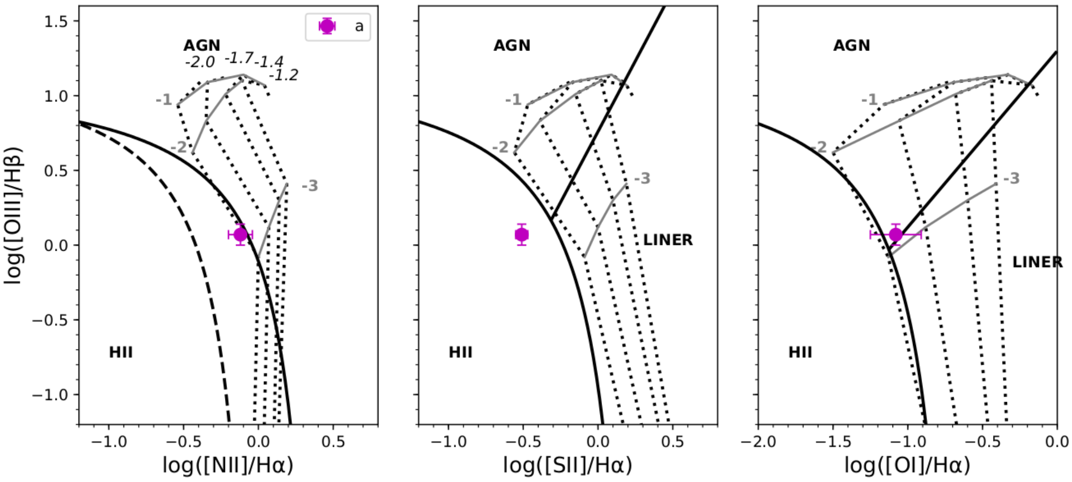

(c) AGN photo-ionisation model for a twice solar metallicity cloud.

Figure 6.30: BPT diagrams for F15462–0450, overplotted with AGN photo-ionisation and shock models. See Chapter 3, Figures 3.7 and 3.8 for model details.

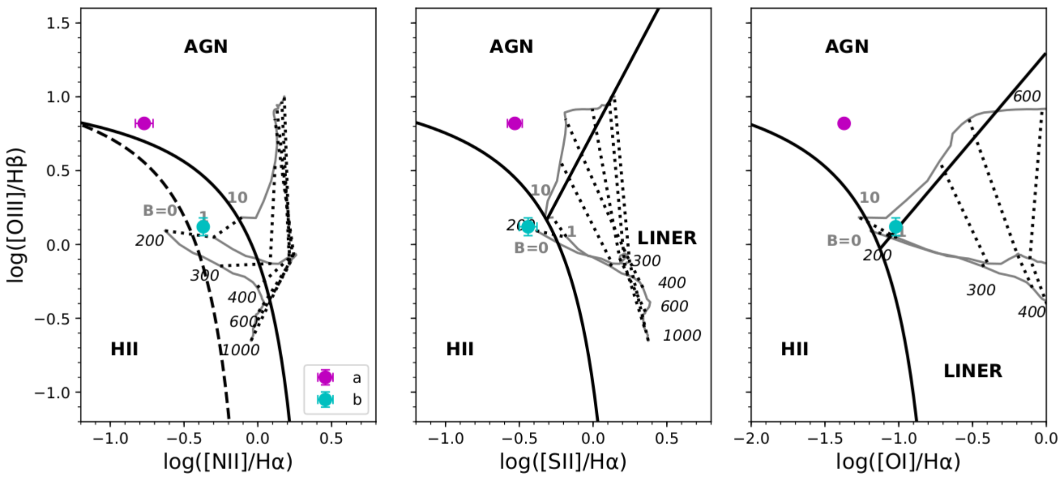

(a) Pure shock model for pre-shock density, $n_e = 1\ \mathrm{cm}^{-3}$

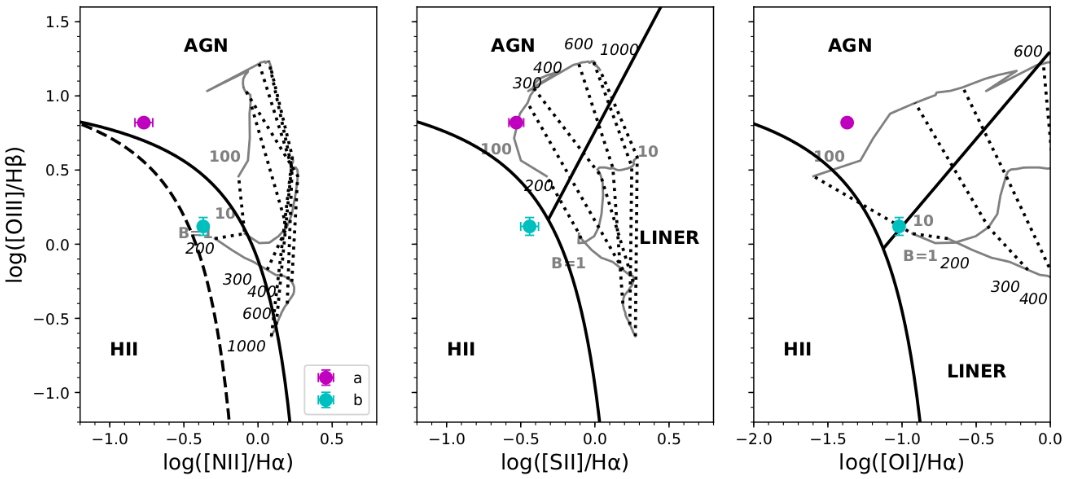

(b) Pure shock model for pre-shock density, $n_e = 10\ \mathrm{cm}^{-3}$

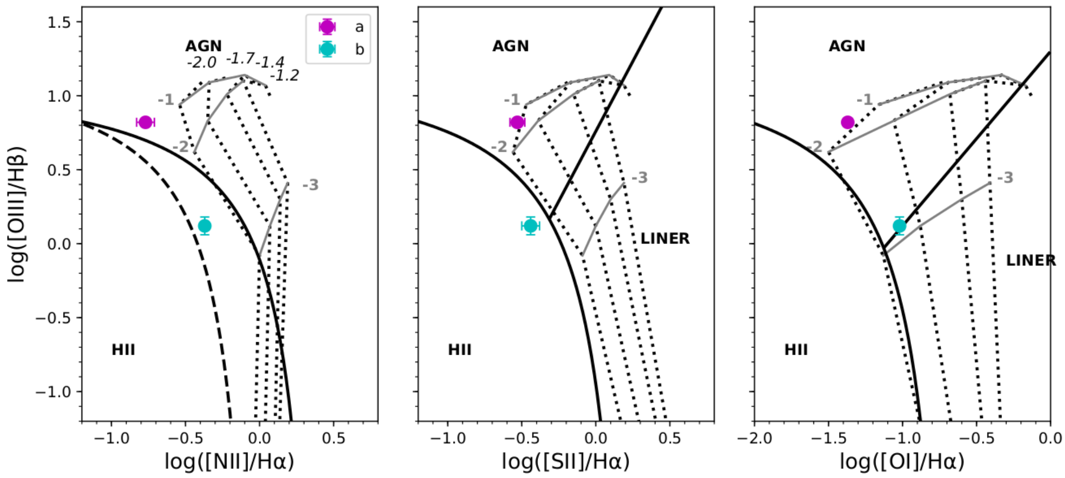

(c) AGN photo-ionisation model for a twice solar metallicity cloud

Figure 6.31: BPT diagrams for F17044+6720, overplotted with AGN photo-ionisation and shock models. See Chapter 3, Figures 3.7 and 3.8 for model details.

F19254–7245S

F19254–7245S shows the most complex structure in the off-nuclear emission line gas, and potential for extended outflows based on the [OIII], Hα and [NII] kinematics. The BPT diagrams for this object are shown in Figure 6.32. In general, all apertures are consistent with AGN photo-ionisation based on the traditional dividing lines, however apertures c, e and g do fall either close to or inside the LINER region on the [SII] and [OI] plots. It is clear though that the extended emission-line gas is not dominated by star formation. In general all apertures could be explained equally well by the AGN photo-ionisation model or the higher density shock model.

F23060+0505

Figure 6.33 shows the BPT diagrams for F23060+0505. Two apertures were extracted for this object, one to the SE (aperture a) and one to the NW (aperture b) of the nucleus. Emission line splitting observed in aperture b indicates the potential for extended outflows in this region. The line ratios for aperture b are consistent with AGN photo-ionisation across all BPT plots. Aperture a is similar, although it does fall close to the HII/LINER dividing lines in the [SII] and [OI] plots. In terms of theoretical models, aperture a is best explained by the shock models, whereas aperture b is best explained by the AGN photo-ionisation model.

F23389+0303N

Finally, the BPT diagrams for F23389+0303N are shown in Figure 6.34. In this case, two apertures were extracted to the south of the continuum centre. Both apertures are consistent with composite/LINER photo-ionisation based on the traditional BPT dividing lines. Given the relatively large error bars, the data could be explained with both the shock models and the AGN photo-ionisation models, or a combination of stellar and AGN photo-ionisation.

Ionisation summary

In general, the significant amount of overlap in the BPT diagrams between AGN photo-ionisation and radiative shock models makes it challenging to distinguish the true ionisation mechanism for the extended apertures in the sample of local ULIRGs. In most of the cases presented here, the measured ratios could be equally well explained using both models, or a combination of stellar and AGN photo-ionisation. The most clear-cut cases are F01004–2237 – for which the data support low velocity shocks as the dominant mechanism across the extended halo (similar to Mrk 273, Chapter 3) – and F13305–1739 – for which the dominant mechanism appears to be AGN photo-ionisation. Interestingly, the line ratios for the apertures which show the clearest kinematic evidence for outflows (F13451+1232W, apertures c and e; F19254–7254S, apertures a and b; and F23060+0505, aperture b do not show any preference to one particular model, and are indistinguishable from the line ratios of the kinematically quiescent regions based on the BPT diagnostic diagrams.

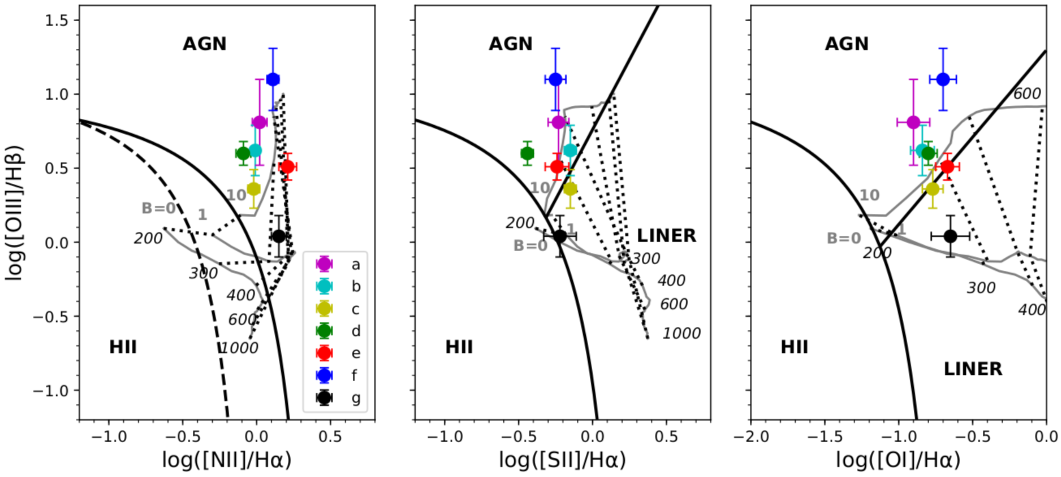

(a) Pure shock model for pre-shock density, $n_e = 1$ cm^{-3}.

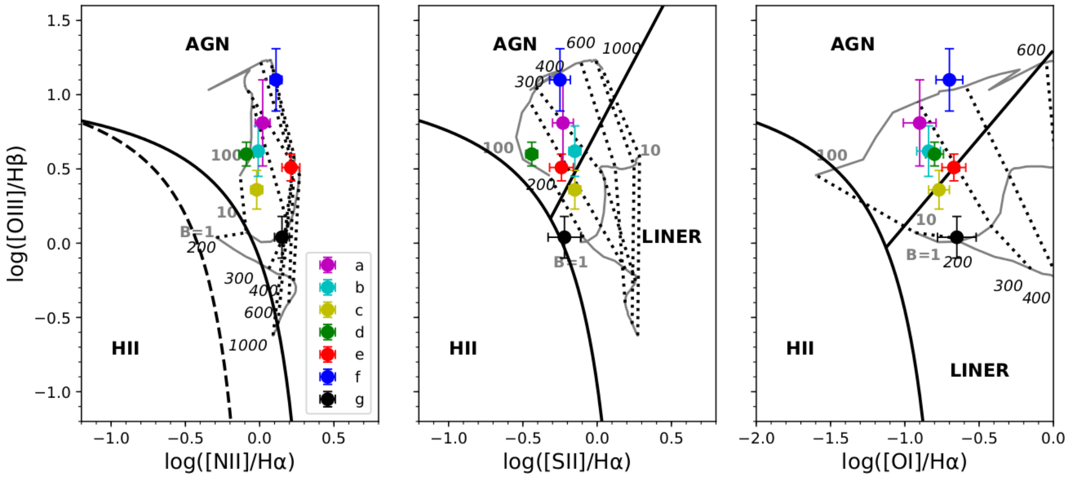

(b) Pure shock model for pre-shock density, $n_e = 10$ cm^{-3}.

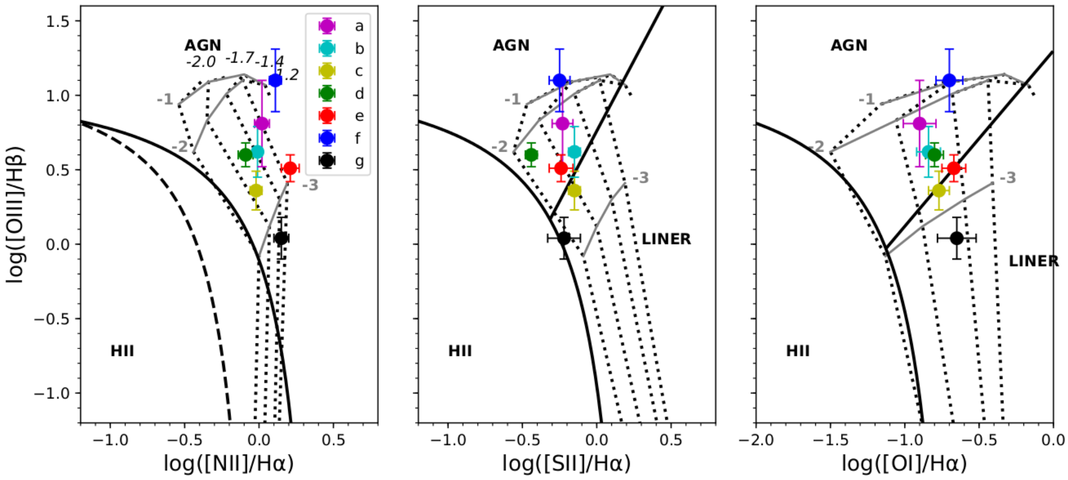

(c) AGN photo-ionisation model for a twice solar metallicity cloud.

Figure 6.32: BPT diagrams for F19254–7245S, overplotted with AGN photo-ionisation and shock models. See Chapter 3, Figures 3.7 and 3.8 for model details.

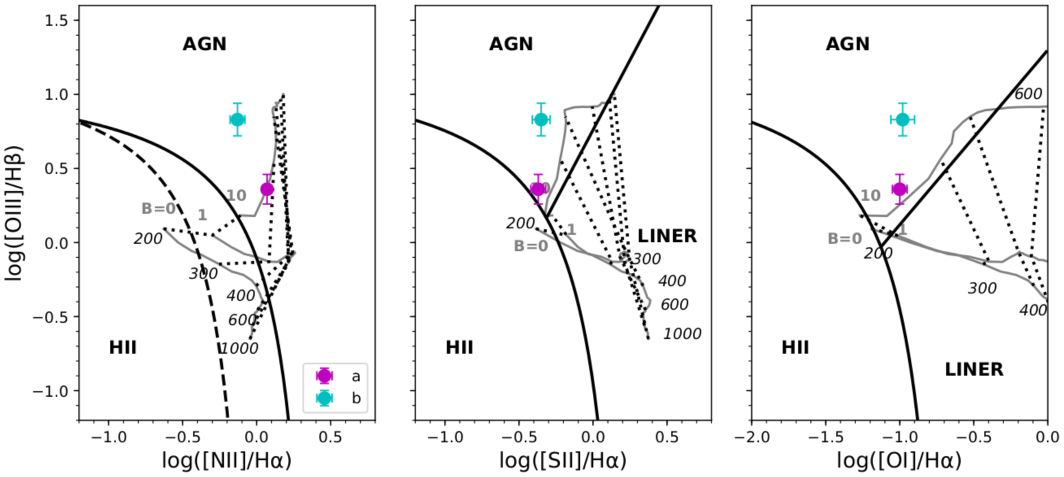

(a) Pure shock model for pre-shock density, $n_e = 1$ cm^{-3}.

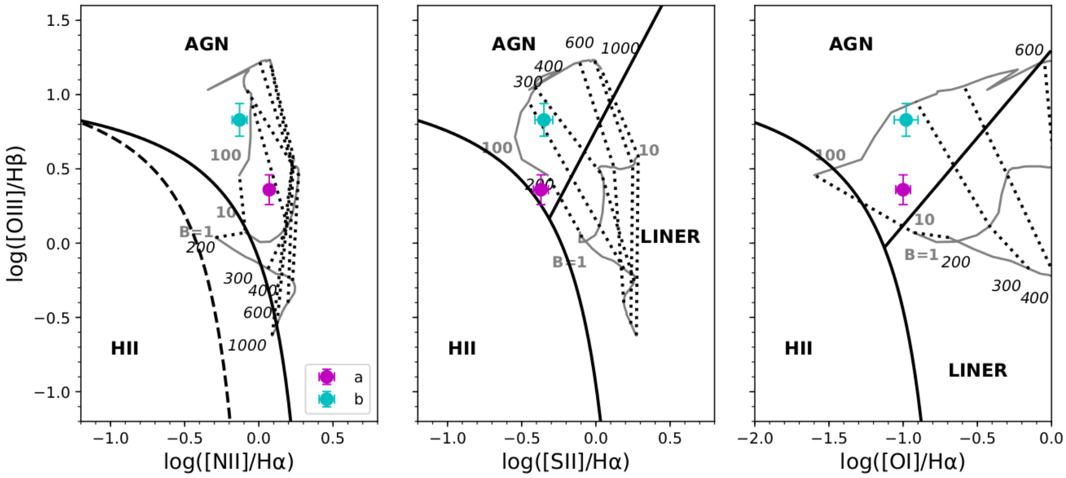

(b) Pure shock model for pre-shock density, $n_e = 10$ cm^{-3}.

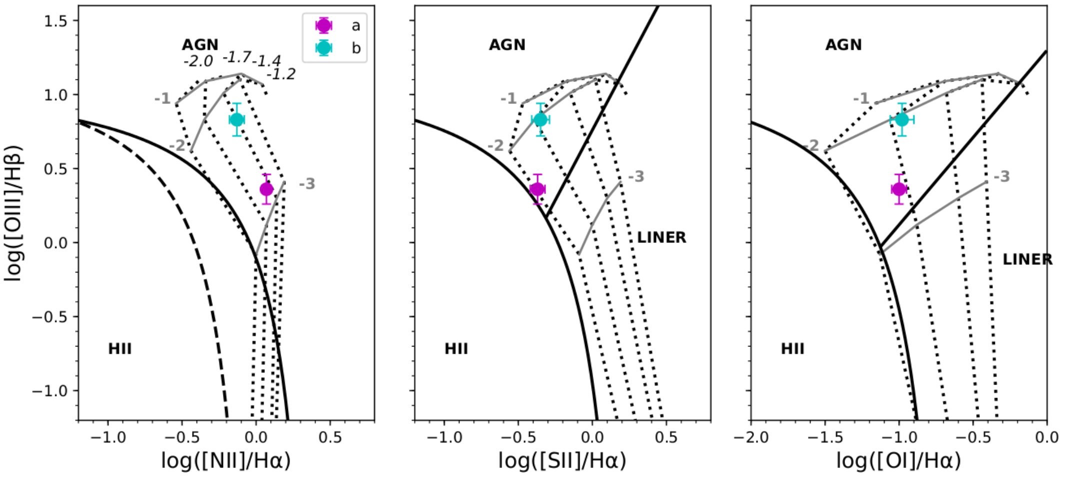

(c) AGN photo-ionisation model for a twice solar metallicity cloud.

Figure 6.33: BPT diagrams for F23060+0505, overplotted with AGN photo-ionisation and shock models. See Chapter 3, Figures 3.7 and 3.8 for model details.

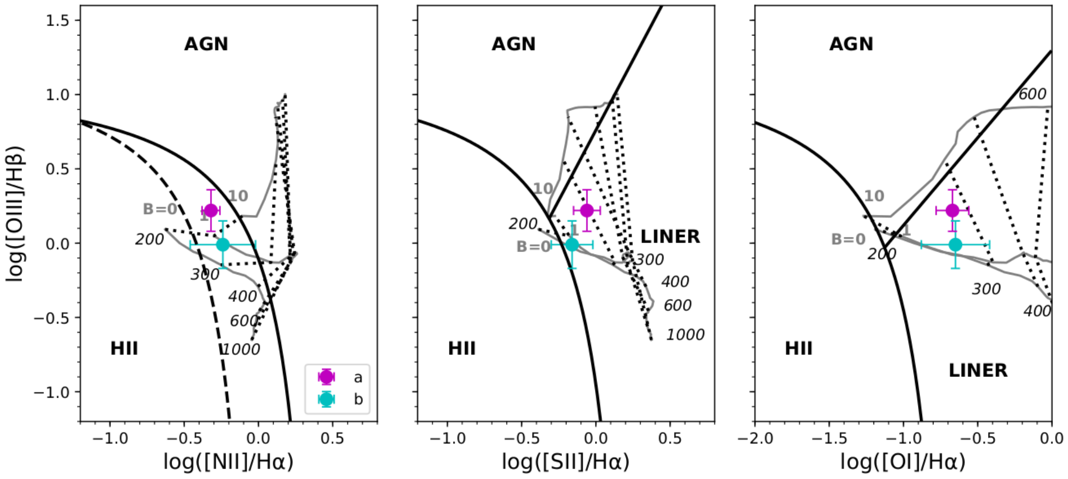

(a) Pure shock model for pre-shock density, $n_e = 1$ cm^{-3}.

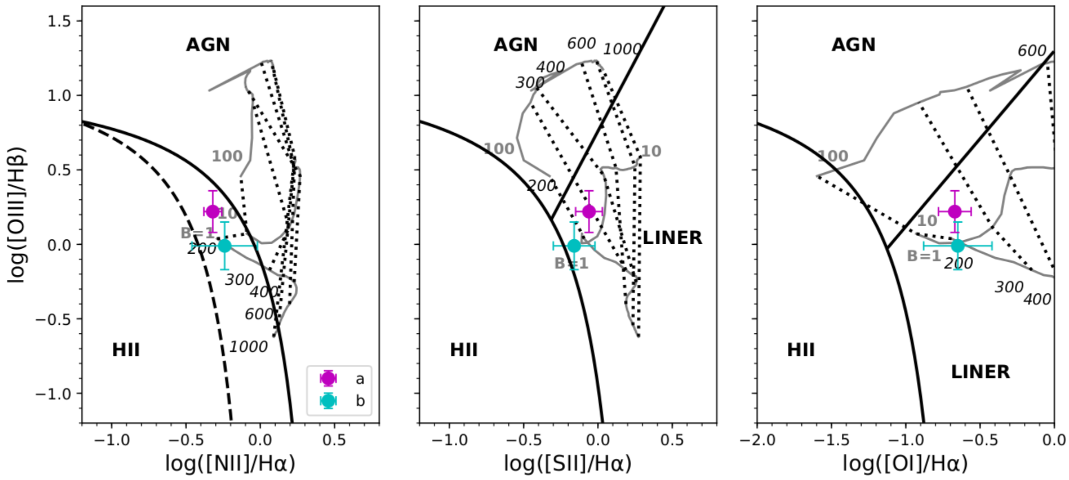

(b) Pure shock model for pre-shock density, $n_e = 10$ cm^{-3}.

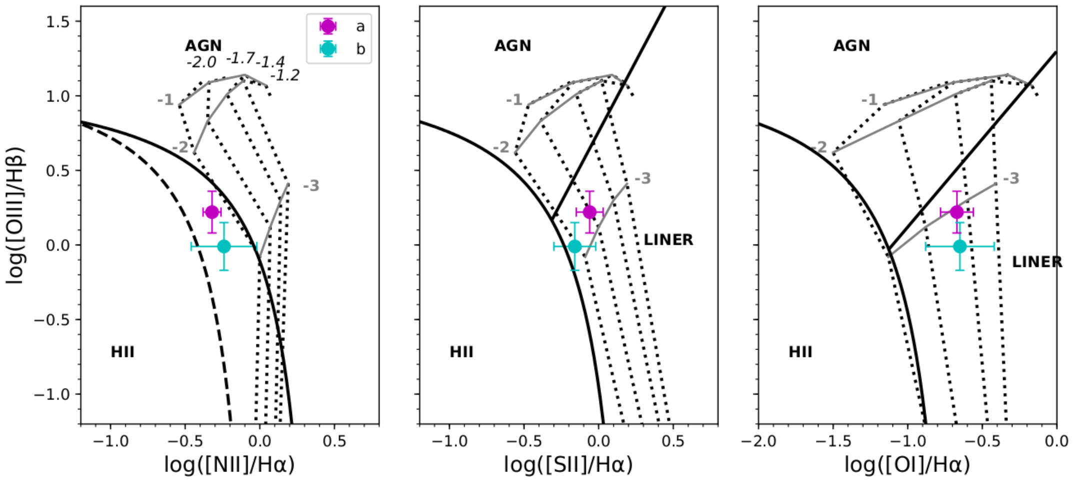

(c) AGN photo-ionisation model for a twice solar metallicity cloud.

Figure 6.34: BPT diagrams for F23389+0303N, overplotted with AGN photo-ionisation and shock models. See Chapter 3, Figures 3.7 and 3.8 for model details.

6.5.4 Extended gas masses

One of the questions this chapter aims to answer is, given that extended emission-line gas is seen in a large proportion (60%) of the e-QUADROS ULIRGS, what is the maximum mass which might be contained off-nucleus and, if this were part of an outflow, what would the typical mass outflow rates and kinetic powers be? The extended gas masses can be calculated using equation 3.2 from Chapter 3.

For these calculations, a maximal velocity, v_{max}, was used, derived by taking the absolute velocity shifts of the extended [OIII] or Hα emission-line components plus 2σ, where $\sigma = \frac{FWHM}{2.355}$. Note that this approach was also used by Rupke & Veilleux (2013). In the case of split components, the absolute velocity shift of the most shifted component, plus 2σ, was used. This maximal velocity approach enables the maximum possible mass outflow rates to be calculated. In addition, it enables comparison with the properties of the nuclear outflows presented in Chapter 4, calculated for the maximal v_{05} velocities [4].

The best available error-weighted mean densities shown in Table 6.3 were used in all aperture mass calculations. Note that no reddening corrections have been made, due to the uncertainties in the Hα/Hβ ratios being too large to draw meaningful conclusions regarding the reddening. This may cause the resulting gas masses (and resultant mass outflow rates) to be under-estimated. Hα, however, is less affected by reddening than Hβ, and the extended regions are expected to be less affected by dust extinction (see Chapter 3). In addition, the flux from any components obviously associated with the nuclear seeing disc was excluded (see Tables 6.1 and 6.2). The gas masses calculated for each aperture are shown in Tables 6.4

---

[4] Note that in this case, 2.5% of the gas has more negative (i.e. higher absolute) velocities than the calculated v_{max}. These velocities are therefore more extreme than the v_{05} values used in Chapter 4, for which 5% of the gas had more negative velocities.

and 6.5. The estimated masses of emission-line gas, M, contained within the extended apertures for each object range from $M = 4.1 \times 10^2\,\mathrm{M}_\odot$ to $M > 1.2 \times 10^6\,\mathrm{M}_\odot$.

Of course, in most cases the spectroscopic slit only samples a section of the extended halo. Considering the simple example of an isotropic outflow centred on the nucleus, which appears as a shell on the sky, an aperture of width T_{ap} extracted from a spectrum obtained with a slit of width T_{slit} samples an area A_{slit} of the outflow. This is illustrated by Figure 6.35. Therefore, using this geometry, a correction factor, f, can be calculated to convert the mass within a particular aperture, M_{ap}, into a total mass within an annulus of the same width, M_{ann} using the following equation:

$$f = \frac{A_{ann}}{A_{ap}} = \frac{\pi(r_2^2 - r_1^2)}{T_{ap}T_{slit}} \tag{6.1}$$

The total annulus gas masses, M_{ann}, calculated this way can be considered upper limits on the total amount of emission-line gas that could be present at the radii of the extended apertures for each of the e-QUADROS ULIRGs. These values are presented in column 6 in Tables 6.4 and 6.5.

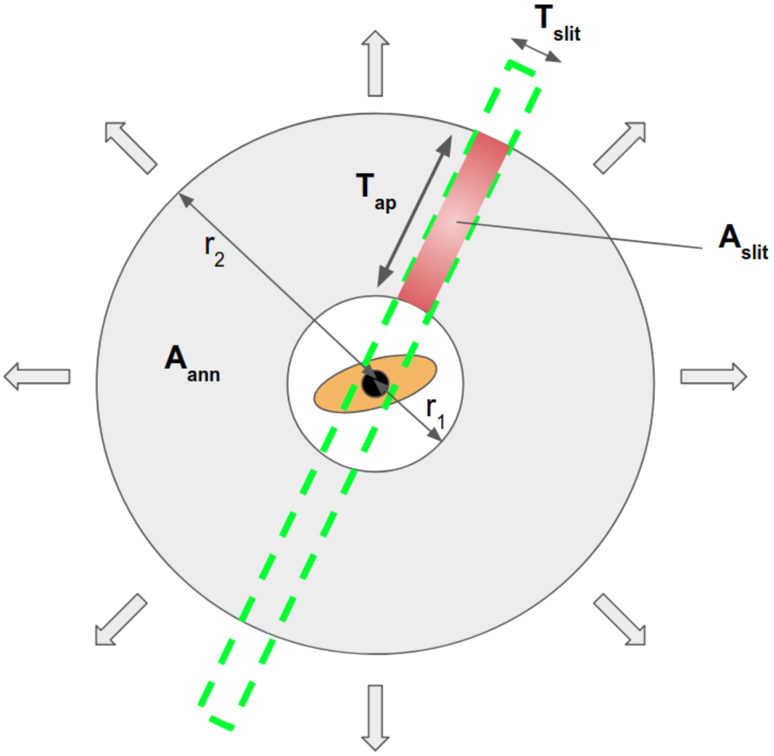

Figure 6.35: Diagram indicating the geometry of an isotropic outflow. The green rectangle represents a spectroscopic slit, illustrating that only a small fraction of the total gas is sampled by the slit. r_1 and r_2 represent the inner and outer radii of an annulus of gas. A_{slit} is the total area sampled by the slit, determined by the slit width, T_{slit}, and aperture width, T_{ap}. A_{ann} is the total area of the annulus. Relative scales exaggerated for clarity.

6.5.5 Mass outflow rates and kinetic powers

The estimated masses contained within each aperture can be converted into a mass outflow rate by considering the aperture crossing-time of the gas. Note that, while only three objects show clear signs of outflows, for completeness mass outflow rates are calculated for all apertures regardless of whether or not the kinematic and BPT analyses support the case for an outflow. Because the velocity criteria and ionisation mechanisms are somewhat uncertain, it is informative to estimate the outflow rates of each aperture in order to assess the *potential* importance of any extended

Table 6.4: Gas masses, mass outflow rates and kinetic powers for the extended apertures.

Object name IRAS	Aperture	v_{max} (km s^{-1})	M_{ap} (M$_\odot$)	$\dot{M}_{ap}$ (M$_\odot$ yr^{-1})	$\dot{E}_{ap}$ (erg s^{-1})	M_{ann} (M$_\odot$)	$\dot{M}_{ann}$ (M$_\odot$ yr^{-1})	$\dot{E}_{ann}$ (erg s^{-1})
(1)	(2)	(3)	(4)	(5)	(6)	(7)	(8)	(9)
F01004–2237	a	-291 ± 140	$(5.7^{+3.4}_{-2.1}) \times 10^4$	$(2.8^{+3.8}_{-1.5}) \times 10^{-3}$	$(7.5^{+31.6}_{-6.6}) \times 10^{37}$	$(1.4^{+0.8}_{-0.5}) \times 10^6$	$(7.0^{+10.0}_{-3.7}) \times 10^{-2}$	$(1.9^{+7.9}_{-1.6}) \times 10^{39}$
	b	-242 ± 145	$(6.2^{+3.5}_{-2.2}) \times 10^4$	$(6.4^{+9.6}_{-3.4}) \times 10^{-3}$	$(1.2^{+6.4}_{-1.1}) \times 10^{38}$	$(8.8^{+5.0}_{-3.1}) \times 10^5$	$(9.0^{+13.7}_{-4.8}) \times 10^{-2}$	$(1.7^{+9.1}_{-1.6}) \times 10^{39}$
	c	-305 ± 85	$(5.4^{+3.3}_{-2.0}) \times 10^4$	$(1.5^{+1.6}_{-0.7}) \times 10^{-3}$	$(4.4^{+10.4}_{-3.2}) \times 10^{37}$	$(2.0^{+1.2}_{-0.7}) \times 10^6$	$(5.5^{+5.8}_{-2.7}) \times 10^{-2}$	$(1.6^{+3.8}_{-1.2}) \times 10^{39}$
F13305–1739	a	-175 ± 27	$(6.0^{+3.0}_{-1.7}) \times 10^4$	$(6.7^{+4.9}_{-2.4}) \times 10^{-3}$	$(6.4^{+8.6}_{-3.5}) \times 10^{37}$	$(1.1^{+0.5}_{-0.3}) \times 10^6$	$(1.2^{+0.9}_{-0.4}) \times 10^{-1}$	$(1.2^{+1.6}_{-0.6}) \times 10^{39}$
	b	-195 ± 22	$(5.7^{+2.6}_{-1.4}) \times 10^5$	$(5.6^{+3.5}_{-1.8}) \times 10^{-2}$	$(6.8^{+6.9}_{-3.2}) \times 10^{38}$	$(1.0^{+0.5}_{-0.3}) \times 10^7$	$1.0^{+0.6}_{-0.3}$	$(9.2^{+9.3}_{-4.3}) \times 10^{39}$
	c	-393 ± 71	$(5.1^{+2.9}_{-1.6}) \times 10^5$	$(1.3^{+1.1}_{-0.5}) \times 10^{-1}$	$(6.2^{+9.8}_{-3.7}) \times 10^{39}$	$(9.1^{+5.2}_{-2.8}) \times 10^6$	$2.3^{+2.0}_{-0.9}$	$(6.6^{+10.4}_{-3.9}) \times 10^{40}$
	d	-262 ± 35	$(1.5^{+0.8}_{-0.4}) \times 10^5$	$(8.4^{+6.1}_{-3.0}) \times 10^{-3}$	$(1.8^{+2.2}_{-0.9}) \times 10^{38}$	$(2.7^{+1.4}_{-0.8}) \times 10^6$	$(1.5^{+1.1}_{-0.5}) \times 10^{-1}$	$(3.9^{+4.7}_{-2.0}) \times 10^{39}$
F13443+0802SE	a	-310 ± 56	$(1.3^{+1.0}_{-0.5}) \times 10^4$	$(2.7^{+3.1}_{-1.2}) \times 10^{-3}$	$(8.1^{+16.2}_{-5.2}) \times 10^{37}$	$(8.5^{+7.1}_{-3.3}) \times 10^4$	$(1.8^{+2.1}_{-0.8}) \times 10^{-2}$	$(5.5^{+11.0}_{-3.5}) \times 10^{38}$
	b	-355 ± 73	$(1.1^{+0.8}_{-0.4}) \times 10^5$	$(9.2^{+9.4}_{-3.9}) \times 10^{-3}$	$(3.7^{+7.1}_{-2.3}) \times 10^{38}$	$(1.8^{+1.2}_{-0.6}) \times 10^6$	$(1.5^{+1.5}_{-0.6}) \times 10^{-1}$	$(5.9^{+11.4}_{-3.7}) \times 10^{39}$
F13451+1232W	a	667 ± 39	$(5.6^{+2.4}_{-1.4}) \times 10^4$	$(1.1^{+0.6}_{-0.3}) \times 10^{-2}$	$(1.6^{+1.1}_{-0.6}) \times 10^{39}$	$(8.9^{+3.7}_{-2.2}) \times 10^5$	$(1.8^{+0.9}_{-0.5}) \times 10^{-1}$	$(2.5^{+1.7}_{-0.9}) \times 10^{40}$
	b	528 ± 24	$(3.5^{+1.4}_{-0.8}) \times 10^5$	$(9.3^{+4.3}_{-2.4}) \times 10^{-2}$	$(8.2^{+4.9}_{-2.7}) \times 10^{39}$	$(2.6^{+1.1}_{-0.6}) \times 10^6$	$(7.1^{+3.2}_{-1.9}) \times 10^{-1}$	$(6.3^{+3.7}_{-2.1}) \times 10^{40}$
	c	687 ± 75	$(2.9^{+2.0}_{-1.2}) \times 10^5$	$(2.9^{+2.5}_{-1.3}) \times 10^{-1}$	$(4.3^{+5.6}_{-2.5}) \times 10^{40}$	$(6.8^{+4.6}_{-2.7}) \times 10^5$	$(6.8^{+5.9}_{-3.1}) \times 10^{-1}$	$(1.0^{+1.3}_{-0.6}) \times 10^{41}$
	d	497 ± 30	$(2.7^{+1.1}_{-0.7}) \times 10^5$	$(1.7^{+0.9}_{-0.5}) \times 10^{-1}$	$(1.4^{+0.9}_{-0.5}) \times 10^{40}$	$(1.1^{+0.5}_{-0.3}) \times 10^6$	$(7.3^{+3.6}_{-2.1}) \times 10^{-1}$	$(5.7^{+3.9}_{-2.1}) \times 10^{40}$
	e	539 ± 28	$(8.2^{+3.6}_{-2.1}) \times 10^5$	$(2.4^{+1.2}_{-0.7}) \times 10^{-1}$	$(2.2^{+1.5}_{-0.8}) \times 10^{40}$	$(6.2^{+2.7}_{-1.6}) \times 10^6$	$1.8^{+0.9}_{-0.5}$	$(1.7^{+1.1}_{-0.6}) \times 10^{41}$
	f	386 ± 74	$(1.1^{+0.8}_{-0.5}) \times 10^5$	$(3.1^{+3.3}_{-1.6}) \times 10^{-2}$	$(1.5^{+2.8}_{-1.0}) \times 10^{39}$	$(1.5^{+1.1}_{-0.6}) \times 10^6$	$(4.1^{+4.4}_{-2.1}) \times 10^{-1}$	$(2.0^{+3.8}_{-1.3}) \times 10^{40}$
	g	-291 ± 59	$(1.1^{+0.6}_{-0.4}) \times 10^5$	$(9.4^{+8.6}_{-4.2}) \times 10^{-3}$	$(2.5^{+4.5}_{-1.6}) \times 10^{38}$	$(2.4^{+1.4}_{-0.8}) \times 10^6$	$(2.1^{+1.9}_{-0.9}) \times 10^{-1}$	$(5.6^{+9.8}_{-3.6}) \times 10^{39}$
F14378–3651	a	122 ± 31	$> 4.1 \times 10^2$	$> 3.9 \times 10^{-5}$	$> 1.0 \times 10^{35}$	$> 4.3 \times 10^3$	$> 4.0 \times 10^{-4}$	$> 1.1 \times 10^{36}$
F14394+5332E	a	443 ± 133	$> 3.6 \times 10^4$	$> 2.6 \times 10^{-3}$	$> 7.9 \times 10^{37}$	$> 6.7 \times 10^5$	$> 4.8 \times 10^{-2}$	$> 1.5 \times 10^{39}$
	b	-327 ± 39	$> 1.3 \times 10^4$	$> 7.2 \times 10^{-4}$	$> 1.9 \times 10^{37}$	$> 2.3 \times 10^5$	$> 1.3 \times 10^{-2}$	$> 3.5 \times 10^{38}$

Table 6.5: Continued from Table 6.4.

Object name IRAS	Aperture	v_{max} (km s^{-1})	M_{ap} (M$_\odot$)	$\dot{M}_{ap}$ (M$_\odot$ yr^{-1})	$\dot{E}_{ap}$ (erg s^{-1})	M_{ann} (M$_\odot$)	$\dot{M}_{ann}$ (M$_\odot$ yr^{-1})	$\dot{E}_{ann}$ (erg s^{-1})
(1)	(2)	(3)	(4)	(5)	(6)	(7)	(8)	(9)
F15462–0450	a	240 ± 24	$> 1.6 \times 10^6$	$> 7.0 \times 10^{-2}$	$> 1.0 \times 10^{39}$	$> 2.1 \times 10^7$	> 0.9	$> 1.4 \times 10^{40}$
F17044+6720	a	189 ± 74	$> 1.4 \times 10^5$	$> 3.7 \times 10^{-3}$	$> 1.6 \times 10^{37}$	$> 2.3 \times 10^6$	$> 6.1 \times 10^{-2}$	$> 2.6 \times 10^{38}$
	b	202 ± 95	$> 4.1 \times 10^4$	$> 2.2 \times 10^{-3}$	$> 8.0 \times 10^{36}$	$> 5.1 \times 10^5$	$> 2.8 \times 10^{-2}$	$> 1.0 \times 10^{38}$
F19254–7245S	a	-476 ± 66	$(3.1^{+2.7}_{-1.1}) \times 10^4$	$(1.5^{+1.7}_{-0.6}) \times 10^{-2}$	$(1.1^{+1.9}_{-0.6}) \times 10^{39}$	$(7.6^{+6.6}_{-2.7}) \times 10^5$	$(3.7^{+4.2}_{-1.6}) \times 10^{-1}$	$(2.7^{+4.7}_{-1.5}) \times 10^{40}$
	b	-398 ± 47	$(5.9^{+4.9}_{-2.0}) \times 10^4$	$(2.0^{+2.1}_{-0.8}) \times 10^{-2}$	$(1.0^{+1.6}_{-0.5}) \times 10^{39}$	$(1.1^{+0.9}_{-0.4}) \times 10^6$	$(3.7^{+3.9}_{-1.5}) \times 10^{-1}$	$(1.9^{+2.9}_{-1.0}) \times 10^{40}$
	c	-385 ± 54	$(4.7^{+3.9}_{-1.6}) \times 10^4$	$(3.1^{+3.4}_{-1.3}) \times 10^{-2}$	$(1.4^{+2.5}_{-0.8}) \times 10^{39}$	$(6.4^{+5.2}_{-2.2}) \times 10^5$	$(4.2^{+4.6}_{-1.8}) \times 10^{-1}$	$(2.0^{+3.4}_{-1.1}) \times 10^{40}$
	d	-321 ± 35	$(9.2^{+7.6}_{-3.1}) \times 10^4$	$(3.3^{+3.5}_{-1.3}) \times 10^{-2}$	$(1.1^{+1.6}_{-0.6}) \times 10^{39}$	$(8.6^{+7.2}_{-2.9}) \times 10^5$	$(3.1^{+3.2}_{-1.3}) \times 10^{-1}$	$(1.0^{+1.6}_{-0.5}) \times 10^{40}$
	e	-255 ± 43	$(1.2^{+1.0}_{-0.4}) \times 10^5$	$(3.5^{+4.1}_{-1.5}) \times 10^{-2}$	$(7.1^{+14.1}_{-4.4}) \times 10^{38}$	$(1.1^{+1.0}_{-0.4}) \times 10^6$	$(3.3^{+3.8}_{-1.4}) \times 10^{-1}$	$(6.7^{+13.3}_{-0.4}) \times 10^{39}$
	f	-320 ± 64	$(6.6^{+5.6}_{-2.3}) \times 10^4$	$(1.7^{+2.0}_{-0.7}) \times 10^{-2}$	$(5.4^{+11.9}_{-3.5}) \times 10^{38}$	$(1.1^{+0.9}_{-0.4}) \times 10^6$	$(2.8^{+3.4}_{-1.2}) \times 10^{-1}$	$(9.1^{+20.0}_{-5.8}) \times 10^{39}$
	g	286 ± 86	$(3.0^{+2.7}_{-1.1}) \times 10^4$	$(8.0^{+11.6}_{-3.8}) \times 10^{-2}$	$(2.1^{+6.6}_{-1.6}) \times 10^{38}$	$(7.1^{+6.3}_{-2.6}) \times 10^5$	$(1.9^{+2.8}_{-0.9}) \times 10^{-1}$	$(4.9^{+15.5}_{-0.4}) \times 10^{39}$
F23060+0505	a	–	–	–	–	–	–	–
	b	-728 ± 57	$(1.2^{+0.8}_{-0.6}) \times 10^5$	$(1.9^{+1.6}_{-1.1}) \times 10^{-2}$	$(3.2^{+3.7}_{-2.0}) \times 10^{39}$	$(1.2^{+0.8}_{-0.6}) \times 10^6$	$(1.9^{+1.6}_{-1.1}) \times 10^{-1}$	$(3.2^{+3.7}_{-2.0}) \times 10^{40}$
F23389+0303N	a	-440 ± 108	$> 2.2 \times 10^5$	$> 7.2 \times 10^{-3}$	$> 2.5 \times 10^{38}$	$> 5.9 \times 10^6$	$> 1.9 \times 10^{-1}$	$> 6.7 \times 10^{39}$
	b	-393 ± 57	$> 1.1 \times 10^6$	$> 9.0 \times 10^{-2}$	$> 3.2 \times 10^{39}$	$> 1.4 \times 10^7$	> 1.1	$> 3.9 \times 10^{40}$

outflows that may be present.

In Chapter 4, when calculating mass outflow rates for the spatially unresolved outflows, the time taken for the outflow to reach a radius R_{out} from the nucleus at a constant velocity, v_{out}, was considered. However, in the case of the extended, spatially resolved apertures, the time taken for the gas to cross the radial extent of the aperture, T_{ap}, at a constant velocity v_{out} must be considered instead. Therefore $\dot{M}$ can be calculated using the following equation:

$$\dot{M} = \frac{L(H\alpha)m_p v_{out}}{\alpha^{H\alpha}_{eff} h\nu_{H\alpha} n_e T_{ap}}, \tag{6.2}$$

where T_{ap} is the radial width of the aperture, which can be inferred from the information given in Tables 6.1 and 6.2, column (3). Similarly to the approach for the nuclear outflows (Chapter 4), v_{out} was taken to be the maximal velocity, v_{max}, for each object, based on the total [OIII] profile in the extended aperture (see section 6.5.4). v_{max} for each object is shown in Tables 6.4 and 6.5, column (3). Note that, while using v_{max} accounts for possible projection effects on the observed velocities, T_{ap} is also affected by projection. The true (de-projected) distance that the gas needs to cross will likely be larger than T_{ap} for a given aperture. This effectively means that T_{ap} is a lower limit, leading to potential over-estimation of the mass outflow rates and kinetic powers.

In this way, and excluding objects where only limits were available, the mass outflow rates for the extended emission-line gas were found to be in the range $1.5\times10^{-3} < \dot{M} < 0.3$ $\mathrm{M_{\odot}yr^{-1}}$, median $\sim 2.0\times10^{-2}$ $\mathrm{M_{\odot}yr^{-1}}$. In comparison, the maximal outflow rates for the nuclear outflows described in Chapter 4 fell in the range $0.1 < \dot{M} < 20$ $\mathrm{M_{\odot}yr^{-1}}$, median ~ 2 $\mathrm{M_{\odot}yr^{-1}}$. While the upper end of the range for the extended mass outflow rates just overlaps with the lower end of the range of nuclear mass outflow rates, in general the extended mass outflow rates are orders of magnitude lower than those of the nuclear regions, indicated by the two orders of magnitude difference in the medians of the two samples.

The extended mass outflow rate estimates have also been converted into kinetic powers, using the following equation:

$$\dot{E} = \frac{\dot{M}}{2}(v_{out}^2). \tag{6.3}$$

These values are given in Tables 6.4 and 6.5. Excluding limits, the kinetic powers within the extended apertures fall in the range $4.4 \times 10^{37} < \dot{E} < 4.3 \times 10^{40}$ erg s^{-1}, median $\sim 8.6 \times 10^{38}$ erg s^{-1}. This range of values is lower than those found in the nuclear regions described in Chapter 4, $9.3 \times 10^{40} < \dot{E} < 2.3 \times 10^{43}$ erg s^{-1}, median $\sim 1.5 \times 10^{42}$ erg s^{-1}. There is a three orders of magnitude difference between the median values for the extended and nuclear regions.

It is worth noting, however, that the above calculations are limited to those regions of the extended line-emitting gas covered by the apertures. If the area covered by the extended gas was significantly larger than that covered by the apertures (see Figure 6.35), then the above calculations could under-estimate the true importance of the extended components. Using the effective upper limit on the extended masses of gas, M_{ann}, obtained by applying the aperture correction, f, of Equation 6.1, effective upper limits on the mass outflow rates and kinetic powers were estimated for each aperture location. These estimates are given in Tables 6.4 and 6.5, columns (8) and (9), and represent the maximum possible mass outflow rates and kinetic powers that could be present in the sub-sample of the e-QUADROS ULIRGs which show evidence for off-nuclear emission. In this way, the maximum mass outflow rates and kinetic powers fall in the ranges $1.8 \times 10^{-2} < \dot{M} < 2.3$ M$_{\odot}$yr^{-1}, median $\sim$0.3 M$_{\odot}$yr^{-1}; and

$5.5 \times 10^{38} < \dot{E} < 1.7 \times 10^{41}$ erg s^{-1}, median $\sim 10^{40}$ erg s^{-1}. These ranges still remain lower on average than those derived for the nuclear apertures, although the agreement is better.

However, these maximal ranges involve the assumption that the slit intersects only a section of a complete shell of ionised gas surrounding the nucleus. For those objects with optical imaging available (see Section 6.4), the distribution of the extended gas is far from a complete shell. Therefore it is likely that the annuli estimates significantly over-estimate the true contribution of the extended gas. The true values are likely to be found somewhere between the aperture and annulus estimates for each aperture location.

6.6 Discussion and conclusions

This chapter aimed to investigate the properties of the extended emission-line gas observed in the e-QUADROS sample, in order to determine the overall impact of any extended AGN-driven outflows on the wider host galaxies. It was interesting to know whether previous studies have missed something by not considering the larger-scale low-surface-brightness emission.

While the large uncertainties in the literature regarding AGN-driven outflows have been discussed in the Chapter 4, the results of the QUADROS project have shown that such outflows are generally compact, concentrated in the nuclear regions, and in most cases fall short of the coupling efficiencies required by hydrodynamical models of galaxy interactions in order for the simulations to produce observed trends.

Therefore, it was important to consider the possible contribution from emission-line gas on larger scales that may be neglected by nuclear studies. Nuclear outflows in ULIRGs are relatively straightforward to detect due to significantly blue-shifted, broad emission line components to the associated emission lines – in general, emission-line velocities greater than 500 km s^{-1} are attributed to outflows, due to the fact that it is challenging for such velocities to be explained by gravitational motions. However, it is still possible for gas moving at velocities less than this to be associated with outflows, if the outflows decelerate with distance from the nucleus. Consequently, this somewhat arbitrary velocity cut of 500 km s^{-1} could be problematic for detecting outflows at larger radii.

Indeed, as demonstrated by the results presented in Chapter 3 for Mrk 273, the position of this velocity cut can have a large impact on the conclusion of the study. In that case, it was concluded that the nuclear outflows were restricted to a radius of ∼6 kpc from the central AGN, based on a velocity cut of 500 km s^{-1} (and ∼5 kpc in the optical study of Tadhunter et al. 2018). This radius would be larger (∼10 kpc) if the velocity was instead cut at 350 km s^{-1}. Furthermore, a lower velocity cut is supported by the hydrodynamical simulations of Debuhr et al. (2012), which showed that gas velocities greater than 300 km s^{-1} were not observed if AGN-driven outflows were switched off.

Therefore it was proposed here that taking 350 km s^{-1} to be the velocity cut between outflowing and quiescent gas may be more appropriate. Tables 6.1 and 6.2 give the velocity widths and shifts of the extended apertures for the sub-sample of e-QUADROS ULIRGs which show evidence for off-nuclear emission-line gas. Based on this velocity cut, only three further objects (F13451+1232W, F19254–7245S and F23060+0505) show potential for large-scale outflows ($5 \lesssim R_{out} \lesssim 9$ kpc) outside of the obvious influence of their nuclear seeing discs.

The electron densities of the extended emission-line gas were then analysed. As shown in Rose et al. (2018) and Spence et al. (2018) (also see Chapter 4), the densities of the nuclear outflows are generally high, falling in the range $3.5 < \log n_e(\mathrm{cm}^{-3}) < 4.5$, median $\log n_e(\mathrm{cm}^{-3}) \sim 3.8$, based on the broad line fluxes. In general, the estimated densities for the extended apertures fall towards the lower end or below this range. Interestingly, F23060+0505, one of the objects which shows the clearest evidence for extended outflows, also shows the highest electron density in its extended apertures out of all the objects studied.

The ionisation mechanism of the gas was then examined using BPT diagnostic diagrams, and comparisons with theoretical photo-ionisation and shock-ionisation models. In most cases it remains difficult to distinguish the dominant ionisation method using the BPT ratios, due to significant overlap between AGN photo-ionisation and shock models. What is clear, however, is that stellar photo-ionisation alone is not able to explain the line ratios in any of these cases.

For the purpose of investigating the possible contribution to the total outflow power that extended emission-line regions may make, potential mass outflow rates and kinetic powers have been calculated for all of the extended apertures, based on maximal estimates of the velocity. However, even making optimistic assumptions, the mass outflow rates and kinetic powers are found to be orders of magnitudes lower than those measured in the nuclear regions (Rose et al., 2018; Spence et al., 2018, also see Chapter 4), despite the fact that in many cases these quantities may be overestimated due to projection effects on the radial extent of the apertures. Therefore, regardless of the uncertainties in distinguishing large-scale outflows from quiescent gas, these results clearly indicate that the observed extended emission-line gas contributes little to the total mass outflow rates and kinetic powers of the warm AGN-driven outflows in local ULIRGs.

These results confirm that the nuclear outflows are the dominant component of any potential galaxy-scale ionised outflows, and therefore the coupling efficiencies calculated in Chapter 4 are representative of the warm, AGN-driven outflows in the local ULIRG population.

Chapter 7

Summary and future work

7.1 Summary

AGN-driven outflows are now routinely incorporated into semi-analytical and hydrodynamical models of major gas-rich mergers as a mechanism for regulating galaxy growth (e.g. Di Matteo et al., 2005; Springel et al., 2005; Johansson et al., 2009). This is required in order to reproduce correct scaling relations between the super-massive black hole and host galaxy properties, as well as galaxies with luminosities, masses and colours consistent with observations. However, despite their potentially key importance for understanding the evolution of galaxies, the true importance of the AGN-driven outflows remains controversial from an observational perspective. It is now clear that a proper comparison of the properties of AGN outflows directly determined from observations is critical for establishing whether the outflows we observe are consistent with those required by the models.

Of specific importance is the coupling efficiency, $\dot{F}$, which is defined as the proportion of the total radiative energy of the AGN which is transferred to the surrounding gas. The expected coupling efficiency predicted by the models is of the order $\dot{F} \sim 5$–10%. Previous studies, however, have failed to accurately quantify this parameter observationally, and it is still not clear what the true coupling efficiencies of the outflows are.

To remedy this situation, a combined high-resolution imaging and wide-spectral-coverage spectroscopy project has been undertaken to accurately calculate the mass outflow rates, $\dot{M}$, kinetic powers, $\dot{E}$, and ultimately the coupling efficiencies in a sample of 18 local ULIRGs ($z < 0.175$) with optical AGN. As the most rapidly evolving galaxies in the local Universe, these objects are predicted to drive particularly powerful outflows. Therefore, they are key targets for studying AGN-driven outflows in detail.

With reference to the questions initially posed in Chapter 1, the main results of this thesis can be summarised as follows.

What are the true spatial extents of AGN-driven outflows? (Chapters 3 and 4)

The total radial extent of the outflows, R_{out}, is a key parameter in calculating the coupling efficiencies of the outflows. Furthermore, the hydrodynamical simulations predict that outflows should be galaxy-wide in scale, and while previous studies have attempted to measure the radial extent of outflows, the results were varied and inconclusive (e.g. see Harrison et al., 2012, 2014; Liu et al., 2013; McElroy et al., 2015). Here, it has been shown that, in a representative sample of local ULIRGs, the warm outflows are compact, with radial extents in the range $0.07 < R_{out} < 1.5$ kpc, median $R_{out} \sim 0.8$ kpc, and confined to the near-nuclear regions (Chapter 4). One exception to this is Mrk 273, for which the outflow was shown to be confined within a radius of ∼6 kpc (Chapter 3).

What are the true electron densities of AGN-driven outflows? (Chapters 4 and 5)

The electron densities, n_e, of the outflows are another key factor in calculating the coupling efficiencies of the outflows. However, the electron density is one of the most challenging properties to measure directly due to difficulties in measuring accurate fluxes for the nebular [OII] and [SII] doublets. Consequently, the electron densities in warm outflows are largely unknown, and typically $n_e = 100$ cm^{-3} has been the assumed value in previous studies. Here, using an alternative approach based on the trans-auroral [OII] and [SII] lines (see Holt et al., 2011; Rose et al., 2018), the near-nuclear outflows are found to have relatively high densities:

- For the WHT/ISIS objects, the densities fall in the range $300 \lesssim n_e \lesssim 18000$ cm^{-3}, median $n_e \sim 2000$ cm^{-1};
- For the e-QUADROS sample as a whole, the densities fall in the range $200 \lesssim n_e \lesssim 56000$ cm^{-3}, median $n_e \sim 4500$ cm^{-1}.

Therefore, studies which assume $n_e = 100$ cm^{-3} could be over-estimating the true kinetic powers, and hence coupling efficiencies, by 1 – 3 orders of magnitude (Chapter 4).

It has also been demonstrated that the trans-auroral [OII] and [SII] lines are likely to be emitted by the same clouds that emit other key diagnostic lines such as Hβ and [OIII]λ5007, thus confirming their utility for this type of study (Chapter 5).

What are the true mass outflow rates, kinetic powers and coupling efficiencies of AGN-driven outflows, and how do they compare to the values required by simulations of major mergers? (Chapter 4)

Prior to this study, estimates for the mass outflow rates of warm outflows in AGN ranged from $0.1 < \dot{M} < 23000$ M$_{\odot}$yr^{-1} – over 6 orders of magnitude. Similarly, kinetic powers were reported in the range $10^{37.7} < \dot{E} < 10^{45.8}$ erg s^{-1} – over 8 orders of magnitude (Harrison et al., 2014; Villar-Martín et al., 2016). These large variations are due to combinations of uncertainties on the radii, densities, reddenings and velocities of the observed outflows. Consequently, observational constraints on the coupling efficiencies, $\dot{F}$, are extremely poor, ranging from a small fraction of a per cent to over 10%. The benchmark value from merger simulations is $\dot{F} \sim$ 5–10%. In this thesis, the mass outflow rates, kinetic powers and coupling efficiencies for the WHT/ISIS ULIRGs are found in the ranges below, based on the most optimistic outflow velocities, v_{05}. The results for the full e-QUADROS sample are also indicated in parentheses.

- $0.1 < \dot{M} < 20$ M$_{\odot}$yr^{-1}, median $\dot{M} \sim 2$ M$_{\odot}$yr^{-1} (e-QUADROS: $0.1 < \dot{M} < 20$ M$_{\odot}$yr^{-1}, median $\dot{M} \sim 4$ M$_{\odot}$yr^{-1});
- $10^{41.0} < \dot{E} < 10^{43.2}$ erg s^{-1}, median $\dot{E} \sim 10^{42.2}$ erg s^{-1} (e-QUADROS: $10^{39.8} < \dot{E} < 10^{43.3}$ erg s^{-1}, median $\dot{E} \sim 10^{42.2}$ erg s^{-1}); and
- $0.03 < \dot{F} < 2.5$ %, median $\dot{F} \sim 0.4$ % (e-QUADROS: $5 \times 10^{-4} < \dot{F} < 2.5$ %, median $\dot{F} \sim 0.2$ %).

These results are based on a maximal representation of the outflow velocity, v_{05}. Even under optimistic assumptions, the above values are relatively modest compared to those of the simulations, and are only consistent with the theoretical expectations if a relatively modest (∼10 %) fraction of the energy initially transferred by the AGN is transmitted to the larger-scale outflows.

Are previous studies missing something by concentrating only on the near-nuclear outflows? (Chapter 6)

The answer to this question has been shown to be no. Many previous studies of ULIRGs have focussed on a radius of only a few kpc, and evidence for larger scale outflows is still lacking. A fraction 11/18 (60%) of the e-QUADROS ULIRGs show evidence for large-scale ($r \gtrsim 5$ kpc) emission-line gas in the imaging and spectroscopic data. Despite this, only 4 ULIRGs (22% of the sample) show kinematic evidence for outflows, in the form of moderately broad (FWHM > 350 km s^{-1}) line-widths and/or split components, extending more than a few kpc from the nucleus. In these cases, $5 \lesssim R_{out} \lesssim 9$ kpc. However, even making extremely optimistic assumptions about the velocity and spatial distributions of the extended gas, the maximum mass outflow rates and kinetic powers calculated for the extended outflows fall in the ranges $1.8 \times 10^{-2} < \dot{M} < 2.3$ M$_{\odot}$yr^{-1}, median $\dot{M} \sim 0.3$ M$_{\odot}$yr^{-1}, and $10^{38.7} < \dot{E} < 10^{41.2}$ erg s^{-1}, median $\dot{E} \sim 10^{40.0}$ erg s^{-1}. These values are, on average, 1–2 orders of magnitude lower than those derived for the nuclear regions. These results, therefore, confirm that the mass outflow rates, kinetic powers and coupling efficiencies derived for the near-nuclear outflows are representative of the warm outflows in the local ULIRG population.

Overall, this thesis work contributes some of the most accurately derived properties for the warm outflows in local ULIRGs, with the aim of addressing the inconsistent results seen in the literature over the past decade. The warm outflows are found to be compact, have relatively high densities and coupling efficiencies that fall short of those required by many recent hydrodynamical simulations of galaxy mergers. This work can be used to assess the validity of the simulations and improve our understanding of the AGN – host galaxy connection going forward.

7.2 Future work

Clearly, based on the results of this thesis, there is still plenty of scope for future work. Here, a number of potential projects are suggested.

Further application of the trans-auroral density diagnostic grids

The QUADROS project has demonstrated a powerful technique for measuring accurate electron densities and reddenings, using the trans-auroral [OII] and [SII] emission lines. This has enabled the most accurate calculations, to date, of the coupling efficiencies of the warm outflows in local ULIRGs to be made. This is the first time this technique has been applied to a systematic study of AGN. Therefore, it would be useful to undertake further deep, optical spectroscopic observations of other types of powerful AGN (e.g. type II quasars), optimised for the trans-auroral emission lines, to determine whether they are similar to the ULIRGs in terms of their outflow properties. Note that this work is red-shift limited – the [OII]$\lambda\lambda$7319,7331 blend enters the near-infrared regime at $z \gtrsim 0.2$.

Furthermore, following the discussion in Chapter 5, a useful project would be to look at nearby AGN in which the outflow regions are clearly spatially resolved, and confirm directly that the trans-auroral lines are produced in the same regions as the other key diagnostic lines (e.g. [OIII], Hα). In addition, spatially-resolved estimates of the properties of the near-nuclear outflows may resolve some of the geometric uncertainty of the techniques used in Rose et al. (2018) and Spence et al. (2018), for which the near-nuclear outflows were spatially resolved in the spectra of only 3/17 (17%) of the objects considered.

The multi-phase nature of the outflows

This thesis quantified the outflow properties of the warm, ionised outflows observed in the population of local ULIRGs. However, this represents only one of the available gas phases: outflows have also been detected in both neutral atomic and cold molecular gas in samples of AGN. In particular, estimates for the mass outflow rates of some molecular outflows (e.g. Cicone et al., 2014) – which are orders of magnitude larger than those calculated here for the warm outflows – suggest that the bulk of the mass of the outflows may actually be contained in this colder phase. However, the relationship between these phases is still largely unknown. So far, the neutral and molecular studies have often considered different samples to those that accurately quantify the warm outflows, such as the QUADROS project (only 3/18 of the e-QUADROS sample had measurements for the neutral and molecular outflows reported in the literature; see Chapter 4), so some uncertainty remains about the comparison. Consequently, more studies are required in which all three phases are studied and compared for the same objects. A useful future project, therefore, would be to make high resolution optical spectroscopic observations of NaID for the neutral gas, and ALMA CO observations for the molecular gas, for the whole e-QUADROS sample.

In addition, it is not clear how the cold gas could survive the outflow without the atoms and molecules being disassociated and ionised. Consequently, it is thought that the cold neutral and molecular gas re-forms in the wake of the warm AGN-driven outflow, accumulating after the warm gas has cooled (e.g Tadhunter et al., 2014; Richings & Faucher-Giguère, 2018b). If this were the case, then the molecular outflow region might be expected to be on a similar scale to, or smaller than, the warm outflow region. However, the spatial extents of the neutral and molecular outflows are often not well determined in existing observations. It would therefore be useful to make high spatial resolution CO observations with ALMA of the southern part of the e-QUADROS sample, to determine whether the molecular and warm ionised outflows are co-spatial. This would provide clues about the acceleration of the molecular outflows. It would also be useful to obtain lower resolution ALMA CO observations to search for, and map, any larger-scale molecular outflows outside the nuclear regions. This could pick up historical warm outflows that have moved to a larger scale and cooled, complementing the results presented in Chapter 6.

Integral field spectroscopy of the QUADROS sample

The warm nuclear outflows were spatially resolved in 3/8 of the WHT/ISIS long-slit spectra, and 11/18 of the e-QUADROS sample showed evidence for spatially extended warm gas ($R > 5$ kpc). However, the emission-line kinematics of the extended gas in only 4 of those objects showed evidence that could be considered consistent with outflows. While long-slit spectroscopy is a powerful tool for analysing the gas kinematics and emission-line fluxes of nearby galaxies, one disadvantage is that the spectroscopic slits do not sample the full extent of the extended warm gas, and it is possible that our existing observations might simply miss the extended outflows because they are not located within the slits.

To address this, an integral field spectrograph, such as MUSE on the ESO VLT, could be used to obtain deep observations of local ULIRGs, which can be used to map the full extent of the extended regions. In this way, the velocities, densities and geometries of the extended outflows can be properly characterised. Currently, the mass outflow rates and hence coupling efficiencies are based on the assumption that the electron density is the same for the entire outflow. An IFU study would help reveal whether this is in fact the case in ULIRGs, or whether a significant gradient is present within the warm outflows (e.g. Kakkad et al., 2018).

In addition, MUSE would have the advantage over our current observations in that it has a higher sensitivity than WHT/ISIS and VLT/Xshooter, and a resolution that is intermediate between ISIS and Xshooter, so would be particularly sensitive to extended outflows that might have been missed due to the relatively low sensitivity of ISIS, or have been "resolved-out" due to the high spectral resolution of the Xshooter observations.

Bibliography

Allen M. G., Groves B. A., Dopita M. A., Sutherland R. S., Kewley L. J., 2008, Astrophysical Journal Supplements, 178, 20

Alonso-Herrero A., Pereira-Santaella M., Rieke G. H., Rigopoulou D., 2012, Astrophysical Journal, 744, 2

Antonucci R., 1993, Annual Review of Astronomy and Astrophysics, 31, 473

Antonuccio-Delogu V., Silk J., 2008, Monthly Notices of the Royal Astronomical Society, 389, 1750

Appenzeller I., Oestreicher R., 1988, Astronomical Journal, 95, 45

Armus L., Heckman T. M., Miley G. K., 1988, Astrophysical Journal Letters, 326, L45

Axon D. J., Capetti A., Fanti R., Morganti R., Robinson A., Spencer R., 2000, Astronomical Journal, 120, 2284

Bañados E., et al., 2018, Nature, 553, 473

Baade W., Minkowski R., 1954, Astrophysical Journal, 119, 206

Baldwin J. A., Phillips M. M., Terlevich R., 1981, Publications of the Astronomical Society of the Pacific, 93, 5

Balick B., Brown R. L., 1974, Astrophysical Journal, 194, 265

Batcheldor D., Tadhunter C., Holt J., Morganti R., O'Dea C. P., Axon D. J., Koekemoer A., 2007, Astrophysical Journal, 661, 70

Bell E. F., McIntosh D. H., Katz N., Weinberg M. D., 2003, Astrophysical Journal Supplements, 149, 289

Bendo G. J., Clements D. L., Khan S. A., 2009, Monthly Notices of the Royal Astronomical Society, 399, L29

Best P. N., Kaiser C. R., Heckman T. M., Kauffmann G., 2006, Monthly Notices of the Royal Astronomical Society, 368, L67

Bischetti M., et al., 2017, Astronomy and Astrophysics, 598, A122

Blain A. W., Smail I., Ivison R. J., Kneib J.-P., Frayer D. T., 2002, Physics Reports, 369, 111

Bolton J. G., 1948, Nature, 162, 141

Booth C. M., Schaye J., 2009, Monthly Notices of the Royal Astronomical Society, 398, 53

Bower R. G., Benson A. J., Malbon R., Helly J. C., Frenk C. S., Baugh C. M., Cole S., Lacey C. G., 2006, Monthly Notices of the Royal Astronomical Society, 370, 645

Bruzual G., Charlot S., 2003, Monthly Notices of the Royal Astronomical Society, 344, 1000

Calzetti D., Armus L., Bohlin R. C., Kinney A. L., Koornneef J., Storchi-Bergmann T., 2000, Astrophysical Journal, 533, 682

Cano-Díaz M., Maiolino R., Marconi A., Netzer H., Shemmer O., Cresci G., 2012, Astronomy and Astrophysics, 537, L8

Cardelli J. A., Clayton G. C., Mathis J. S., 1989, Astrophysical Journal, 345, 245

Carniani S., et al., 2015, Astronomy and Astrophysics, 580, A102

Carniani S., et al., 2016, Astronomy and Astrophysics, 591, A28

Choi E., Ostriker J. P., Naab T., Johansson P. H., 2012, Astrophysical Journal, 754, 125

Cicone C., et al., 2014, Astronomy and Astrophysics, 562, A21

Cid Fernandes R., Mateus A., Sodré L., Stasińska G., Gomes J. M., 2005, Monthly Notices of the Royal Astronomical Society, 358, 363

Clark N. E., Tadhunter C. N., Morganti R., Killeen N. E. B., Fosbury R. A. E., Hook R. N., Siebert J., Shaw M. A., 1997, Monthly Notices of the Royal Astronomical Society, 286, 558

Colina L., Lipari S., Macchetto F., 1991, Astrophysical Journal, 379, 113

Croton D. J., et al., 2006, Monthly Notices of the Royal Astronomical Society, 365, 11

Dasyra K. M., Combes F., 2012, Astronomy and Astrophysics, 541, L7

Dasyra K. M., et al., 2006, Astrophysical Journal, 651, 835

De Robertis M. M., Dufour R. J., Hunt R. W., 1987, Journal of the Royal Astronomical Society of Canada, 81, 195

Debuhr J., Quataert E., Ma C.-P., 2012, Monthly Notices of the Royal Astronomical Society, 420, 2221

Di Matteo T., Springel V., Hernquist L., 2005, Nature, 433, 604

Dicken D., et al., 2014, Astrophysical Journal, 788, 98

Dopita M. A., Sutherland R. S., 1995, Astrophysical Journal, 455, 468

Duc P.-A., Mirabel I. F., Maza J., 1997, Astronomy and Astrophysics Supplements, 124, 533

Fabian A. C., 1999, Monthly Notices of the Royal Astronomical Society, 308, L39

Fabian A. C., 2012, Annual Review of Astronomy and Astrophysics, 50, 455

Farrah D., et al., 2001, Monthly Notices of the Royal Astronomical Society, 326, 1333

Farrah D., et al., 2007, Astrophysical Journal, 667, 149

Fath E. A., 1909, Popular Astronomy, 17, 504

Ferland G. J., Netzer H., 1983, Astrophysical Journal, 264, 105

Ferland G. J., et al., 2013, Revista Mexicana de Astronomia y Astrofisica, 49, 137

Feruglio C., Maiolino R., Piconcelli E., Menci N., Aussel H., Lamastra A., Fiore F., 2010, Astronomy and Astrophysics, 518, L155

Fiore F., et al., 2017, Astronomy and Astrophysics, 601, A143

Freudling W., Romaniello M., Bramich D. M., Ballester P., Forchi V., García-Dabló C. E., Moehler S., Neeser M. J., 2013, Astronomy and Astrophysics, 559, A96

Gaskell C. M., Ferland G. J., 1984, Publications of the Astronomical Society of the Pacific, 96, 393

Genzel R., Tacconi L. J., Rigopoulou D., Lutz D., Tecza M., 2001, Astrophysical Journal, 563, 527

González-Alfonso E., et al., 2017, Astrophysical Journal, 836, 11

Groves B. A., Dopita M. A., Sutherland R. S., 2004, Astrophysical Journal Supplements, 153, 9

Harrison C. M., et al., 2012, Monthly Notices of the Royal Astronomical Society, 426, 1073

Harrison C. M., Alexander D. M., Mullaney J. R., Swinbank A. M., 2014, Monthly Notices of the Royal Astronomical Society, 441, 3306

Harrison C. M., Costa T., Tadhunter C. N., Flütsch A., Kakkad D., Perna M., Vietri G., 2018, Nature Astronomy, 2, 198

Heckman T. M., 1980, Astronomy and Astrophysics, 87, 152

Heckman T. M., Miley G. K., van Breugel W. J. M., Butcher H. R., 1981, Astrophysical Journal, 247, 403

Heckman T. M., Kauffmann G., Brinchmann J., Charlot S., Tremonti C., White S. D. M., 2004, Astrophysical Journal, 613, 109

Hey J. S., Parsons S. J., Phillips J. W., 1946, Nature, 158, 234

Holt J., Tadhunter C. N., Morganti R., 2003, Monthly Notices of the Royal Astronomical Society, 342, 227

Holt J., Tadhunter C. N., Morganti R., 2008, Monthly Notices of the Royal Astronomical Society, 387, 639

Holt J., Tadhunter C. N., Morganti R., Emonts B. H. C., 2011, Monthly Notices of the Royal Astronomical Society, 410, 1527

Hopkins P. F., Elvis M., 2010, Monthly Notices of the Royal Astronomical Society, 401, 7

Hopkins P. F., Hernquist L., Cox T. J., Di Matteo T., Robertson B., Springel V., 2006, Astrophysical Journal Supplements, 163, 1

Houck J. R., Schneider D. P., Danielson G. E., Beichman C. A., Lonsdale C. J., Neugebauer G., Soifer B. T., 1985, Astrophysical Journal Letters, 290, L5

Husemann B., Scharwächter J., Bennert V. N., Mainieri V., Woo J.-H., Kakkad D., 2016a, Astronomy and Astrophysics, 594, A44

Husemann B., Scharwächter J., Bennert V. N., Mainieri V., Woo J.-H., Kakkad D., 2016b, Astronomy and Astrophysics, 594, A44

Johansson P. H., Burkert A., Naab T., 2009, Astrophysical Journal Letters, 707, L184

Kakkad D., et al., 2018, preprint, (`arXiv:1806.02839`)

Karouzos M., Woo J.-H., Bae H.-J., 2016, Astrophysical Journal, 819, 148

Kauffmann G., et al., 2003, Monthly Notices of the Royal Astronomical Society, 346, 1055

Kewley L. J., Dopita M. A., Sutherland R. S., Heisler C. A., Trevena J., 2001, Astrophysical Journal, 556, 121

Kewley L. J., Groves B., Kauffmann G., Heckman T., 2006, Monthly Notices of the Royal Astronomical Society, 372, 961

Kilerci Eser E., Goto T., Doi Y., 2014, Astrophysical Journal, 797, 54

Kim D.-C., Sanders D. B., 1998, Astrophysical Journal Supplements, 119, 41

Kim D.-C., Veilleux S., Sanders D. B., 2002, Astrophysical Journal Supplements, 143, 277

King A., 2005, Astrophysical Journal Letters, 635, L121

King A., Pounds K., 2015, Annual Review of Astronomy and Astrophysics, 53, 115

King A. R., Zubovas K., Power C., 2011, Monthly Notices of the Royal Astronomical Society, 415, L6

Kormendy J., Ho L. C., 2013, Annual Review of Astronomy and Astrophysics, 51, 511

Kormendy J., Sanders D. B., 1992, Astrophysical Journal Letters, 390, L53

Lamastra A., Bianchi S., Matt G., Perola G. C., Barcons X., Carrera F. J., 2009, Astronomy and Astrophysics, 504, 73

Lee J. C., Hwang H. S., Lee M. G., Kim M., Kim S. C., 2011, Monthly Notices of the Royal Astronomical Society, 414, 702

Lípari S., Terlevich R., Díaz R. J., Taniguchi Y., Zheng W., Tsvetanov Z., Carranza G., Dottori H., 2003, Monthly Notices of the Royal Astronomical Society, 340, 289

Liu G., Zakamska N. L., Greene J. E., Nesvadba N. P. H., Liu X., 2013, Monthly Notices of the Royal Astronomical Society, 436, 2576

Magorrian J., et al., 1998, Astronomical Journal, 115, 2285

Maiolino R., et al., 2017, Nature, 544, 202

Marconi A., Risaliti G., Gilli R., Hunt L. K., Maiolino R., Salvati M., 2004, Monthly Notices of the Royal Astronomical Society, 351, 169

McConnell N. J., Ma C.-P., 2013, Astrophysical Journal, 764, 184

McElroy R., Croom S. M., Pracy M., Sharp R., Ho I.-T., Medling A. M., 2015, Monthly Notices of the Royal Astronomical Society, 446, 2186

McNamara B. R., Nulsen P. E. J., 2007, Annual Review of Astronomy and Astrophysics, 45, 117

Mirabel I. F., Lutz D., Maza J., 1991, Astronomy and Astrophysics, 243, 367

Monreal-Ibero A., Arribas S., Colina L., 2006, Astrophysical Journal, 637, 138

Monreal-Ibero A., Arribas S., Colina L., Rodríguez-Zaurín J., Alonso-Herrero A., García-Marín M., 2010, Astronomy and Astrophysics, 517, A28

Morganti R., 2015, in Massaro F., Cheung C. C., Lopez E., Siemiginowska A., eds, IAU Symposium Vol. 313, Extragalactic Jets from Every Angle. pp 283–288 (`arXiv:1411.6107`), doi:10.1017/S1743921315002331

Morganti R., Tadhunter C. N., Oosterloo T. A., 2005, Astronomy and Astrophysics, 444, L9

Morganti R., Fogasy J., Paragi Z., Oosterloo T., Orienti M., 2013, Science, 341, 1082

Mullaney J. R., Alexander D. M., Fine S., Goulding A. D., Harrison C. M., Hickox R. C., 2013, Monthly Notices of the Royal Astronomical Society, 433, 622

Mutch S. J., Croton D. J., Poole G. B., 2013, Monthly Notices of the Royal Astronomical Society, 435, 2445

Nagar N. M., Wilson A. S., Falcke H., Veilleux S., Maiolino R., 2003, Astronomy and Astrophysics, 409, 115

Narayan R., Quataert E., 2005, Science, 307, 77

Nardini E., Risaliti G., Watabe Y., Salvati M., Sani E., 2010, Monthly Notices of the Royal Astronomical Society, 405, 2505

Nesvadba N. P. H., Lehnert M. D., De Breuck C., Gilbert A. M., van Breugel W., 2008, Astronomy and Astrophysics, 491, 407

Netzer H., 2015, Annual Review of Astronomy and Astrophysics, 53, 365

Netzer H., Trakhtenbrot B., 2014, Monthly Notices of the Royal Astronomical Society, 438, 672

Oke J. B., Gunn J. E., 1983, Astrophysical Journal, 266, 713

Osterbrock D. E., Ferland G. J., 2006, Astrophysics of gaseous nebulae and active galactic nuclei

Peebles P. J. E., 1972, Astrophysical Journal, 178, 371

Pequignot D., Petitjean P., Boisson C., 1991, Astronomy and Astrophysics, 251, 680

Pereira-Santaella M., Rigopoulou D., Farrah D., Lebouteiller V., Li J., 2017, Monthly Notices of the Royal Astronomical Society, 470, 1218

Perna M., et al., 2015, Astronomy and Astrophysics, 574, A82

Peterson B. M., 1997, An Introduction to Active Galactic Nuclei

Pringle J. E., Rees M. J., Pacholczyk A. G., 1973, Astronomy and Astrophysics, 29, 179

Ramos Almeida C., Ricci C., 2017, Nature Astronomy, 1, 679

Rees M. J., 1974, The Observatory, 94, 168

Reynolds C., et al., 2014, preprint, (`arXiv:1412.1177`)

Richings A. J., Faucher-Giguère C.-A., 2018a, Monthly Notices of the Royal Astronomical Society, 474, 3673

Richings A. J., Faucher-Giguère C.-A., 2018b, Monthly Notices of the Royal Astronomical Society, 474, 3673

Risaliti G., Imanishi M., Sani E., 2010, Monthly Notices of the Royal Astronomical Society, 401, 197

Robinson T. G., Tadhunter C. N., Axon D. J., Robinson A., 2000, Monthly Notices of the Royal Astronomical Society, 317, 922

Rodríguez Zaurín J., Tadhunter C. N., González Delgado R. M., 2009, Monthly Notices of the Royal Astronomical Society, 400, 1139

Rodríguez Zaurín J., Tadhunter C. N., González Delgado R. M., 2010, Monthly Notices of the Royal Astronomical Society, 403, 1317

Rodríguez Zaurín J., Tadhunter C. N., Rose M., Holt J., 2013, Monthly Notices of the Royal Astronomical Society, 432, 138

Rodríguez Zaurín J., et al., 2014, Astronomy and Astrophysics, 571, A57

Rose M., Tadhunter C., Ramos Almeida C., Rodríguez Zaurín J., Santoro F., Spence R., 2018, Monthly Notices of the Royal Astronomical Society, 474, 128

Rupke D. S. N., Veilleux S., 2013, Astrophysical Journal, 768, 75

Rupke D. S., Veilleux S., Sanders D. B., 2005a, Astrophysical Journal Supplements, 160, 87

Rupke D. S., Veilleux S., Sanders D. B., 2005b, Astrophysical Journal Supplements, 160, 115

Rupke D. S., Veilleux S., Sanders D. B., 2005c, Astrophysical Journal, 632, 751

Rupke D. S. N., Veilleux S., Baker A. J., 2008, Astrophysical Journal, 674, 172

Sanders D. B., Mirabel I. F., 1996, Annual Review of Astronomy and Astrophysics, 34, 749

Sanders D. B., Soifer B. T., Elias J. H., Madore B. F., Matthews K., Neugebauer G., Scoville N. Z., 1988, Astrophysical Journal, 325, 74

Schlafly E. F., Finkbeiner D. P., 2011, Astrophysical Journal, 737, 103

Schmidt M., 1963, Nature, 197, 1040

Seyfert C. K., 1943, Astrophysical Journal, 97, 28

Silk J., Rees M. J., 1998, Astronomy and Astrophysics, 331, L1

Singh R., et al., 2013, Astronomy and Astrophysics, 558, A43

Slipher V. M., 1915, Popular Astronomy, 23, 21

Soifer B. T., Sanders D. B., Madore B. F., Neugebauer G., Danielson G. E., Elias J. H., Lonsdale C. J., Rice W. L., 1987, Astrophysical Journal, 320, 238

Spence R. A. W., Zaurín J. R., Tadhunter C. N., Rose M., Cabrera-Lavers A., Spoon H., Muñoz-Tuñón C., 2016, Monthly Notices of the Royal Astronomical Society, 459, L16

Spence R. A. W., Tadhunter C. N., Rose M., Rodríguez Zaurín J., 2018, Monthly Notices of the Royal Astronomical Society,

Spoon H. W. W., Holt J., 2009, Astrophysical Journal Letters, 702, L42

Spoon H. W. W., et al., 2013, Astrophysical Journal, 775, 127

Springel V., Di Matteo T., Hernquist L., 2005, Monthly Notices of the Royal Astronomical Society, 361, 776

Stasińska G., 2002, ArXiv Astrophysics e-prints,

Sturm E., et al., 2011, Astrophysical Journal Letters, 733, L16

Su M., Slatyer T. R., Finkbeiner D. P., 2010, Astrophysical Journal, 724, 1044

Sun A.-L., Greene J. E., Zakamska N. L., 2017, Astrophysical Journal, 835, 222

Surace J. A., Sanders D. B., Vacca W. D., Veilleux S., Mazzarella J. M., 1998, Astrophysical Journal, 492, 116

Tacconi L. J., Genzel R., Lutz D., Rigopoulou D., Baker A. J., Iserlohe C., Tecza M., 2002, Astrophysical Journal, 580, 73

Tadhunter C., Wills K., Morganti R., Oosterloo T., Dickson R., 2001, Monthly Notices of the Royal Astronomical Society, 327, 227

Tadhunter C., Morganti R., Rose M., Oonk J. B. R., Oosterloo T., 2014, Nature, 511, 440

Tadhunter C., Spence R., Rose M., Mullaney J., Crowther P., 2017, Nature Astronomy, 1, 0061

Tadhunter C., et al., 2018, Monthly Notices of the Royal Astronomical Society,

Terlevich R., Melnick J., 1985, Monthly Notices of the Royal Astronomical Society, 213, 841

Tombesi F., Meléndez M., Veilleux S., Reeves J. N., González-Alfonso E., Reynolds C. S., 2015, Nature, 519, 436

Tremaine S., et al., 2002, Astrophysical Journal, 574, 740

U V., et al., 2013, Astrophysical Journal, 775, 115

Urry C. M., Padovani P., 1995, Publications of the Astronomical Society of the Pacific, 107, 803

Veilleux S., 2002, in Green R. F., Khachikian E. Y., Sanders D. B., eds, Astronomical Society of the Pacific Conference Series Vol. 284, IAU Colloq. 184: AGN Surveys. p. 111 (`arXiv:astro-ph/0201118`)

Veilleux S., Osterbrock D. E., 1987, Astrophysical Journal Supplements, 63, 295

Veilleux S., Sanders D. B., Kim D.-C., 1997, Astrophysical Journal, 484, 92

Veilleux S., Kim D.-C., Sanders D. B., 2002, Astrophysical Journal Supplements, 143, 315

Veilleux S., et al., 2006, Astrophysical Journal, 643, 707

Veilleux S., et al., 2009, Astrophysical Journal, 701, 587

Veilleux S., et al., 2013, Astrophysical Journal, 776, 27

Veilleux S., Bolatto A., Tombesi F., Meléndez M., Sturm E., González-Alfonso E., Fischer J., Rupke D. S. N., 2017, Astrophysical Journal, 843, 18

Villar-Martín M., Tadhunter C., Morganti R., Axon D., Koekemoer A., 1999, Monthly Notices of the Royal Astronomical Society, 307, 24

Villar-Martín M., Arribas S., Emonts B., Humphrey A., Tadhunter C., Bessiere P., Cabrera Lavers A., Ramos Almeida C., 2016, Monthly Notices of the Royal Astronomical Society, 460, 130

Villar-Martín M., et al., 2017, Monthly Notices of the Royal Astronomical Society, 472, 4659

Westmoquette M. S., Clements D. L., Bendo G. J., Khan S. A., 2012, Monthly Notices of the Royal Astronomical Society, 424, 416

Whittle M., Pedlar A., Meurs E. J. A., Unger S. W., Axon D. J., Ward M. J., 1988, Astrophysical Journal, 326, 125

Yuan T.-T., Kewley L. J., Sanders D. B., 2010, Astrophysical Journal, 709, 884

Zakamska N. L., Greene J. E., 2014, Monthly Notices of the Royal Astronomical Society, 442, 784

Zakamska N. L., et al., 2003, Astronomical Journal, 126, 2125

Zubovas K., 2018, Monthly Notices of the Royal Astronomical Society, 473, 3525

Zubovas K., King A. R., 2014, Monthly Notices of the Royal Astronomical Society, 439, 400

Zubovas K., King A. R., Nayakshin S., 2011, Monthly Notices of the Royal Astronomical Society, 415, L21

Zubovas K., Nayakshin S., King A., Wilkinson M., 2013, Monthly Notices of the Royal Astronomical Society, 433, 3079